Imperial College of Science, Technology & Medicine

University of London

Windmilling in Aero-Engines

Götz von Groll

A thesis submitted to the University of London
for the degree of Doctor of Philosophy

Abstract

The 'windmilling imbalance' scenario occurs in aero-engines after a fan-blade has come off during flight and the incoming airflow rotates the fan after engine shut-down. It is the task of this project to develop an understanding of the contributing mechanisms of the post-fan-blade-off dynamics and the capability to perform a reliable numerical windmilling analysis.

Large out-of-balance forces caused by the missing fan-blade provide a source of excitation for the whole engine-wing-aircraft structure. Clearances which are sufficient during normal operation can now be overcome by vibrating components, thus leading to rotor/stator interaction, which in turn can cause a rich mixture of effects associated with rub related phenomena. The presence of these effects manifest themselves in the occurrence of multiple solutions for steady-state scenarios, amplitude jumps during rotor acceleration, and vibration responses at generally different/multiple frequencies of the exciting unbalance force.

The numerical simulation of these effects is achieved with time domain shooting methods and harmonic balance in the frequency domain. The quantitative aspects of these effects are sensitive to dynamic models used. Therefore, the choices of particular models are verified by correlating the simulated results against measurements from a test rig build during the course of this project. This provides the necessary confidence that the mathematical modelling performs well enough to capture the underlying physical effects measured on a real system.

Acknowledgements

Contents

IV

List of Figures

List of Tables

Notation

Latin Symbols

A	system state-space matrix
B	transfers force vector into state-space notation
$\mathbb{C}^2$	set of functions with a continuous second derivative
c, C	damping coefficient, damping matrix
F	Fourier coefficients of force
f	force (vector)
h	gap size between rotor and stator
$\Im$	imaginary part of complex value
i	$\sqrt{-1}$
k, K	stiffness, stiffness matrix
m, M	mass, mass matrix
n, N	index of harmonic component, number of harmonics
$\Re$	real part of complex value
R	Fourier coefficients of deflection
r	deflection (vector) in y-z plane (in complex co-ordinates)
t, T	time, period of oscillation
x, y, z	co-ordinates, x along shaft, in radial plane

Greek Symbols

α	arc-length (continuation), or rate of shaft acceleration ($\dot{\Omega}$)
γ_{c}	ratio of contact to rotor stiffness
γ_{k}	ratio of stator to rotor stiffness
γ_{m}	ratio of stator to rotor mass
δ	rotor/stator contact depth
ϵ_{m}	mass eccentricity of rotor
$\epsilon_{\mathrm{r}}, \epsilon_{\mathrm{s}}$	geometric eccentricity of rotor, stator
ζ	critical damping coefficient
λ	eigenvalues (complex)
μ	coefficient of friction
ν	sub-harmonic component
ρ	force angle due to friction
ϕ	phase angle of rotor ($\int \Omega\, dt$)
ψ	angle of rotor/stator contact
Ω	rotor speed of rotation
ω	whirl frequency
$\omega_{\mathrm{r}}, \omega_{\mathrm{s}}$	rotor, stator natural frequencies

Subscripts

c	rotor/stator contact
n	harmonic component
u	unbalance
r	rotor system
s	stator system

Superscripts

$\cdot$	differentiation with respect to time
$\tilde{}$	hyper-matrices
$\hat{}$	matrices of reduced system
$\star$	root of algebraic equation or particular solution of BVP

Abbreviations

BVP	boundary value problem
DOF	degree-of-freedom
EO	engine order (rotor shaft speed)
FEM	finite element method
FFT	fast Fourier transform
FRF	frequency response function
HBM	harmonic balance method
IVP	initial value problem
ODE	ordinary differential equation

Chapter 1

Introduction

1.1   Definition of Windmilling

Windmilling is a phenomenon which can occur in aero-engines after a fan-blade has come off during flight. A fan-blade-off event is rare with only very few incidents per year and is, in most cases, no threat to the safety of the aeroplane. For an aero-engine to be certified by the aviation regulatory bodies, one requirement is that the manufacturer proves (with 'fan-blade-off tests') that the fan-blade stays contained within the engine. However, internal damage to the integrity of the engine is usually such that the engine immediately stops to produce any power. For the remainder of the flight the incoming airflow will cause the engine to rotate, thus the name 'windmilling imbalance' for this scenario. As one blade is missing, large out-of-balance forces of the order of a few tonnes from the now-asymmetric fan provide an excitation for the engine-wing-aircraft structure. Clearances which are sufficient during normal operation might now be overcome by vibrating components excited by the large out-of-balance force. This leads to rotor/stator interaction, which can potentially cause a rich mixture of effects associated with rubs and impacts.

1.2   Description of the Problem

The windmilling phase starts after the transient events of a blade-off have decayed — the blade containment and related calculations are an intricate issue in itself and subject to a separate ongoing development effort and therefore not part of this task — and stops when the aircraft has landed. For the remainder of the flight the engine will rotate at a particular speed which is determined by the incoming airflow and which, in turn, depends on the speed of the aeroplane. The plane changes its speed only slowly, so that the whole flight can be regarded as a concatenation of time-slices with constant

speeds. This allows the assumption that the vibration behaviour of a windmilling engine is in a steady-state.

The large out-of-balance forces due to the missing blade are by far the dominant source of excitation for the airframe structure. Its frequency of excitation is equal to the windmill speed of the shaft carrying the fan and low pressure (LP) turbine. This frequency is also referred to as first engine-order speed of that shaft. Rotor/stator interaction within the engine can provide a wide range of further excitation frequencies which, should some of them be close to natural frequencies of the airframe structure, can lead to excessive vibration in the wing, fuselage, or cabin in particular. In engineering structures it is the lower frequency components in the excitation spectrum that have the biggest potential to cause large-amplitude vibration. A typical windmill speed of the fan (and thereby primary frequency of the out-of-balance forces) lies somewhere around 1000rpm (17Hz), which is still in the range of airframe modes but well above the lower modes of vibration of the airframe/wing/engine. It is therefore the response frequencies which lie below the out-of-balance excitation (sub-harmonics to the first engine-order) that are of bigger interest in the windmill scenario than the super-harmonic components (above first engine-order).
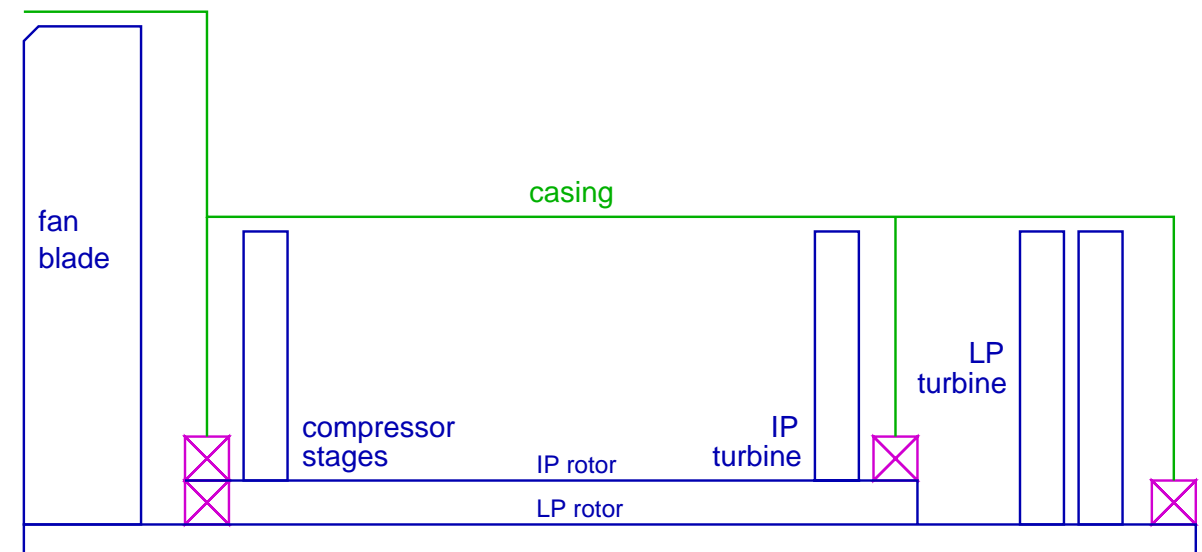
Figure 1.1: Sketch of whole engine

Figure 1.1 is a sketch of an engine showing two spools. In the sketch, LP is the low-pressure and IP or HP the intermediate-pressure or high-pressure spool. The four crossed boxes signify bearing and/or squeeze-film-damper locations. In case of a fan-blade loss or front-bearing failure, the bearings and squeeze-film-damper in the front half of the engine may be destroyed. The analysis therefore focuses on the front-half of the engine, a post-fan-blade-off sketch is shown in Figure 1.2. Points A and D refer to locations where blades are touching a casing, and B and C to inter-shaft contact.
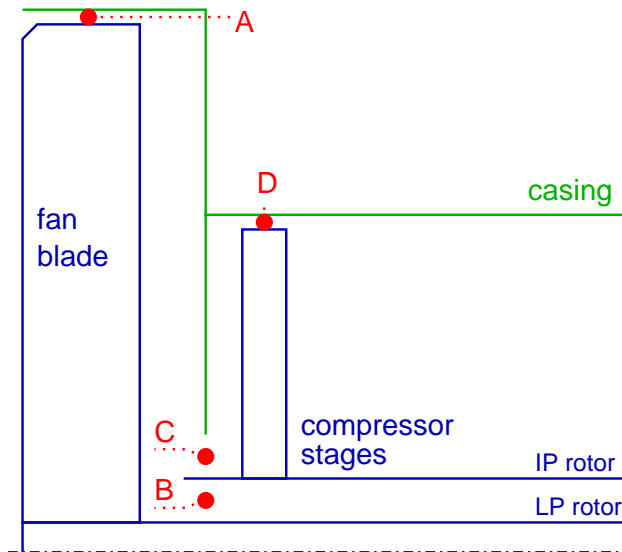
Figure 1.2: Analysis focus on front part of engine

Figure 1.3 shows an overview of the main physical ingredients of a windmilling system, and their effect on the dynamics of the system. When rotor and stator are in contact at any of the locations A–D described above, the overall rotor stiffness is higher than without the stator contact. The rotor stiffness is therefore time-variant depending on the current contact condition. This time-variance in stiffness causes sub- and super-harmonic frequency responses to occur, as well as sudden 'amplitude jumps' (discussed later in literature review). Intermittent impacts between rotor and stator can facilitate chaotic vibration and the emergence of sub-harmonic frequency components. These are the factors of primary importance for the global dynamic behaviour of the system. Furthermore, the missing fan-blade is responsible for the non-axisymmetric inertia (which causes super-harmonics) and mistuning in the overall fan-blade-assembly (which can couple the shaft/disc/fan-blade vibration). During rotor/stator contact, friction is induced which may potentially lead to high-amplitude reverse whirling of the rotor shaft.

When building a numerical model that represents these physical properties, the resulting equations of motion are nonlinear. To solve these equations, time-domain methods such as time-integration and frequency-domain methods such as harmonic balance have been used in this study and, where possible, both methods were used in parallel to cross-check results.
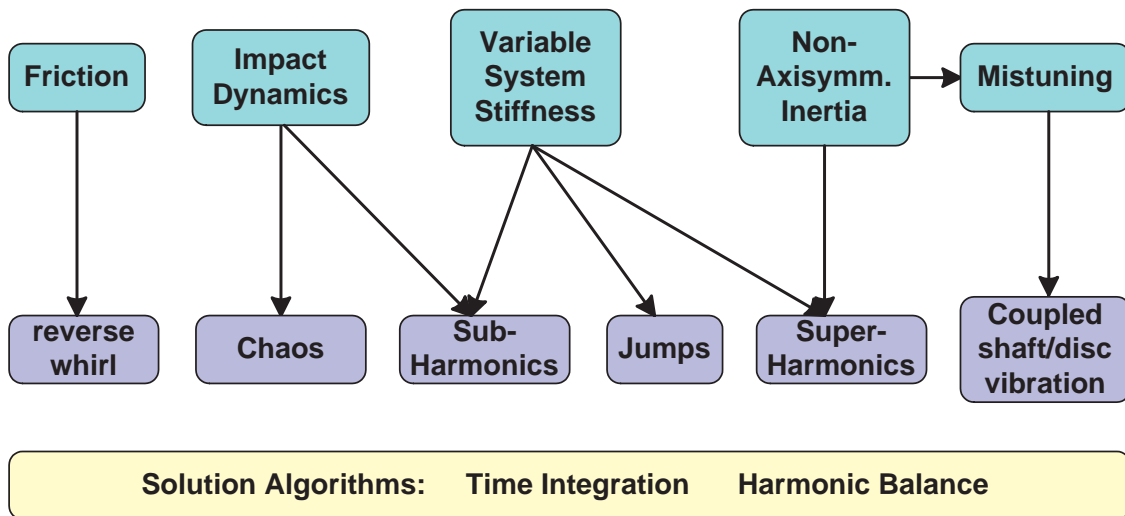
Figure 1.3: Model ingredients

1.3   Historical Background and Motivation

Without referring to specific incidents, details of which are not in the public domain and thus not readily accessible, the next paragraph quotes from FAA regulations, which is uncharacteristically explicit in its description:

"BACKGROUND. The vibratory loads resulting from the separation of a fan blade has [have] traditionally been regarded as insignificant relative to other portions of the design load spectrum for the airplane. However, the progression to larger fan diameters and fewer blades with larger chords has changed the significance of engine structural failures that result in an imbalanced rotating shaft. This condition is further exacerbated by the fact that the fans will continue to windmill in the imbalance condition following engine shut down. Although current rules require provisions to stop the windmilling rotor if it could jeopardize safe flight, these fans are practically impossible to stop in flight. The loss of a fan blade, and the subsequent damage to other rotating parts of the fan and engine, may induce significant structural loads and vibration throughout the airframe that may damage [the] primary structure, including, but not limited to, the engine mounts, nacelles, and wing, as well as critical equipment mounted on the engine or airframe. Also, the effect of flight deck vibration on displays and equipment is of significance to the crew's ability to make critical decisions regarding the shut down of the damaged engine and to carry out other operations during the remainder of the flight. Several recent in-service events have shown that failures of the shaft bearings and shaft support structure have also resulted in sustained high vibratory loads. These vibratory loads from the loss-of-centerline condition produce vibratory loading similar to the sustained imbalance loads resulting from fan blade loss. Experience has demonstrated that there are two sustained imbalance conditions that may effect [affect] safe flight: the high power condition and the windmilling condition.

The high power imbalance condition may result just after blade failure but before the engine is shut down or otherwise spools down. This case usually involves losing a smaller portion of a single blade and lasting several seconds. In some cases it has caused difficulty in reading instruments that may have aided in determining which engine was damaged, and the extent of the damage. The windmilling imbalance condition results from loss of centerline support or loss of a fan blade along with additional collateral damage. This case may last until the airplane completes its diversion flight, which could be several hours." (FAA, 1999)

As problematic windmill incidents with large amplitude vibration have started to occur only fairly recently, there is not yet a routine analysis procedure that the civil aviation industry could use to determine the windmill conditions of engines/airframes in existence or in development. The FAA is currently inviting industry contributions to aid the setting up of a regulatory framework that would provide guidelines for a windmill analysis procedure:

"FAA POSITION. It must be shown by a combination of tests and analyses that, after partial or complete loss of an engine fan blade, including ensuing damage to other parts of the engine, or loss of centerline shaft support, the (model) airplane is capable of continued safe flight and landing. The evaluation must show, that before spool down and during continued operation at windmilling engine rotational speeds, the engine induced vibrations will not cause damage to either the primary structure of the airplane, or to critical equipment that would jeopardize continued safe flight and landing. The degree of flight deck vibration must not prevent the flight crew from operating the airplane in a safe manner. This includes the ability to read and accomplish checklist procedures. This evaluation must consider the effects on continued safe flight and landing from the possible damage to primary structure, including, but not limited to, engine mounts, inlets, nacelles, wing, and flight control surfaces, as well as critical equipment (including connectors) mounted on the engine or airframe. For the windmilling condition, the evaluation must cover the expected diversion time for the airplane." (FAA, 1999)

Thus, industry needs a detailed understanding of the vibration mechanisms involved in these cases and to develop the necessary analytical tools with sufficient predictive capabilities to aid the design process, possibly even tools of such reliability that tests where these failure modes are imposed do not need to be carried out in practice.

1.4   Objectives of this Study

It is the aim of this project to gain some insight into the rotor/stator interaction and overall system dynamics in a windmill situation. This insight is sought to develop an understanding of the contributing mechanisms which are activated by the rotor/stator

interaction and to provide an approach of how these mechanisms may be modelled numerically.

The specific objectives of this project are to:

- build a mathematical model for dynamic behaviour that includes a numerical representation for the nonlinear elements representing the rotor/stator contact

- develop appropriate routines capable of solving the resulting non-linear differential equations which describe the dynamic behaviour of the model

- conduct parameter studies with the numerical model to map out the range of dynamic behaviour of the system and possible vibration phenomena

- build a test rig as a simple physical model of the windmill scenario to measure its dynamic behaviour

- compare the simulated with the measured results to establish whether the numerical approach is capable of predicting the behaviour of the physical test rig in a qualitative and quantitative way

Depending on the level of agreement that is found between simulated and measured behaviour, a certain amount of confidence can be drawn from this exercise. If the same categories of dynamic behaviour seen in the measurements (for example amplitude jumps, sub- and super-harmonic frequency components) can be found in the numerical results, that at least shows that the numerical dynamic model is sophisticated enough to reproduce qualitatively the behaviour seen in a physical system. If the quantitative agreement is not within the same order of magnitude, one can conclude that the model ingredients, in particular the non-linear features such as gap/rub, do not represent the physics of the problem in a very accurate way, perhaps because some features are not included or the chosen input parameters such as friction coefficient are wrong. If the quantitative agreement is within the same order of magnitude, the numerical model can at least provide some rough guidelines for the designer. Ultimately, of course, it will be the industry and its regulators who decide, based on practical experience, what level of agreement is sufficient so that the simulated results can be fed back into the design or troubleshooting process or even be used for certification purposes.

1.5 Literature Review

1.5.1 Overview

Windmilling is a relatively new phenomenon and there exists no literature in the public domain on the topic as such. However, the dynamics of windmilling encompass a range

of mechanisms which are not unique to the windmilling problem, and thus have been studied in other contexts.

A number of dynamics topics are relevant for successfully conducting a windmilling simulation. The rotor/stator interaction effects include impact and rub (between blade and housing, or between LP and IP rotors), which cause friction (with thermal effects) and modification of system stiffness due to contact. It has been shown in some of the literature discussed here that relatively simple models including these components can exhibit a wide range of non-linear phenomena such as sudden amplitude jumps triggered by a change in excitation frequency, or sub- and super-harmonic and chaotic vibration.

There are two literature surveys which include such topics related to windmilling. Ehrich (1988) deals with non-linear vibration in rotating machinery and focuses on non-linear stiffness, thermal and aerodynamic effects. This survey covers not only gas-turbine related papers but also work concerning centrifugal pumps and compressors. Muszynska (1989) focuses on rub occurring in rotating machinery and thus covers papers in the areas of friction, impacting, non-linear stiffness, and thermal effects.

Work which seems directly applicable to windmilling is briefly discussed in this section, however, for a more general, non-windmilling specific overview of the topics mentioned above, the reader is referred to these two aforementioned surveys. As discussed earlier in this Chapter, the following elements might be relevant to a windmilling system:

- variable system stiffness
- rub between rotor and stator
- impacts between rotor and stator
- coupled shaft/disc vibration and mistuning
- thermal effects due to rub
- non-axisymmetric inertia
- aerodynamic cross-coupling

In the following sections, the papers dealing with these various aspects of rotor/stator interaction listed above are reviewed.

1.5.2   Variable System Stiffness

The effect of variable system stiffness on the vibration of rotating machinery, mostly as a result of rub and bearing clearances, has been studied in a large number of papers. The studies of rub and bearing clearances with respect to stiffness can be grouped together, as both effects cause a periodic change in the system stiffness. In addition to a change

in the system stiffness, rub also includes local impact, friction, and thermal effects, which are covered separately. The majority of studies deal with a modified Jeffcott rotor (see the example shown in Figure 1.4), and only a few analyse representatively complex multi-degree-of-freedom systems.
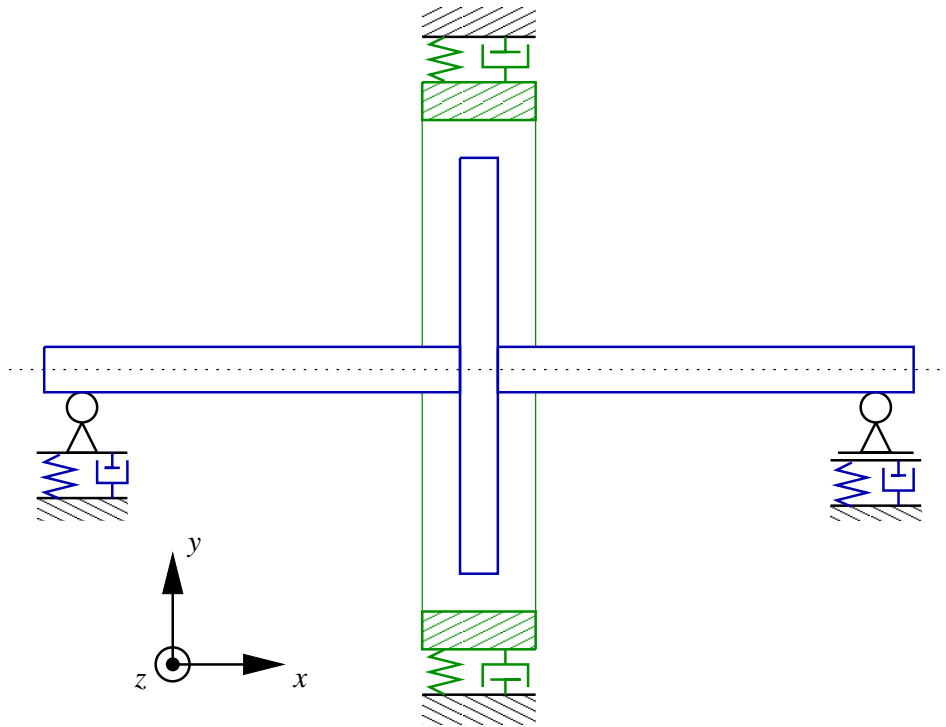
Figure 1.4: A Jeffcott rotor with stator

All studies covering some form of rotor/stator interaction treat the stator as a rigid body, flexibly suspended on springs, but which is not capable of deforming flexibly, with the exception of Schmiechen (1997), whose rotor and stator are both modelled as flexible bodies. Most studies do not attribute the stator with its own dynamic behaviour, i.e. the stator is assumed to have negligible mass. However, a simple system such as that shown in Figure 1.4 is already capable of rich bifurcational and chaotic behaviour (Kleczka et al., 1992), even with all the simplifications stated above. Hence, once can expect that modelling a realistic system with realistic mass and stiffness characteristics is a difficult task indeed.

The jump phenomenon

In systems with rub or bearing clearance the system stiffness changes with respect to the state of contact or non-contact, and while the stiffnesses of the individual states may well have a linear characteristic, the global behaviour is non-linear. Possibly the

simplest model of a system with a non-linear stiffness is the Duffing[*] oscillator, which exhibits an interesting effect regarding the amplitude of the system, the so-called 'jump phenomenon'. In some frequency ranges, a slight change in excitation frequency can cause the steady-state response to 'jump' to a higher or lower level, depending on whether the change in excitation frequency is positive or negative. Shown in Figure 1.5 is the amplitude response of the system depicted in Figure 1.4. There is a distinct similarity to the behaviour of the Duffing oscillator, although a notable difference is the presence of kinks at $r = 1$ in the amplitude curve in this Figure, which arise from the sudden change in system stiffness when the rotor comes into contact with the stator.
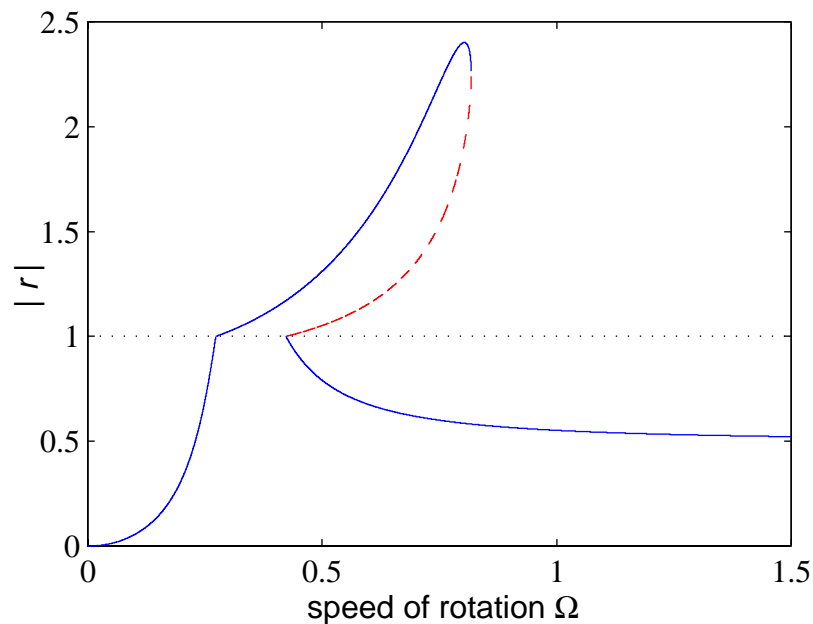
Figure 1.5: The jump phenomenon

Ehrich & O'Connor (1967) and Crandall (1987) studied the behaviour of the system shown in Figure 1.4 analytically, and Isaksson (1994) extended the analysis to the investigation of the influence of stator-offset to the turning points and stability of the solution branches. Ishida et al. (1997) discussed non-stationary oscillations of such a system during acceleration through critical speeds. Markert & Wegener (1995) included the stator mass in their model, and solve the equations via time integration for both transient and steady-state simulations.

Sub- and super-harmonic vibration

The literature treating sub-and super-harmonic vibration in rotor dynamics evolved with the initial aim of explaining the physics behind the observed sub- and super-synchronous vibration phenomena (Ehrich, 1966; Bently, 1974; Ek, 1980; Childs, 1978;

---

[*]see any text book on nonlinear dynamics, the Duffing equation is: $a\ddot{x} + b\dot{x} + cx + dx^3 = f \cos \omega t$

Ehrich, 1988, 1992), with the final aim of providing methods with which general rotor-stator systems could be analysed. To emphasise that these harmonic components can have a notable influence, Ehrich (1988) reported that strong sub-harmonic vibrations of orders as low as $\Omega/9$ have been observed in aero-engines under operating conditions. It is found in the papers cited below that a simple Jeffcott rotor with bearing clearances or a clearance between rotor and stator (Figure 1.4) produces a sufficiently complex analytical model to demonstrate the existence of sub- and super-synchronous rotor vibration. An essential condition for these non-synchronous components to build up is that the system stiffness must be non-symmetric when seen from the static equilibrium position (Choi & Noah, 1988; Ehrich, 1989). In turn, this can be caused by a side force, e.g. gravity, or by an eccentricity in the rotor/bearing assembly.

(a) y, z are symmetric   (b) y, z non-isotropic   (c) y is symmetric, z is not
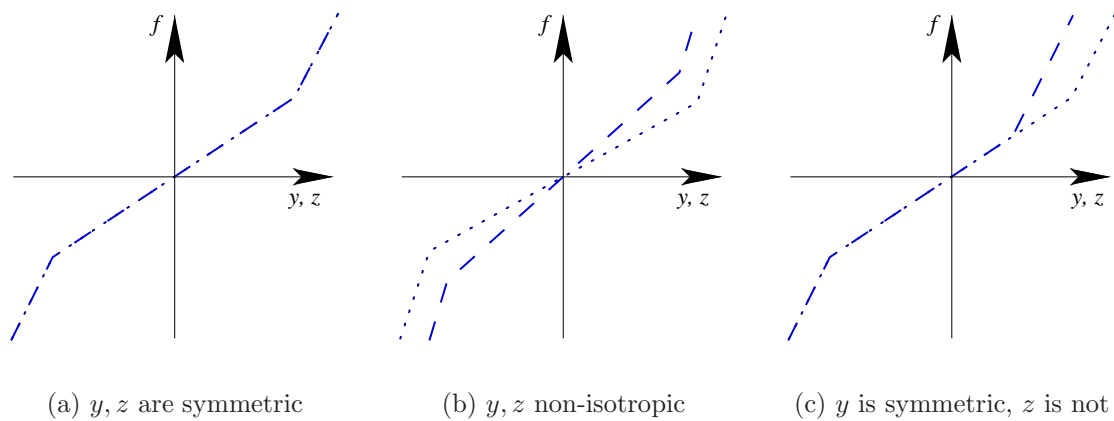
Figure 1.6: Examples of symmetric and non-symmetric system stiffnesses

Figure 1.6 shows symmetric and non-symmetric stiffnesses, where force f is plotted versus displacement y (in vertical direction, dotted line) and z (horizontal direction, dashed line). In a Jeffcott rotor, the vibration in y and z planes is uncoupled, so the change in stiffness isotropy in Figure 1.6(b) affects the vibration characteristics independently from the change in $+z$ and $-z$ symmetry in Figure 1.6(c). The deviation from isotropy causes different natural frequencies in y and z planes, whereas the deviation from symmetry causes sub-and super-harmonic vibration to emerge in the vibration spectrum.

Analytical studies   Childs (1978) used the perturbation method for a Jeffcott rotor which had a bearing clearance. Muszynska (1984) analysed a system with rub caused by an obstacle in the whirl orbit. The change in stiffness over one orbit was modelled as a periodic step function, approximated as a truncated Fourier-series. In both papers the orbit of the rotor was derived analytically, and the resulting equations were cast in

the well-known Mathieu[†] form. However, the Mathieu equation has periodic solutions with the lowest component being $\Omega/2$, so lower frequency components like $\Omega/3$, which have also been measured previously (Ehrich, 1966; Bently, 1974; Ek, 1980), cannot be explained with this equation. Childs (1982) used a more extensive approach by performing a perturbation analysis after Linstedt & Poincaré, which yielded an expression with a higher harmonic forcing function, thereby explaining the existence of the subharmonic $\Omega/3$ as well as that at $\Omega/2$. Theoretically, the perturbation analysis can be carried further by including perturbations of higher orders, which, in turn, would exhibit a richer vibration spectrum. However, such a task is cumbersome and nowadays available numerical methods are used to carry the analysis further.

Numerical studies Markert & Wegener (1995) investigated parameter fields for a Jeffcott rotor with a retainer bearing, similar to the system shown in Figure 1.4. Their model included the stator mass, and the equations were solved by time integration. Géradin & Kill (1988) used equivalent linearisation for small non-linearities with harmonic balance[‡] of the Taylor series expressions, and they used time integration for large non-linearities. Choi & Noah (1987) made use of the harmonic balance method to extract sub- and super-harmonic components in the vibration spectrum. The rotor orbit was derived numerically in the time-domain and then transformed into the frequency domain.

General rotor systems with non-linear components such as rub locations and bearing clearances cannot be solved analytically, and so numerical procedures are essential. Kim et al. (1991) used the aforementioned harmonic balance method to solve a multi-degree-of-freedom system, using impedance matrix reduction to retain only the non-linear co-ordinates. Kim & Noah (1991) expanded the system by including the stator dynamics. A limitation of the harmonic balance method is that it can only capture harmonic components. Any frequencies which are not pure sub- or super-harmonics of the excitation (as can be the case with backward whirl, for example, or chaotic vibration), will be not be found. As these papers deal with dead-band clearance in bearings, there is no rub, and thus no impact dynamics are included in the models, which typically worsen the conditioning for numerical analysis. By trying to duplicate the results in Choi & Noah (1987), it became clear that the numerical solution of the harmonic balance system is tricky, as the efficiency strongly depends upon a good initial guess for the iterative solution procedure. Another disadvantage of this approach is that the number of equations to be solved increases to a multiple depending on the number of harmonics included in the harmonic balance analysis.

As a remedy for the shortcomings of the harmonic balance analysis, Sundararajan & Noah (1997) proposed a time-domain shooting algorithm which was adapted for non-autonomous systems. It was suitable to find multiple periodic solutions, and a continuation method

---

[†]the Mathieu oscillator is: $\ddot{x} + (a + 2\epsilon \cos 2t)x = 0$, see for example Nayfeh & Balachandran (1995)
[‡]covered in Chapter 3

was proposed to pass through the turning points (bifurcation nodes). The numerical algorithm is supposedly better behaved than the harmonic balance method, and the number of equations to be solved is the same as the number of degrees of freedom of the system.

1.5.3 Full annular rub — forward and backward whirl

All the studies mentioned in section 1.5.2 assumed full annular rub when investigating the jump phenomenon. Besides the jump phenomenon, some studies deal with full annular rub at constant speed, investigating contact and bearing loads, frequency spectra, and rub conditions. Using a simple Jeffcott rotor with a stator (see Figure 1.4), any frequency in the interval bounded by the natural frequencies of the rotor and stator can occur (Ehrich, 1989). Isaksson (1996) extended the single disc rotor shown in Figure 1.4 to a model with two discs, showing that whirling along a stator annulus even with small clearance could cause high amplitudes elsewhere along the shaft. Choy & Padovan (1987) performed a non-linear transient analysis describing the development from the initial phases of rub to backward whirl. As the mass of the casing was neglected, this analysis did not include any impact modelling. Choy et al. (1989) used a multi-degree-of-freedom model where the casing was rigid but is flexibly suspended. Interestingly, the rotor contained blades rubbing against the casing, where the blade/casing interaction was modelled with a combined longitudinal/flexural stiffness for the blades. As the casing is assumed to be massless, there are no impact dynamics in this model, either. The blade/casing interaction was described in more detail in Padovan & Choy (1987).

Crandall (1990) investigated the backward whirling of a shaft under pure rolling conditions, the so called 'dry whirl'. Dry whirl was only possible within a certain speed interval $[\Omega_1, \Omega_2]$, where Ω_1 was the speed which causes a sufficient out-of-balance force to trigger rotor/stator contact, and Ω_2 was the combined rotor/stator frequency. For a rotational speed $\Omega > \Omega_2$, slip occurred, which the author called 'dry whip', and the whip frequency was 'locked': the frequency as well as the deflection remained constant for increasing speeds. Lingener (1990) investigated the whirl frequency 'lock' effect experimentally and analytically. Rolling dictates that the reverse whirl (dry whirl) frequency is the product of the speed of rotation Ω and the ratio of shaft radius to clearance ($\frac{r}{c}$). However, from a certain speed onwards, an increase in running speed no longer increases the reverse whirl frequency. Slip is added to the rolling motion, the level of vibration increases greatly, but the whirling frequency remains constant, giving rise to the expression frequency 'lock' effect.

Williams (1996b) used an analytical model to examine the contact loads and limit cycles of backward (reverse) whirl. The stator was included with its own dynamic behaviour, but as rotor and stator were assumed to be in continuous contact, there were no impact dynamics in this model. In Williams (1997), however, a multi-degree-of-freedom time integration was performed, and the impact was modelled as fully elastic.

It was found that light contact between rotor and stator could be sufficient to initiate severe reverse whirl. The results of the steady-state limit-cycle compared well with the previous analytical model. The simulated characteristics were observed in principle in the reported measurements of Williams (1996a), but quantitatively there was little agreement, which was explained by possible non-linearities of the test rig which were not accounted for in the simulation.

1.5.4   Impact

All papers reviewed so far consider the impacting bodies to be rigid, although introducing some 'penalty' stiffness in the case of rotor to stator impact. Muszynska (1984) included in her analysis an impact model which regarded the impact force as an 'average' force over one period of rotation. The coefficient of restitution in the model was zero. Using these assumptions, the results were presented analytically for a Jeffcott rotor with an obstacle such as a protrusion in the whirl orbit. The order of the sub-synchronous vibration was related to the radial impact force, e.g. if $\Omega > 3\omega_n$, increasing radial force caused the sub-synchronous regime to switch from $\Omega/3$ to $\Omega/2$. Notable was that friction seemed to influence the partial rub vibration very little. Goldman & Muszynska (1993) used a piece-wise, continuous, local stiffness and damping during contact. In the subsequent analysis, the local stator stiffness was assumed to be much higher than the stiffness of the shaft centerline radial deflection, an assumption which is valid only for rigid stators. This allowed the displacements and frequencies to be expressed as truncated power series with higher order terms of only second degree. The authors divided rub into two parts: the 'chattering regime', which was caused by relatively elastic impacts, where the rotor bounced off the stator with enough energy to hit the stator again at a different location, and so on, and the 'normal force controlled regime', where the rotor lost sufficient energy during the impact to stay in continuous contact with the stator.

Ghauri et al. (1996) studied the transient dynamics of a system with a step change in unbalance. A corresponding change in rotating inertia (e.g. when simulating blade loss) was ignored. The impact is modelled as classic rigid body impact with infinitesimally small duration time, inhibiting the simulation from accounting for changes in rotor displacement during contact, as was possible e.g. in the model of Goldman & Muszynska (1993).

Fumagalli & Schweitzer (1996) focused on the onset of whirl motion due to impact. Using a sophisticated test rig with magnetic bearings, experimental data were produced as well as a theoretical impact model. This impact model built on the Hertz theory of static, normal contact between linear elastic bodies. The derived spring/damper characteristic of the impact was non-linear and the coefficient of restitution was speed-dependent. However, only normal impact was considered, and an impact-free, dry-friction sliding motion in the tangential direction was used to model tangential forces.

It was therefore viable to model e.g. inter-shaft impacts using this approach. It is, however, not suitable for blade/stator impacts, as the geometry is different in such a case and impacts in the tangential direction with corresponding restitution coefficients can occur. Schmiechen (1997) dealt with the impact of flexible rotating and stationary bodies by using speed-dependent stiffness characteristics, where the speed-dependent term allowed for energy dissipation during impact.

1.5.5   Mistuning and Coupled Shaft/Disc Vibration

It appears that there is currently no large-scale, commercially-available finite element program that offers the possibility to model the gyroscopic moments of a rotating flexible disc which is mounted on a flexible shaft. As a consequence, at present the disc is either modelled as flexible (although the gyroscopic moments caused by the spin are ignored) or the disc is modelled as rigid (in which case the gyroscopic terms can easily be included in the FE analysis, Hohlrieder & Irretier (1996)). With a blade missing, the assembly would be heavily mistuned, with the nodal lines no longer running through the centre of the disc. The rotor vibration, if it included higher frequency components which matched the blade/disc natural frequencies, could therefore excite a range of modes in the fan-blades which are not excited in normal running conditions.

An experiment has been conducted to investigate the influence of coupled shaft/disc vibration in the presence of bearing clearances. Flowers & Wu (1996) reported on measurements taken from a rig with a stiff rotor and tuned, flexible disc, where the bearing clearances present at one end of the support for the rotor shaft caused in some configurations high-amplitude backward whirling modes with higher harmonics present. The forward whirling modes had lower amplitudes. In order to excite coupled shaft/disc vibration at higher-order speeds, the 3Ω, 5Ω, ... speed had to coincide with a natural frequency. It was observed that this coincidence had to be fairly exact, i.e. the speed range within which the rig would show higher order excitation is very narrow.

1.5.6   Thermal Effects

Heat-induced vibrations (due to rub, not related to combustion heat) have been studied primarily in connection with power-plant turbines, but the same mechanism is in principle also applicable to aero-engine gas turbines. When a rotating shaft rubs against a stationary component, for example packings or labyrinth seals, heat is generated due to friction, and some of the heat transfers into the shaft. As the temperature at the point of contact on the shaft is higher than at a point diametrically opposite, the shaft bows. Depending on the angular relationship between the rub location, shaft centre of gravity an centre of geometry, the thermally-induced bow can increase or decrease the resulting unbalance, thereby causing vibration levels to rise or fall. With increasing vibration, there will be higher friction at the rub location, resulting in higher heat

transfer, an increase in shaft bow and unbalance, resulting in even higher vibration. On the other hand, if the angular relationship causes the thermally-induced bow to reduce the amount of unbalance, the level of vibration is reduced.

Both scenarios have a spiral characteristic on an amplitude/phase-angle plot, giving name to this mechanism of thermally-induced vibration as 'spiral vibrations' or 'Newkirk effect'. Newkirk (1926) brought the vibration he observed into context with heat-induced bowing of the shaft, and Kroon & Williams (1939) noted the spiraling nature of the vibration when plotting amplitude against associated phase angle of the measured vibration in the synchronous rotating frame of reference.

Kellenberger (1980) and Dimarogonas & Paipetis (1983) performed an analytical analysis of a uniform rotor model which rubs midway along the shaft. Kellenberger (1980) introduced four proportionality factors concerning heat distribution, conductivity, thermal expansion, and geometry, together with the assumption that the thermal bow is proportional to the excess temperature. In this way, he obtained a linear set of equations, and concluded that the case of opening or closing spiral vibration depends mainly on the ratio of heating power absorbed into the shaft to heating power transferred out of the shaft. Dimarogonas & Paipetis (1983) provided a more detailed analysis, which was possible to this extent because a simple geometry configuration was chosen for the problem. It was found that the main factor determining the stability of the system was the phase angle between static and dynamic bow. This clearly depends on the speed of rotation of the shaft as it affects the phase angle at which the static bow (or eccentricity) relates to the dynamic bow due to the resulting unbalance. Liebich & Gasch (1996) expanded Kellenberger's model of a Jeffcott rotor to a multi-span rotor by using mode-shapes determined by a finite element analysis. As the paper built on the work by Kellenberger (1980) and Schmied (1987), the same conclusion was drawn that the stability depends mainly on the heat inflow/outflow ratio and is thus independent of speed of rotation.

1.5.7   Non-Axisymmetric Inertia

The presence of non-axisymmetric parts in the rotor, e.g. a fan with a blade missing, produces equations of motion with periodic coefficients when these equations are expressed in inertial co-ordinates (Xu & Gasch, 1993). As the engine support is assumed to be non-isotropic, nothing would be gained by expressing the equations in rotating co-ordinates, as the non-isotropic stator would then produce periodic coefficients in the equation of motion (Genta, 1988). Such a system with periodic mass and stiffness matrices features higher harmonic components in its response to a harmonic excitation (Yakubovitch & Starzinskii, 1975).

In a windmilling scenario it is the sub-synchronous vibrations rather than the super-synchronous components that are of greater concern, as vibration in the low frequency range of the sub-synchronous components with $\Omega/2$, $\Omega/3$ have the potential to transmit

larger amounts of energy into the wing/airframe structure than the higher frequency range of the super-synchronous components. It is therefore possible that the super-synchronous components created by non-axisymmetric inertia or stiffness parts are not relevant in a windmilling analysis.

1.5.8   Aerodynamic Cross-Coupling

'Aerodynamic cross-coupling' refers to blade-fluid interaction forces. Structural vibration affects the blade-fluid interaction, as relevant parameters such as airstream/blade angle are changed by the structural vibration of the system. This causes different forces on the blades interacting with the fluid. Such a change in force can destabilise the whole system under certain conditions. One such phenomenon is the tip-clearance effect. Instability due to the tip-clearance effect has been observed in impellers of turbines as well as compressors (Tondl, 1990; Ehrich, 1993; Ziegler, 1996; Ehrich, 1988, includes a summary of previous publications). It is reasoned that an impeller, which is whirling within the clearance between rotor and stator, inevitably has blades along its annulus which are closer to the stator, and the blades diametrically opposite are further away from the stator. The blades closer to the stator operate at a higher efficiency, and the opposite is true for the blades further away from the stator. It follows, therefore, for a turbine impeller that the blades operating at higher efficiency produce a larger tangential force than the blades operating at lower efficiency, resulting in a destabilising net torque in direction of the shaft rotation. These forces are called Thomas or Alford forces (Thomas, 1958; Alford, 1965).

1.5.9   Conclusions

It is discussed now, after reviewing these features that have been studied in the literature with different problems in mind, what their relative importance to the 'windmill imbalance' problem is. At this early stage in the windmilling analysis, one wants to concentrate on the primary factors that will dominate the global dynamic behaviour. These primary factors that make up the basis of windmilling are: (i) variable system stiffness, (ii) local impact or continuous contact resulting in (iii) rub with friction. Given the capability to incorporate these factors (i) – (iii) into a numerical model, it would also be no difficulty to add: (iv) non-axisymmetric inertia, and (v) mistuning and coupled shaft/disc vibration effects, as these are automatically covered by more detailed finite-element models of a system. However, as argued in the literature review, these effects are not expected to dominate the global dynamic system behaviour and, therefore, it would not be very useful at this stage to conduct a detailed parameter study of (iv) and (v).

It would be difficult to include: (vi) thermal effects, and (vii) aerodynamic cross-coupling, as they are not easily incorporated into a structural dynamics model. The

analysis of thermal effects requires the generation of a heat flow model which is based on local rub conditions. Furthermore, the feedback of heat-flow into the equations of motion has an influences on the dynamic properties of the rotor. However, heat generated by blade/casing contact is sufficiently far away from the rotor shaft to have a significant effect on the rotor shaft bow. In situations where the rotor shaft is rubbing directly, for example against another shaft or bearing housing, thermal effects may have an influence on the dynamic behaviour and are not to be dismissed lightly. However, the rubs under windmill conditions are expected to be (a) less continuous and more intermittent in nature and (b) on a much smaller time scale than heat flow effects, so that the influence of heat at this early stage of investigation into the vibration phenomena of the windmilling problem is neglected.

The analysis of aerodynamic cross-coupling involves the modelling of fluid dynamics. However, the engine is not producing any power output under windmilling conditions, and the rotation is merely caused by the incoming airflow. It is therefore assumed that the actual pressure difference at the blades is small compared with normal operating conditions. Furthermore, the airflow will be heavily disturbed due to the missing fan-blade, which further reduces the blade efficiency. Hence it seems reasonable to ignore aerodynamic cross-coupling effects in a windmilling analysis, but more caution might be necessary when related abnormal running conditions, for example a front-bearing failure (which might not cause a power shut-down), are analysed.

There are other features not yet mentioned here that might be added to the numerical model in future. For example, squeeze-film-dampers (SFD) and active-magnetic-bearings (AMB) might be introduced into the model. Whereas the derivation of accurate models for SFDs and AMBs is a difficult task and an active field of research, the inclusion of their numerical representation into a windmilling model would not be problematic. The reason is that SFDs and AMBs are mainly described by non-linear damping and stiffness terms, which merely add to the nonlinear terms already present in the model due to the rotor/stator interaction. The presence of elements such as SFDs and AMBs will certainly change the behaviour of the overall system, but the task of analysing such a system is not expected to become more difficult, as the 'fundamental' windmilling system is already strongly non-linear.

1.6   Outline of the Thesis

Chapter 1   introduces the relatively new problem of windmilling in aero-engines. A definition of windmilling and a more detailed description of the phenomenon is given together with the historical background of the problem and the motivation which lead to this research project. The specific objectives of the project are stated and a literature review of the work carried out in related areas of rotor/stator interaction in power plant or aircraft turbo-machinery is conducted.

Chapter 2 deals with the dynamic modelling of the rotor/stator contact and the kinematic constraints that need to be upheld. Linear and a nonlinear contact models are introduced, both of which can be used in various general systems with rigid body, blades/casing, or flexible inter-shaft contact. The equations of motion are derived for a typical Jeffcott rotor with stator configuration. Some basic systems often found in the literature are also considered, where these equations simplify considerably, so some qualitative deliberations about the dynamic behaviour can be made. Accordingly, this chapter concentrates on simple, fundamental systems and the treatment of general, complex rotor/stator systems is left to Chapter 3.

Chapter 3 outlines the numerical solution algorithms that are used for the simulation studies. The equations of motion of general rotor/stator systems are presented in the time-domain in the respective formats of initial value, boundary value, and shooting problems. In the frequency domain the harmonic balance method is used, and an algorithm analysing the stability of a solution entirely in the frequency domain is introduced. The arc-length continuation scheme is also outlined, which can be used with both time-domain and frequency-domain methods to follow solution branches along a changing parameter such as shaft speed.

Chapter 4 presents the simulation results for a variety of parameter studies, where the system configuration parameters have been varied over physically relevant values. These parameters include rotor and stator mass, stiffness, and damping properties, coefficient of friction in the contact zone, gap size, non-isotropic geometry or stiffness and different contact models. The suitability of frequency sweep (a slow acceleration or deceleration of the shaft speed) or steady-state numerical solutions is also discussed. The study seeks to ascertain how the parameters affect the system response, thereby giving an overview of the range of possible dynamic behaviour and establishing which ingredients are necessary in the model to capture certain behaviour. It also provides experience for the usefulness of the numerical tools presented in Chapter 3.

Chapter 5 introduces the design of the test rig. It explains the reasoning behind the implementation that was chosen so that the variation of parameters, which are used for the simulation runs in Chapter 4, can be realised. It also covers briefly the non-standard signal processing routines that are used, the features of the data acquisition system, and the setup used for the measurements.

Chapter 6 presents the measured results that were obtained from the test rig. The tests were performed under different configurations, in particular with rigid disc and bladed contact disc test pieces, with the purpose of repeating the behaviour found in the variety of parameter combinations studied in the numerical simulations of Chapter 4. It is hoped to establish what constitutes consistent behaviour or to find anomalies.

Chapter 7   seeks to establish the level of agreement between the numerical results presented in Chapter 4 and the measured results presented in Chapter 6. To this end, an FE model representation of the test rig is updated against results from a modal test on the rig. This FE model is then used to validate the 4-degree-of-freedom lumped mass model which forms the basis of the numerical analysis in Chapter 4, thereby justifying *a posteriori* the dynamic modelling approach for the chosen parameter configurations. Finally, the key dynamic characteristics of measurements and simulation are compared, facilitating a judgment of how successful the numerical representation models the test rig.

Chapter 8   revisits the objectives stated in Chapter 1 and discusses the extend to which they have been met. Based on these, and on the technical discussions of the measured and simulated results, conclusions of the project are drawn from a strategic perspective and an attempt made to envisage future areas of further study.

Chapter 2

Dynamic Modelling

2.1 Overview

After discussing the physical properties of a windmilling system in the previous Chapter, this Chapter details the approach used in this thesis to model the dynamics of rotor/stator interaction numerically. The following two sections deal with the contact geometries of rigid and flexible bodies, respectively, and the resulting kinematic constraints. Rigid body contact assumes that the shape of the contacting objects does not change during contact (for example two stiff rings, which keep their circular circumference even during impact), whereas the flexible contact model allows for the shape of the contacting objects to change (for example a blade that bends while contacting the casing). In the subsequent sections linear and a nonlinear models for the contact force are introduced. The rigid body contact model is implemented into the equations of motion of a typical Jeffcott rotor system with a contacting stator as sketched in Figure 1.4. The last sections make use of various simplifying assumptions frequently encountered in the literature dealing with rotor/stator contact problems, thereby reducing the complexity of the presented system to much simpler ones, leading to the conditions of full annular rub and quasi-static equilibrium. These systems can be studied without extensive numerical procedures, and so some basic dynamic behaviour of rotor/stator contact can easily be deduced.

2.2 Kinematics of a Rigid Rotor/Stator Interaction System

As mentioned in the introduction of this thesis, a simple, and in the literature widely-used, rotor/stator interaction model can be produced by a Jeffcott rotor with a stator ring suspended on springs (Figure 1.4). In this section the contacting rotor disc and

stator casing are modelled as circular, rigid bodies. For the purpose of numerical simulation, a small contact penetration of the rotor and stator rings is allowed. The contact stiffness in this penetration region is usually a value which is set to orders of magnitude higher than the rotor shaft or stator suspension stiffnesses, so that the contact depth is orders of magnitude lower than the rotor or stator deflections. This may justify the approach of simplifying the contact area numerically to a single point. The contact depth is defined as

$$\delta(t) = \begin{cases} r_{\mathrm{r}} + \epsilon_{\mathrm{r}}\, \mathrm{e}^{\mathrm{i}\Omega t} - r_{\mathrm{s}} - \epsilon_{\mathrm{s}} - h\, \mathrm{e}^{\mathrm{i}\psi} & \text{if } |r_{\mathrm{r}} + \epsilon_{\mathrm{r}}\, \mathrm{e}^{\mathrm{i}\Omega t} - r_{\mathrm{s}} - \epsilon_{\mathrm{s}}| > h \\ 0 & \text{otherwise} \end{cases} \tag{2.1}$$

where $r_{\mathrm{r}}, r_{\mathrm{s}}$ are rotor and stator displacements in the complex plane, h is the gap size, ψ the angular position of contact, ϵ_{r} an (optional) offset of the rotor disc and ϵ_{s} a stator offset. These entities are depicted in Figure 2.1.
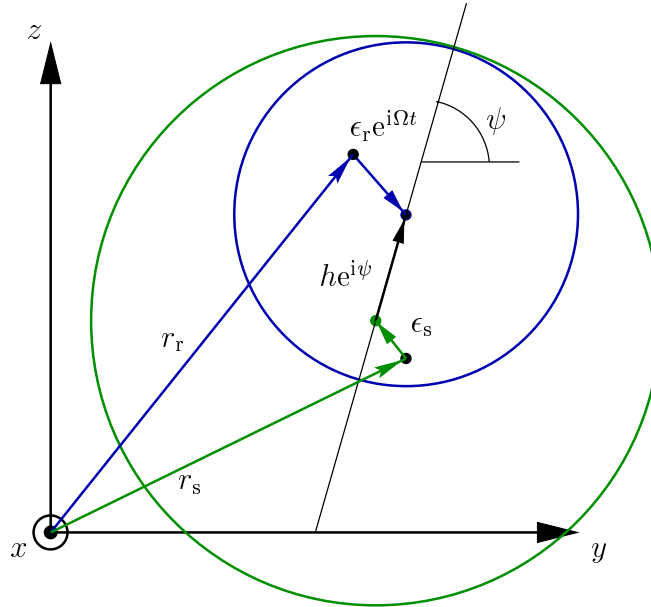

Figure 2.1: Geometry of a Jeffcott rotor with stator

2.3   Kinematics of Flexible Rotor/Stator Interaction Systems

In certain situations one has to move away from the simple approach described above, where rotor and stator are modelled locally as rigid circular rings with a concentrated mass at their centre. The need for a more sophisticated approach arises for example,

when wishing to model the blades on a turbine or compressor disc, or when the casing cannot be treated as locally rigid.

If the shaft or casing is discretised with only a few nodes on the circumference to keep the size of the overall problem small, it is useful to increase the resolution when computing the contact condition and the resulting rotor/stator contact force by means of interpolation. Too coarse a discretisation on the circumference leads to numerical problems when computing the state in the contact zone, as the results of the conditional switch in the simulation algorithm, which determines contact or no contact, are based on sparse spatial information. The cross-section of a shaft or casing is by definition cyclic, and any arbitrary deflection circumferentially can therefore always be represented as a periodic function. The deflection at the nodes on the circumference can thus be decomposed via Fourier transformation into components of standing and travelling waves of different wavelengths. This information can then be used in an inverse Fourier transform to calculate the deflection at any number of interpolation points along the circumference.

For blade/casing interactions, the contact zone is modelled as a discrete point, as the blade contact surface is regarded as small in this first approach. The contact load on the blade can then be distributed among the two neighbouring casing nodes, be they interpolated as discussed above or actual nodes in the model. With a large number of (interpolated) nodes on the casing, this may be further simplified to mapping the blade nodes to their nearest casing nodes, as described below.

For interaction between two flexible circular bodies, for example inter-shaft contact between LP and IP rotor shafts, the geometry of the impact zone is not a discrete point but a line contact (Figure 2.2). At present, this problem is approached in a simple way: the spatial information around the circumference is increased by means of Fourier interpolation, as described above, to such an extent that there are 1024 circumferential points on each structure. The nodes of the inner and outer structures (for example LP and IP rotor shafts) are then mapped one to one to their nearest neighbour (Figure 2.2), assuming that any difference in angular position for each node-pair is negligible. The contact forces are then determined for each node pair as described in the following section. The computational overhead for the interpolation is low, as the fast Fourier transform used for the process is very efficient.

2.4 Contact Force Models

In reality the contact force will have a complex dependency on geometry and material properties as well as on impact depth and speed. Naturally, one is interested to choose the simplest representation that still leads to acceptable results. To this end Wegener & Markert (1999) investigated four still relatively simple contact models in a rotor system with retainer bearings, varying from linear contact stiffness and damping
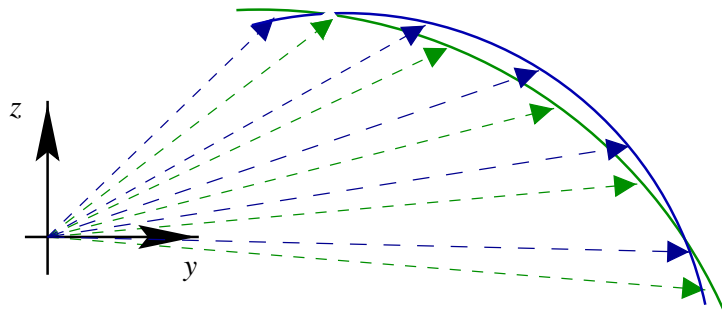
Figure 2.2: Mapping nodes in flexible body contact

to non-linear stiffness and damping. The observation was made that parameters could be found for each contact model, so that they all produced similar global dynamic behaviour of the system. Thus, it seems, one is fairly free to chose a contact model and the greater difficulty lies in finding physically meaningful parameters. However, the choice of contact model will have a very strong influence on the convergence properties of the numerical simulation procedure, and therefore needs to be chosen with great care. In the following, the two models which have been used in the simulations in this thesis are presented.

(a) linear   (b) nonlinear
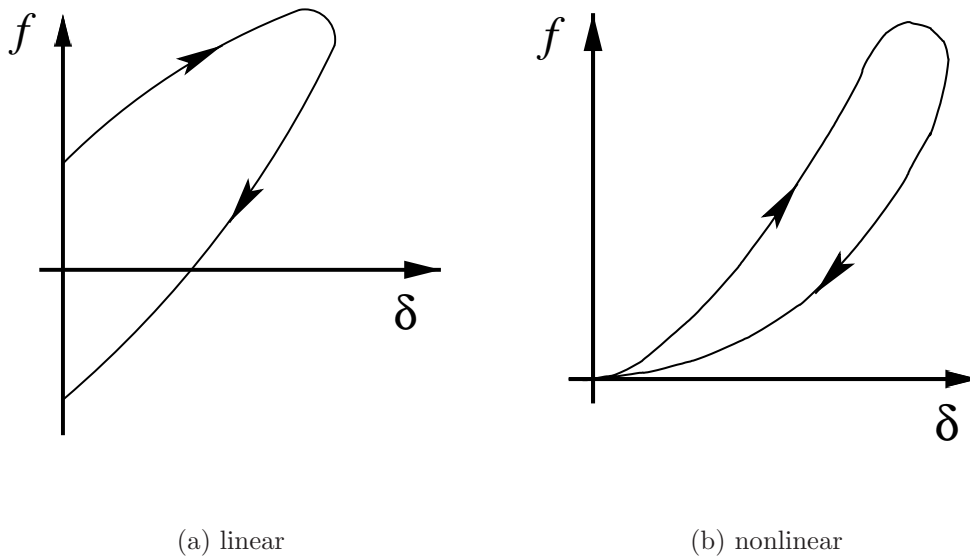
Figure 2.3: force–displacement characteristics

Let f_n denote the normal contact force between rotor and stator. As a first attempt in a numerical implementation one might want to simplify the relationship to a linear

one with

$$f_{\mathrm{n}} = k_{\mathrm{c}}\delta + c_{\mathrm{c}}\dot{\delta} \tag{2.2}$$

where δ is the depth of the contact described in (2.1), $\dot{\delta}$ its derivative with respect to time, k_{c} a local linear contact stiffness, and c_{c} a local damping coefficient. Figure 2.3(a) shows a typical force–displacement characteristic and illustrates two deficiencies of this model: (i) when the contact displacement returns to zero, the model provides a physically meaningless negative contact force, and (ii) the function is not differentiable at $\delta = 0$. Numerical procedures in general are not tolerant of non-differentiable or even discontinuous functions (usually $f \in \mathbb{C}^2$ is required), and examples will be shown later where one pays the price of using them with difficult convergence behaviour. One can avoid the occurrence of a negative contact force by using this model with a damping value of $c_{\mathrm{c}} = 0$, and by choosing a relatively low contact stiffness k_{c}, the convergence behaviour of the numerical solution methods can be improved.

These difficulties can be solved more elegantly by implementing a nonlinear contact force relationship. There are many different possibilities to design a nonlinear function that has not got the previously described deficiencies. Fumagalli & Schweitzer (1996) use the relationship in equation (2.3) to investigate a rotor which falls into its retainer bearings when the main active magnetic bearings suddenly fail. The force–displacement characteristic for this case is shown in Figure 2.3(b). The equation (2.3) below is taken from the work of Hunt & Crossley (1975), in which the stiffness is derived from Hertzian theory for normal contact of two spheres and whose damping coefficient, for a limited range of impact speeds $\dot{\delta} < 500\,\mathrm{mm/s}$, is related to the coefficient of restitution ϵ, equation (2.4).

$$f_{\mathrm{n}} = k_{\mathrm{c}}\delta^{\frac{3}{2}}\left(1 + \frac{3}{2}c_{\mathrm{c}}\dot{\delta}\right) \tag{2.3}$$

$$\epsilon = 1 - c_{\mathrm{c}}\dot{\delta}\big|_{\delta=0} \tag{2.4}$$

$\dot{\delta}$ of equation (2.3) can be determined by using equation (2.1) and developing:

$$a = r_{\mathrm{r}} + \epsilon_{\mathrm{r}}\,\mathrm{e}^{\mathrm{i}\Omega t} - r_{\mathrm{s}} - \epsilon_{\mathrm{s}} \tag{2.5}$$

$$\dot{a} = \dot{r}_{\mathrm{r}} + \mathrm{i}\Omega\epsilon_{\mathrm{r}}\,\mathrm{e}^{\mathrm{i}\Omega t} - \dot{r}_{\mathrm{s}} \tag{2.6}$$

$$\tan\psi = \frac{\Im(a)}{\Re(a)} \tag{2.7}$$

$$\dot{\psi} = \frac{\Im(\dot{a})\Re(a) - \Im(a)\Re(\dot{a})}{|a|^2} \tag{2.8}$$

$$\dot{\delta} = \dot{r}_{\mathrm{r}} + \mathrm{i}\Omega\epsilon_{\mathrm{r}}\,\mathrm{e}^{\mathrm{i}\Omega t} - \dot{r}_{\mathrm{s}} - \mathrm{i}\dot{\psi}h\,\mathrm{e}^{\mathrm{i}\psi} \tag{2.9}$$

The total contact force is the sum of the normal contact force and the friction force, which acts in the direction of the relative surface velocity of the sliding bodies. In this work the contact force is specified from the perspective of the stator. With the rotor speed being defined in the mathematically positive direction (counter-clockwise) and the out-of-balance fore being the only external excitation, the friction force of the rotor sliding against the stator therefore leads the normal contact force by 90 ˚ from the stator's perspective (see section 2.7.2 on backward whirl for a sketch and more detailed discussion). Again, simple or elaborate models for friction are possible. Here, the simple Coulomb friction model with constant coefficient, μ, is used, and the total contact force, f_c, in complex co-ordinates is thus:

$$f_c = (1 + i\mu)f_n \tag{2.10}$$

It is noted that stick-friction is unlikely in the windmill scenario, as the size of the gap, h, relative to the outer diameter of the rotor, R, is small. A non-sliding contact would thus demand a very high backward whirl frequency, ω, compared with the speed of rotation Ω:

$$\omega = -\frac{R}{h}\Omega \tag{2.11}$$

2.5 Equations of Motion

It is, of course, easy to implement the above-mentioned contact models into general, multi-degree-of-freedom rotor/stator structures. This process is discussed in Chapter 3, along with the numerical procedures that can be used to solve the resulting equations of motion. For the remainder of this chapter, however, a simple 4 degree-of-freedom lumped-mass system is used. For simplicity only, and without loss of generality, the previously discussed linear contact force without damping ($c_c = 0$) is implemented into the system as a basis for the discussion in the following sections. Furthermore, the complex notation widely used in the rotor-dynamics literature and introduced in section 2.3 is used here, as it allows to present the material in a very compact form. Thus, all displacements, eccentricities, and forces are complex numbers. The equations of motion for a Jeffcott rotor interacting with a linear stator structure (Figure 1.4) are:

$$m_r\ddot{r}_r + c_r\dot{r}_r + k_r r_r = -f_c + \Omega^2 m_r \epsilon_m e^{i\Omega t} \tag{2.12}$$

$$m_s\ddot{r}_s + c_s\dot{r}_s + k_s r_s = f_c \tag{2.13}$$

Introducing the parameters

$$\omega_r^2 = \frac{k_r}{m_r} \qquad \omega_s^2 = \frac{k_s}{m_r} \equiv \gamma_k \omega_r^2$$

$$\zeta_r = \frac{\omega_r c_r}{2k_r} \qquad \zeta_s = \frac{\omega_s c_s}{2k_s}$$

$$\gamma_m = \frac{m_s}{m_r} \qquad \gamma_k = \frac{k_s}{k_r} \qquad \gamma_c = \frac{k_c}{k_r}$$

and substituting into equations (2.12) and (2.13) yields

$$\ddot{r}_{\mathrm{r}} + 2\zeta_{\mathrm{r}}\omega_{\mathrm{r}}\dot{r}_{\mathrm{r}} + \omega_{\mathrm{r}}^2 r_{\mathrm{r}} = -\omega_{\mathrm{r}}^2(1+\mathrm{i}\mu)\gamma_{\mathrm{c}}\delta + \Omega^2 \epsilon_{\mathrm{m}}\,\mathrm{e}^{\mathrm{i}\Omega t} \tag{2.14}$$

$$\gamma_{\mathrm{m}}\ddot{r}_{\mathrm{s}} + 2\zeta_{\mathrm{s}}\omega_{\mathrm{s}}\dot{r}_{\mathrm{s}} + \omega_{\mathrm{s}}^2 r_{\mathrm{s}} = \omega_{\mathrm{r}}^2(1+\mathrm{i}\mu)\gamma_{\mathrm{c}}\delta \tag{2.15}$$

Note that the stator parameter, ω_{s}, is defined with respect to rotor parameter, m_{r}. This hybrid approach is chosen to allow a direct comparison with some papers in the literature which do not consider the stator mass, m_{s}, for example Isaksson (1994); Markert & Wegener (1995). In this way γ_{m} can simply be set to zero.

2.6   Full Annular Rub

In the case of full annular rub (used in the following sections), the rotor and stator move jointly so that there is permanent contact between them. Thus, substituting (2.1) into (2.14) and (2.15), the governing equations of motion are:

$$\begin{bmatrix} 1 & 0 \\ 0 & \gamma_{\mathrm{m}} \end{bmatrix}\begin{pmatrix} \ddot{r}_{\mathrm{r}} \\ \ddot{r}_{\mathrm{s}} \end{pmatrix} + \begin{bmatrix} 2\zeta_{\mathrm{r}}\omega_{\mathrm{r}} & 0 \\ 0 & 2\zeta_{\mathrm{s}}\omega_{\mathrm{s}} \end{bmatrix}\begin{pmatrix} \dot{r}_{\mathrm{r}} \\ \dot{r}_{\mathrm{s}} \end{pmatrix}$$
$$+ \begin{bmatrix} \omega_{\mathrm{r}}^2(1+(1+\mathrm{i}\mu)\gamma_{\mathrm{c}}) & -\omega_{\mathrm{r}}^2(1+\mathrm{i}\mu)\gamma_{\mathrm{c}} \\ -\omega_{\mathrm{r}}^2(1+\mathrm{i}\mu)\gamma_{\mathrm{c}} & \omega_{\mathrm{r}}^2((1+\mathrm{i}\mu)\gamma_{\mathrm{c}}+\gamma_{\mathrm{k}}) \end{bmatrix}\begin{pmatrix} r_{\mathrm{r}} \\ r_{\mathrm{s}} \end{pmatrix}$$
$$= \begin{pmatrix} \Omega^2 \epsilon_{\mathrm{m}}\,\mathrm{e}^{\mathrm{i}\Omega t} + \omega_{\mathrm{r}}^2(1+\mathrm{i}\mu)\gamma_{\mathrm{c}}(\epsilon_{\mathrm{s}} + h\,\mathrm{e}^{\mathrm{i}\psi} - \epsilon_{\mathrm{r}}\,\mathrm{e}^{\mathrm{i}\Omega t}) \\ \omega_{\mathrm{r}}^2(1+\mathrm{i}\mu)\gamma_{\mathrm{c}}(\epsilon_{\mathrm{r}}\,\mathrm{e}^{\mathrm{i}\Omega t} - \epsilon_{\mathrm{s}} - h\,\mathrm{e}^{\mathrm{i}\psi}) \end{pmatrix} \tag{2.16}$$

The system can now be considered as a system of two masses, connected to each other by a spring (the contact stiffness) and grounded individually. The system has two modes, the in-phase and out-of-phase movements of the masses. Assuming that the contact stiffness is much higher than the rotor and stator stiffnesses ($\delta \ll r$), and ignoring damping, the natural frequency of rotor and stator moving in phase can be approximated as:

$$\omega_{\mathrm{rs}}^2 = \frac{k_{\mathrm{r}} + k_{\mathrm{s}}}{m_{\mathrm{r}} + m_{\mathrm{s}}} = \omega_{\mathrm{r}}^2 \frac{1 + \gamma_{\mathrm{k}}}{1 + \gamma_{\mathrm{m}}} \tag{2.17}$$

The assumption that any local contact stiffness between rotor and stator is far larger than the rotor or stator stiffness allows the penetration depth δ to be set to zero. The kinematic relationship between rotor and stator deflection simplifies to:

$$r_{\mathrm{s}} = r_{\mathrm{r}} + \epsilon_{\mathrm{r}}\,\mathrm{e}^{\mathrm{i}\Omega t} - \epsilon_{\mathrm{s}} - h\,\mathrm{e}^{\mathrm{i}\psi} \tag{2.18}$$

Some authors, e.g. Ehrich (1969); Zhang (1988); Isaksson (1994), model their systems without any stator mass and stator damping, so that $r_{\mathrm{r}}(t)$ (*complex co-ordinates*) represents the two remaining independent degrees-of-freedom, as the stator acts purely

as a spring coming into play during contact. Allowing for $\epsilon_r, \epsilon_s \neq 0$ (also complex co-ordinates) and defining the angle of the friction force as $\rho = \tan^{-1}\mu$, the stator deflection, $r_s(t)$, can be described by as

$$|r_s|\,e^{i\psi}\,e^{i\rho} = r_r + \epsilon_r\,e^{i\Omega t} - \epsilon_s - h\,e^{i\psi} \quad \text{for friction acting on stator or,} \qquad (2.19)$$

$$|r_s|\,e^{i\psi} = r_r + \epsilon_r\,e^{i\Omega t} - \epsilon_s - h\,e^{i\psi} \quad \text{ignoring friction on stator.} \qquad (2.20)$$

The two equations (2.19) and (2.20) refer to a variation in the way in which the effect of the friction force on the stator is modelled in the literature. Isaksson (1994), for example, completely excludes the effect of friction forces on the stator, but not on the rotor. While not accurate, this set-up allows a much simpler analysis, as the stator deflection always has the same direction as the normal force of the contact point. The different kinematic relationships of excluding or including the influence of the friction force on the stator are shown in Figure 2.4. For a clearer display, the rotor disc and stator ring are chosen to be concentric ($\epsilon_r, \epsilon_s = 0$).

(a) ignoring friction on stator   (b) including friction on stator
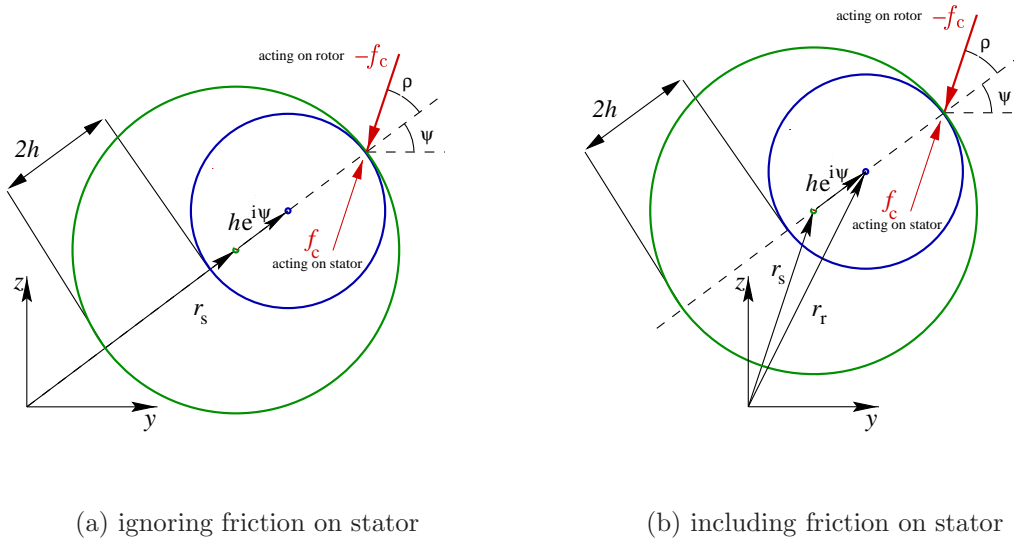
Figure 2.4: Geometries of simple rotor/stator friction configurations

2.7   Quasi-Static Equilibrium

For the special case of $\epsilon_r, \epsilon_s = 0$ and isotropic supports, the equations of motion become quasi-static for pure forward or backward whirl — in other words, when there is only one frequency component in the whirl. This component can be either in the forward (due to out-of-balance) or backward (due to friction) directions. This presence of

only one frequency component has the effect that at a given speed, the steady-state conditions of rotor whirl are such that the radial deflections of the rotor and stator are constant.

2.7.1 Forward whirl

A system with the above simplifications, which is driven by out-of-balance forces, may of course still produce intermittent contact (see Chapter 4 with simulation results). However, if the contact is of the full annular type then, given these simplifications, the whirl is purely circular. The only frequency component in the response spectrum is thus the engine-order speed, Ω. Substituting

$$r_{\mathrm{r}}(t) = \hat{r}_{\mathrm{r}}\, \mathrm{e}^{\mathrm{i}\Omega t} \quad r_{\mathrm{s}}(t) = \hat{r}_{\mathrm{s}}\, \mathrm{e}^{\mathrm{i}\Omega t} \tag{2.21}$$

into equations (2.12) and (2.13) leads to a set of (non-linear) time-independent algebraic equations which can be solved (numerically) for the complex amplitudes of rotor deflection $\hat{r}_{\mathrm{r}}$, stator deflection $\hat{r}_{\mathrm{s}}$, and contact force $\hat{f}_{\mathrm{c}}$:

$$\left(\Omega^2 + 2\zeta_{\mathrm{r}}\omega_{\mathrm{r}}\Omega + \omega_{\mathrm{r}}^2\right)\hat{r}_{\mathrm{r}} = \Omega^2\epsilon_{\mathrm{m}} - \hat{f}_{\mathrm{c}} \tag{2.22}$$

$$\left(\gamma_{\mathrm{m}}\Omega^2 + 2\zeta_{\mathrm{s}}\omega_{\mathrm{s}}\Omega + \omega_{\mathrm{s}}^2\right)\hat{r}_{\mathrm{s}} = \hat{f}_{\mathrm{c}} \tag{2.23}$$

$$\hat{r}_{\mathrm{s}} = \hat{r}_{\mathrm{r}} - h\, \mathrm{e}^{\mathrm{i}\psi} \tag{2.24}$$

This approach may be used to determine the speed ranges over which rotor and stator stay in contact. It may also provide multiple solutions, allowing for the over-hanging sections in the amplitude curve introduced in Figure 1.5 . The majority of papers dealing with backward whirl in the literature also use this easy setup that remains after the mentioned simplifications (albeit the backward whirl frequency is not the engine order speed).

2.7.2 Backward whirl

Backward whirl is also called reverse whirl or whip in the literature. It can be shown to exist as a self-sustaining phenomenon even without any external forces present (Zhang, 1988; Crandall & Lingener, 1990), numerical results are provided in Chapter 4. In particular, with the above-mentioned simplifications, and without the presence of (or ignoring) the out-of-balance forces, a simple equilibrium model can be set up. As in the previous paragraph, the motion contains only one frequency component, and that is the whirl frequency, ω, (same definition of direction as Ω, so for backward whirl $\omega < 0$). Thus,

$$r_{\mathrm{r}}(t) = \hat{r}_{\mathrm{r}}\, \mathrm{e}^{\mathrm{i}\omega t} \quad r_{\mathrm{s}}(t) = \hat{r}_{\mathrm{s}}\, \mathrm{e}^{\mathrm{i}\omega t} \tag{2.25}$$

which leads to the equilibrium equations:

$$\left(-\omega^2 + 2\mathrm{i}\zeta_{\mathrm{r}}\omega_{\mathrm{r}}\omega + \omega_{\mathrm{r}}^2\right)\hat{r}_{\mathrm{r}} = -\hat{f}_{\mathrm{c}} \tag{2.26}$$

$$\left(-\gamma_{\mathrm{m}}\omega^2 + 2\mathrm{i}\zeta_{\mathrm{s}}\omega_{\mathrm{s}}\omega + \omega_{\mathrm{s}}^2\right)\hat{r}_{\mathrm{s}} = \hat{f}_{\mathrm{c}} \tag{2.27}$$

$$\hat{r}_{\mathrm{s}} = \hat{r}_{\mathrm{r}} - h\,\mathrm{e}^{\mathrm{i}\psi} \tag{2.28}$$

It may be noted that with the presence of out-of-balance-forces, there would no longer be only one frequency present in the system, invalidating this approach of simplifying the equilibrium condition to a set of algebraic equations. The following paragraphs are a few simple deliberations based on these equations to determine whether the stator leads or lags the rotor and under which conditions the modeshape is inverted. Figure 2.5 shows two possible origins, A and B, which refer to the two cases where rotor is leading or lagging the stator, respectively. A number of contact forces 1,..,6 with different angles are shown, which allow for different directions of whirl.
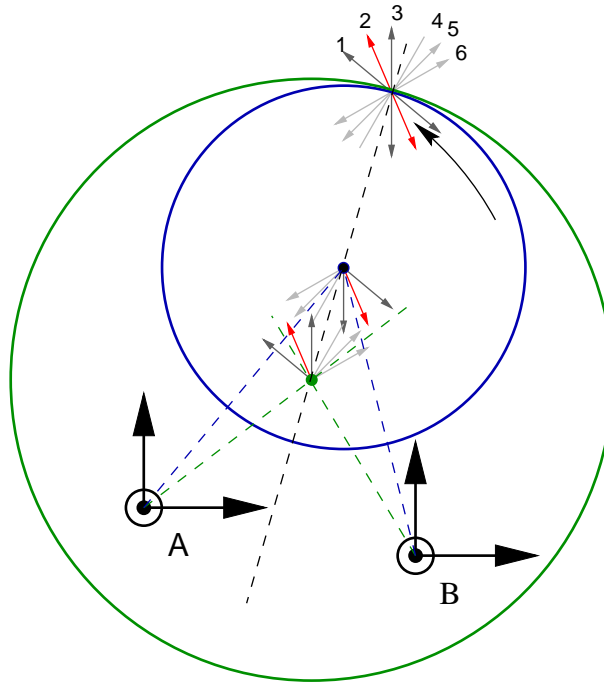
Figure 2.5: Possible angles of contact force

Table 2.1 takes a look at the combinations of the origins and whirl directions the rotor and stator have to be in if equilibrium of the inertia, stiffness, damping, and contact forces holds. The whirl direction is determined by the contact force component which is perpendicular to the line passing through the centres of rotor and stator. Whereas it is kinematically possible for rotor and stator to have different directions of whirl but still to stay in continuous contact, this means dynamically that over part of the rotation period, energy is flowing from the stator into the rotor. It also means

Table 2.1: Possible forward (FW) and backward (BW) whirl directions

	rotor	stator
B1	BW	FW
B2	BW	BW
B3,..,B6	FW	BW
A1,..,A4	BW	FW
A5	FW	FW
A6	FW	BW

that the angle between rotor and stator is no longer constant, violating the assumption of a quasi-equilibrium only under which the single frequency assumption used in this approach is valid. Mixed FW/BW directions are therefore not possible. This leaves as only candidates configuration B2 or A5. As for the contact forces 4,..,6 it is pointed out that they refer to cases where the energy is actually flowing from the stator to the rotor. Given that in this model the only source of energy is the rotation of the rotor, it is not possible for the contact force to have these directions. This leaves B2 as only possible configuration, meaning the rotor is leading the stator in backward whirl.

However, this conclusion is only valid for the modeshape drawn here, in which $|\hat{r}_r| > |\hat{r}_s|$. A similar figure can be drawn for an inverted whirl mode, $|\hat{r}_s| > |\hat{r}_r|$, where the rotor/stator contact point is actually closer to the origin than to the centre of either rotor or stator. Such a sketch leads to a similar arrangement of forward/backward whirl combinations for rotor and stator positions. Using the same arguments as in the previous case, it emerges that the only valid scenario is the stator leading the rotor.

The question remains as to when the modeshape is regular or inverted. Intuitively, it would be not surprising to find that the 'regular' mode with $|\hat{r}_r| > |\hat{r}_s|$ occurs when the rotor is softer than the stator support, and the 'inverted' mode $|\hat{r}_s| > |\hat{r}_r|$ with a rotor stiffer than the stator support. The same conclusion can be reached by using the equations above and defining, without loss of generality, $\angle\hat{r}_r = 0$ and $\angle\hat{r}_s = \phi$. It follows from Figure 2.1 that $\angle\hat{f}_c = \rho + \psi$, where $\rho = \tan^{-1}\mu$. Using this information, we proceed to look at the rotor and stator equations in turn. Briefly setting $\zeta_r = 0$ for the sake of clarity, equation (2.26) leads to

$$|\hat{f}_c|\,\mathrm{e}^{\rho+\psi} = \left(\omega^2 - \omega_r^2\right)|\hat{r}_r| \tag{2.29}$$

which yields:

$$\rho + \psi = \begin{cases} 180\,^\circ & \text{for } \omega_r > \omega,\ \text{inverted modeshape} \\ 0\,^\circ & \text{for } \omega_r < \omega,\ \text{regular modeshape} \end{cases} \tag{2.30}$$

Again, setting $\zeta_s = 0$, equation (2.27) leads to

$$|\hat{f}_c|\,\mathrm{e}^{\rho+\psi} = \left(-\gamma_m\omega^2 + \gamma_k\omega_r^2\right)|\hat{r}_s|\,\mathrm{e}^{\phi} \tag{2.31}$$

which yields (using the more natural definition $\omega_{\mathrm{s}}^2 = \frac{k_{\mathrm{s}}}{m_{\mathrm{s}}} = \frac{\gamma_{\mathrm{k}}}{\gamma_{\mathrm{m}}}\omega_{\mathrm{r}}^2$):

$$\rho + \psi = \begin{cases} \phi \text{ for } \omega_{\mathrm{s}} > \omega, \text{ regular modeshape} \\ \phi + 180\,^{\circ} \text{ for } \omega_{\mathrm{s}} < \omega, \text{ inverted modeshape} \end{cases} \qquad (2.32)$$

2.7.3   Summary

Although the conditions for quasi-static equilibrium to exist (isotropy in stiffness and geometry) are too restrictive for realistic systems, it is has nonetheless been useful to study this special case. As the equations of motion in this case could be solved with a simple mono-frequency approach, some characteristics of the dynamic behaviour of such a system could be extracted easily. For example, in backward whirl for $\omega_{\mathrm{s}} < \omega < \omega_{\mathrm{r}}$ the modeshape is inverted and the rotor is lagging the stator, and for $\omega_{\mathrm{r}} < \omega < \omega_{\mathrm{s}}$ the modeshape is regular and the rotor is leading the stator. This behaviour has served as a useful test case, for example when validating the more general numerical analysis codes (presented in the following Chapter 3) with respect to the correct implementation of the direction of friction.

Chapter 3

Numerical Simulation Methods

3.1 Overview

After designing a simple numerical model and deriving the equations of motion for windmilling analysis in the previous Chapter, this Chapter presents a few numerical algorithms which are capable of solving these non-linear equations of motion. Given sufficient computing resources, the methods mentioned in this Chapter are easily applicable to problems with large numbers of degrees-of-freedom, so they are not restricted to the simple 4DOF model discussed in Chapter 2. Typically, such a more general problem consists of finite element models of large parts of the structure or substructures where a linear representation is adequate, plus some 'problematic' (nonlinear) DOFs for special areas, where friction, impacts, or other interaction occurs for example. Usually, the linear DOFs outnumber the nonlinear ones by a large ratio. Only linear DOFs can be easily reduced with the various common reduction methods, the nonlinear ones need to be retained fully. So, with a large ratio of linear to nonlinear DOFs, one expects the reduction of the linear substructures to be able to deliver a significantly reduced overall problem size.

The rotor and stator components are modelled as linear structures, and there will be some linear external forces such as gravity and out-of-balance. The contact region supplies the nonlinear behaviour at a few degrees of freedom on both rotor and stator. For simplicity of notation and without loss of generality, the complete system is split into its linear part, represented by the usual mass, stiffness, damping matrices, with a linear external force vector, $\{f_\mathrm{u}\}$ (unbalance), and its nonlinear part (as a function of displacement and possibly velocity), which is represented here as a single force vector $\{f_\mathrm{c}\}$ combining all nonlinear effects (contact between rotor and stator):

$$[M]\{\ddot{r}\} + [C]\{\dot{r}\} + [K]\{r\} = \{f_\mathrm{u}(t)\} + \{f_\mathrm{c}(r)\} \qquad (3.1)$$

A chart illustrating this approach is given in Figure 3.1. The rotor and stator substructures are linear finite element models, and both are linked to nonlinear DOFs
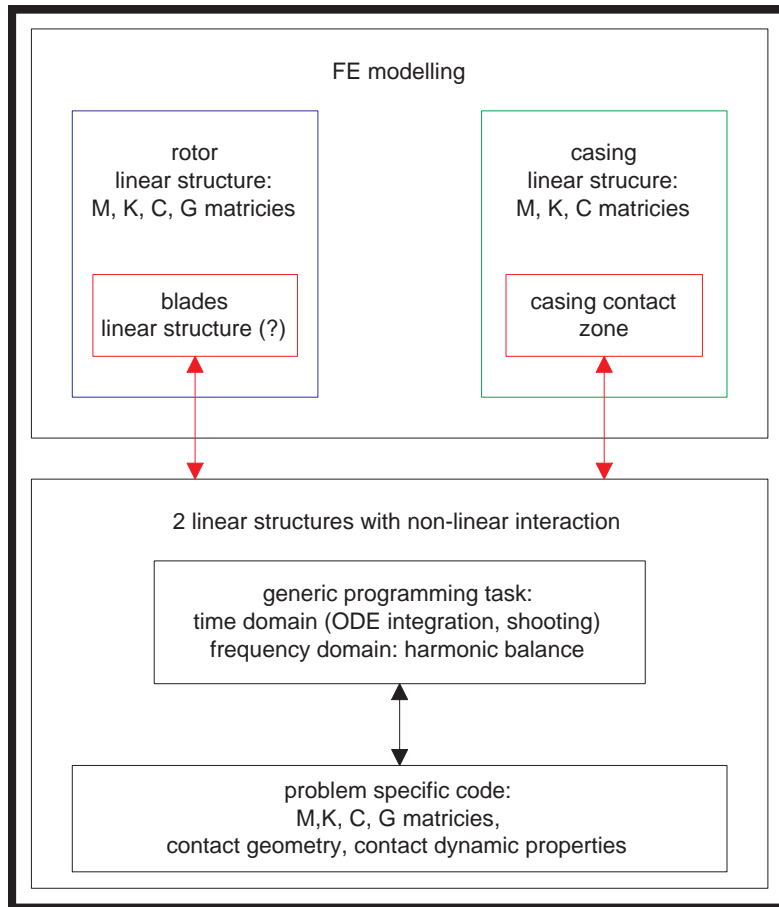
Figure 3.1: Numerical modelling approach

describing the contact problem. The programming task can be split into two separate modules: the first module consists of the problem-specific code that delivers the mass, stiffness, damping, gyroscopic matrices of the linear substructures as well as an implementation of the contact geometry and a particular contact model (linear, cubic, generally nonlinear) for each windmill scenario. Modelling the linear substructures with finite elements is surely engineering routine and is well documented in the literature, and will not be discussed here any further. This is not to say that it is not something of an art in itself and at times quite a tricky task to do well, as the strong ongoing effort in the areas of model correlation and updating with test data proves. The implementation of the nonlinear degrees of freedom related to the contact problem has been described in the previous chapter. The second module consists of the generic code that 'inherits' these specific matrices set up by the first module and can be used without any change in setup between different windmill scenarios or models. However, function calls in between iterations to the problem specific code are necessary. These generic solution procedures are described in the following sections.

The most widely-used approach is to find a time-marching solution to equation (3.1) given a particular set of initial conditions. The advantages of this approach over the following ones are that transient events can be modelled and that no *a priori* knowledge about the system behaviour is necessary. Drawbacks are (i) the fact that in many cases much larger computational times are required compared with the other methods, and (ii) the only indirect way of finding periodic solutions by integrating over many cycles and hoping that the transient effects will die away sufficiently quickly. 'Sufficient' in this case means that the final stretch of the time marching run that is used for further analysis contains transient effects only below a certain level deemed acceptable. Furthermore, in some cases such as the windmilling scenario, one is more interested in the periodic solution under certain parameters rather than a particular trajectory resulting from a specific initial condition.

Other numerical algorithms that can be used to find the periodic solution of a non-linear differential equation are: (i) boundary value, (ii) shooting, and (iii) harmonic balance methods. These methods are well known and most of them covered in a range of text books dealing with (nonlinear) ordinary differential equations or (nonlinear) dynamics, see for example Ascher et al. (1995); Genta (1999); Nayfeh & Balachandran (1995); Parker & Chua (1989); Seydel (1994). It is not the purpose of this thesis to repeat the presentations which are given in these texts, often with very good didactics and clarity. So, borrowing from a 'documentation' of a slightly convoluted research code: "this program assumes a friendly user", this chapter does the same. The methods mentioned above are thus only briefly presented, mainly to present the numerical setup in the same notation used in the other chapters.

However, it seems that among these methods the harmonic balance method is much less commonly used for engineering problems than the other ones, and is not included in many text books. It is thus outlined here in slightly more detail than the other methods. Specifically, the stability analysis in the frequency domain for nonlinear systems has not been encountered in the literature. The advantages and disadvantages or specific problems relating to these methods are not discussed in this chapter, but will be dealt with later on in conjunction with the simulation results of individual cases where these methods have been deployed.

3.2   Initial Value Problem

Typically, ODE solvers expect the problem to be of first order, and hence vibration problems need to be transformed into state space. Formulating the problem in equation (3.1) in state space one obtains

$$\{\dot{q}\} = [A]\{q\} + [B]\{f(t, q)\} \tag{3.2}$$

where

$$\{q\} = \begin{pmatrix} r \\ \dot{r} \end{pmatrix} \quad [A] = \begin{bmatrix} 0 & I \\ -[M]^{-1}[K] & -[M]^{-1}[C] \end{bmatrix} \quad [B] = \begin{bmatrix} 0 \\ [M]^{-1} \end{bmatrix}$$

Equation (3.2), together with an initial condition $\{q(t=0)\} = x$, can then be used with the large number of integration codes available.

The results presented here have been produced entirely with MATLAB, which provides a small assortment of time integration solvers for ordinary differential equations given some initial conditions: single-step solvers based on Runge-Kutta formulas, a multi-step Adams algorithm, and, for stiff problems, a variable-order solver based on numerical differentiation. These solvers work reasonably well with the type of non-linearities considered here.

However, the usual care needs to be taken when integrating a system with matrices derived with the finite element method (Lipschitz criterion for convergence, Ascher et al. (1995)). Even with relatively few DOFs (for example 50), the eigenvalues of the linear system span a wide range such that the problem is sufficiently ill-conditioned to cause convergence or step-length problems for the integration routine, if the matrices are left untreated. The higher modes of the system, if not heavily damped, feature strongly in the trajectory and cause the step-length to become small. So, even if the problem size is not so large as to make a form of reduction absolutely necessary, it is found to be advantageous to perform the time integration in modal space, retaining only the block of lower modes. The computational cost of expanding the modal space back into physical space to calculate the nonlinear forces accurately is found to be very small by comparison.

As some of the systems in this investigation are modelled with a lumped parameter approach and have thus only a very small number of degrees-of-freedom, they were implemented in MATLAB using classical block-diagrams with feedback loops, examples of which are given in Figures 3.2(a) and 3.2(b). There is a big speed advantage in doing this, the block-diagram model in SIMULINK (which is a MATLAB add-on) integrates easily up to 20 times faster than the equivalent 'longhand' MATLAB code. Figure 3.2(a) shows the 2-DOF rotor system in the two outputs r, deflection of shaft centre, and r_{disc}, which is the deflection of the disc in the Jeffcott rotor model and might have a geometric eccentricity $\epsilon_{\text{r}} > 0$ from the shaft centre. The inputs in this block are the externally-determined phase angle (function of independent variable speed of rotation) and contact and excitation (unbalance) forces. In Figure 3.2(b) one can see how these forces and displacements interact in the whole system via the (in this case simple linear) contact model with the stator system.

3.3   Boundary Value Problem

When searching for the periodic solution, $\{q(t)\}$, of a non-linear ODE it is possible to express this as a boundary value problem, where the boundaries are the periodic
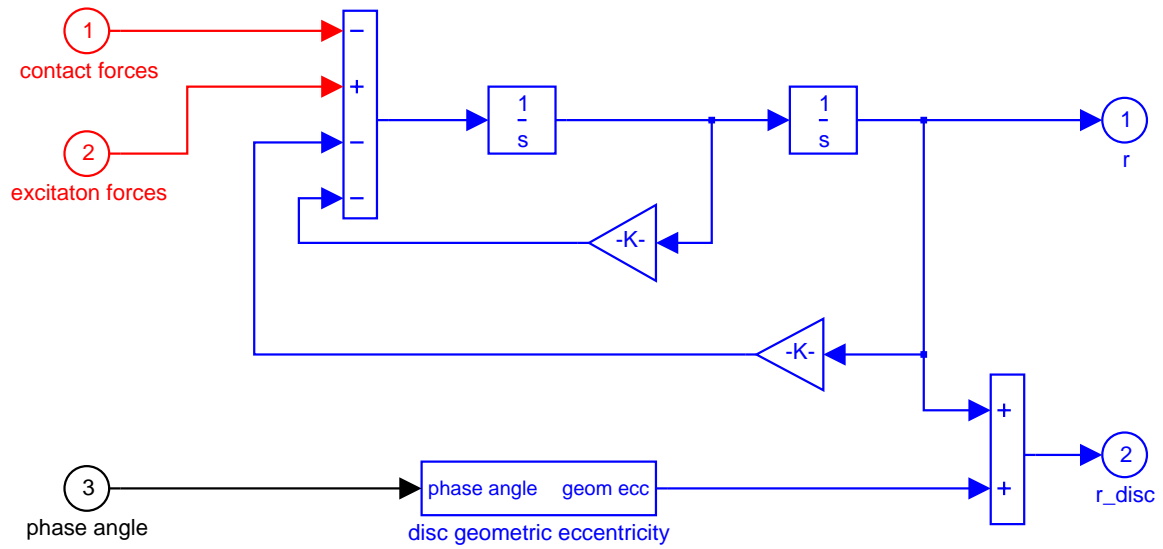
(a) rotor
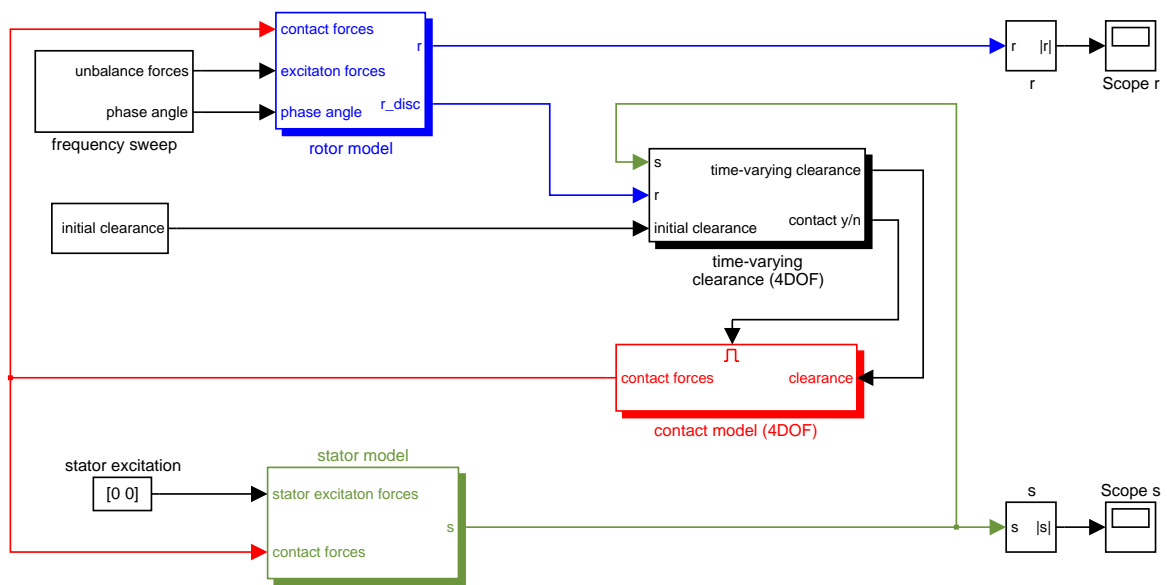
(b) whole rotor/stator system

Figure 3.2: Differential equation of rotor substructure and complete system

solutions at times $t = 0$ and $t = T$. At first, the problem in equation (3.2) has the non-separated and unknown boundary condition:

$$\{q(0)\} - \{q(T)\} = g\left(q(0), q(T)\right) = 0 \tag{3.3}$$

However, it is always possible to convert such a problem into 'standard' form with separated boundary conditions (Ascher et al., 1995). This might be a necessary step if the numerical tool at hand, such as a finite difference or collocation solver, demands (and most do) that the problem be stated in standard form:

$$\begin{aligned} \{\dot{q}\} &= [A]\{q\} + [B]\{f(t, q)\} \\ g_1(q(0)) &= 0 \quad g_2(q(T)) = 0 \end{aligned} \tag{3.4}$$

By adding the trivial ODEs

$$\{\dot{p}\} = 0 \tag{3.5}$$

to equation (3.2), one can imply $\{p(0)\} = \{p(T)\}$ without the use of boundary conditions, albeit at the cost of doubling the problem size, and the system to be solved can then be stated as:

$$\begin{aligned} \begin{pmatrix} \dot{q} \\ \dot{p} \end{pmatrix} &= \begin{bmatrix} A & 0 \\ 0 & 0 \end{bmatrix} \begin{pmatrix} q \\ p \end{pmatrix} + \begin{bmatrix} B & 0 \\ 0 & 0 \end{bmatrix} \begin{pmatrix} f \\ 0 \end{pmatrix} \\ \begin{bmatrix} I & -I \end{bmatrix} \begin{pmatrix} q \\ p \end{pmatrix} (0) &= 0 \quad \begin{bmatrix} -I & I \end{bmatrix} \begin{pmatrix} q \\ p \end{pmatrix} (T) = 0 \end{aligned} \tag{3.6}$$

Equation (3.6) is a boundary value problem (BVP) in standard form, with linear boundary conditions, that can be processed readily by a range of BVP solvers found in numerical maths libraries or software packages. A set of nodes at various times t_i is spanned in the time interval T. The calculation of the solution at these nodes is formulated with a collocation or finite difference approach that transforms the BVP into an algebraic set of equations.

3.4   Shooting Method

The time domain shooting method (Parker & Chua, 1989) is another approach to tackle the task of finding a periodic solution to equation (3.2). In its simplicity it is a very elegant method based on an intuitive trial and error approach (hence the name "shooting"). The boundary conditions for periodicity are stated in equation (3.3). Now, denoting a particular solution $\{q(t; x)\}$ of (3.2) as subject to the initial conditions $\{x\}$

$$\{q(t = 0; x)\} = \{x\} \tag{3.7}$$

one can change the problem to finding a suitable $\{x\} = \{x^\star\}$ such that the boundary condition (3.3) is met:

$$g\left(x, q(T; x)\right) = \{x\} - \{q(T; x)\} = 0 \tag{3.8}$$

Equation (3.8) is a non-linear algebraic equation that can be solved with standard iterative procedures such as quasi-Newton methods. Note that with every iteration, a time integration over T needs to be carried out so that $\{q(T; x)\}$ is obtained. Potential pitfalls for this simple version of the shooting method are cases where the time integration over T becomes unstable, even if the BVP is well-conditioned. More involved multiple-shooting methods try to overcome this problem, but the method then loses much of its simplicity and intuitiveness. In this project the simple shooting method was not found to be more problematic than solving the BVP described in the previous section, so an investigation into more advanced shooting methods were not deemed necessary.

3.5   Harmonic Balance Method

The harmonic balance method (HBM) offers a frequency-domain alternative to time-domain methods for analysis of cases where a steady-state, periodic solution to the equation of motion is sought, and exists. It seems that in the research effort published in the literature, the HBM is a far less commonly-used approach than the time-domain methods, although it can be very elegant and is computationally very fast. It is, therefore, presented here in slightly more detail than the well-established time-domain methods. The general idea is to represent each time history, $r(t)$, by its frequency content, $R(\omega)$, and to obtain a set of equations by balancing the terms with the same frequency components and to start an iterative procedure to find the roots of these equations.

An integer variable, ν, is introduced to accommodate possible sub-harmonics of an external excitation frequency, Ω (e.g. shaft rotation). The displacements, $r(t)$, and forces, $f(t)$, are represented as truncated Fourier series with N harmonics:

$$r(t) = \sum_{n=1}^{N} R_n \, e^{i\frac{n\Omega}{\nu}t} \qquad f_c(t) = \sum_{n=1}^{N} F_{c_n} \, e^{i\frac{n\Omega}{\nu}t} \qquad f_u(t) = \sum_{n=1}^{N} F_{u_n} \, e^{i\frac{n\Omega}{\nu}t} \tag{3.9}$$

Substituting these expressions, (3.9), into the rotor equation of motion, (3.1), and balancing the harmonic terms yields, for a harmonic n:

$$\left(-\left(\frac{n\Omega}{\nu}\right)^2 [M] + i\frac{n\Omega}{\nu}[C] + [K] \right) \{R_n\} = \{F_{c_n}\} + \{F_{u_n}\}. \tag{3.10}$$

Bringing all N harmonics into one equation can be symbolised as

$$\left[\tilde{K}\right]\{R\} - \{F_\mathrm{c}\} - \{F_\mathrm{u}\} = 0 \tag{3.11}$$

where $\{R\}$ and $\{F\}$ are the vectors of Fourier coefficients of displacements and forces, respectively, and $\left[\tilde{K}\right]$ is a complex block-diagonal matrix of the following form,

$$-\left(\frac{n\Omega}{\nu}\right)^2 [M] + \mathrm{i}\frac{n\Omega}{\nu}[C] + [K] = \left[\tilde{K}_{n,n}\right] \tag{3.12}$$

As the Fourier coefficients, F_{c_n}, of the non-linear forces, f_c, are functions of the displacements (and thus their respective Fourier coefficients),

$$F_{\mathrm{c}_n} = F_{\mathrm{c}_n}(R_0(\omega_0), R_1(\omega_1), \ldots, R_N(\omega_N)), \tag{3.13}$$

equation (3.11) is non-linear and must be solved iteratively. This iteration process (Kim et al., 1991) can be sketched as:

$$R(\omega)^{(k)} \xrightarrow{\mathrm{FFT}^{-1}} r(t)^{(k)} \rightarrow f_\mathrm{c}(t)^{(k+1)} \xrightarrow{\mathrm{FFT}} F_\mathrm{c}(\omega)^{(k+1)} \rightarrow R(\omega)^{(k+1)}$$

The fast Fourier transform (FFT) and its inverse (FFT^{-1}) could be replaced with a (costlier) curve-fitting or integration routine that does not rely on an integer number of cycles so that the procedure also works with incommensurate frequency components (quasi-periodic solution). The roots of equation (3.11) are found using a quasi-newton algorithm, variants of which are widely available in FORTRAN libraries on the web or in MATLAB's optimisation toolbox.

Finite element models of rotor/stator structures can contain quite a large number of degrees-of-freedom. Setting up equation (3.11) then leads to a much bigger problem with $2N + 1$ times more unknowns (real and imaginary components for N harmonics and a DC component). Any reduction of the original problem, therefore, leads to a huge saving in computational cost. The harmonic balance method offers an elegant means of reducing the problem order, so that only the non-linear DOFs need to be kept (Kim et al., 1991). Clearly, being able to keep only the non-linear DOFs vastly increases the speed in cases of large linear structures which have a few additional non-linear elements, as is typical for many classes of practical problems. The equation (3.10) is re-ordered for every harmonic, n (the subscripts $_n$ are omitted in this section for clarity):

$$\begin{bmatrix} \tilde{K}_\mathrm{mm} & \tilde{K}_\mathrm{ms} \\ \tilde{K}_\mathrm{sm} & \tilde{K}_\mathrm{ss} \end{bmatrix} \begin{pmatrix} R_\mathrm{m} \\ R_\mathrm{s} \end{pmatrix} = \begin{pmatrix} F_\mathrm{c} \\ 0 \end{pmatrix} + \begin{pmatrix} F_{\mathrm{u}_\mathrm{m}} \\ F_{\mathrm{u}_\mathrm{s}} \end{pmatrix} \tag{3.14}$$

where subscripts $_\text{m}$ and $_\text{s}$ stand for non-linear (master) and linear (slave) degrees-of-freedom, respectively. It follows that

$$\left[\hat{\tilde{K}}\right] = \left[\tilde{K}_\text{mm}\right] - \left[\tilde{K}_\text{ms}\right]\left[\tilde{K}_\text{ss}\right]^{-1}\left[\tilde{K}_\text{sm}\right] \tag{3.15}$$

$$\left\{\hat{F}_\text{u}\right\} = \left\{F_\text{u}_\text{m}\right\} - \left[\tilde{K}_\text{ms}\right]\left[\tilde{K}_\text{ss}\right]^{-1}\left\{F_\text{u}_\text{s}\right\} \tag{3.16}$$

and

$$\left[\hat{\tilde{K}}\right]\left\{R_\text{m}\right\} - \left\{F_\text{c}\right\} - \left\{\hat{F}_\text{u}\right\} = 0 \tag{3.17}$$

In contrast to the widely-used Guyan reduction, equation (3.17) is an exact reduction of the original problem as long as the prerequisites for applying the harmonic balance method are met and the number of harmonics included in the decomposition is sufficient. This reduction makes the repetitive task of calculation solutions at various parameters for the continuation of a solution branch much cheaper indeed.

3.6 Arc-Length Continuation

Usually, the system behaviour is of interest over a range of values for at least one parameter (e.g. speed of shaft rotation), so that the solution has to be calculated at different parameter values respectively. As time-domain methods seem to be used more often than frequency-domain methods, the use of continuation schemes in conjunction with the harmonic balance method appears to be not as common in engineering applications as, say, with shooting methods. However, arc-length continuation is just as applicable in the frequency domain as it is in the time-domain. The task of finding a periodic solution for equation (3.1) can be transformed into an equivalent root-finding problem, for example by means of BVP, shooting, HBM etc (see equations (3.8) and (3.11)):

$$F(y, \Omega) = 0 \tag{3.18}$$

where Ω is an independent, externally controlled (exogenous), scalar parameter, such as the excitation frequency, over a range in which the solution to equation (3.1) is of interest.

Using the notation $F_y = \frac{\partial F(y, \Omega)}{\partial y}$ and $F_\Omega = \frac{\partial F(y, \Omega)}{\partial \Omega}$, the differential of equation (3.18) can be written as:

$$\frac{\mathrm{d}y}{\mathrm{d}\Omega} = -(F_y)^{-1}F_\Omega \tag{3.19}$$

Choosing Ω directly as a continuation parameter (called 'sequential' or 'natural continuation') fails at turning points because of the singularity of F_y (see transition from

stable to unstable at $\Omega \approx 1.4$ in Figure 3.3). To overcome this limitation, a continuation parameter, α, along the arc-length of a solution branch is chosen, so that $y = y(\alpha)$ and $\Omega = \Omega(\alpha)$. From equation (3.18) one obtains:

$$F_y \frac{\mathrm{d}y}{\mathrm{d}\alpha} + F_\Omega \frac{\mathrm{d}\Omega}{\mathrm{d}\alpha} = \begin{bmatrix} F_y & F_\Omega \end{bmatrix} \begin{pmatrix} y' \\ \Omega' \end{pmatrix} = 0 \tag{3.20}$$

The arc-length, α, may be normalised so that the tangent vector, $\begin{pmatrix} y' \\ \Omega' \end{pmatrix}$, has unit length (Nayfeh & Balachandran, 1995):

$$\left(\frac{\mathrm{d}y_1}{\mathrm{d}\alpha}\right)^2 + \cdots + \left(\frac{\mathrm{d}y_N}{\mathrm{d}\alpha}\right)^2 + \left(\frac{\mathrm{d}\Omega}{\mathrm{d}\alpha}\right)^2 = 1 \tag{3.21}$$

With $\big(y(\alpha^{[k]}), \Omega(\alpha^{[k]})\big)$ denoting a solution previously calculated during continuation, an additional equation can be gained for the additional unknown, α, by multiplying equation (3.21) with $(\mathrm{d}\alpha)^2$,

$$\begin{aligned} 0 = g(y, \Omega, \alpha) \\ = \big(y_1 - y_1(\alpha^{[k]})\big)^2 + \cdots + \big(y_N - y_N(\alpha^{[k]})\big)^2 \\ + \big(\Omega - \Omega(\alpha^{[k]})\big)^2 - \big(\alpha - \alpha^{[k]}\big)^2 \end{aligned} \tag{3.22}$$

Equation (3.22) can now be used to parameterise equation (3.11) by formulating an extended system (Seydel, 1994)

$$\tilde{F}(y, \Omega, \alpha) = \begin{pmatrix} F(y, \Omega) \\ g(y, \Omega, \alpha) \end{pmatrix} = 0. \tag{3.23}$$

Equation (3.23) allows the solver to move along the arc-length, α, of a solution branch. The reader is referred to Seydel (1994); Parker & Chua (1989); Nayfeh & Balachandran (1995) for predictor-corrector and step control schemes that facilitate the following of a solution of $\tilde{F}(y, \Omega, \alpha)$ along a range of values for α. For simplicity, the results of the previous step $\big(y(\alpha^{[k]}), \Omega(\alpha^{[k]})\big)$ may be used as an initial guess for the next, and a simple step control $\alpha^{[k+1]} = \alpha^{[k]} + \frac{p}{q}$ can be employed, where p is a constant and q is the number of iterations needed for the previous solution. With quasi-Newton solvers an optimal ratio of $\frac{p}{q}$ is suggested by Seydel (1994) such that roughly $q = 6$ iterations of the quasi-Newton solver are necessary in between arc-length steps. As will be demonstrated in numerical simulations later on, there arc-length continuation procedure facilitates the passing turning points and following the over-hung part of the solution branch. Obtaining information about the stability of such a solution branch being followed is discussed in the following section.

3.7   Stability Analysis in the Frequency Domain

As stated earlier, BVP, shooting, and HBM methods transform the problem into a set of algebraic equations. As the underlying system is non-linear, this set of equations can have multiple solutions. Furthermore, some of these solution might not be stable. The term "instability" is used throughout all the chapters in a local sense, and whenever global instability is meant (in other words, a solution that grows out of bounds), this is stated explicitly.

So, when arc-length continuation (or any other continuation scheme) is employed, there is nothing in the algorithm *per se* that can warn the user that a particular solution branch followed has stepped over a turning or bifurcation point and the solution has switched stability, from stable to unstable, or vice versa. For example, there might only be a little change in the conditioning of the Jacobian of the system before and after such a change, nor is there a change in the convergence behaviour of the algorithm. This is a practical problem (not a theoretical one, as the Jacobian F_y is indeed singular exactly on a turning or bifurcation point) as change in conditioning of the Jacobian could occur far more rapidly than the step-length is able to resolve. Figures 3.3 and 3.4 show examples of how the condition numbers (ratio of largest singular value over smallest, ∞ for singular matrices) of F_y and $\begin{bmatrix} F_y & F_\Omega \end{bmatrix}$ change over the parameter Ω (green curves). The scale of the condition numbers is plotted on the right in [dB], and in order to relate these condition numbers more easily to the physical state of the system at these points, the displacement envelope is plotted as well (blue curves). It can be seen in Figure 3.3 that at the upper turning point (roughly $\Omega = 1.4$) the condition number of F_y has a sharp peak, and had the spacing been finer the singularity of F_y would have been more apparent. In contrast the condition number of $\begin{bmatrix} F_y & F_\Omega \end{bmatrix}$, shown in Figure 3.4, does not undergo any big changes and remains reasonably low.

Stability in the time-domain is usually determined by the well-known Floquet multipliers, which are extensively covered, for example in the previously-cited text books. Many papers employing HBM either ignore the stability issue or revert back to the time domain to investigate the stability properties. However, at little computational cost, stability can be analysed in the frequency domain with a modification of an algorithm employed for *linear* time-variant systems. The algorithm is called Hill's method and transforms a linear time-variant system into an eigenvalue problem of a linear time-invariant system (Gasch & Knothe, 1989).

In order to use the same approach for non-linear systems, the stability analysis is carried out by investigating the effect of a perturbation around a periodic solution $r^\star(t)$. Although Hill's method for linear systems is documented in text books, and the approach to study the stability of nonlinear systems typically involves the linearisation around that solution (Floquet theory (Seydel, 1994)), the following approach of the combination of the two has not been previously encountered in the literature. Let the perturbation be described as $p(t)$, where $p(t)$ consists of a decay term $e^{\lambda t}$ and a periodic
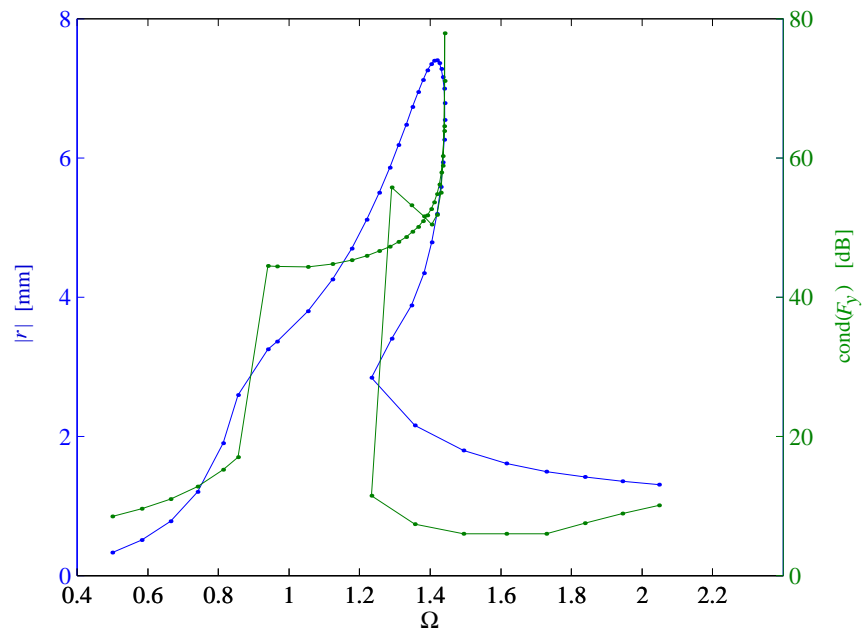
Figure 3.3: Condition number of F_y
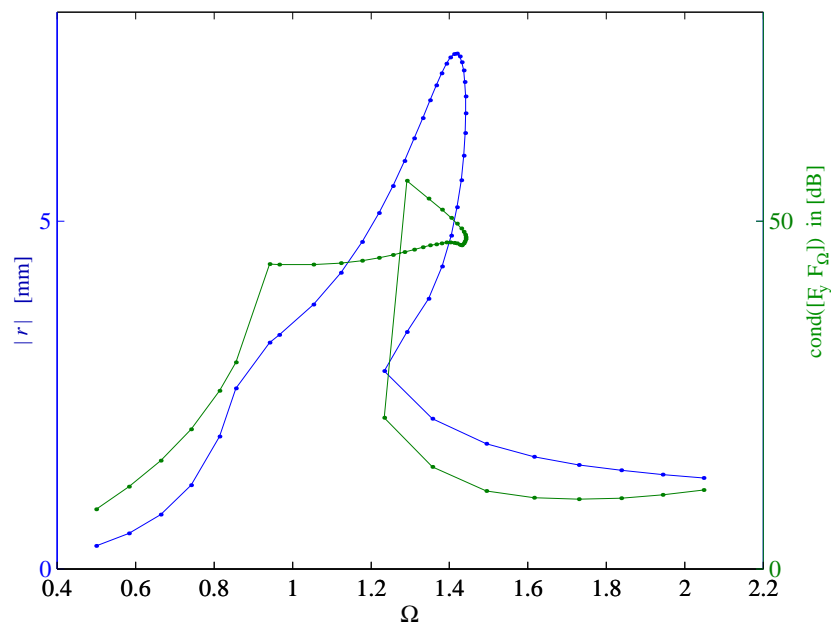
Figure 3.4: Condition number of $[F_y \ F_\Omega]$

term $s(t)$ (Gasch & Knothe, 1989; Genta, 1999):

$$p(t) = \mathrm{e}^{\lambda t}\, s(t) \qquad s(t) = \sum_{n=-N}^{N} S_n\, \mathrm{e}^{\mathrm{i}\frac{n\Omega}{\nu}t} \tag{3.24}$$

Substituting

$$r(t) = r^{\star}(t) + p(t) \tag{3.25}$$

into equation (3.1), one obtains

$$[M]\left\{\ddot{r^{\star}}\right\} + [C]\left\{\dot{r^{\star}}\right\} + [K]\left\{r^{\star}\right\} +$$
$$\left(\lambda^2 [M]\{s\} + \lambda\left(2\,[M]\{\dot{s}\} + [C]\{s\}\right) + [M]\{\ddot{s}\} + [C]\{\dot{s}\} + [K]\{s\}\right)\mathrm{e}^{\lambda t}$$
$$= \left\{f_{\mathrm{u}}(t)\right\} + \left\{f_{\mathrm{c}}\left(r^{\star} + s\,\mathrm{e}^{\lambda t}\right)\right\}. \tag{3.26}$$

By substituting the Fourier representations of $r^{\star}(t), s(t)$ into equation (3.26), the harmonic components can be balanced in an analogue manner to equation (3.11):

$$\left[\tilde{K}\right]\{R^{\star}\} + \left(\lambda^2\left[\tilde{M}\right] + \lambda\left[\tilde{C}\right] + \left[\tilde{K}\right]\right)\{S\}\,\mathrm{e}^{\lambda t}$$
$$= \{F_{\mathrm{u}}\} + \left\{F_{\mathrm{c}}\left(R^{\star} + S\,\mathrm{e}^{\lambda t}\right)\right\} \tag{3.27}$$

where $\left[\tilde{M}\right], \left[\tilde{C}\right]$ are constructed in a similar manner to $\left[\tilde{K}\right]$ in equation (3.12) and $\{R^{\star}(\omega)\}, \{S(\omega)\}$ are the vectors of Fourier coefficients for $r^{\star}(t), s(t)$, respectively.

In what follows, an attempt is being made to find a cost-effective linearisation for the term $\left\{F_{\mathrm{c}}\left(R^{\star} + S\,\mathrm{e}^{\lambda t}\right)\right\}$ so that equation (3.27) can be developed further. Consider a variant of equation (3.11):

$$\{F_{\mathrm{c}}\} = \left[\tilde{K}\right]\{R\} - \{F_{\mathrm{u}}\} - \{E(R)\} \tag{3.28}$$

where $\{E(R)\}$ is the error in the balancing terms. Developing this as a Taylor series around a known solution of equation (3.11), $\{R^{\star}\}$, one obtains

$$\{F_{\mathrm{c}}(R)\} = \left[\tilde{K}\right]\{R\} - \{F_{\mathrm{u}}\} - [E'(R^{\star})]\left(\{R\} - \{R^{\star}\}\right) + \text{higher order terms} \tag{3.29}$$

with the abbreviation

$$[E'] = \left[\frac{\partial E}{\partial R}\right].$$

Substituting equation (3.29) into (3.27) and neglecting terms of higher order, equation (3.27) simplifies to the following eigenvalue problem:

$$\left(\lambda^2\left[\tilde{M}\right] + \lambda\left[\tilde{C}\right] + [E'(R^{\star})]\right)\{S\} = 0. \tag{3.30}$$

It is important to note that the term $[E'(R^\star)]$ is already available as a by-product of the quasi-Newton solution technique, most probably as a numerical approximation, as it is the Jacobian of the objective function defined by equation (3.11).

Solving for the eigenvalues of equation (3.30), one obtains a set of λ_i with real and imaginary parts, where a negative real part indicates stability of the solution, as the perturbation $p(t)$ decays with time, and a positive real part indicates instability. Then, by solving this eigenvalue problem at the end of the overall iteration procedure, and simply checking if any λ_i possesses a positive real part, one can easily determine whether a periodic solution, $r^\star(t)$, is unstable. This also helps with finding possible bifurcation points. A change in stability of a solution branch is a sufficient indicator that a turning or bifurcation point has been passed, and the algorithm could be directed to determine the cross-over point within this interval of change more closely. Should this be of interest, and the cross-over point found, the rank of F_y and $\begin{bmatrix} F_y & F_\Omega \end{bmatrix}$ at the cross-over determines whether the point in question is a turning or bifurcation point (Seydel, 1994). If, indeed, it is a bifurcation point, an additional solution branch may be followed.

Chapter 4

Numerical Parameter Studies

4.1 Overview

The previous Chapters 2 and 3 covered the design of a numerical windmill model and the algorithms to solve the resulting equations. This Chapter presents various simulation results of mainly the simple model presented in section 2.5, using the methods described in Chapter 3. In order to relate individual effects to certain parameters, the numerical model has to be built in a modular fashion, increasing its complexity only as required by the addition of new parameters. Figure 4.1 shows a map of the model configurations (listed below with their respective simplifying assumptions), which are used to investigate the different phenomena:

- A (isotropy of stiffness, geometry, and inertia properties; no friction; no stator mass, but stator stiffness) – studied: effects of acceleration in run-up, influence of gap size and rotor and stator damping

- B (isotropy, no friction) – influence of the ratio rotor to stator mass, contact stiffness, and rotor/stator separation

- C (isotropy, no stator mass) – influence of friction

- D (no friction) – geometric eccentricity, wing degree-of-freedom

- E – contact of flexible bodies

The last section notes a few numerical difficulties that were encountered, specifically regarding the time-marching solution, contact model, and multiple periodic solutions. The default values for the following parameter studies in this Chapter are shown in Table 4.1, any deviations of the values will be specified in the context of each simulation case.

The plot which typically shows the results of the simulation runs in this chapter, Figure (4.2) in section 4.2 is such an example, may be introduced briefly. The vibration
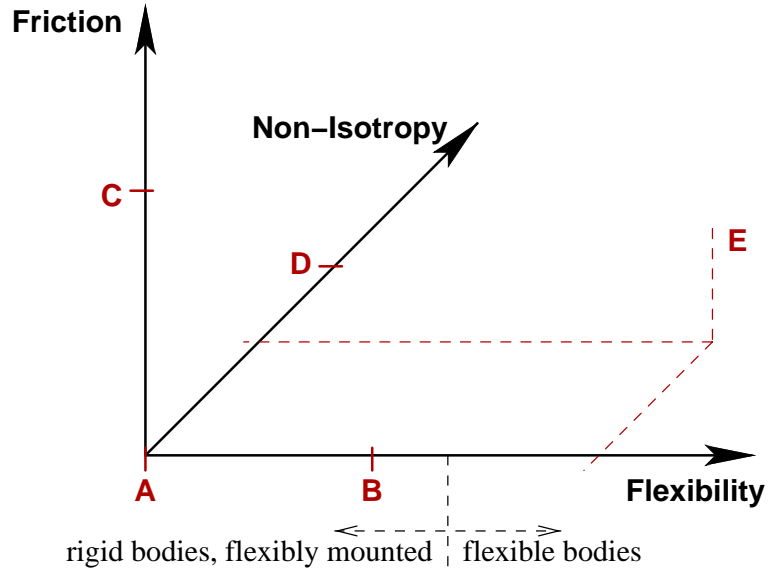
Figure 4.1: road map for parameter configurations

Table 4.1: parameter values (deviations are indicated in the text or figure) used for all simulations (linear contact model, including friction on rotor and stator).

$$\epsilon_r = 0 \qquad \epsilon_s = 0 \qquad \epsilon_m = 1\,e^{i\frac{\pi}{2}}$$

$$\omega_r = 1\,\text{rad/s} \qquad \omega_s^2 \equiv \gamma_k \omega_r^2 \qquad \zeta_r = 0.05 \qquad\qquad \zeta_s = 0.07$$

$$\gamma_m = 0.5 \qquad \gamma_k = 2 \qquad \gamma_c = 20 \qquad\qquad c_c = 0$$

$$\mu = 0.1 \qquad h = 2 \qquad \dot{\Omega} = 0.001\,\text{rad/s}^2$$

envelope of the rotor is plotted against the shaft speed, Ω. In most cases the shaft speed is normalised with respect to the first (or sole) natural frequency, ω_r, of the rotor system, so that for $\frac{\Omega}{\omega_r} = 1$ the shaft speed is at rotor resonance. It is made clear in the context of each case whether a particular plot is the result of a (slow, time-marching) sweep, be it a run-up or run-down of the shaft, or a series of discrete steady-states (time-marching or frequency-domain). A horizontal dashed line, typically at $|r| = 2$ or $|r| = 3$, signifies the gap size used. A response below the gap size, however, does not necessarily mean that rotor and stator are not in contact. Again, these particulars are covered in the relevant context.

4.2   Case A - no stator mass

4.2.1   Sweeps

Frequency sweeps (continuously increasing or decreasing shaft speed) are not only used when one wishes to simulate a system actually undergoing acceleration or deceleration, but it is also a typical approach to cover the steady-state vibration over a range of shaft speeds. If these sweeps are carried out slowly enough, the system has time to settle into its steady-state response before the next small change in shaft speed. However, if not conducted carefully, and if insufficient time is allowed for the sweep, the transient effects can skew the results significantly.

Figure 4.2 shows the effect on the vibration envelope of r_r of different acceleration and deceleration values for the change in shaft speed, $\dot{\Omega}$, which is noted as α in the legend of the plot. As reference, the steady-state response of the system is plotted as a dotted line. For $\dot{\Omega} = 0.0001 \, \text{rad/s}^2$ and $\dot{\Omega} = 0.001 \, \text{rad/s}^2$ the run-ups and run-downs are quite similar, suggesting that by further reducing $\dot{\Omega}$ not much more similarity would be gained with the reference steady-state response. So with an acceleration level of $\dot{\Omega} = 0.001 \, \text{rad/s}^2$ it is more the steady-state rather than the transient components which dominate the behaviour of the system. For larger values of $\dot{\Omega}$, not surprisingly, the overshoots become larger compared with the steady-state response. As noted earlier, the over-hanging branch of a steady-state cannot be traced with a sweep.
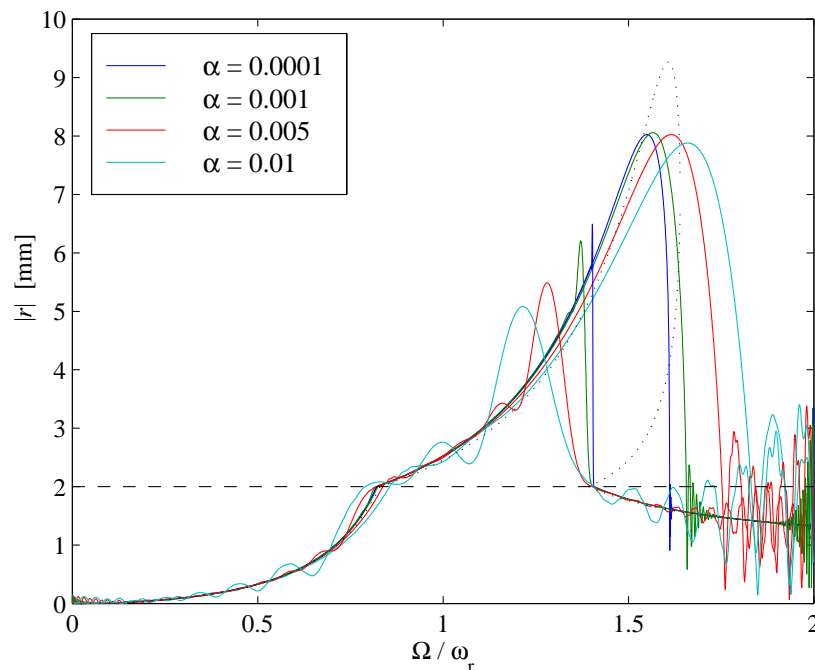
Figure 4.2: rotor amplitude with varying rates of acceleration/retardation, $\alpha \equiv \dot{\Omega}$, $\gamma_m = 0$, other paraters as in Table 4.1 (reference dotted line is steady-state response).

4.2.2   Rotor and stator damping
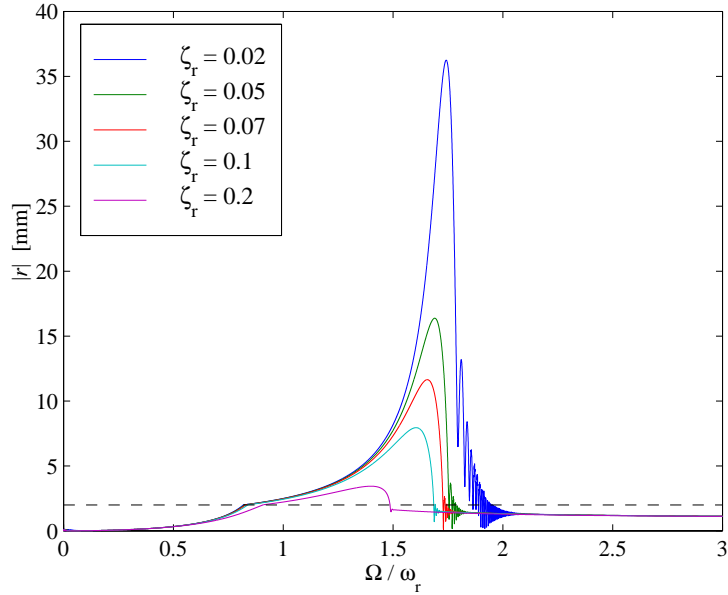
Figure 4.3: rotor amplitude (run-ups) with varying rotor external damping, $\gamma_\mathrm{m} = 0$, $\zeta_\mathrm{s} = 0$, other parameters as in Table 4.1
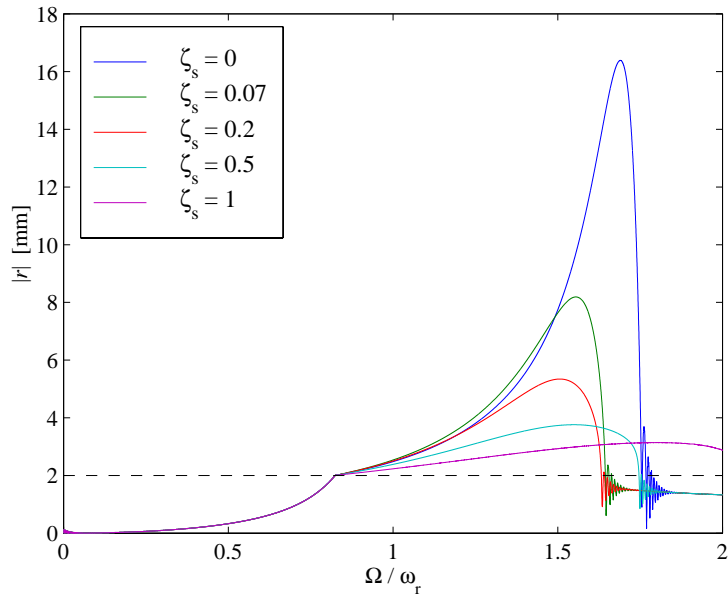
Figure 4.4: rotor amplitude (run-ups) with varying stator damping, $\gamma_\mathrm{m} = 0$, other parameters as in Table 4.1

Figures 4.3 and 4.4 show the effect of rotor external damping and stator damping,

respectively, during a slow run-up. Naturally, higher damping values reduce the response levels. However, higher rotor external damping also reduces the speed interval where the rotor and stator remain in contact. In contrast, high levels of stator damping expand the speed interval of rotor/stator contact.

Figure 4.5 shows the vibration envelope calculated with the harmonic balance method but using the same system parameters as in Figure 4.4 and also incrementing the speed (as in a run-up). The curves for the given damping values are very similar in shape and the jump phenomenon occurs at roughly the same speeds as for the time-domain solution. This signifies that the acceleration used in Figures 4.3 and 4.4 is sufficiently low so that the system is close to being in steady-state. In Figure 4.5 a peculiarity can be observed: around $\Omega/\omega_{\mathrm{r}} = 1.4$ there is a patch of dots of the various run-downs. At these points the non-linear solver failed to converge to a solution for the harmonic balance equation (the solver became stuck at a local minimum which is not a root). The iteration process uses a very simple continuation here: the solution of the previous step is used as a starting guess for the next, pre-determined, frequency. So, at the turning point $\Omega/\omega_{\mathrm{r}} = 1.4$, the algorithm obviously has some difficulties in finding the upper branch of the solution during run-down. Once found, however, the algorithm continues efficiently. This problem will be circumvented, as shown in later examples, by employing an arc-length continuation scheme (see also Chapter 3).
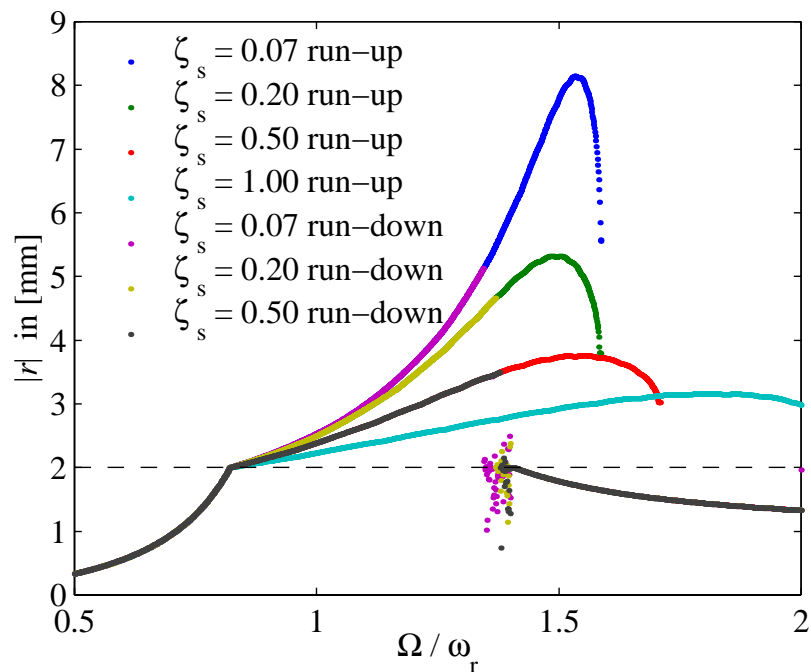
Figure 4.5: rotor amplitude (steady-state, HBM) with varying stator damping, $\gamma_{\mathrm{m}} = 0$, other parameters as in Table 4.1

4.2.3   Gap

The gap size in the system obviously dictates when contact between rotor and stator may be established under low levels of excitation. But it also has an effect on the response levels. Figure 4.6 shows that the smaller the gap between rotor and stator, the higher the response level. As a smaller gap results in a higher system stiffness, the resonance of the joint system shifts upwards. Thus, the resonance is excited at higher speeds at which the unbalance force is also higher, resulting in a larger deflection. This is also in line with what Williams (1996b) reported. It can also be seen that rotor and stator drop out of contact later (during run-up) for smaller gap sizes. Again, this is linked to the upward shift in natural frequency of the joint system.
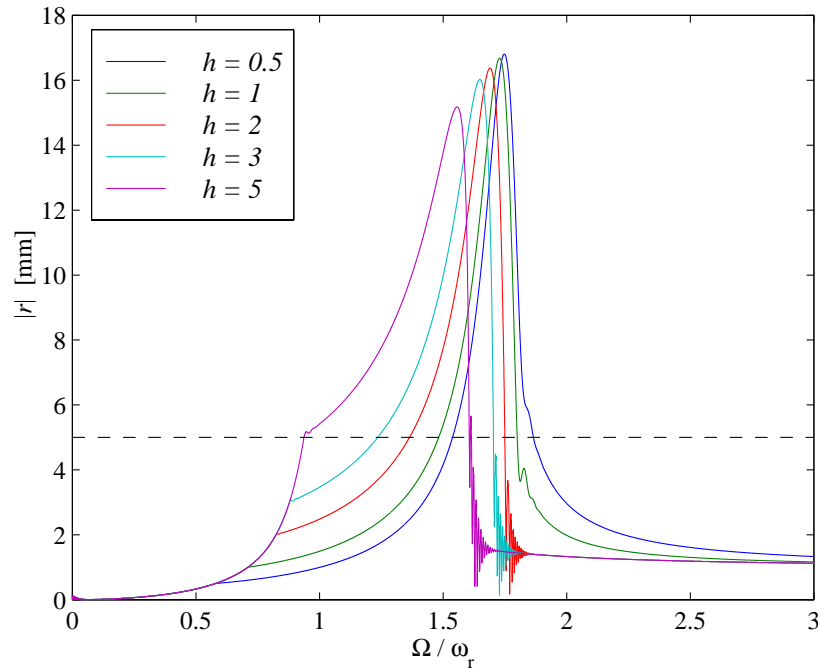
Figure 4.6: rotor amplitude (run-ups) with varying gap size, $\gamma_m = 0$, $\zeta_s = 0$, other parameters as in Table 4.1

4.3   Case B - rigid rotor and stator, flexibly mounted

4.3.1   Stator mass

Many papers in the literature model rotor/stator contact problems where the stator mass seems to be negligible and is therefore not included in the model. In this section,

the phenomena that occur when the stator mass is *not* neglected in the simulations are investigated. Increasing the stator mass of the system produces a reduction in response level (Figure 4.7), as one would expect when increasing the inertia of the overall system, and also increases the contact load (discussed in the following section, Figures 4.11, 4.12, 4.13).
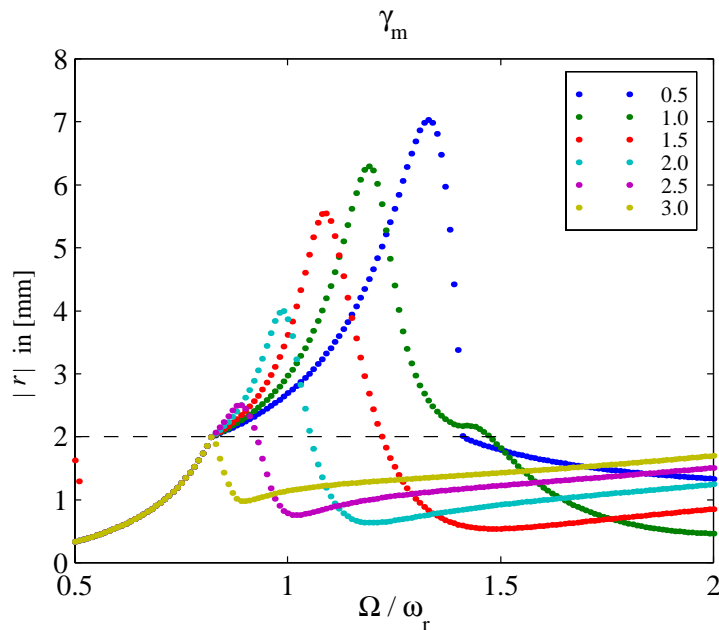
Figure 4.7: rotor amplitude with varying stator mass, other parameters as in Table 4.1

Beyond a certain level of stator mass, the rotor and stator do not separate again when stepping up the speed, but continue to oscillate in continuous contact around their joint centre of gravity. This is not obvious from Figure 4.7, but will be investigated in detail in the following section. The amplitude of oscillation with rotor and stator in contact may even be lower than the initial value of the gap. As a side note about this configuration (results shown in a later discussion, Figure 4.27), during run-down, accordingly, the rotor amplitude drops sharply when the rotor response overcomes the gap and full annular rub is initiated, before the system passes through its joint resonance.

4.3.2 Separation of rotor and stator

In order to investigate further why the rotor and stator do not separate at higher speeds, a number of plots are shown below. There are three figures in each group of plots, referring to $\gamma_m = 0.5, 1.0, 2.5$. For $\gamma_m = 0.5$, rotor and stator separate after the

amplitude jump (Figure 4.8); for $\gamma_\mathrm{m} = 1.0$, rotor and stator come close to separation as the contact drops to a minimum level at around $\Omega/\omega_\mathrm{r} = 1.38$ (Figure 4.9); and for $\gamma_\mathrm{m} = 2.5$, there is a strong contact force component throughout the speed range (Figure 4.10).

The first group of plots (Figures 4.8, 4.9, 4.10, referring to $\gamma_\mathrm{m} = 0.5, 1.0, 2.5$ respectively) show the displacement envelopes of rotor and stator and contact depth. In the second group (Figures 4.11, 4.12, 4.13) each figure contains four compass plots of rotor inertia, stiffness and damping forces (blue), the contact force acting on the rotor (red), and the unbalance force (black). The third group (Figures 4.14, 4.15, 4.16) shows the vector sums of the inertia, stiffness, and damping forces of rotor and stator (blue and green, respectively), the contact force acting on the stator (red), and the unbalance force (black). Each compass plot shows these forces in phase relation to each other at one particular speed of rotation, Ω. Note that each compass plot has a different scale of magnitude (radial lines) to accommodate the widely varying magnitudes. The unbalance force was chosen as the reference phase position ($0\,^\circ$). As the contact force is the only external force on the stator, it has to be equal in magnitude, and in opposite direction, to the combined stator inertia, stiffness and damping forces. The magnitude of the contact force in relation to the vector sum of the rotor system forces thus shows how much energy of the unbalance excitation is transferred into the stator movement in relation to the rotor movement. For $\gamma_\mathrm{m} = 0.5$ the stator has its natural frequency at $\Omega/\omega_\mathrm{r} = 1.41$. So as the excitation frequency is approaching the natural frequency of the stator, less energy from the unbalance excitation gets transferred into the stator and more into the rotor movement. For $\gamma_\mathrm{m} = 1.0$ the natural frequency of the stator is at $\Omega/\omega_\mathrm{r} = 1.22$. In this case the drop of rotor amplitude occurs around $\Omega/\omega_\mathrm{r} = 1.38$ and the stator amplitude and contact force go through a minimum. However, this minimum at $\Omega/\omega_\mathrm{r} = 1.38$ occurs after the natural frequency of the stator ($\Omega/\omega_\mathrm{r} = 1.22$) has been passed, so that after the drop in rotor amplitude a sufficient amount of energy is transferred from the unbalance excitation to the stator via the contact force, thereby rotor and stator stay in contact.
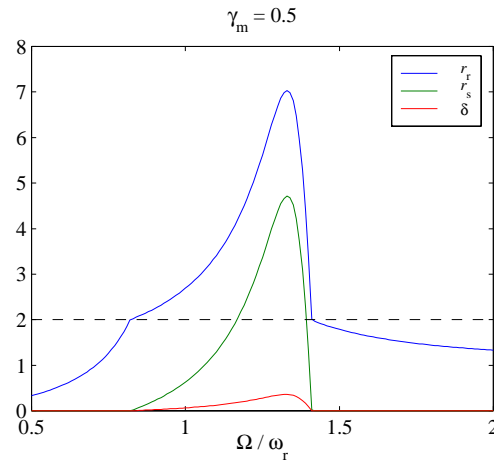
Figure 4.8: rotor, stator and contact penetration envelopes [mm], $\gamma_\mathrm{m} = 0.5$
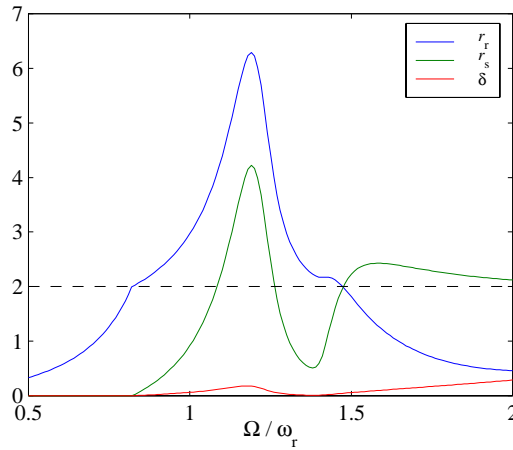
Figure 4.9: rotor, stator and contact penetration envelopes [mm], $\gamma_\mathrm{m} = 1.0$
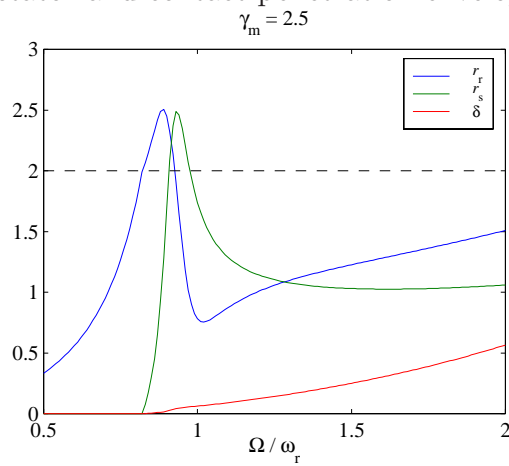
Figure 4.10: rotor, stator and contact penetration envelopes [mm], $\gamma_\mathrm{m} = 2.5$
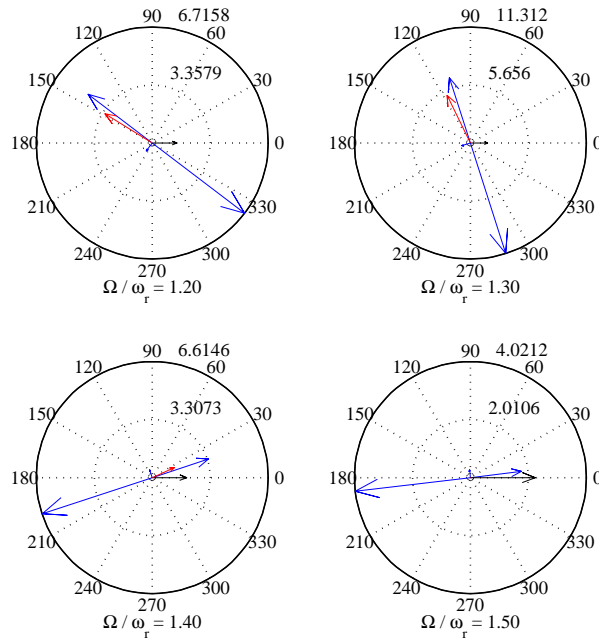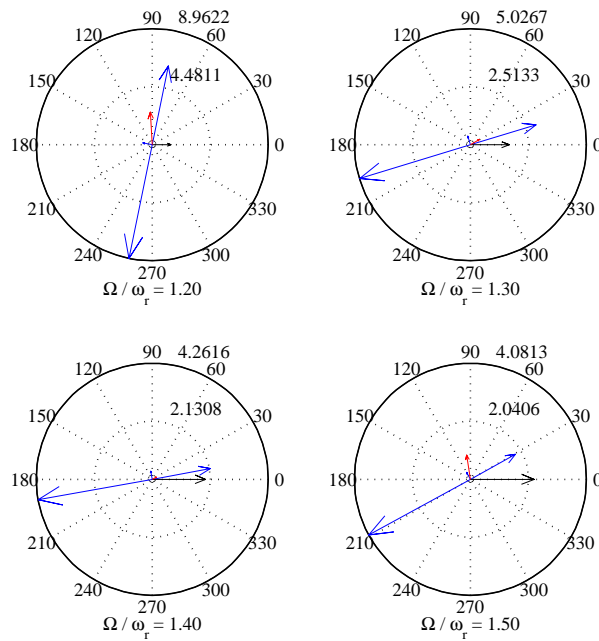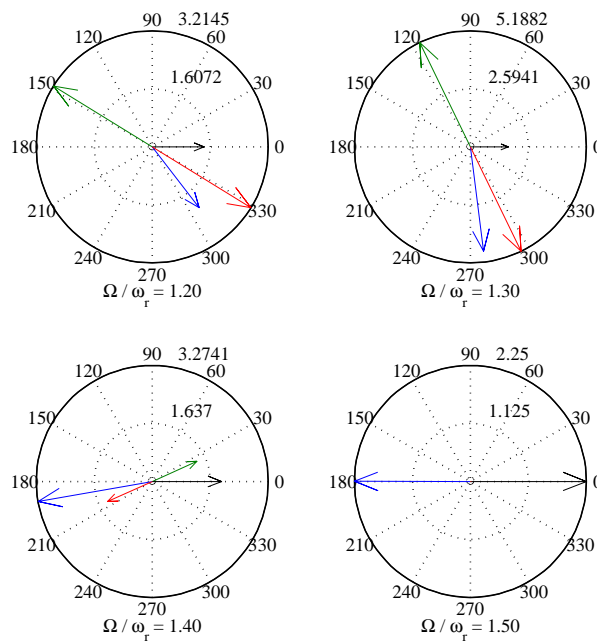$\gamma_\mathrm{c} = 15$, all other parameters as in Table 4.1

Figure 4.11: rotor forces, $\gamma_{\mathrm{m}} = 0.5$

Figure 4.12: rotor forces, $\gamma_{\mathrm{m}} = 1.0$
rotor inertia, stiffness and damping forces (blue),
contact force acting on the rotor (red), unbalance force (black) in [N]
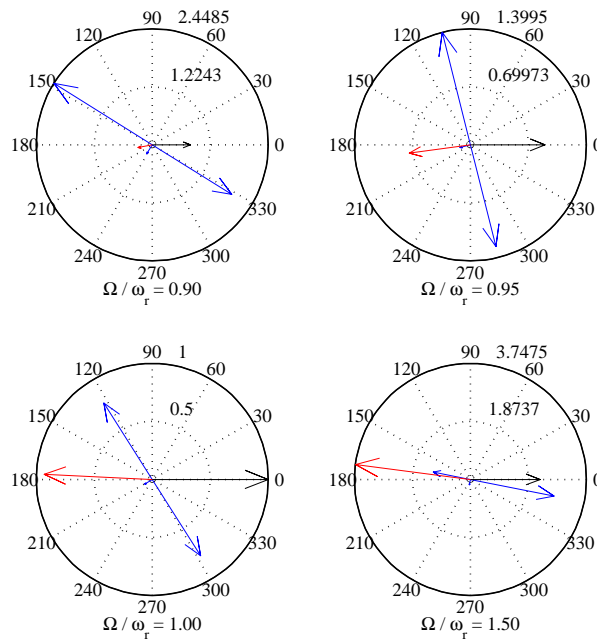
Figure 4.13: $\gamma_m = 2.5$, rotor inertia, stiffness and damping forces (blue), contact force acting on the rotor (red), unbalance force (black) [N]

Figure 4.14: $\gamma_m = 0.5$, sums of the inertia, stiffness, and damping forces of rotor and stator (blue and green, respectively), contact force acting on stator (red), unbalance force (black) in [N]
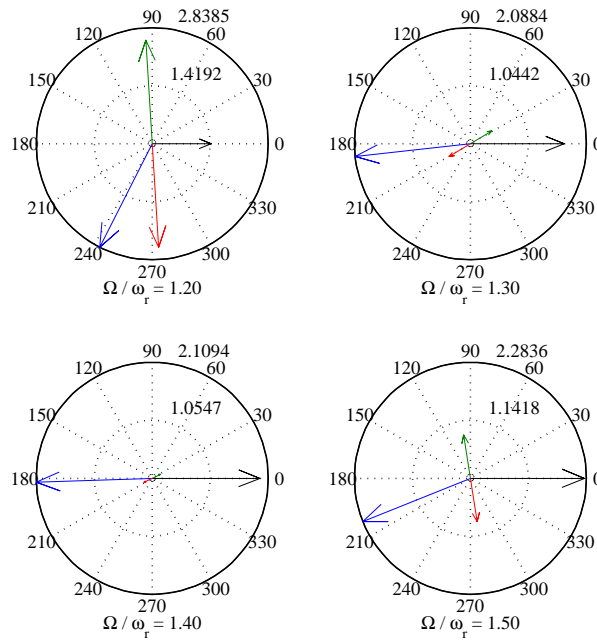
Figure 4.15: stator and rotor forces, $\gamma_{\mathrm{m}} = 1.0$
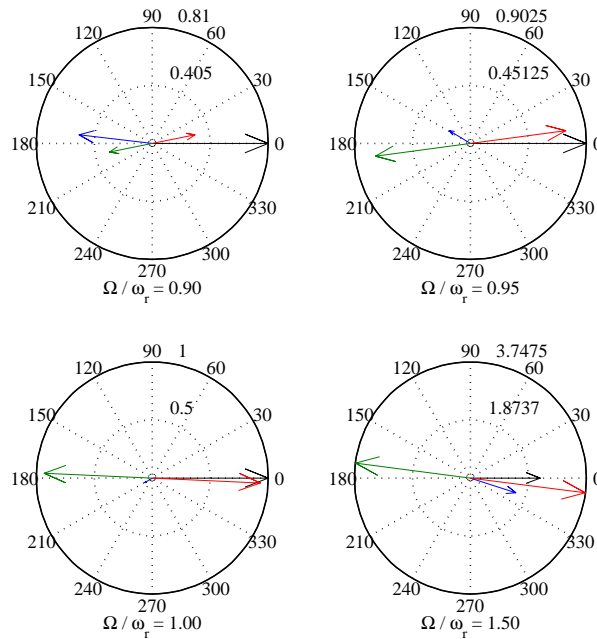
Figure 4.16: stator and rotor forces, $\gamma_{\mathrm{m}} = 2.5$

sums of the inertia, stiffness, and damping forces of rotor and stator (blue and green, respectively), contact force acting on stator (red), unbalance force (black) in [N]

4.3.3   Contact stiffness

In Figure 4.17 the influence of different contact stiffnesses is shown for higher speeds
in cases where rotor and stator are still in contact. Above a certain speed, the rotor
deflection of a system with a relatively low contact stiffness (10 times larger than the
rotor stiffness) is much higher than with a larger contact stiffness (100 times rotor
stiffness). This is due to an increasing penetration depth of the contact zone for lower
contact stiffnesses, making the effect of the higher mode of vibration, which is the
out-of-phase motion of rotor and stator, more prominent.
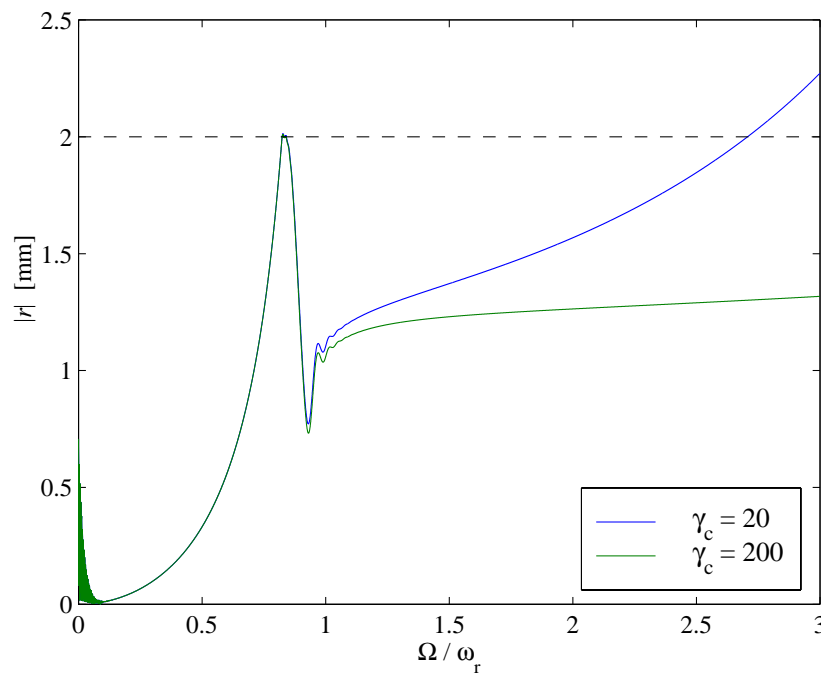
Figure 4.17: rotor deflection with varying contact stiffness, $\gamma_m = 3$, other parameters
as in Table 4.1

4.4   Case C - friction

4.4.1   Forward whirl

Figure 4.18 shows the vibration envelopes for the two friction models, as presented in
section 2.6, with various friction coefficients. One can see that there is no qualitative
difference in system behaviour but, especially for low values of friction, the quantitative
difference in deflection can be as much as 50%. A general tendency that higher values
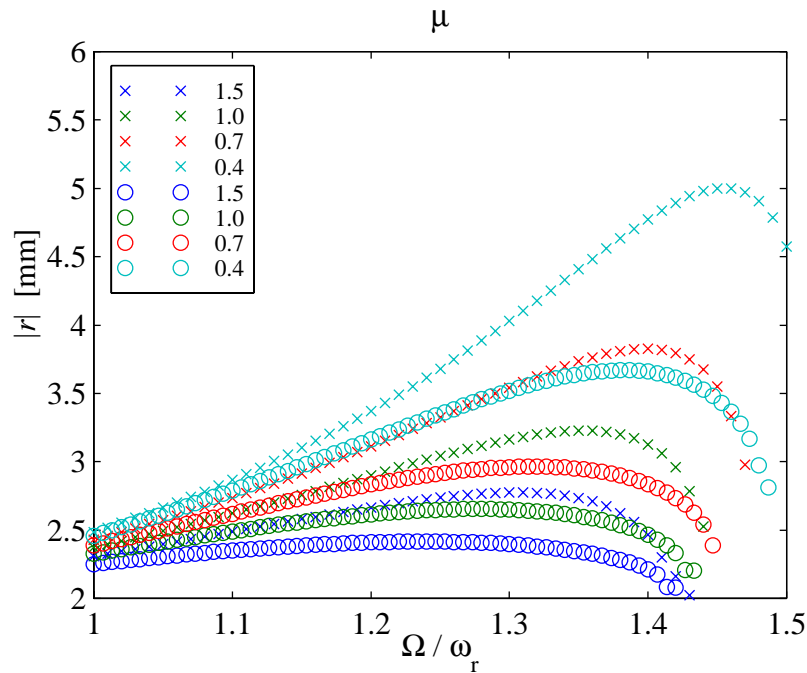of friction coefficient cause lower levels of vibration can also be observed.

Figure 4.18: rotor amplitudes when neglecting friction on stator (o) and including friction on stator (x), other parameters as in Table 4.1

With a softer stator however, the amount of friction does influence considerably the range over which rotor and stator stay in contact, as shown in Figure 4.19. The most obvious feature of this Figure is probably that there are multiple solutions for $\mu = 1.0, 1.5$ in the range of $\Omega = [1.4, 1.6]$. How these are found is covered in section 4.7.4. What is of greater concern here is that just after $\Omega = 1.4$ the two solution branches for $\mu = 1.0, 1.5$ change radically and rotor and stator lose contact. This is not true for the solution branches with the lower friction values, $\mu = 0, 0.1, 0.5$. On these branches rotor and stator stay in contact even for increasing speeds. So one can say that the *larger* the amount of friction for this configuration, $\omega_s < \omega_r$, the *smaller* the range in which rotor and stator stay in contact, whereas for $\omega_r < \omega_s$ the range of contact *increases*.
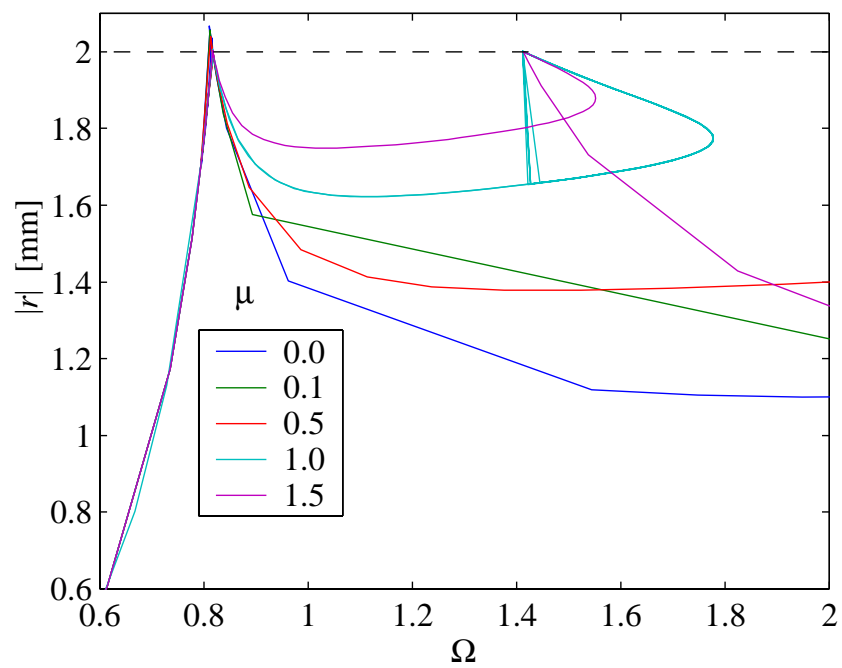
Figure 4.19: rotor amplitudes with friction on soft stator, $\gamma_\mathrm{m} = 2$, $\gamma_\mathrm{k} = 0.5$, other parameters as in Table 4.1

4.4.2 Backward whirl

As already mentioned in section 2.7.2, it is possible for a rotor/stator system (even with damping), to settle into a backward whirl without the presence of an out-of-balance force. After an initial event, which brings rotor and stator into contact, the energy provided by the rotation of the shaft is transmitted into the rotor/stator system via the friction force at the contact point. It can be shown that this motion is a stable limit cycle (with possibly large amplitudes) (Crandall & Lingener, 1990), and thus not necessarily destructive. Figure 4.20(a) shows the relationship between coefficient of friction and whirl frequency, and Figure 4.20(b) the respective whirl amplitudes at these frequencies. Not surprisingly, higher amplitudes are caused by higher coefficients of friction. The reverse whirl equilibrium seems only possible within the interval $[\omega_{\mathrm{r}}, \omega_{\mathrm{rs}}]$ (in this example $\omega_{\mathrm{rs}}/\omega_{\mathrm{r}} = 1.36$). Exactly under which initial and contact conditions backward whirl is initiated is the subject of many studies, and a research topic in its own right. However, it is found in the course of these simulations, and also during the measurement runs in Chapter 6, that in the presence of large out-of-balance forces the systems that are studied (numerically and experimentally) do not show any backward whirl behaviour, and it is therefore not dealt with here in more detail.
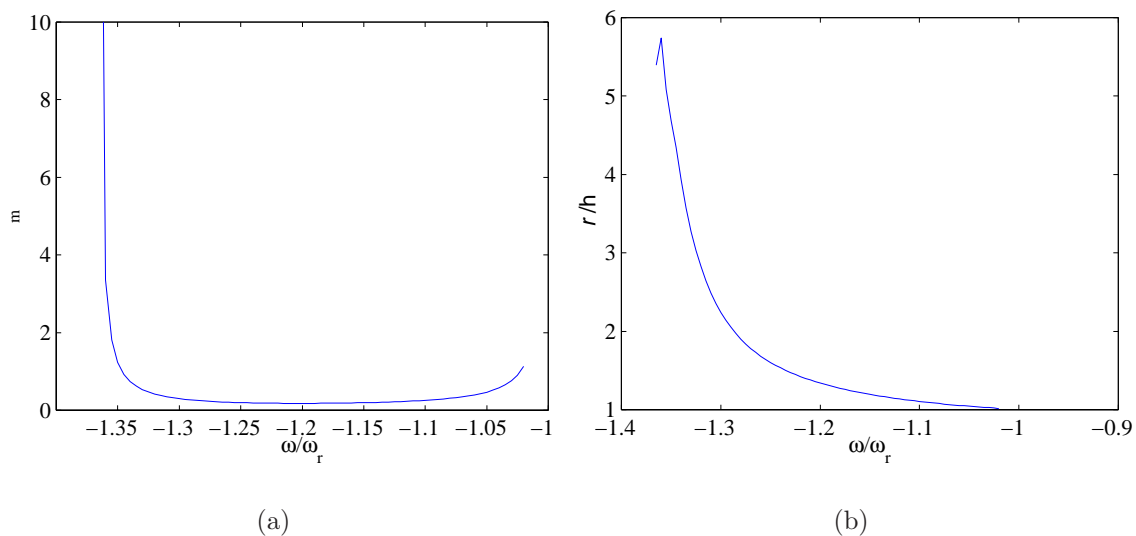

(a)

(b)

Figure 4.20: backward whirl friction and amplitudes

4.5 Case D – non-isotropic geometry or stiffness

4.5.1   Geometric eccentricity

Specifying an eccentricity of the stator ring ($\epsilon_s \neq 0$) causes the rotor/stator contact to become intermittent in some speed intervals and gives rise to sub- and super-harmonic vibration components. A non-isotropic stiffness in either rotor or stator (or both) has a similar effect. Figure 4.21 shows the displacement envelopes and spectral content of the vibrational behaviour during a slow run-up and run-down. The vibration envelopes show the amplitude of the rotor displacement, the horizontal line at $|r| = 2$ indicates the gap between rotor and stator, and as a comparison the response of a Jeffcott rotor without stator is also given (in red). The Z-mod plots (see section 5.4 for defini-tion) show a dominant first engine-order component but also higher and sub-harmonic components. The sign of the frequency component indicates forward whirl (+) and backward whirl (-) directions. The DC component during rotor-stator contact results from the stator eccentricity, which is also responsible for the build up of sub-harmonic vibration components in the speed range $2 < \Omega/\omega_r < 3$.
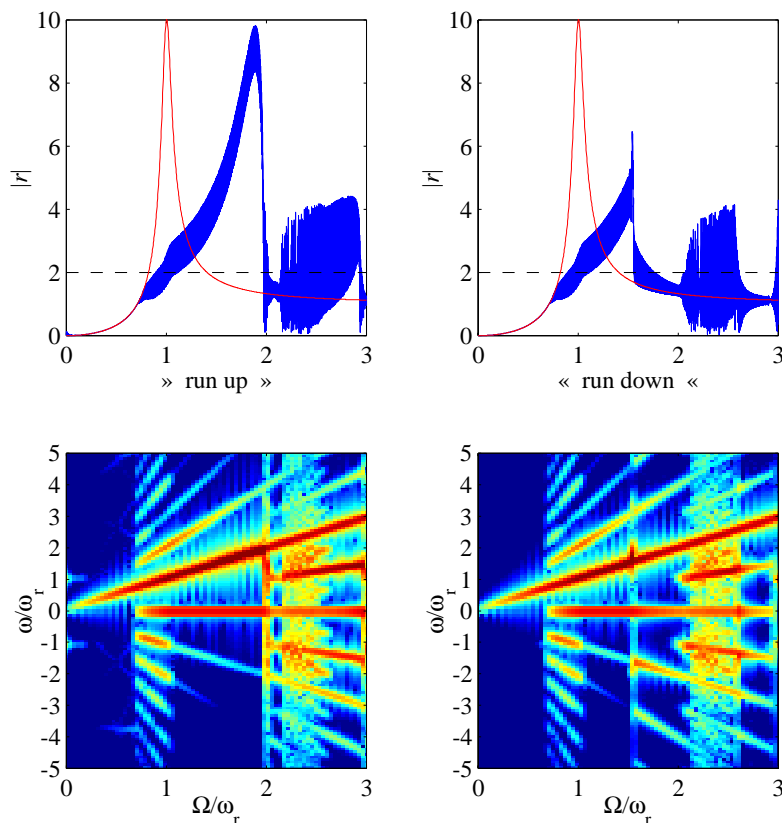

Figure 4.21: sub- and super-harmonics, $\epsilon_s = 1\,e^{i\Omega t}$, $\gamma_m = 0$, other parameters as in Table 4.1

4.5.2　Wing degree-of-freedom

Adding to the non-isotropy, a further degree-of-freedom is added to the model in this section to simulate a wing, which for now only vibrates in vertical motion. The parameters other than in Table 4.1 are:

$$\gamma_\mathrm{m} = 2 \qquad \gamma_\mathrm{k} = 0.5 \qquad \frac{m_\mathrm{wing}}{m_\mathrm{r}} = 2 \qquad \frac{k_\mathrm{wing}}{k_\mathrm{r}} = 1.6 \qquad \epsilon_\mathrm{r} = 0 \qquad \epsilon_\mathrm{s} = \mathrm{e}^{\mathrm{i}\frac{\pi}{2}}$$

In principle, no new behaviour is encountered (orbits in Figure 4.22 and response spectra in Figure 4.23), although the presence of the wing of course changes the vibration of rotor and stator. The response of the same system without the wing degree-of-freedom is shown in Figures 4.24 and 4.25. A major difference is that rotor and stator stay in contact over a wider range of shaft speeds compared with the system without a wing DOF. The vibration spectrum is full of frequency components, higher as well as lower than the shaft speed. The two cases of 21Hz and 22Hz are exceptions, where the orbit consists only of integer multiples of engine-order speed. This behaviour is also found in the measurements and is discussed in more detail in Chapter 6.

A note about the following orbit and spectra plots: Generally, the units for all the orbit plots throughout are in [mm], and all the frequency spectra are plotted in [dB] on a frequency axis in [Hz]. The grid spacing of the dotted lines in the frequency spectra is usually based on integer multiples of the engine-order, unless stated otherwise. Positive frequencies are forward, negative ones are backward whirl components. Rotor data are plotted in blue, stator data in green. The recorded time-histories each have lengths of many thousand shaft revolutions to allow for a high frequency resolution. The time-histories each contain an exact integer number of revolutions, thus minimising leakage and avoiding the need to use windows in the signal processing. A strobe[*] is superimposed on the orbit plots, so as to highlight every rotor and stator position (plotted as lighter dots) occurring when excitation (unbalance) phase passes through zero.

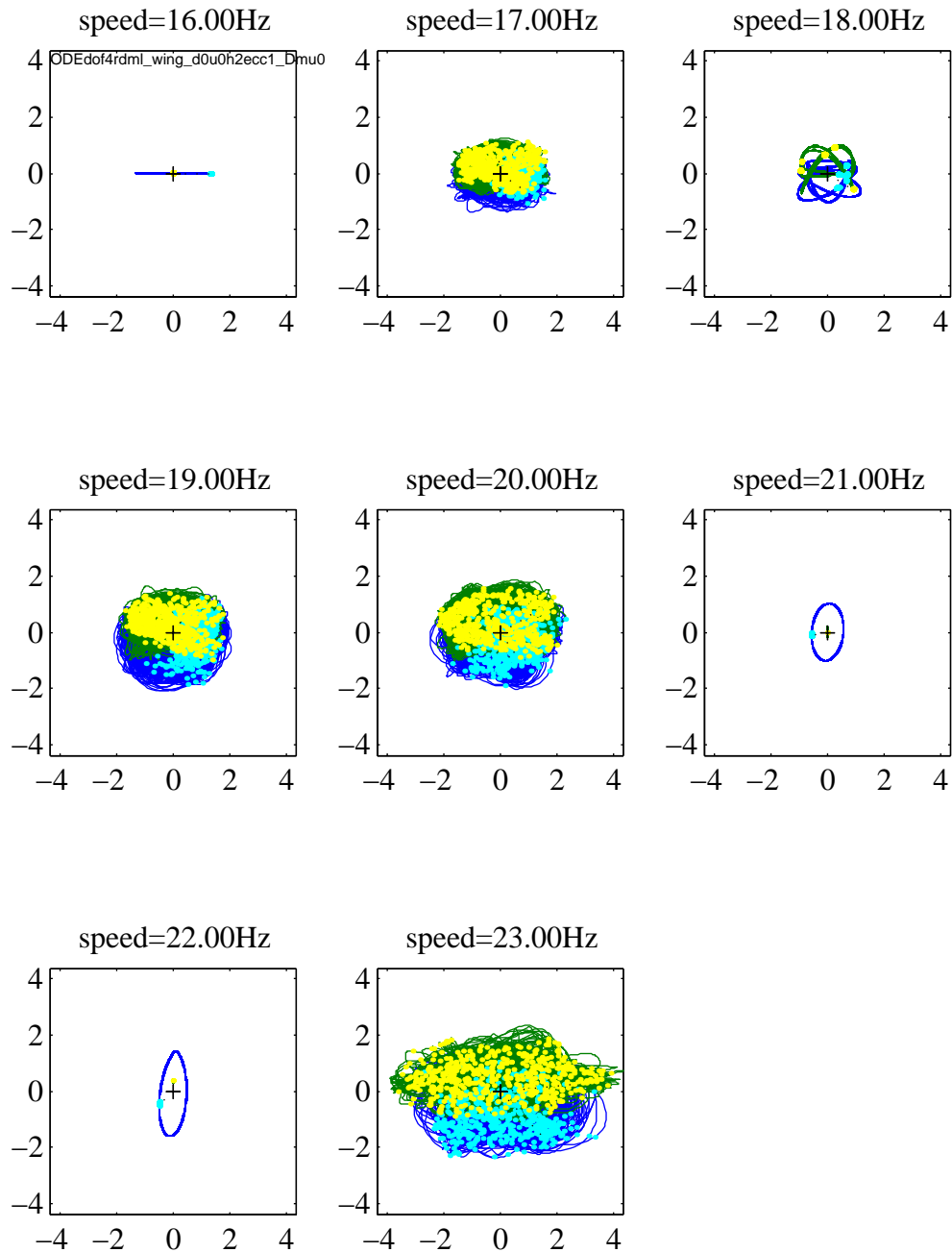[*]stroboscope: capturing displacement at known time intervals, usually at shaft speed

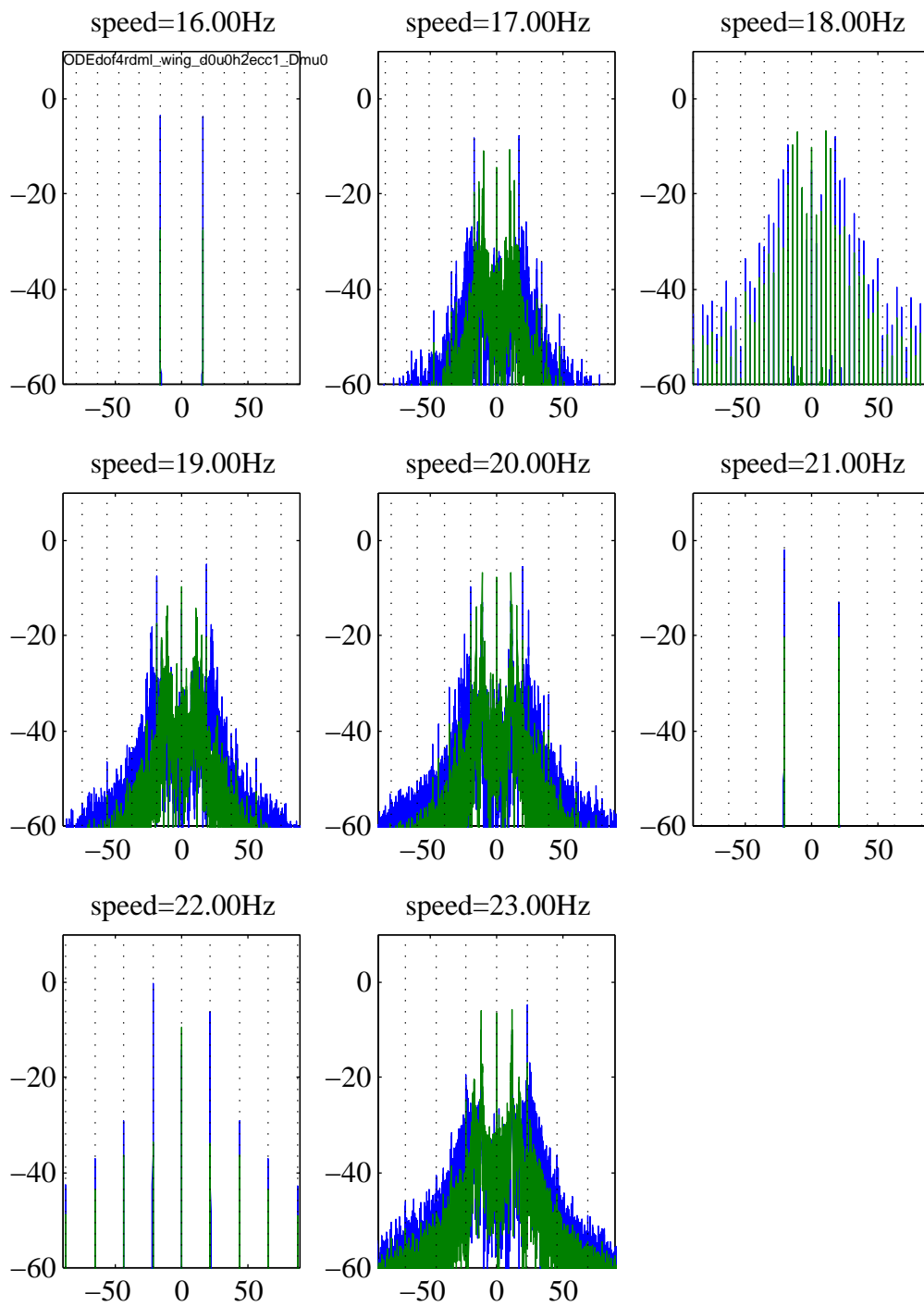Figure 4.22: orbits [mm] with wing degree-of-freedom

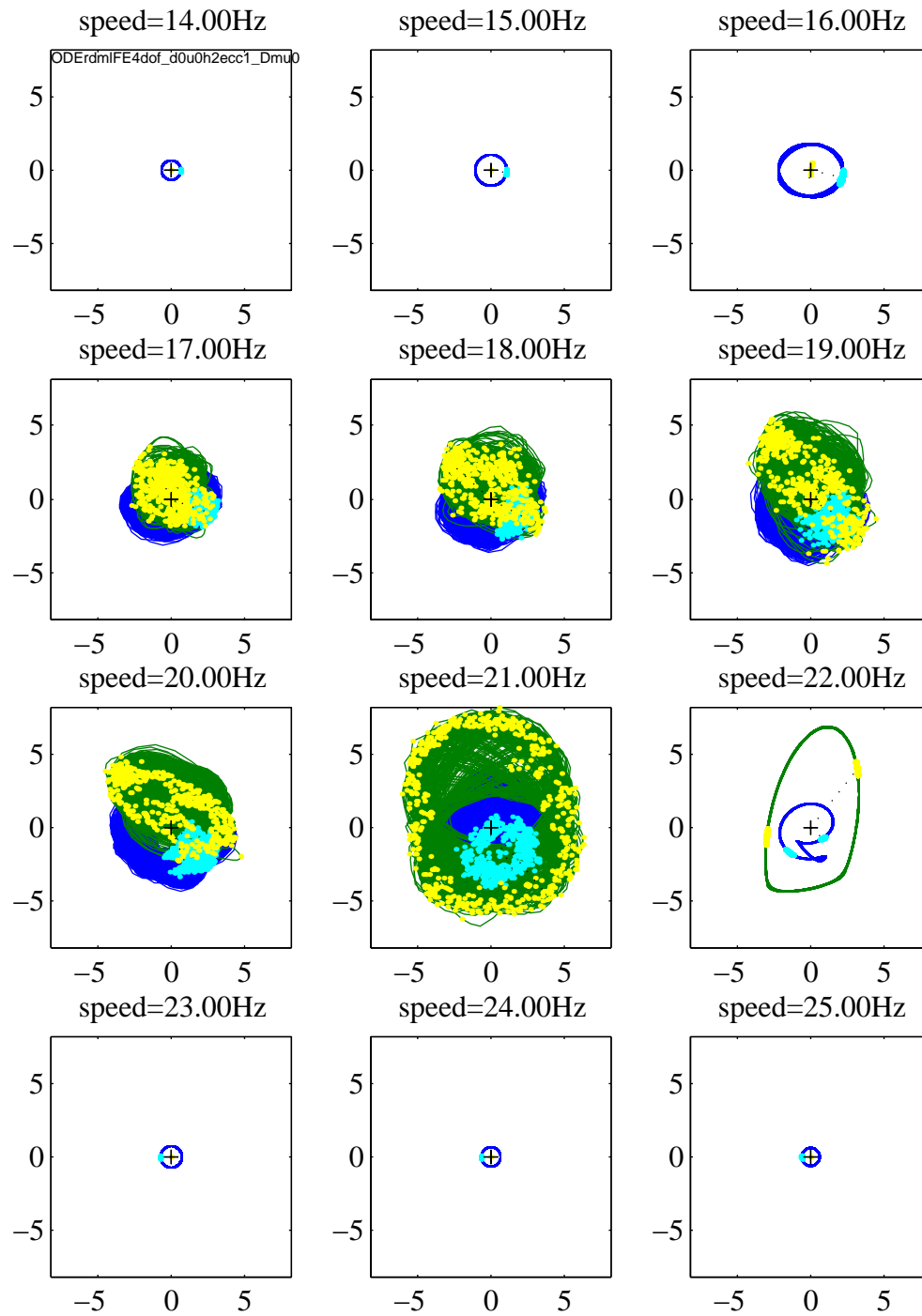Figure 4.23: response spectra [Hz] with wing degree-of-freedom

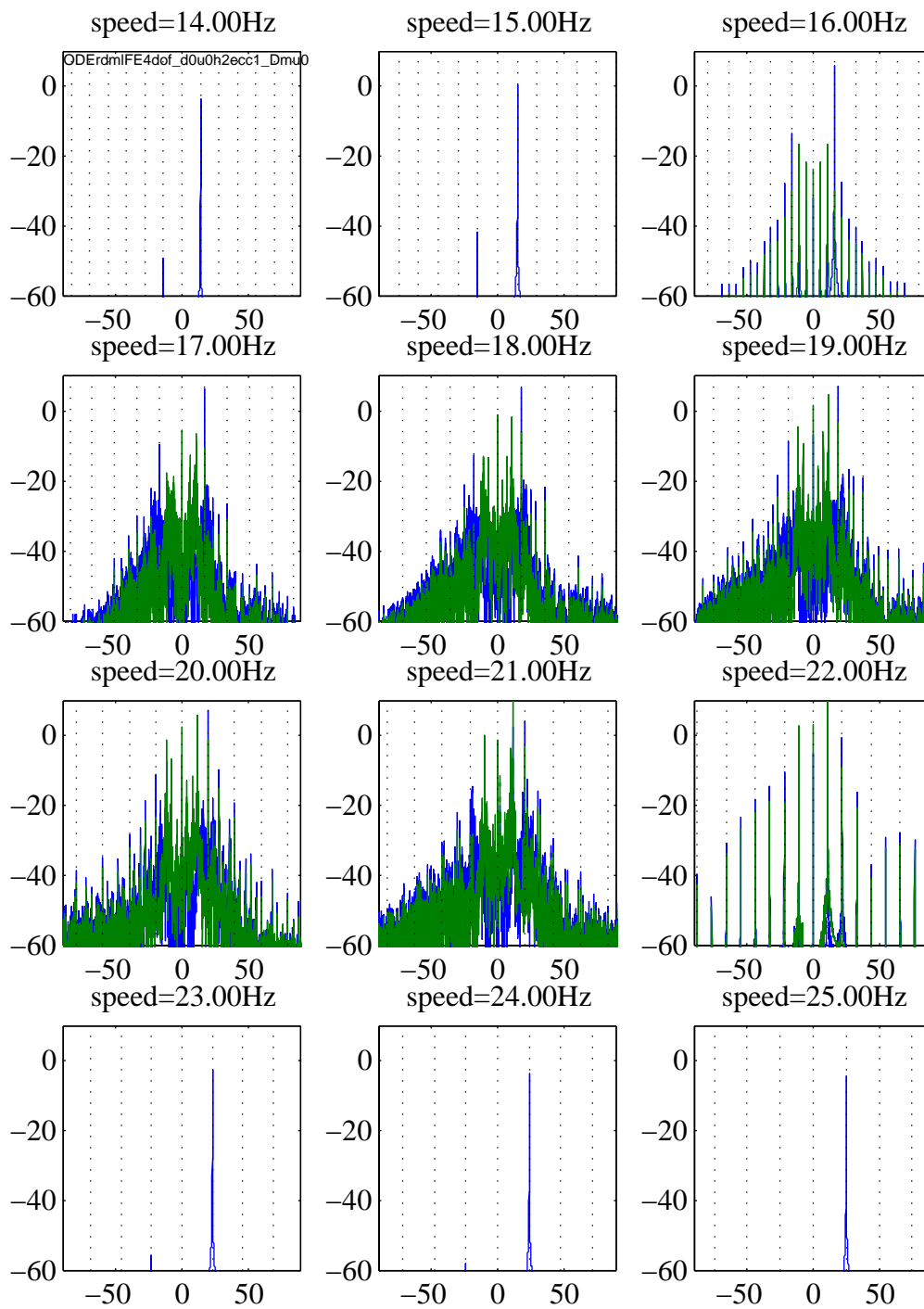Figure 4.24: orbits [mm] of 4DOF model without wing degree-of-freedom

Figure 4.25: response spectra [Hz] of 4DOF model without wing degree-of-freedom

4.6   Case E - fully flexible rotor and stator

Contact of flexible rings   In order to test the developed code for its suitability for general N-degree-of-freedom systems, an inter-shaft contact is simulated. Both rotor and stator shafts are modelled as flexible tubes, and the corresponding FE model imported into the program suite. In emulating the physical behaviour of the material, the rotor mesh is actually rotated around the spin axis at every time step in accordance with the speed of shaft rotation. In this way no symmetry is required and the modeling of discs with blades (even with irregular lengths) can easily be realised. In this particular example, the tubes were chosen not to be concentric, and as observed in case D (where rotor and stator were rigid bodies), higher harmonic components are emerging as soon as rotor and stator establish contact (Figure 4.26). As the speed does not start at $\Omega/\omega_{\mathrm{r}} = 0$, engine-orders EO1 to EO5 are plotted in the spectrum as white dashed lines.
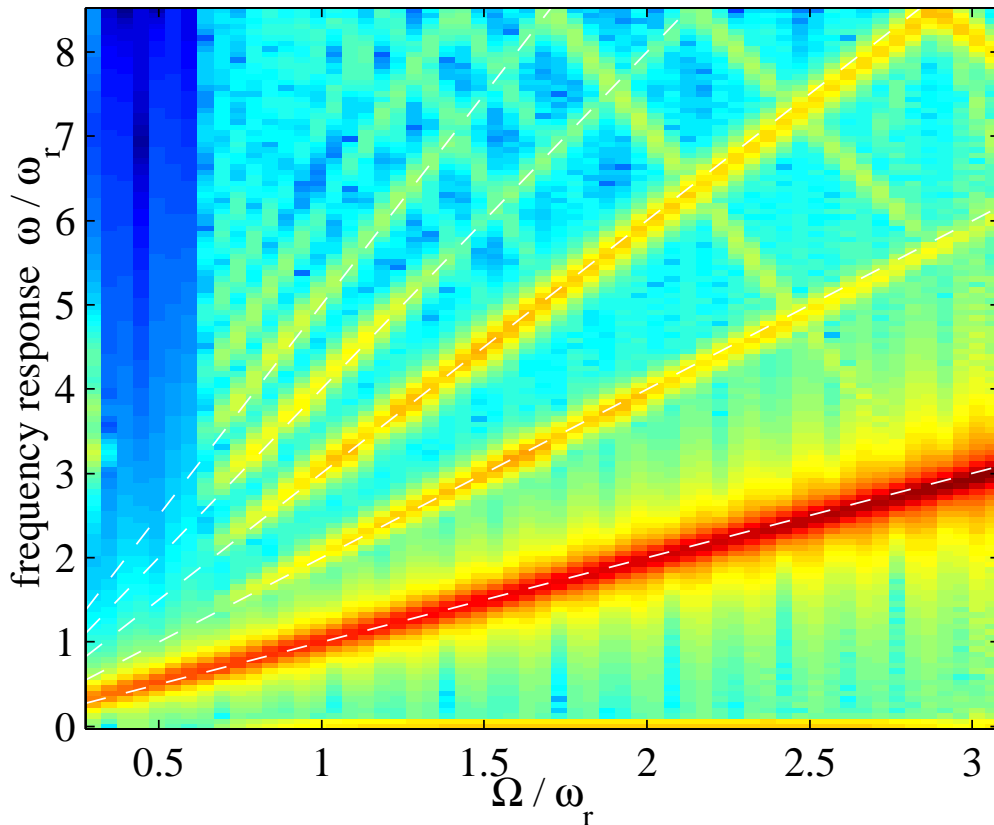

Figure 4.26: super-harmonics at one contacting node during flexible body contact

4.7　Notes on Numerical Difficulties

4.7.1　Time-Integration

In this section case B from chapter 4 is run again with a sweep in the time domain (Figure 4.27) and the results compared with the series of steady-state conditions at different speeds previously obtained with the HBM (Figure 4.7). Not surprisingly, the results match in general. Interestingly, though, the time-integration algorithm does not seem to cope very well in cases of light rotor/stator contact, as can be observed (Figure 4.27) for $\gamma_{\mathrm{m}} = 1.0$ in the interval of $\Omega/\omega_{\mathrm{r}} = [1.4, 2.5]$. It can be seen in Figure 4.28 that in this interval the penetration depth, δ, in the contact zone is oscillating wildly, and sometimes even reaches zero, implying that rotor and stator cease to be in contact for short periods of time followed by transient vibration due to renewed impact. The harmonic balance method does not show any of this behaviour (Figure 4.7) for that solution, rotor and stator stay in contact (full annular rub), and the oscillation consists purely of the 1EO (unbalance) component. The bouncing behaviour predicted by the time-marching analysis during the sweep (Figure 4.27) is attributed to the failure of the adaptive step size control in the numerical integration routine. The sub-plots in the Figures 4.27, 4.28, and 4.29 each contain a response envelope of a run-up and a run-down.

The step length control is of course also influenced by the error settings. The error specified during the simulations is: maximum error $< 10^{-6}$ and the relative error $< 10^{-4}$. By comparison, Figure 4.29 shows the same simulation as in Figure 4.7, but run with lower error requirements: $< 10^{-4}$ for the absolute error and $< 10^{-2}$ for the relative error. It can be observed that the run-up with heavier stator mass ($\gamma_{\mathrm{m}} = 2, 3$) oscillates strongly as compared with the smooth curve obtained with tighter error tolerances. This shows that although a result with a precision higher than two orders of magnitude (error $< 10^{-2}$ for a deflection magnitude $> 10^{0}$) would seem satisfactory, it is not sufficiently high for the algorithm to deal with these numerical difficulties.
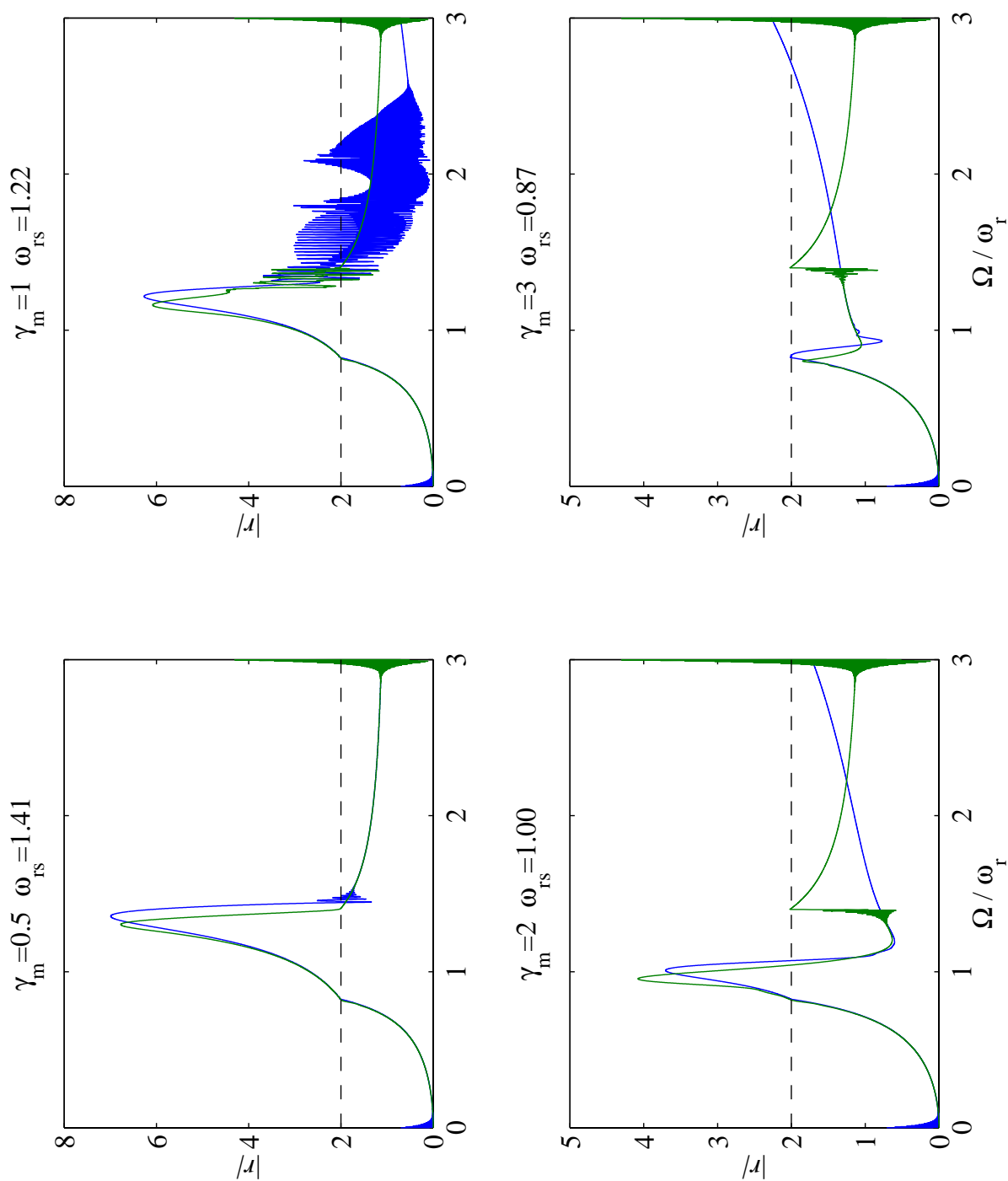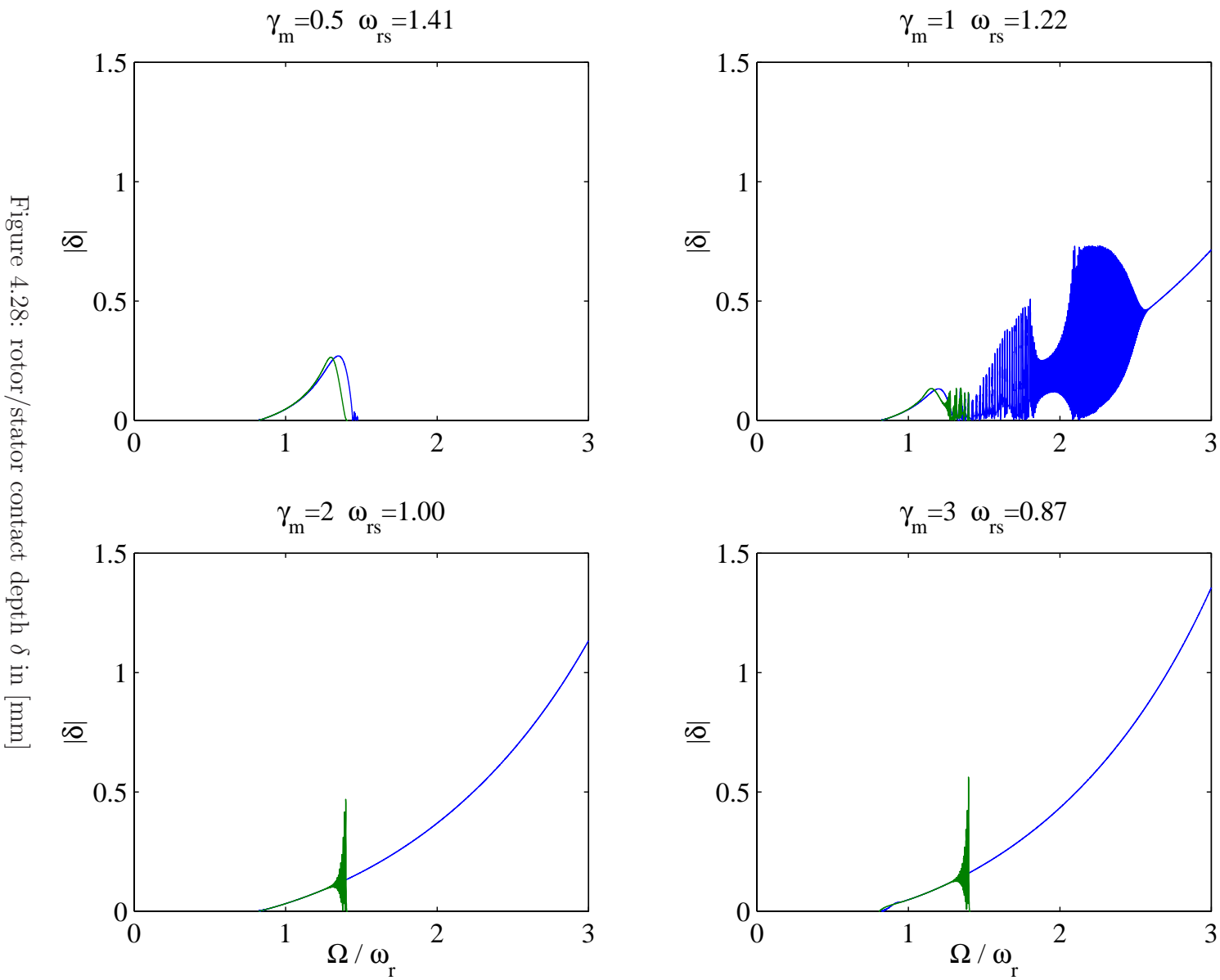
Figure 4.27: rotor amplitude in [mm] during slow shaft acceleration (blue) and deceleration (green) with various stator masses, other parameters as in Table 4.1
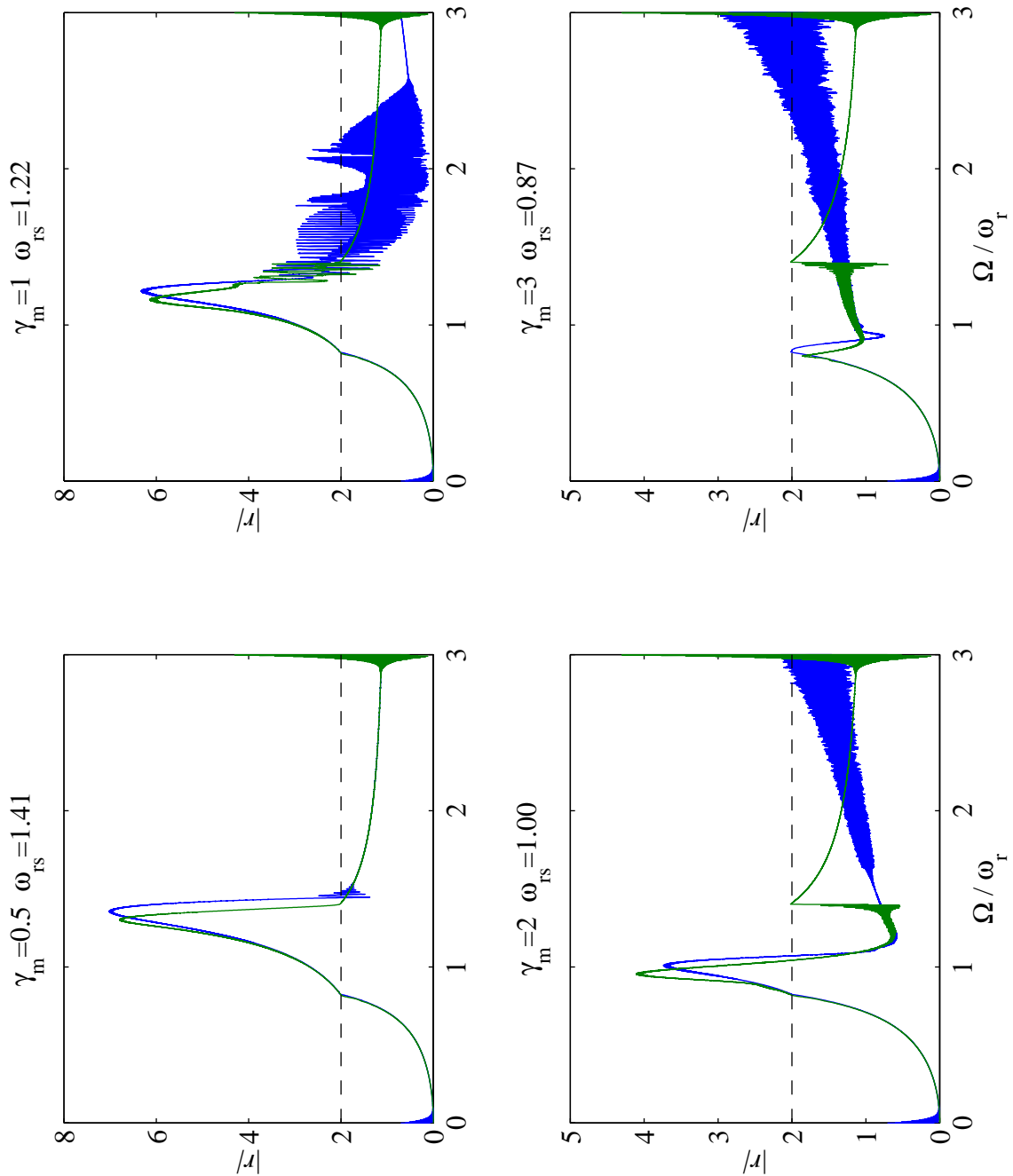
Figure 4.28: rotor/stator contact depth δ in [mm]

Figure 4.29: rotor amplitude in [mm] during slow accel. and decel. runs with relaxed error requirements for time integration

4.7.2   Contact Model

With the presence of friction a further problem is added to time-marching solutions: numerical instability. Figure 4.30 shows the contact history of a rotor/stator system calculated with a time-marching solver at a constant shaft speed. For contact $> 0\,\text{mm}$, the rotor is penetrating into the stator wall, and for contact $< 0\,\text{mm}$ rotor and stator are moving separately, meaning smallest distance between rotor and stator. In Figure 4.30(a) the rotor/stator contact condition occurs frequently, and the system remains in this state of intermittent contact over the whole time span (which was 10 times longer than shown in the figure). One sees clearly that in Figure 4.30(b) the contact depth between rotor and stator quite suddenly rises sharply towards infinity. A plot zooming into this area is shown in Figure 4.31(a). The very stiff, but undamped, contact poses a problem for the time-marching process. Vibration energy slowly shifts (only numerically) into the mode where rotor and stator oscillate out-of-phase, and all the energy is concentrated in the undamped contact zone. The smallest amount of friction then still leads to large friction forces, as the normal tangential force is growing large. These large friction forces then send the rotor into a self-excited unstable backward whirl.
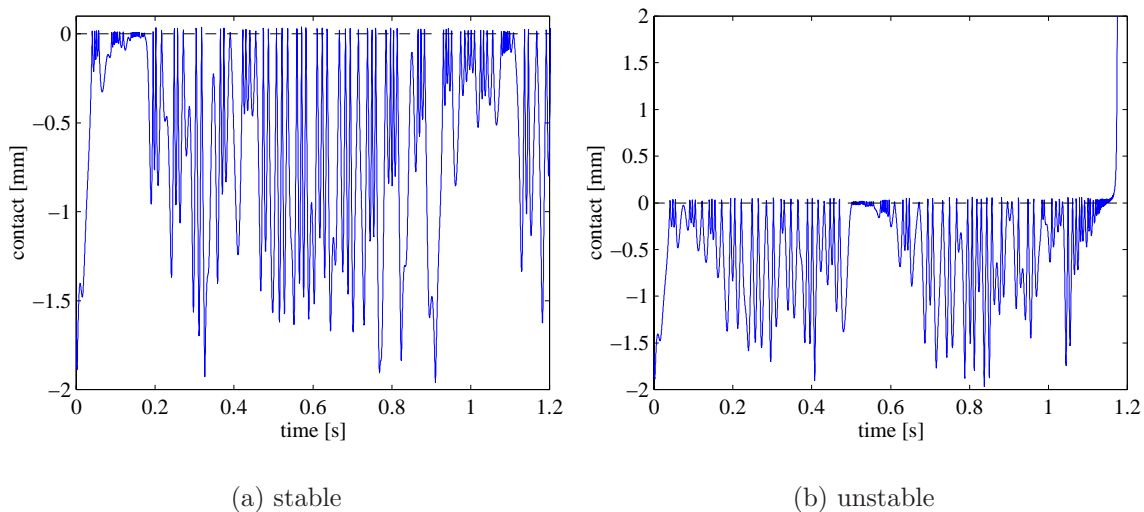

(a) stable   (b) unstable

Figure 4.30: rotor/stator interaction for friction > 0

Both runs that are shown in Figure 4.31 start with the same initial conditions and the same parameters except for the contact force model. The contact in the unstable solution was modelled with the nonlinear contact model presented in chapter 2, but the damping was set to zero. The stable solution uses the same contact model but with a damping value of $c_\text{c} = 0.01$, and one can interpret the results as follows: The damping provided in the contact zone dissipates some of the impact energy. The area enclosed by the upper and lower branch of the fore–displacement curve in Figure

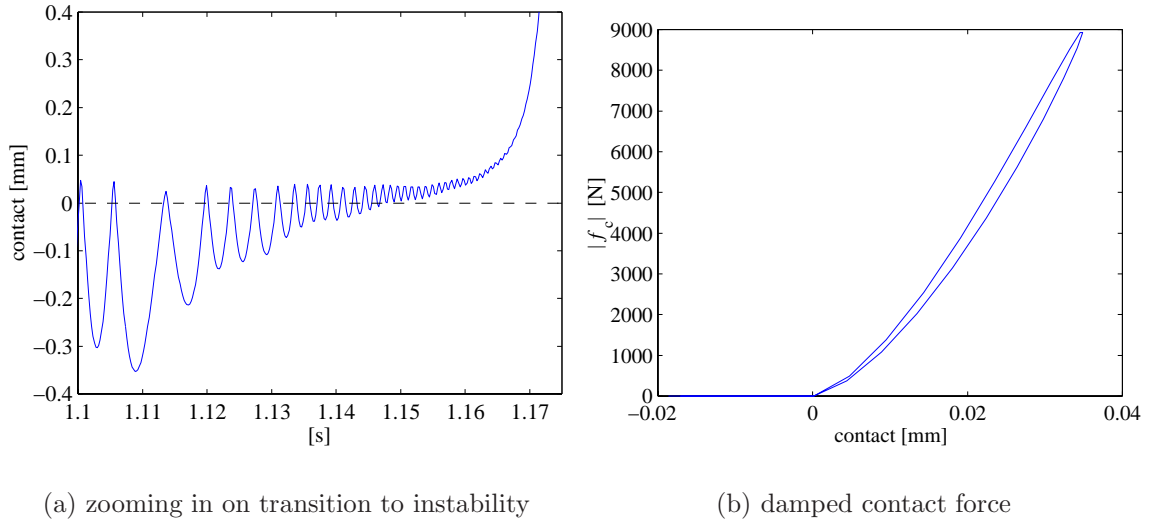(a) zooming in on transition to instability

(b) damped contact force

Figure 4.31: instability and its remedy

4.31(b) is equal to amount of energy dissipated. As the upper and lower branches are close in this example, the amount of energy dissipated is small. However, it is sufficient to prevent the energy shifting into the contact penetration and thus to stabilise the time-marching solution. In further investigating this instability, the contact force of equation (2.3) is broken down into stiffness and damping components (in normal and tangential direction):

$$f_{\mathrm{n}} = f_{\mathrm{k}} + f_{\mathrm{c_n}} + f_{\mathrm{c_t}} \tag{4.1}$$

$$f_{\mathrm{k}} = k_{\mathrm{c}} |\delta|^{\frac{3}{2}} \, \mathrm{e}^{\mathrm{i}\psi} \tag{4.2}$$

$$f_{\mathrm{c_n}} = k_{\mathrm{c}} |\delta|^{\frac{3}{2}} \frac{3}{2} c_{\mathrm{n}} \dot{\delta}_{\mathrm{n}} \tag{4.3}$$

$$f_{\mathrm{c_t}} = k_{\mathrm{c}} |\delta|^{\frac{3}{2}} \frac{3}{2} c_{\mathrm{t}} \dot{\delta}_{\mathrm{t}} \tag{4.4}$$

where $\dot{\delta}_{\mathrm{n}}$ and $\dot{\delta}_{\mathrm{t}}$ are the normal and tangential components of $\dot{\delta}$, respectively:

$$\dot{\delta}_{\mathrm{n}} = |\dot{\delta}| \cos(\angle\dot{\delta} - \psi) \, \mathrm{e}^{\mathrm{i}\psi} \tag{4.5}$$

$$\dot{\delta}_{\mathrm{t}} = |\dot{\delta}| \sin(\angle\dot{\delta} - \psi) \, \mathrm{e}^{\mathrm{i}(\psi + \frac{\pi}{2})} \tag{4.6}$$

In practice, though, one would also like to ensure that when the contact is in a decreasing phase, the damping force, $f_{\mathrm{c_n}}$, which in this case has the opposite direction from the normal contact force, f_{k}, is not larger than the normal contact force, thus causing an unnatural attracting force between rotor and stator. It is unlikely that in such a situation the normal relative velocity in the contact zone $\dot{\delta}_{\mathrm{n}}$ is large (compared with

the velocity on impact), but the following safeguard was built into the algorithm:

$$
f_{c_n} = k_c|\delta|^{\frac{3}{2}} \begin{cases} \min\left(\frac{3}{2}c_n|\dot{\delta}_n|; 1\right)e^{i\psi} & \text{if } \cos(\psi - \angle\dot{\delta}) < 0 \\ \frac{3}{2}c_t\dot{\delta}_n & \text{otherwise} \end{cases} \tag{4.7}
$$

One can always force a system into a backward or forward whirl time-marching solution simply by changing the amount of damping used in the contact model. For example by increasing c_n to a high enough value such that the tangential damping force, f_{c_t}, counteracts and outgrows the friction force, the system then vibrates in a forward whirl motion. The effects of different ranges of normal and tangential damping are mapped out in Figure 4.32 using the following parameters:

$$
\begin{array}{lll}
\epsilon_r = 0\,\text{mm} & \epsilon_s = 0\,\text{mm} & h = 0.3\,\text{mm} \\
\omega_r = 23.5\,\text{Hz} & \omega_s = 105\,\text{Hz} & \Omega = 9\,\text{Hz} \\
\zeta_r = 0.03 & \zeta_s = 0.03 & \\
m_r = 36\,\text{kg} & m_s = 24\,\text{kg} & \\
\mu = 0.5 & k_c = 10^{10}\,\text{N/m} & \Omega^2 m_r \epsilon_m = 700\,\text{N}
\end{array}
$$

The damping coefficient for velocities in the normal direction seems to influence the behaviour only very crudely. For values of (c_n) around 10^{-2} and larger, the system always responds in a forward whirl motion. When considering that the impact speeds of this system roughly lie around $\dot{\delta} \approx 100\,\text{mm/s}$, this threshold damping value coincides with a coefficient of restitution $\epsilon \approx 0$ (equation (2.4)). So in the (unrealistic) case of almost all impact energy being dissipated, the system always goes into forward whirl, for lesser values the behaviour depends entirely on the tangential damping coefficient. For very low levels of tangential damping, the system goes into unstable backward whirl (large coefficient of friction, $\mu = 0.5$). For increasing levels of damping in the tangential direction, the system stabilises in a backward whirl limit cycle, until the tangential damping force becomes so large that it becomes larger than the friction force and thus forces the system into forward whirl. The lower case letters in Figure 4.32 refer to the positions of the examples with orbits, frequency spectra, and force plots that are shown in the following. There is an as yet inexplicable small band of solutions around $(c_t) = 10^{-2}$ (hashed area in Figure 4.32), which grow unstable very slowly, see slowly rising contact penetration amplitudes in following cases (c) and (f).
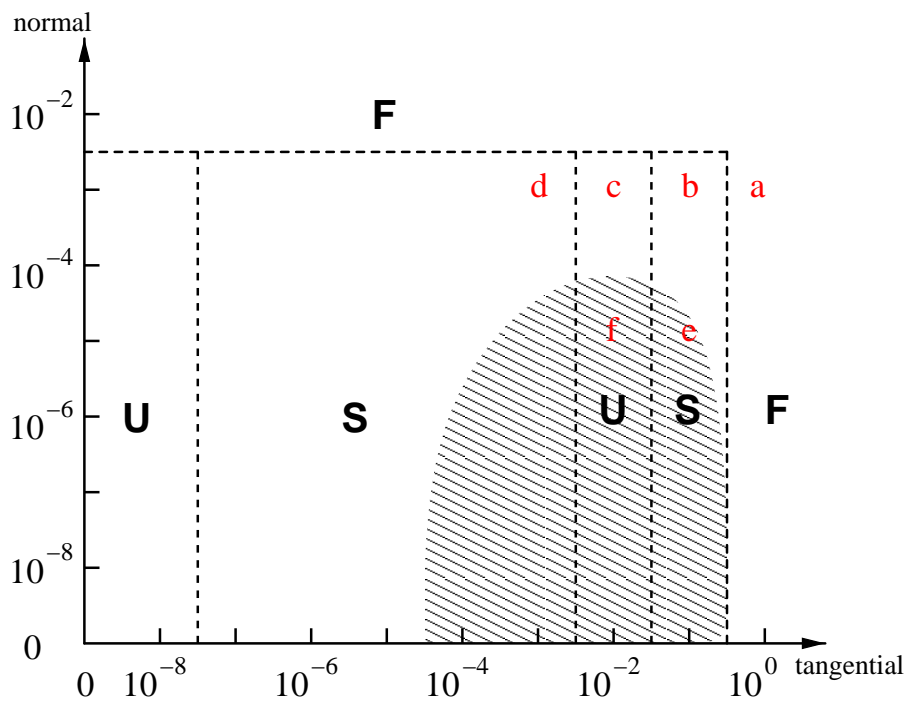
Figure 4.32: effect of tangential (c_t) and normal (c_n) contact damping values [sN/m] on whirl: U = unstable backward whirl, S = stable backward whirl, F = stable forward whirl, hashed area denotes 'creeping' instability
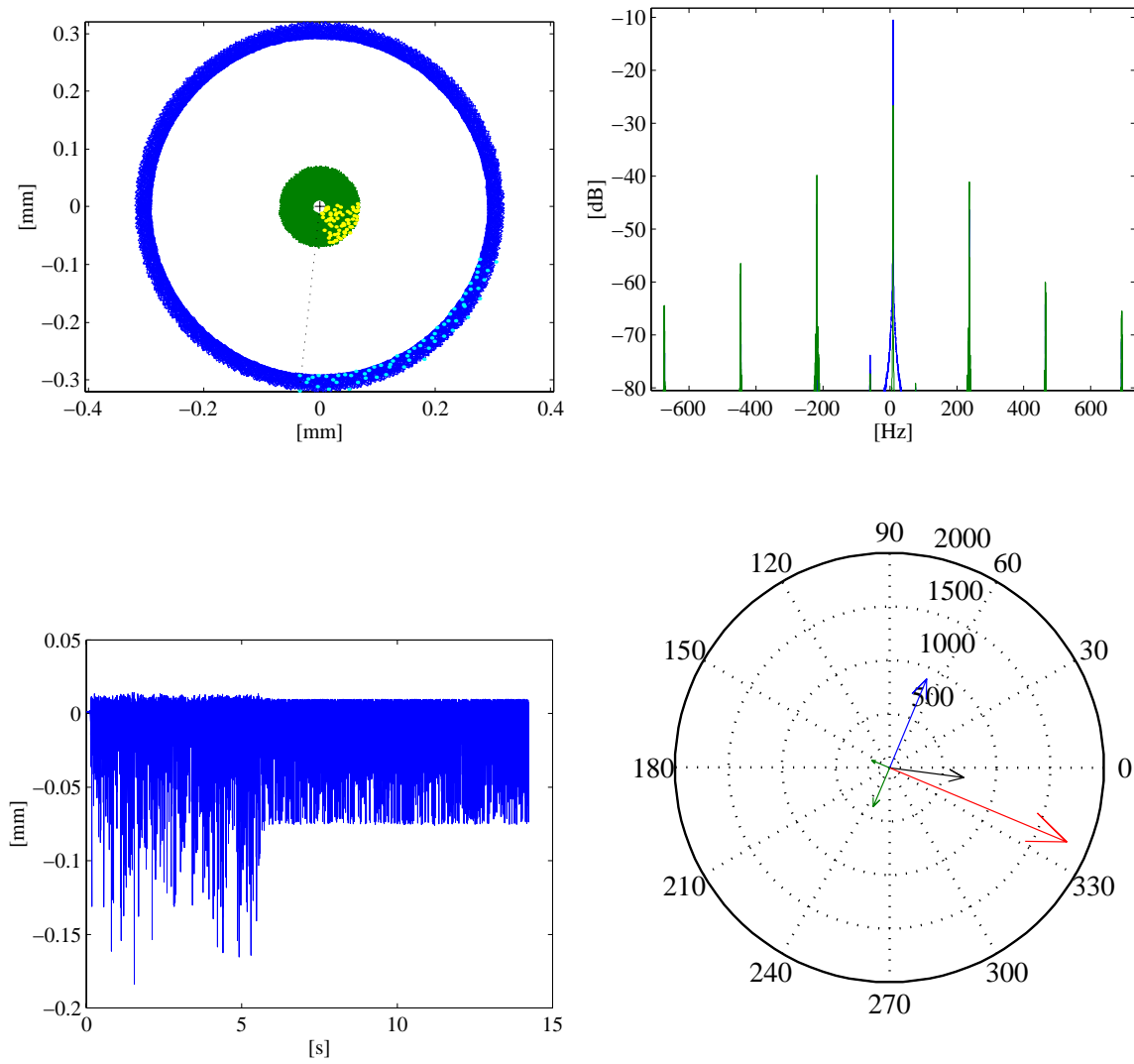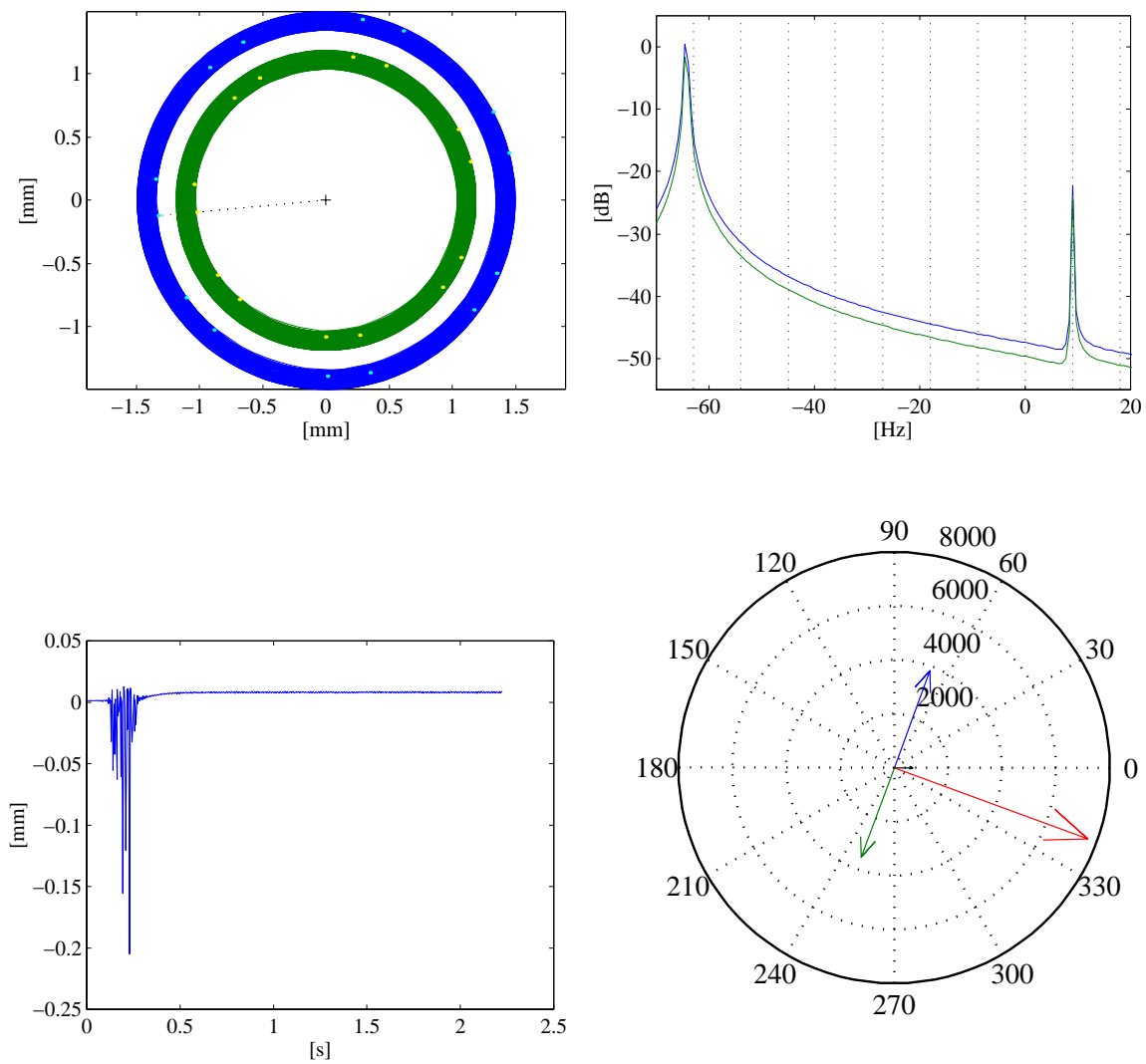
Figure 4.33: (a) forward whirl

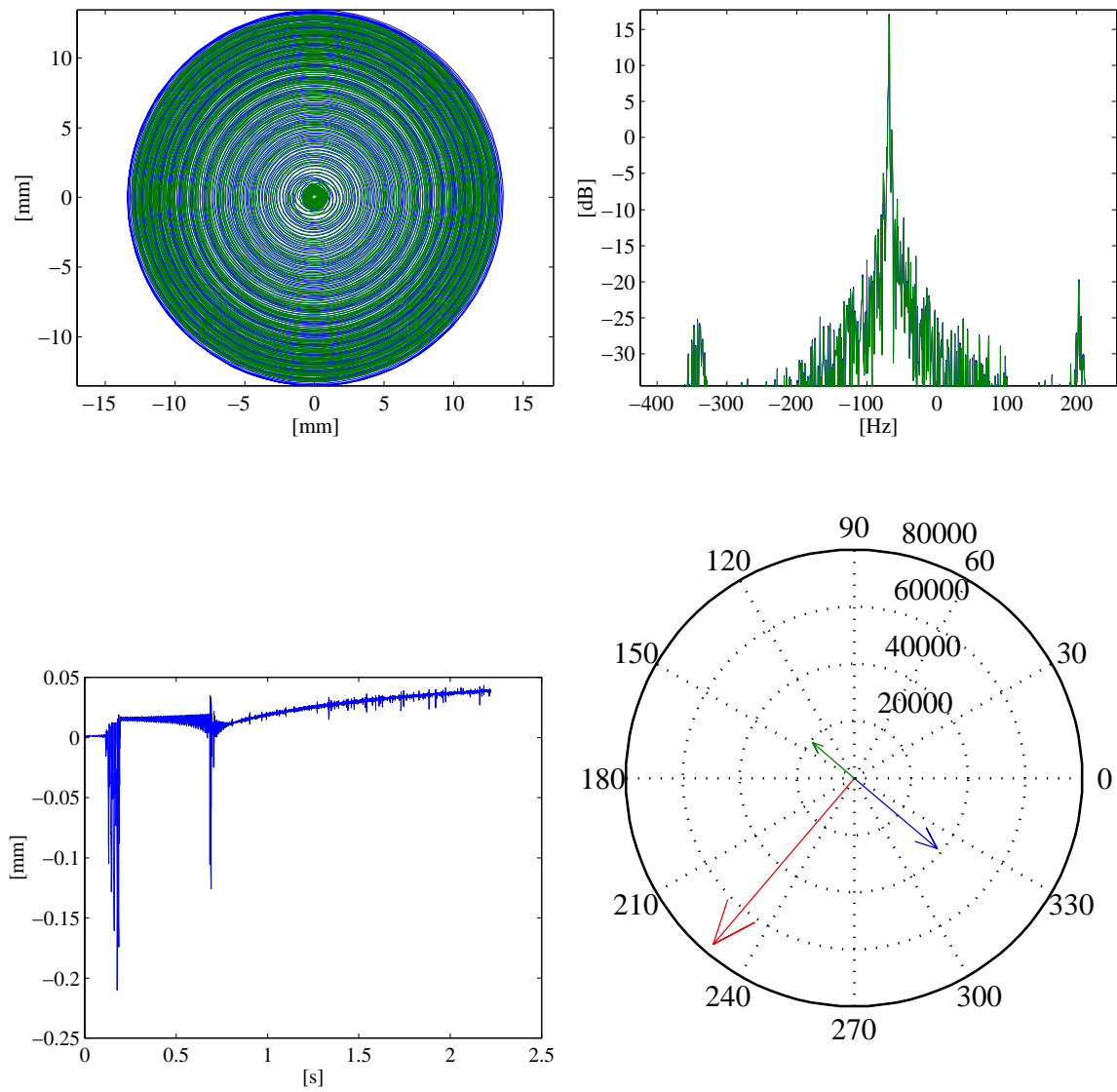Figure 4.34: (b) stable backward whirl
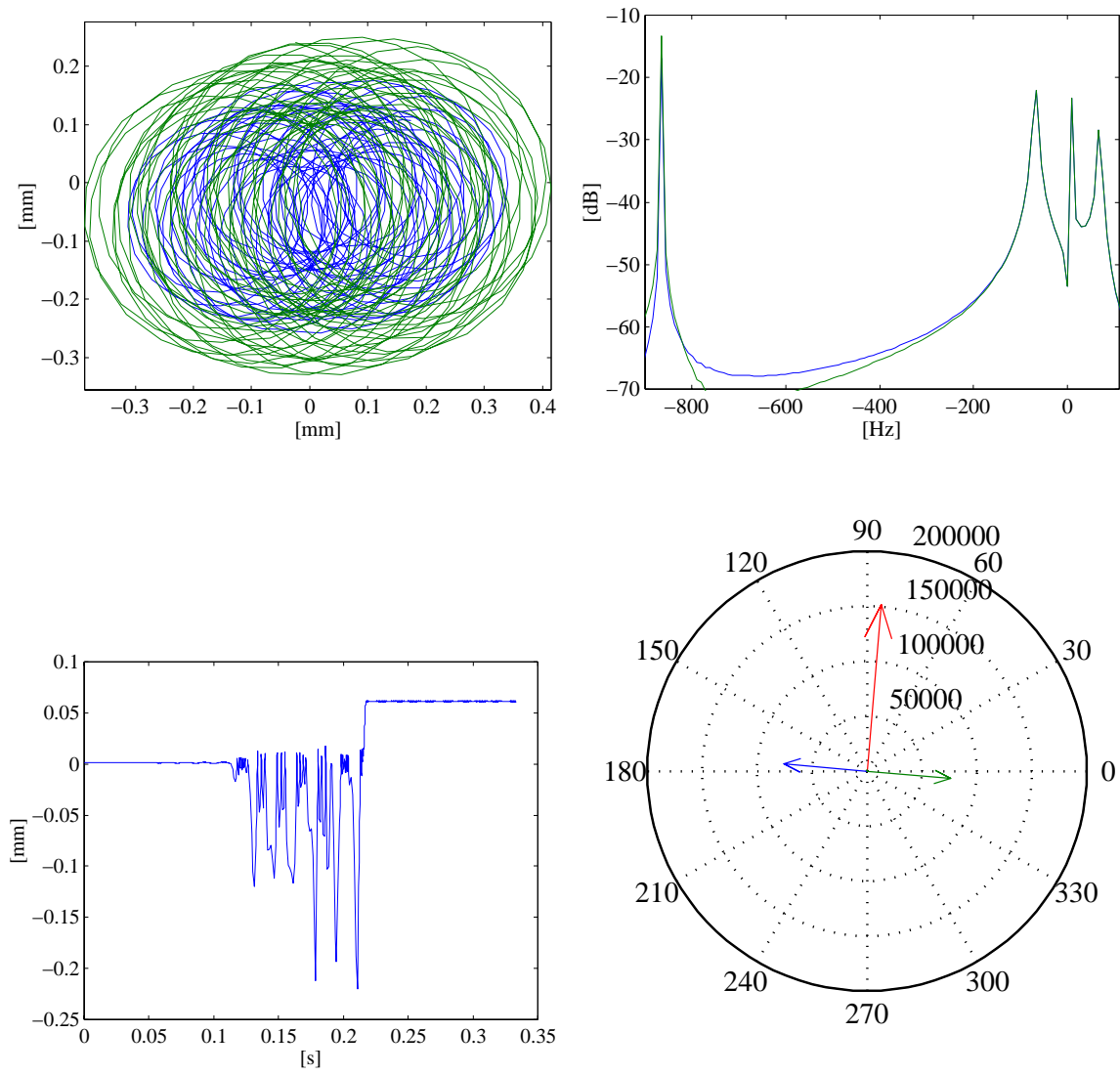
Figure 4.35: (c) forward whirl

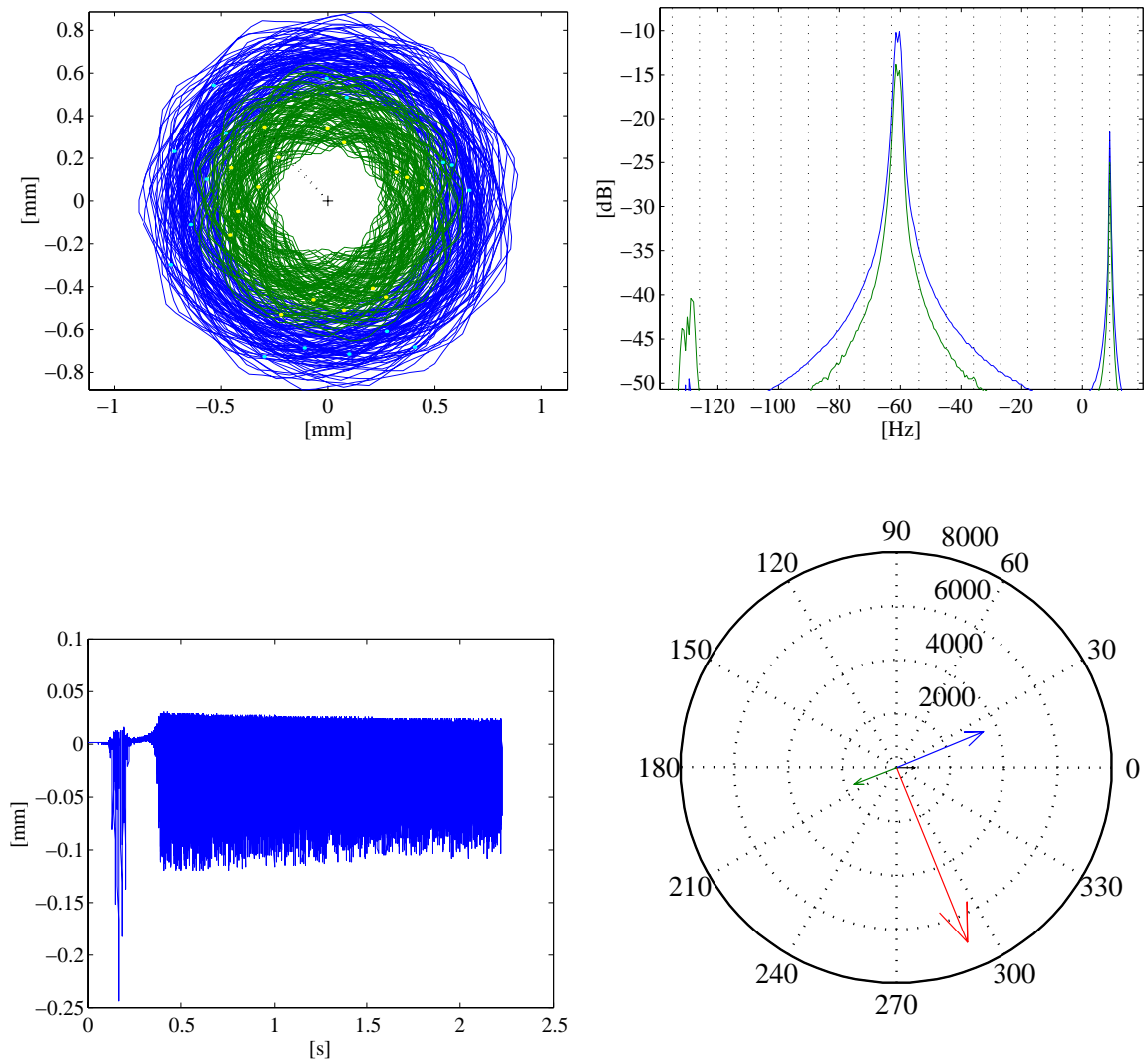Figure 4.36: (d) stable backward whirl

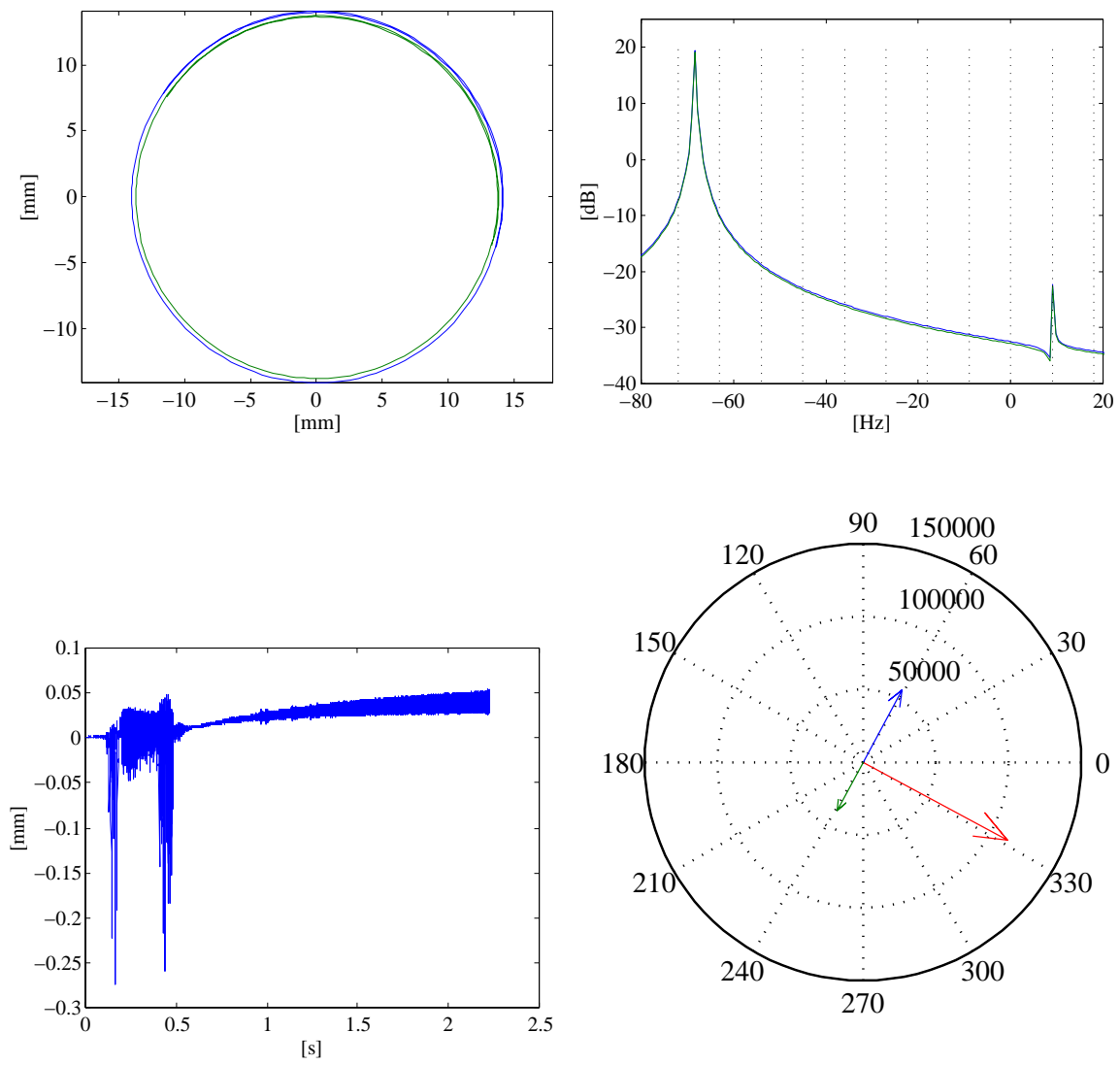Figure 4.37: (e) stable backward whirl

Figure 4.38: (f) forward whirl

4.7.3   Harmonic Balance Frequencies

Before a problem is attempted to be solved with the harmonic balance method, a clear idea is need of how many (and which) harmonics are to be included in the setup. Figure 4.39 shows the orbits of (a) rotor and (b) stator for the solutions obtained with 32 (blue), 4 (green), and 1 (red) harmonic components. Figure 4.40 shows the amplitude of each harmonic, (a) for 32 components, (b) for 4 components, separated
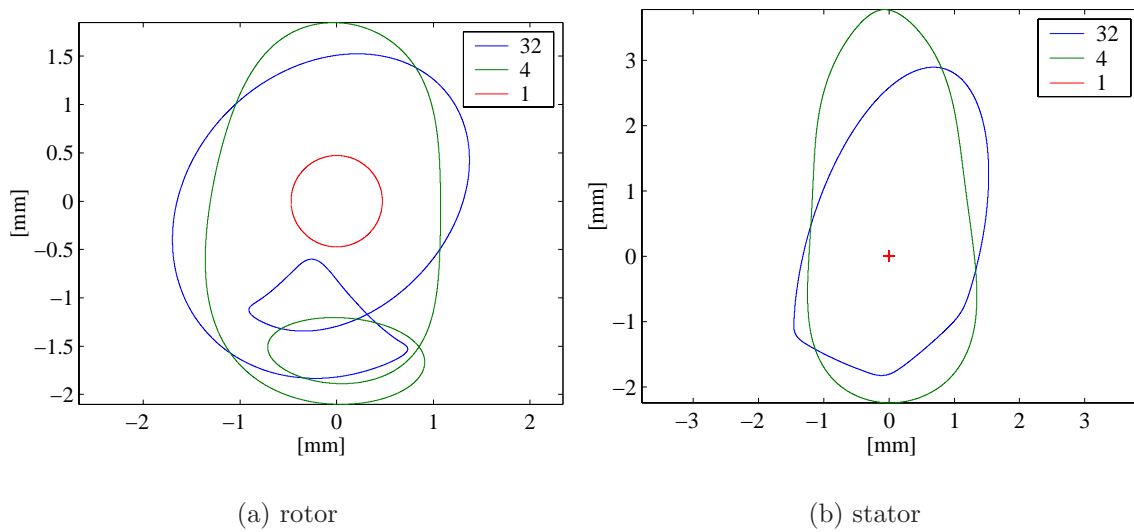

(a) rotor   (b) stator

Figure 4.39: solution with various harmonics in HBM setup

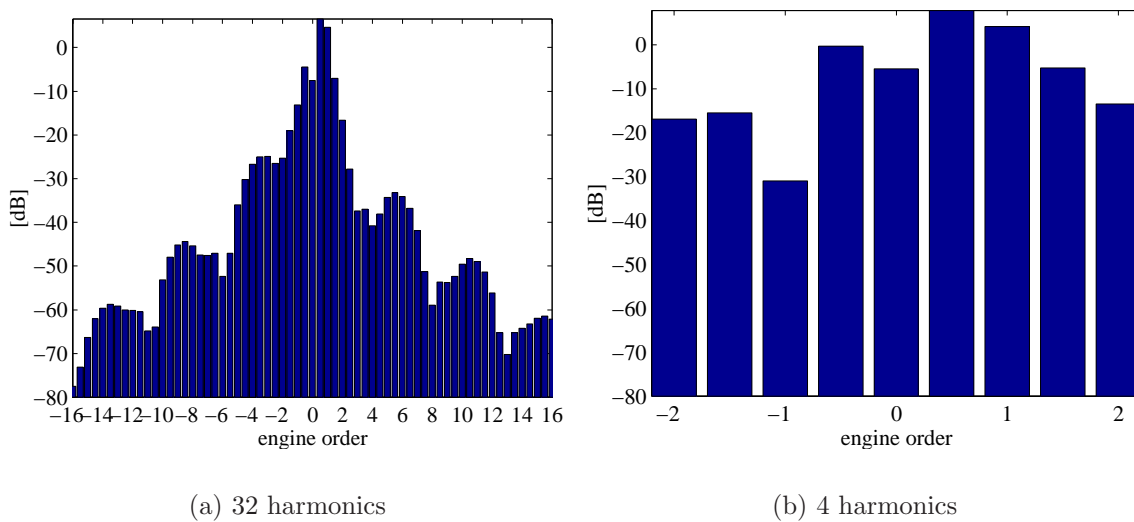(a) 32 harmonics   (b) 4 harmonics

Figure 4.40: response at various harmonics

into forward and backward directions. It is important to note that the setup for the 32 and 4 components included the 1/2 engine order components, whereas the setup for 1 harmonic consisted only of the engine order. The very high number of 32 components was chosen because the resulting orbit lies exactly over the orbit that is produced by a time-marching solution. As the orbit is periodic, the solution found over one period with the time marching process is, for the purposes of this section, exact. The solution with the 32 harmonics comes extremely close, is therefore regarded as equivalent. Once can see that the solution with 4 components produces a different orbit, but nonetheless a good (and computationally much cheaper) approximation. The main characteristic of rotor/stator contact and the sub-harmonic loop is retained. A further reduction to 1 harmonic component fails: the result is entirely different as rotor and stator are no longer in contact. It also fails if a solution is attempted that includes higher harmonics, but not the 1/2 engine order components. This does not mean that a better approximation with rotor and stator in contact does not exist (albeit without the sub-harmonic loop), but just indicates that the solver does not find it. The initial guess for the solver was computed by a least-squares fit of the harmonics used in the setup and the orbit from the time-marching solution. One can conclude that even in the presence of many higher harmonics, a setup with far fewer harmonics can produce acceptable approximations, as long as the right frequencies/sub-harmonics are kept. The difficulty remains to judge beforehand which sub-harmonics are essential in the setup.

4.7.4   Multiple solutions

In Figure 4.41 the stable and unstable periodic solutions of the rotor and stator responses $r_\mathrm{r}, r_\mathrm{s}$ are plotted versus the rotor speed of rotation Ω. One can see that at speeds $\Omega < 0.9$ the rotor unbalance response is too low to overcome the clearance ($h = 3$, dashed line) and rotor and stator are not in contact (stator response zero). At speeds $0.9 < \Omega < 1.4$ rotor and stator are in contact (non-zero stator response), although the over-hanging part of the curve represents an unstable solution. At speeds $\Omega > 1.4$, well above the natural frequency of the rotor (which has been normalised to $\omega_\mathrm{r} = 1$), the super-critically running rotor loses contact with the stator.

Figure 4.42 shows a second solution branch at $\Omega > 6$, which is not seen in the 1 DOF Duffing-type oscillator model that displays only the over-hung behaviour in Figure 4.41. It must be noted that by following the branch previously discussed — the one that lost contact with the stator and is coming into this picture from the left — there is no indication of the existence of the second branch. The branches of the rotor deflections intersect, but in the whole space of rotor and stator deflections these curves do not come near each other (see stator solution branches in Figure 4.42b), so there is no warning in terms of changes in stability or conditioning of the Jacobian.
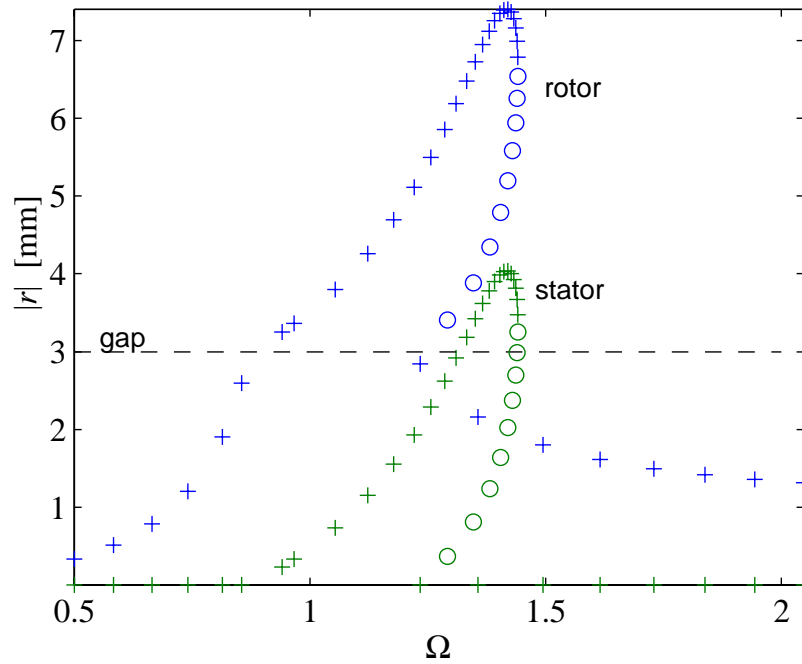
Figure 4.41: magnitude of rotor and stator responses at constant speeds. solution: $+$ stable, o unstable, $h = 3$, $\gamma_\mathrm{m} = 0.1$, other parameters see Table 4.1
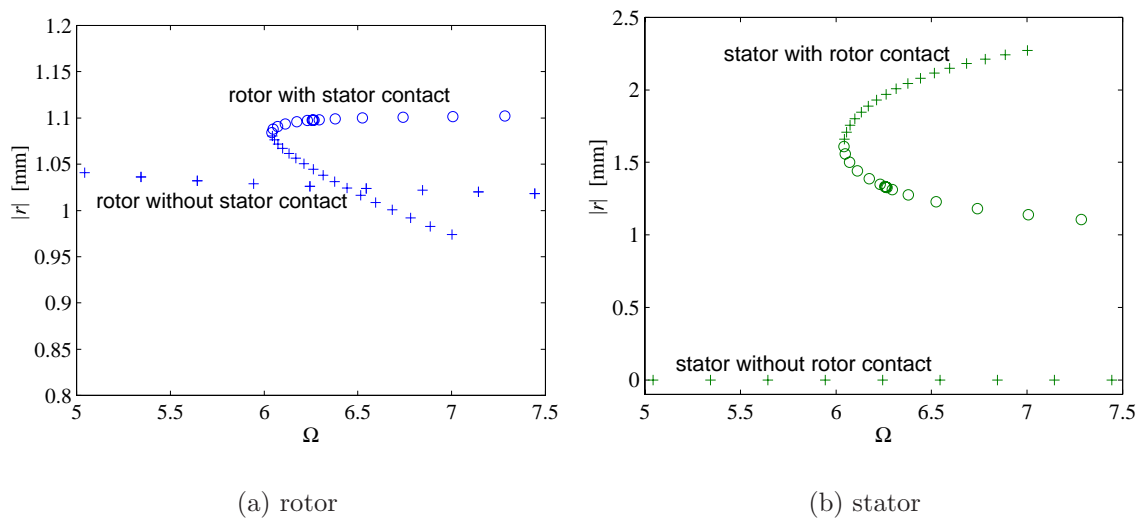

(a) rotor

(b) stator

Figure 4.42: second solution branch at $\Omega > 6$. solution: $+$ stable, o unstable

This second solution branch was found by brute force, using hundreds of random initial guesses at different speeds, in a quest to find out whether the system could vibrate in an 'inverted' modeshape where the stator, which has twice the rotor mass in this example, is moving like a hula-hoop around the rotor. The success rate of finding the second branch from the random initial guesses as a whole was poor: many did not converge to any solution at all, and most settled on the solution where rotor and stator were out of contact. Figure 4.43 show some results of the brute force approach in a simple graph: 8 initial conditions (cyan rings), converged solutions (blue crosses), and stranded (not-converged) iterations (red dots). The ones that did settle on the second solution branch seemed to settle just as easily in terms of convergence on the unstable part of the branch as on the stable one, although a physical system would probably object to that. Once a solution on that branch is found, it is easy to follow with a continuation scheme.
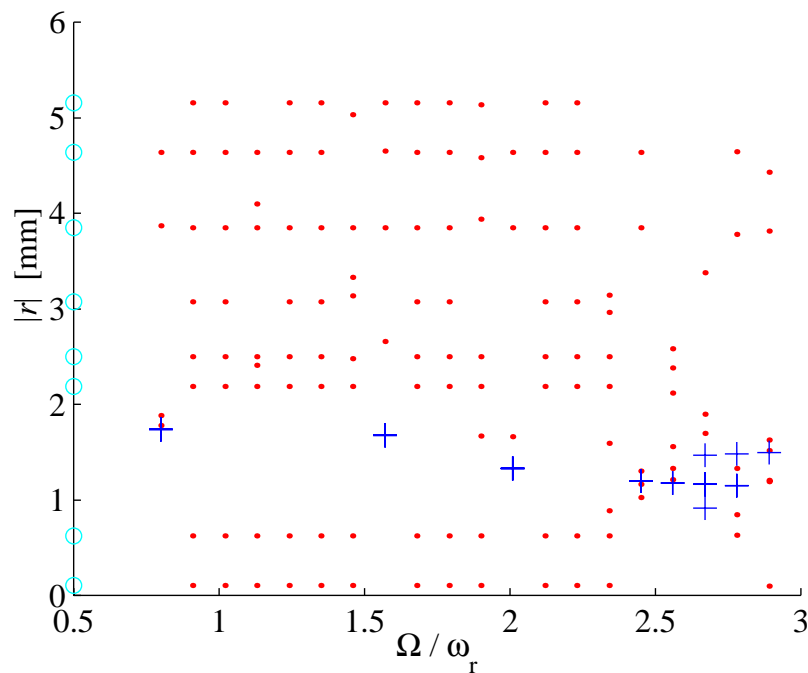

Figure 4.43: solutions found by brute force trial and error, rotor initial conditions (cyan rings), converged solutions (blue crosses), and stranded (not-converged) iterations (red dots)

4.8   Summary

Numerical results from different rotor/stator configurations with intermittent contact possibilities are presented in this Chapter. The aim of the study was to be able to

model and to understand the dynamic aspects which distinguish the various configurations and to investigate which parameters are responsible for which sort of particular behaviour. Specific points to note include:

- The harmonic balance method and time integration method were used to obtain the magnitude and frequency components in the vibration of the non-linear systems. Generally, the harmonic balance method was found to be computationally far more efficient and did not contain the transient disturbances of the time-marching solution. It is, however, a problem to know before setting up a solution with harmonic balance which frequencies to include.

- Great care has to be taken when calculating a run-up or run-down response analysis by integrating the equation of motion in the time domain. With certain parameters such as $\mu > 0$ or $\gamma_k > 0$, one obtains frequency components in the response which the harmonic balance method for a steady-state solution does not show. This is due to the numerical ill-conditioning of the system model with the rather stiff rotor/stator contact zone and the non-negligible effect of the acceleration rate, although the acceleration rates used in these examples have been chosen to be as low as was bearable (one sweep completed per night).

- Amplitude jumps, which are familiar from the Duffing equation, occur and are caused by the bi-linear system stiffness.

- Higher levels of stator damping have been shown to prolong the speed range where rotor and stator stay in contact. Both higher levels of rotor and stator damping decrease the vibration amplitude.

- Sub-harmonic vibration can be clearly attributed to misalignment in the geometry or to a constant side force, both of which manifest themselves in geometric eccentricity in static equilibrium. The excitation has to be sufficiently large for the rotor to overcome the gap at speed ratios larger than $\Omega/\omega_r > 2$ in order for sub-harmonics to build up.

- At certain ratios of rotor/stator mass, rotor and stator stay in continuous contact, irrespective of the speed of rotation. This effect is influenced by the relationship between frequency ratio (Ω/ω_r) where the amplitude jump occurs and the rotor and stator natural frequencies.

- Friction at the rotor/stator contact has the overall effect of reducing the amplitude of vibration. Depending on how the friction force is absorbed by the stator, different models are possible and result in quantitatively different results.

- As the equations of motion are non-linear, multiple solutions are found over some speed ranges. The stability of these multiple solutions is easily determined with the method introduced in chapter 3. Some of these multiple solutions are easily

found by following a solution branch with the arc-length continuation scheme, other solutions, which are part of a different solution branch, are only found by brute force trial-and-error numerical studies.

The studies reported in this Chapter establish reasonable confidence in the modelling of the different mechanisms and provides an insight into the occurrence of the related phenomena. A test rig is to be built to confirm the type of dynamic behaviour encountered and to validate these predictions against actual measurements. The measurements, together with simulation results of the actual test rig configuration, is covered in the following chapters.

Chapter 5

Design and Development of the Test Rig

5.1   Overview

So far a distinctly analytical route from the physical phenomenon of windmilling via numerical modelling to obtaining simulation results has been travelled. It is now time to challenge the construction of the numerical model and the resulting numerical simulations by building a test rig that the numerical model ought to be able to simulate. The rig is also used to map out a range of physical behaviour, and verify the results from numerical simulations including a validation that there are no phenomena occurring on the test rig that are not predicted numerically. Furthermore, it is always somewhat uncertain what values ought to be used for properties like friction or contact stiffness in numerical analysis, and by being able to correlate simulation with measurements one might be able to infer the sensitivity of the system behaviour with respect to these parameters.

In the numerical simulation of the preceding chapter a few parameters were identified as having significant effect on the dynamics of the system. Naturally, it is desirable to design the rig such that the value of these parameters can be varied. These key parameters and their implementation (with attention to allow for the necessary flexibility) are as follows:

- ratio of rotor/stator mass variable by adding weights to rotor disc
- rotor and stator support stiffnesses variable by changing rotor shaft and stator support lengths
- gap size variable by positioning rotor disc relative to tapered stator ring
- offset between rotor and stator geometric centre variable by positioning non-concentric rings in stator assembly

- unbalance load variable by adding masses to rotor disc

The different configurations also include various states of lubrication, different contact materials (aluminium and polyethylene) and, finally, a bladed disc configuration.
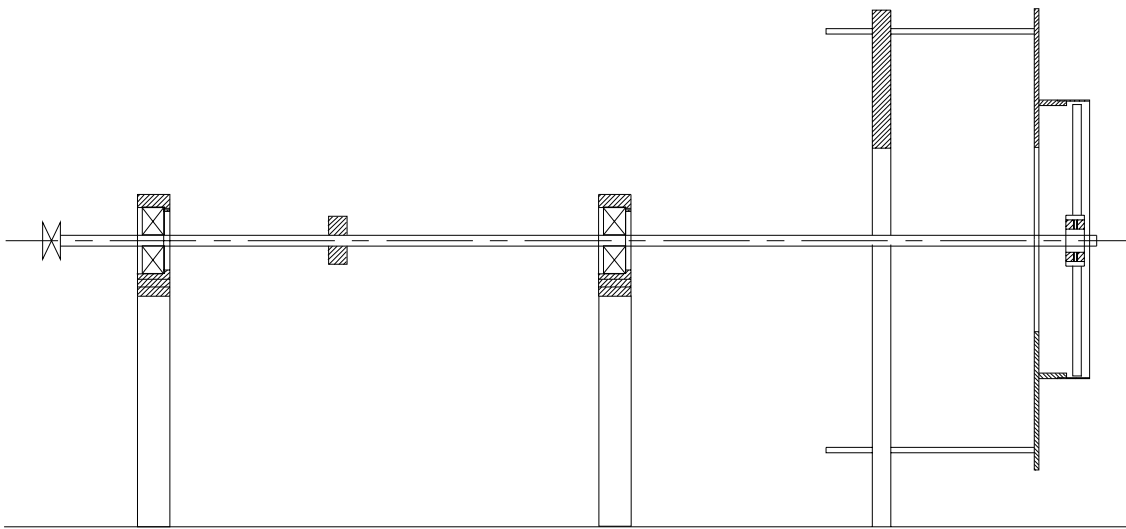
5.2   Rotor and Stator

Figure 5.1: sketch of rotor and stator assembly (scaled proportionally)

The design of the bearing support arrangement is not insignificant and warrants special mention. In normal operation of rotating machinery some play in the bearings does not cause any problems, and thus most off-the-shelf solutions contain clearances. However, when performing vibration tests on the structure, even a very small amount of play can cause rattling which will affect the phenomena under investigation and distorts the results. The bearing housings were designed as integral plummer-blocks (Figure 5.2), as a previous project carried out in this research group has had the experience that it was difficult to adjust the split-housing plummer-blocks so that they would provide a virtually clearance-free support without putting too much pressure on the races. The approach adopted here was to have the outer bore made to a tight sliding tolerance, and then to clamp the bearing race axially with a lid against the stator housing, thereby also locating the race in radial direction. The same approach was also used for the inner race of the bearing, and this way the clearances could be minimised to the play between the balls/cylinders and the races. A cylindrical bearing was used as a non-locating bearing and was placed close to the motor coupling, and a double-groove self-aligning ball bearing was used close to the over-hung part of the rig. Press-fits or shrink-fits were not an option in this case as it was necessary to move the bearing position easily to run the test rig in various configurations.
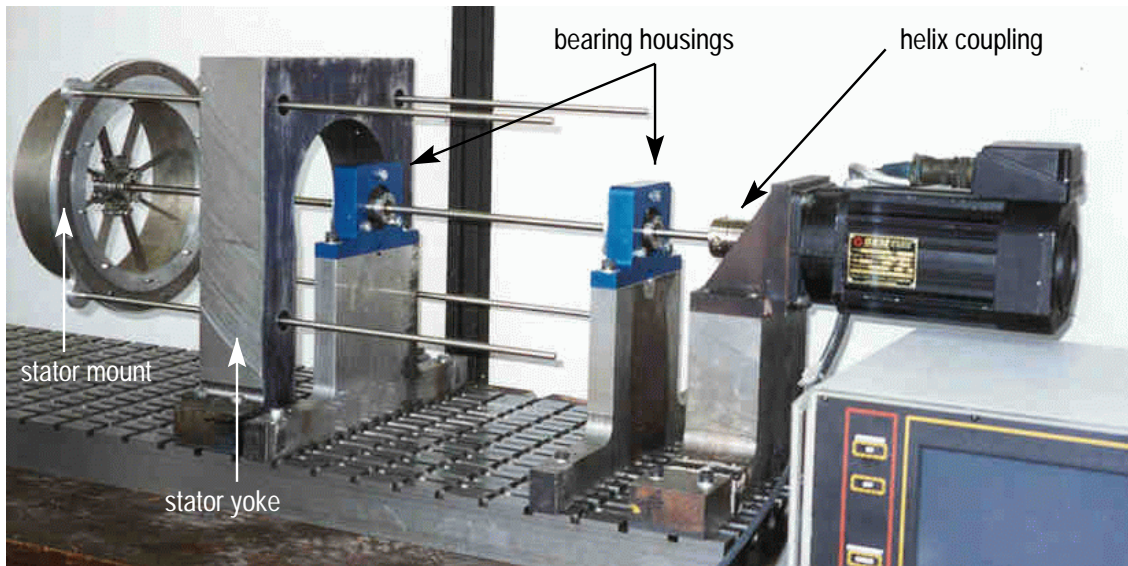
Figure 5.2: rotor and stator assembly in overhung configuration

The shaft was 1m in length and 12mm in diameter and had no shoulders. With such a relatively flexible shaft it was easier to realise larger motion and may, in turn, have helped to accommodate imperfections such as large tolerances or misalignments. This was deemed necessary as the precision of the departmental workshop was very limited.

Without any shoulders on the shaft it was easy to mount the bearings at any position, for example in the over-hung configuration (Figures 5.1, 5.2) or with the disc at mid-span (Figure 5.3), thereby providing a means of controlling the stiffness/natural frequency of the rotor system. The inner bearing race was mounted on an adaptor sleeve (Figure 5.4a) with a tapered inner bore, which together with a collet (Figure 5.4b) clamps onto the shaft.

The stator yoke (Figure 5.2) carries the stator mount (Figure 5.2) by four shoulder-free stator suspension bars (10mm diameter), and the stator mount itself holds the stator with which the rotor contacts. The stator suspension bars are clamped into the yoke with a similar taper arrangement as shaft/bearing or shaft/discs. Hence, the stator can be positioned at variable lengths from the yoke and thereby allows for a variable stator support stiffness/stator natural frequency. The rings of the stator mount (Figure 5.6) are not concentric so as to compensate for misalignment or to create an offset by rotating the rings against each other. The eccentricity is 5mm per ring, so any eccentricity or misalignment within a 10mm radius can be accommodated. The stator itself can take on different forms, either a tapered rigid ring as counterpart to a rigid disc shown in Figure 5.7, or a thin-walled tube as counterpart to the bladed disc shown in Figure 5.8.
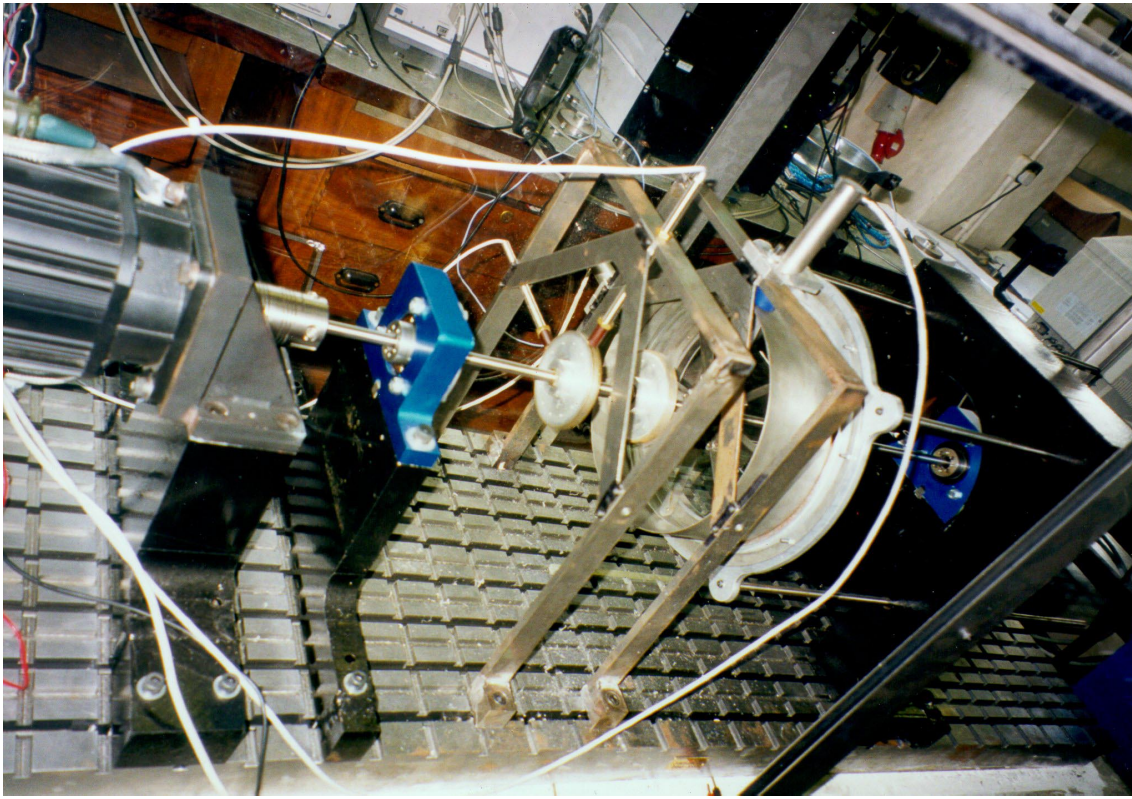
Figure 5.3: rotor and stator assembly in midspan configuration

(a) shaft adaptor   (b) collet

Figure 5.4: bearing/disc adaptor and collet fixture for rotor shaft
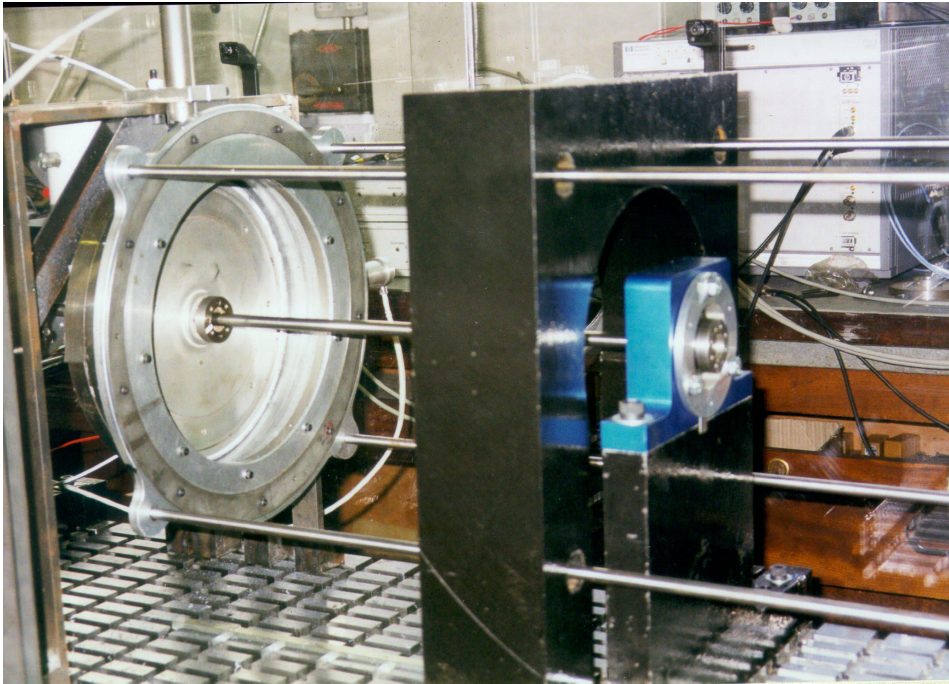
Figure 5.5: bearing housing

Figure 5.6: stator mount

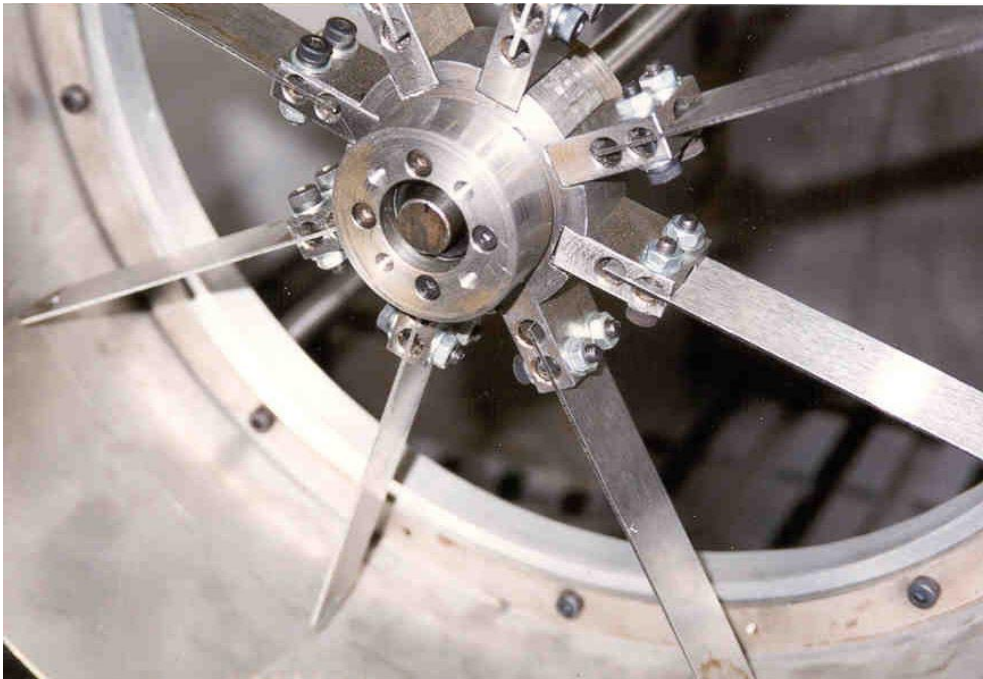Figure 5.7: rigid disc assembly

Figure 5.8: bladed disc assembly
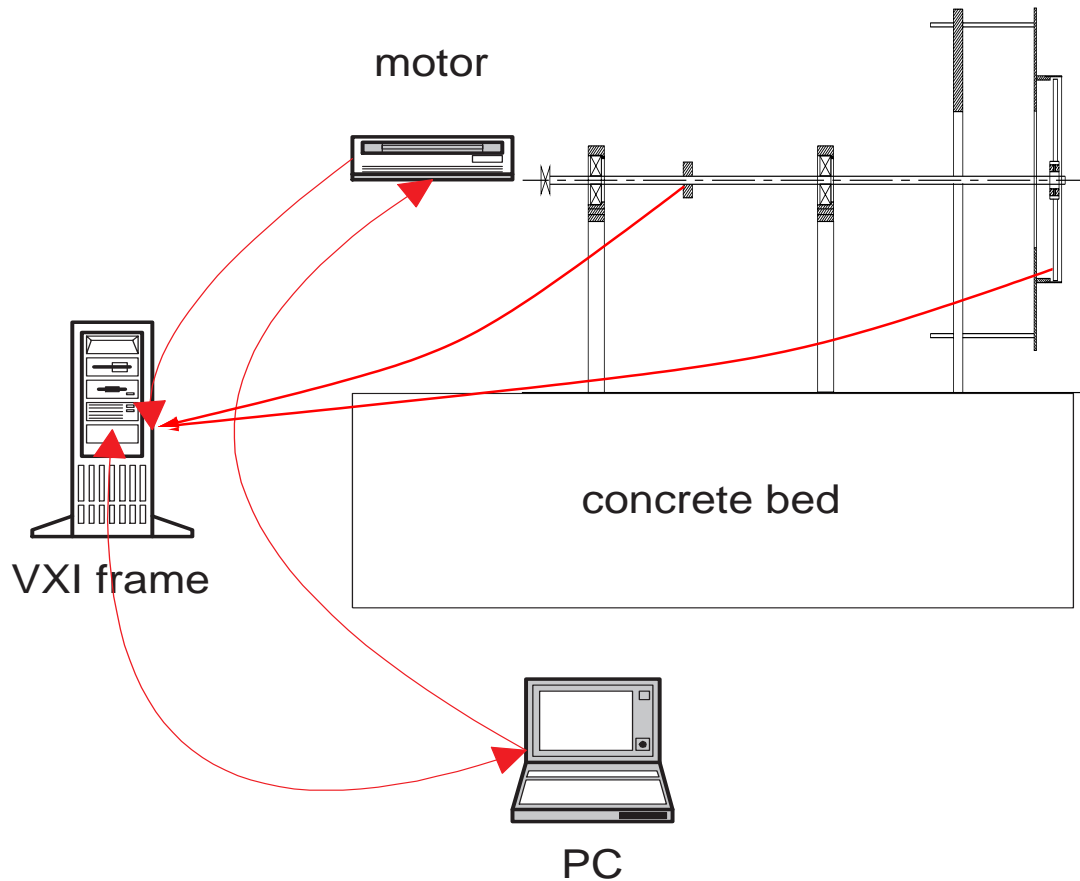
5.3   Data Acquisition System

Figure 5.9: measurement setup

Past experience of severe noise and reliability problems with cheap PC A/D cards teaches caution when choosing the measurement hardware. Fortunately, a VXI* based measurement system, consisting of a digital–analogue converter and a waveform generator, was available. The system was controlled via MATLAB running on a stand-alone PC connected to the VXI frame via a FireWire bus (IEEE 1394). The low-level drivers manipulating the registers of the cards were provided by the manufacturer of the VXI system, but the higher-level routines such as measurement or signal generation functions were developed in this project. A hammer excitation (impulse) and multiple-shaker MIMO[†] step-sine testing programs were written to extract the frequency response functions of the linear parts of the structure, such as the shaft suspended free-free or in bearings. Furthermore, the motor settings (speed, torque, PDI controller

---

*a high-spec standard in the data acquisition industry supported by many manufacturers
[†]multiple inputs, multiple outputs

parameters) were controlled via self-made MATLAB routines accessing one of the PC's serial ports that communicate with the motor's RS232 port. The data acquisition routines for the rotor/stator contact measurements are simpler than the impulsive or step-sine testing procedures, as it is a more passive task of data streaming (the excitation comes solely from the out-of-balance of the spinning rotor and lies outside of the control of the measurement system) with only some simple trigger requirements.

The hardware specifications for the digitiser (HP E1432) were: 16-channel, 16bit A/D converter per channel (no multiplexer), 51.2kHz max sampling rate, 32MB memory on-board (32bit per sample, 8 million samples); and for the generator: 4-channel, 16–20bit D/A converter, 64kHz output speed, built-in and arbitrary waveforms, 32MB on-board memory.

On rotating structures the easiest choice is to use non-contacting transducers. Possibilities are laser micrometers, laser Doppler devices, or proximity probes. Proximity probes (eddy-current) transducers are the least expensive of these and were used here to measure not only the rotor but also the stator deflection. Accelerometers were not used for the stator as the rotor/stator impacts were expected to have strong higher-frequency components which could corrupt the integration necessary to obtain deflections. The proximity probes (Bently Nevada) had only a very limited range ($\pm$2mm and $\pm$4mm for our sets), so that larger out-of-balance masses caused the rotor to touch the probes. In order to reduce this limitation on the deflections, the measurement disc had to be moved away from the rotor/stator contact zone.

The motor was fitted with an encoder that delivered 1024 pulses/rev and a 1/rev signal. These were fed into a circuit which counted the pulses and converted the counter into a 0–10V output signal. This voltage was also connected to one of the VXI input channels, so it was possible to correlate the rotor and stator displacements with instantaneous rotor shaft angles and thereby to provide absolute phase information.

5.4   Signal Processing Requirements

The signal processing routines related to vibration testing are covered in detail in text books (for example Ewins (1984)). In addition, this thesis makes frequent use of frequency spectrum and Z-mod plots, which are basically standard tools, but which use an extension to negative frequencies. While not a new invention (Bucher & Ewins, 1997), this extension is rarely seen in the literature, but is a big help in spatially separating the patterns of vibration. This section gives a brief coverage of this procedure and justifies the requirements of two probes per location and the need to measure the 1/rev signal.

The discrete Fourier transform of a signal, $r(n)$, which leads to the Fourier coefficients $R(k)$, and the inverse Fourier transform of the signal are (where n refers to time, t_n, and k to frequency, ω_k):

$$R(k) = \frac{1}{N} \sum_{n=0}^{N-1} r(n)\, \mathrm{e}^{-\mathrm{i}\frac{2\pi kn}{N}} \qquad r(n) = \sum_{k=0}^{N-1} R(k)\, \mathrm{e}^{\mathrm{i}\frac{2\pi kn}{N}} \tag{5.1}$$

The frequencies in the discrete Fourier transform above half the sampling frequency $\omega_{N/2}$ can be interpreted as negative frequencies or rotations in the negative direction (Randall, 1987), more specifically $R(\frac{N}{2} + k) = R(-k)$. For real signals $r(n)$ these negative frequencies are simply complex conjugates of their positive counterparts, but for complex signals $r(n)$ this is no longer true.

At each measurement position of rotor or stator there are two proximity probes which are mounted with a $90\,^\circ$ angle between them. These sensors do not have to be perpendicular to each other, but it simplifies the following analysis if they are. The two discretised signals delivered from these two sensors, $y(n)$ and $z(n)$, can be combined into one complex quantity (assuming $90\,^\circ$ angle between probes): $r(n) = y(n) + \mathrm{i}z(n)$. The Fourier coefficients $R(k)$ constitute positive and negative frequencies that can be interpreted as the decomposition into forward and backward whirl. In the following example, this decomposition is carried out at one particular frequency, k, only:

$$r(n) = r_{\mathrm{f}}(n) + r_{\mathrm{b}}(n) = \hat{R}_{\mathrm{f}}\, \mathrm{e}^{\mathrm{i}\frac{2\pi kn}{N}} + \hat{R}_{\mathrm{b}}\, \mathrm{e}^{-\mathrm{i}\frac{2\pi kn}{N}} \tag{5.2}$$

where $\hat{R}_{\mathrm{f}}$ and $\hat{R}_{\mathrm{b}}$ are the amplitudes of the forward and backward whirls, respectively. After applying the Fourier transform of equation (5.1) to the forward whirl, $r_{\mathrm{f}}(n)$ only, the Fourier coefficients are $R(k) = \hat{R}_{\mathrm{f}}$ and $R(-k) = 0$, showing that the frequency information above half the sampling frequency does not contain any forward whirl information. For the reverse whirl it follows that $R(k) = 0$ and $R(-k) = \hat{R}_{\mathrm{b}}$, and this time the frequency information is exclusively above half the sampling frequency. Therefore, a whirl orbit measured with two perpendicular probes can easily be decomposed into forward and backward whirl orbits and their respective frequencies.

The application of the measured signal directly to the Fourier transform is especially easy if a complete (and sufficient) number of shaft revolutions have been measured. If the frequencies present in the vibration are pure sub- and super-harmonics of the engine order, the measured signal is periodic. The frequency spectrum of a periodic signal has distinct sharp peaks at the frequency components present. If the peaks in the frequency spectrum of a measured signal are not sharp but have sidebands, one can conclude that leakage occurs as the vibration is not periodic but has other, shaft speed independent, frequencies present. Therefore, to facilitate the processing of the measurements with respect to full shaft revolutions, it is important that a 1/rev signal from the motor encoder is measured as well (or used as trigger to start and stop data acquisition).

Chapter 6

Experimental Studies

6.1 Overview

The purpose of the measurements and the configuration of the setups is described in the previous Chapter on the design of the test rig. With the measurements presented in this Chapter the following characteristics of the test rig are investigated:

- amplitude jumps – speed range over which rotor/stator contact is sustainable
- frequency components in the vibration spectrum
- different lubrication and contact materials
- rigid disc and bladed disc as rotor contact bodies

After the measurements on the rotor system without stator contact are shown, results are presented from the rotor/stator interaction with the rigid disc configuration. Measurements are conducted in this configuration with a variety of setups. Finally, the results from the bladed disc configuration are discussed.

Generally, the units for all the orbit plots in this chapter are in [mm], and all the frequency spectra are plotted in [dB] on a frequency axis in [Hz]. The grid spacing of the dotted lines in the frequency spectra is usually based on integer multiples of the engine order, unless stated otherwise. Positive frequencies are forward, negative ones are backward whirl components. Rotor data are plotted in blue, stator data in green.

6.2 The 'linear' Rotor System

It can be seen in Figures 6.2 and 6.3 that the rotor, which is treated as a linear structure in the analysis (see for example Figure 6.1, showing a representation of an FE model),

98

shows some behaviour typical of non-linear structures and hence gives an indication as
to what the limits of the correlation between measurements and simulation might be.
In Figure 6.2, rotor orbits at different constant speeds are shown, the only excitation
in the system being the residual out-of-balance of the rotor. In isotropic supports one
expects perfectly circular orbits, and in non-isotropic supports the whirl orbits become
elliptical. However, as can be seen, a periodic orbit with multiple frequencies exists for
speed $\Omega = 8.48$ Hz. Figure 6.3 shows the frequency components of these orbits, and it
becomes clear that a strong second harmonic component is involved. There are only a
few reasons for this sort of behaviour that come to mind, most notably play in the roller
bearings. The frequency spectra generally have only very sharp spikes. This indicates
that the vibration is related to the shaft speed, as no leakage occurs (data is measured
over integer shaft revolutions, no windowing before FFT). However, these effects do
not seem to dominate the behaviour of the rotor/stator contact measurements. As
discussed earlier in the previous Chapter on design, the measurements could not be
taken directly at the rotor disc, as the clearances of the probes are not sufficient, and
so a measurement disc is mounted onto the shaft closer to the bearings, see Figure 6.1
and also in the photographs of the previous chapter. As a side note, the split rotor
disc shown in this Figure 6.1 is purely for finite element modelling purposes (Chapter
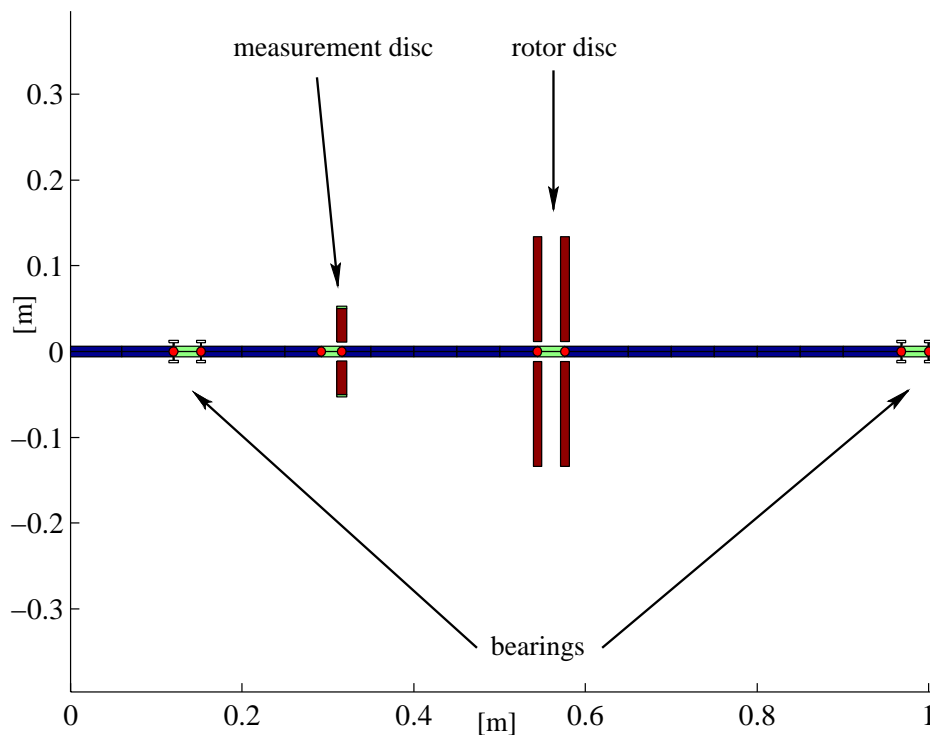7), the physical disc is not split.

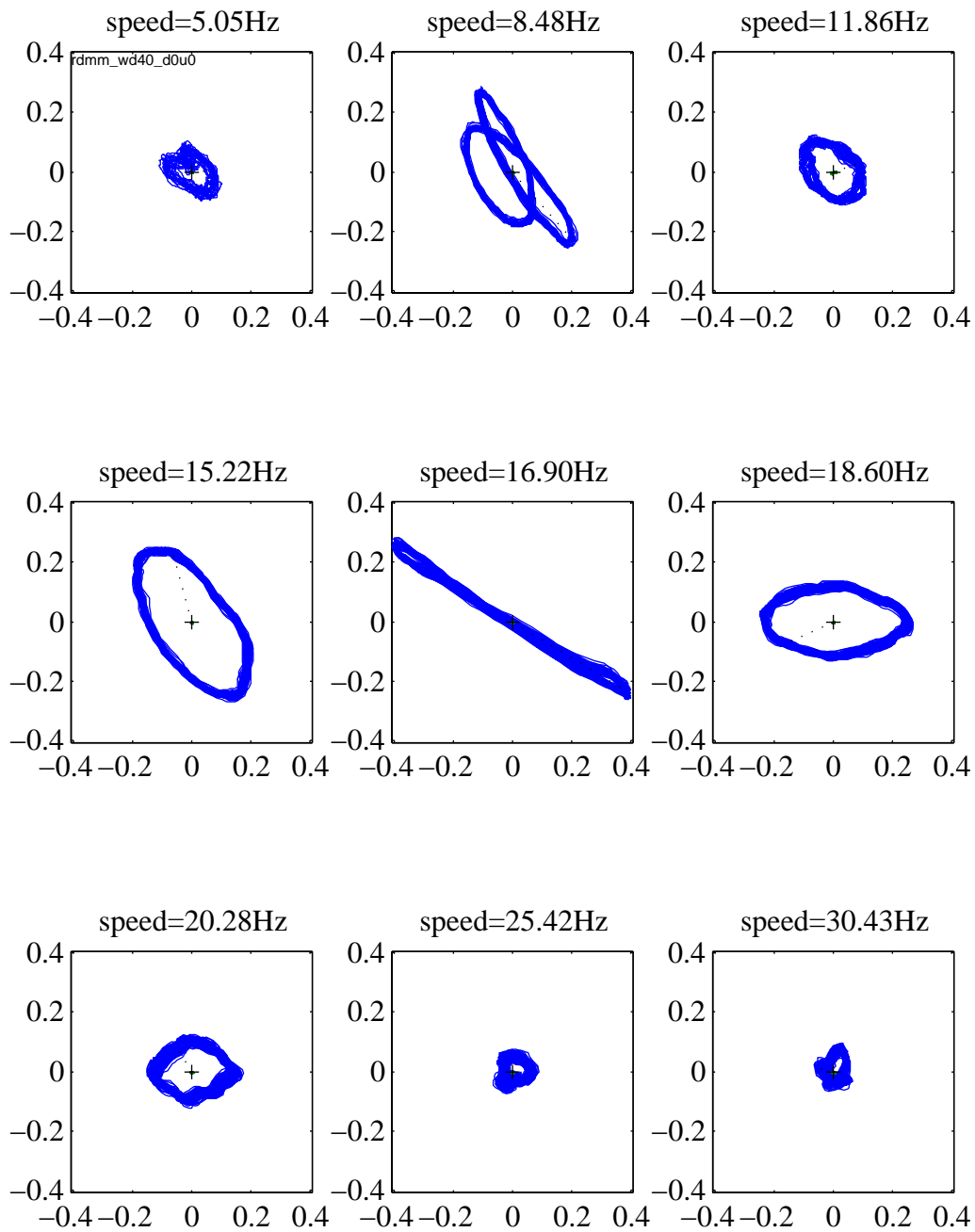Figure 6.1: simple rotor FE model with measurement disc

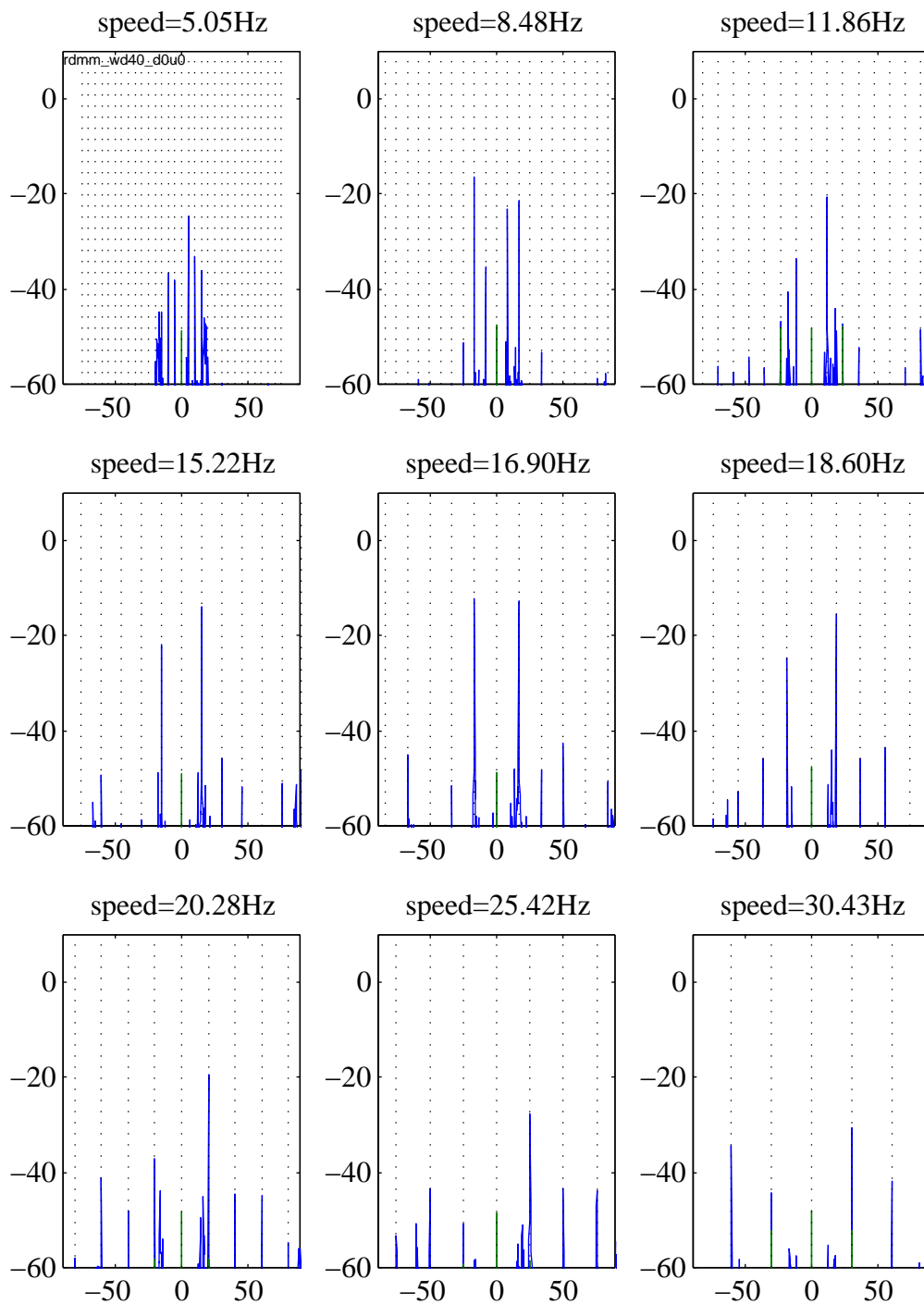Figure 6.2: rotor orbit plots [mm] at different speeds

Figure 6.3: rotor frequency components [Hz] at different speeds

6.3   Rigid Disc, Rigid Stator

6.3.1   Configuration

Generally, the rig was run in two main setups for the rigid disc/rigid stator configuration: (i) medium stator support stiffness (the stator system has a natural frequency higher than that of rotor, but not rigid) and (ii) low stator support stiffness (stator frequency lower than rotor). Both setups can be varied further by changing the rotor mass, m_r. These configurations will be abbreviated as A–C and D–F in the text, respectively (Tables 6.1 and 6.2). In between measurement runs, the amount of out-of-balance, ϵ_m, gap size, h, and stator eccentricity, ϵ_s, can be varied easily and thus will be specified with the particular measurements shown.

Table 6.1: rig parameters for medium stator support

setup	$m_r\,[\,\mathrm{kg}\,]$	$m_s\,[\,\mathrm{kg}\,]$	$\omega_r\,[\,\mathrm{Hz}\,]$	$\omega_s\,[\,\mathrm{Hz}\,]$	γ_m	γ_s	$\approx \omega_{rs}\,[\,\mathrm{Hz}\,]$
A	3.3	6.6	17.1	24.0	2.0	4.0	22
B	5.4	6.6	13.3	24.0	1.2	4.0	20
C	7.5	6.6	11.3	24.0	0.9	4.0	18

Table 6.2: rig parameters for soft stator support

setup	$m_r\,[\,\mathrm{kg}\,]$	$m_s\,[\,\mathrm{kg}\,]$	$\omega_r\,[\,\mathrm{Hz}\,]$	$\omega_s\,[\,\mathrm{Hz}\,]$	γ_m	γ_s	$\approx \omega_{rs}\,[\,\mathrm{Hz}\,]$
D	3.3	6.6	17.1	9.2	2.0	0.6	12
E	5.4	6.6	13.3	9.2	1.2	0.6	11
F	7.5	6.6	11.3	9.2	0.9	0.6	10

6.3.2   Amplitude Jumps

The following two measurements, with the setups A and D, show very different speed ranges of rotor/stator contact. In both cases, the rotor was run-up from standstill, the speed kept constant for the duration of a measurement, and then slowly incremented to the next speed level. Figure 6.5 shows that the rotor and stator lose contact somewhere above $\Omega > 18\,\mathrm{Hz}$, which is, as expected from the simulations, after passing the natural frequency of the rotor. At very low speeds, the unbalance forces are insufficient to overcome the gap; at higher speeds, the rotor and stator lose contact with each other, whereupon the rotor envelope asymptotically approaches the mass eccentricity. In

Figure 6.4 it can be seen that as speed is increased, rotor and stator continue to stay in contact for as long as it was possible to increase the speed (30 Hz, the rectangular orbit of the rotor indicates that the rotor is impacting against the displacement probes).
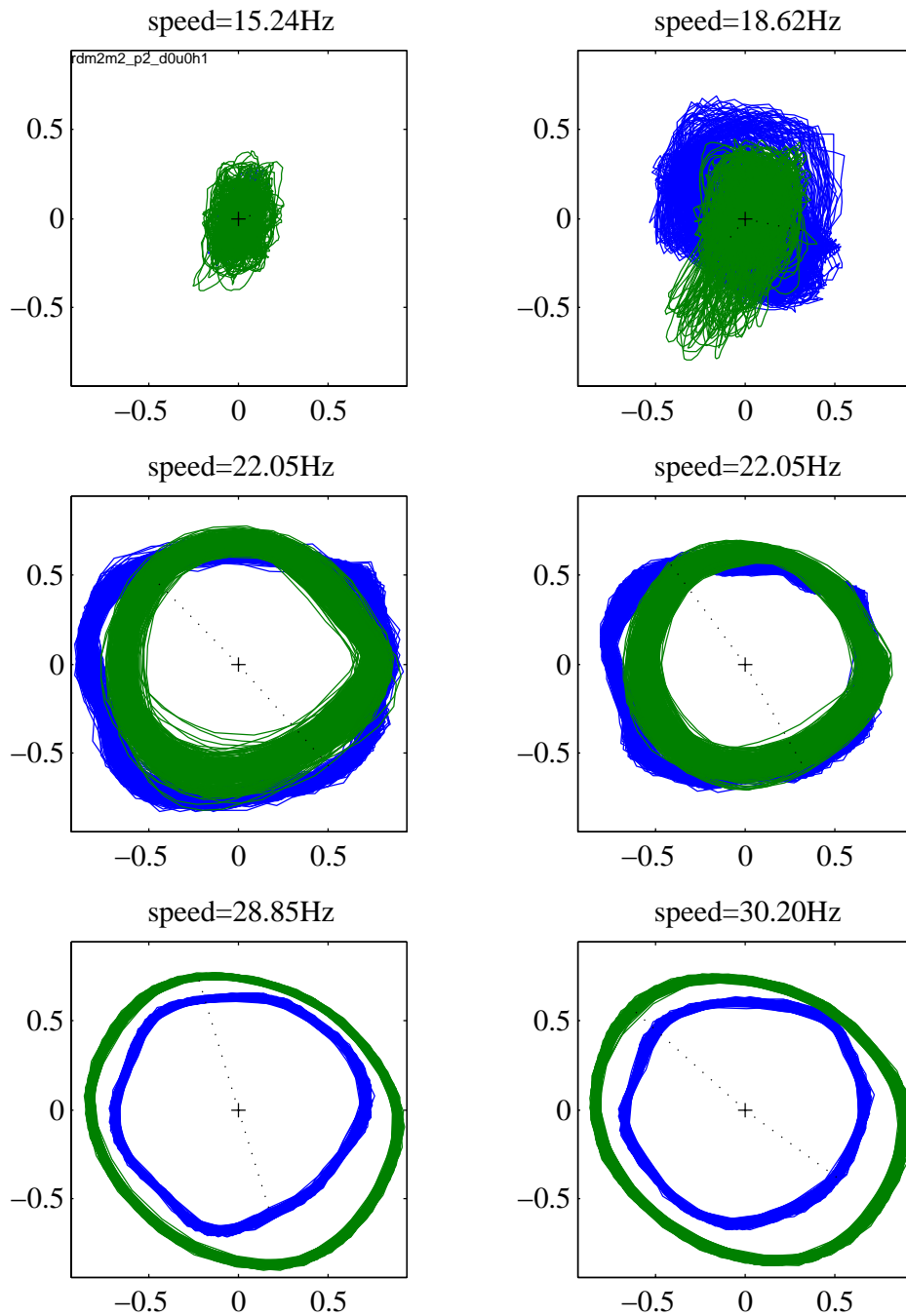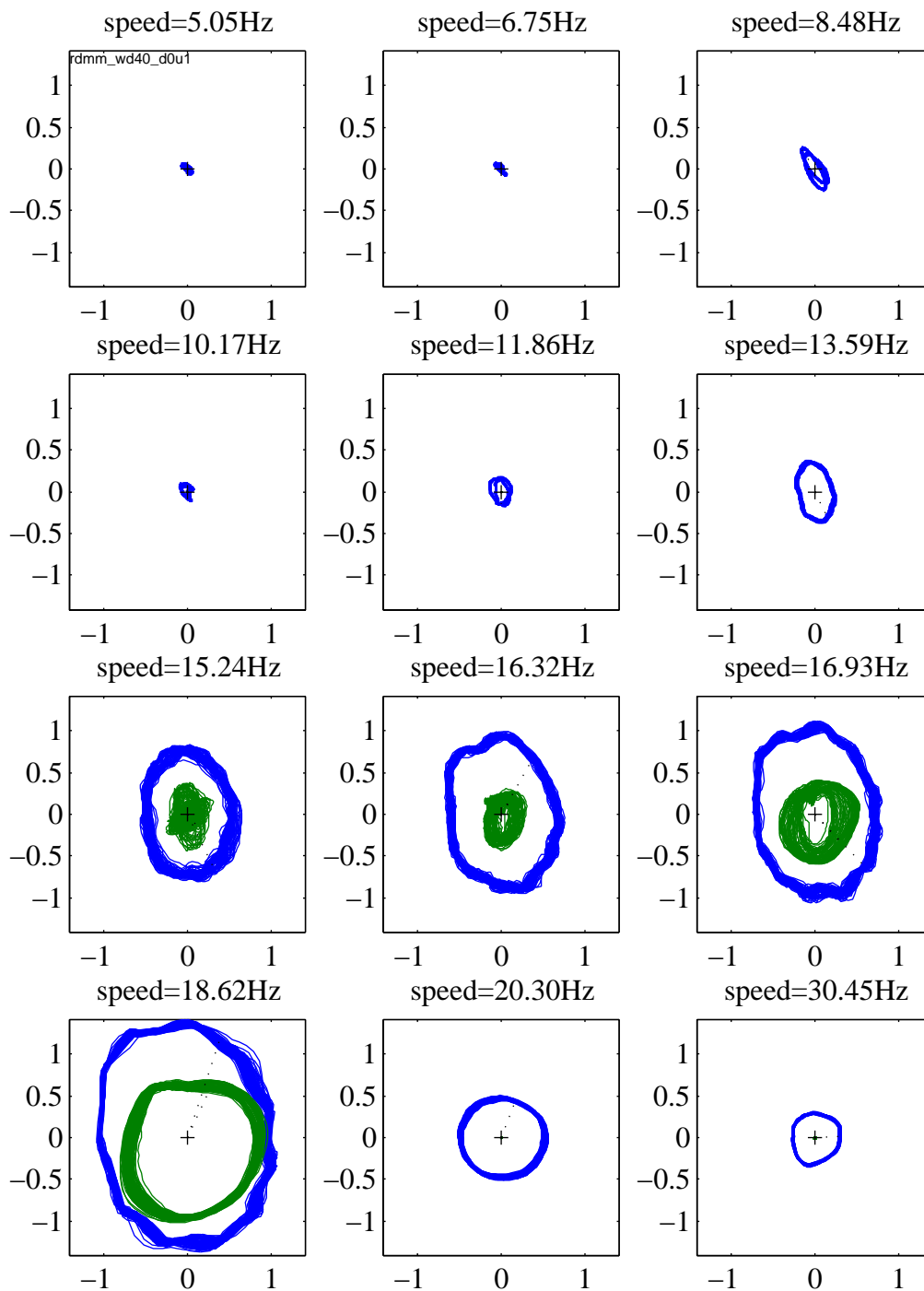

Figure 6.4: orbits [mm] with setup D, $h = 1.7$ mm

Figure 6.5: orbits [mm] with setup A, $h = 2.2\,\text{mm}$

6.3.3   Sub- and Super-Harmonics

The following plots (Figures 6.8–6.11) show the orbits and the frequency spectra of the rotor/stator system in configuration D at constant speeds. An overview of the orbits of the complete run is given in Figures 6.6 and 6.7. The measured time histories each have a length of over 300 shaft revolutions and the frequency spectra have a resolution of 0.064Hz. Again, the data were truncated by a few points so that each time record contained an exact integer number of revolutions, thus minimising leakage and avoiding the need to use windows in the signal processing.

Figure 6.10 shows a Lissajous figure with 2 main periodic components, the others are more complex and some even look like random 'bouncing around', e.g. the rotor orbits in Figure 6.9 and 6.11. However, if a strobe* is superimposed on such a plot, so as to highlight every data point occurring at say the 1/rev signal (plotted as lighter dots), one can clearly see different patterns emerging. These patterns vary from 4 clusters (Figure 6.10), through an increasing number of clusters (11 in Figure 6.8) to tracing out ellipses (Figures 6.9 and 6.11).

With each orbit the frequency spectrum is plotted over a range of 40dB. The sharpness of the peaks gives a good indication that the main vibration response frequencies are indeed multiples of the shaft speed, justifying the decision not to use windows in the processing as there were no significant leakage problems. Each of these frequency plots has a different grid spacing of dotted lines which attempt to match the dominant frequency components. In Figure 6.8 the dominant frequency is the resonance frequency of the combined rotor/stator system at $\omega_{\mathrm{rs}} \approx 12.00\,\mathrm{Hz}$ and a shaft speed of $\Omega = 21.95\,\mathrm{Hz}$. The ratio of these two frequencies is $\omega_{\mathrm{rs}}/\Omega \approx 6/11$, resulting in a frequency spacing of $\Delta\omega = \Omega/11$. Strong components occur at $i\Delta\omega$ with $i = 1, 2, \ldots, 7, 11, 16$. Data for the other cases is summarised in Table 6.3.

Table 6.3: measured frequency relationships for rigid discs
setup D, $h = 2.1\,\mathrm{mm}$, $\epsilon_{\mathrm{s}} = 0.4\,\mathrm{mm}$

Figure	$\Omega\,[\,\mathrm{Hz}]$	$\omega_{\mathrm{rs}}\,[\,\mathrm{Hz}]$	$\approx \frac{\omega_{\mathrm{rs}}}{\Omega}$	sidebands i
6.8	21.95	12.00	$\frac{6}{11}$	$1, 2, \ldots, 7, 11, 16$
6.9	23.63	12.33	$\frac{12}{23}$	$1, 11, 12, 13, 23, 24, 34$
6.10	25.32	12.63	$\frac{1}{2}$	$0.5, 1, 1.5, 2, 3, 4$
6.11	27.00	12.63	$\frac{15}{32}$	$2, 4, 13, 15, 17, 28, 30, 32, 49$

---

*stroboscopic measurement: capturing displacement at known time intervals, usually — but not necessarily — synchronous with rotation of the shaft
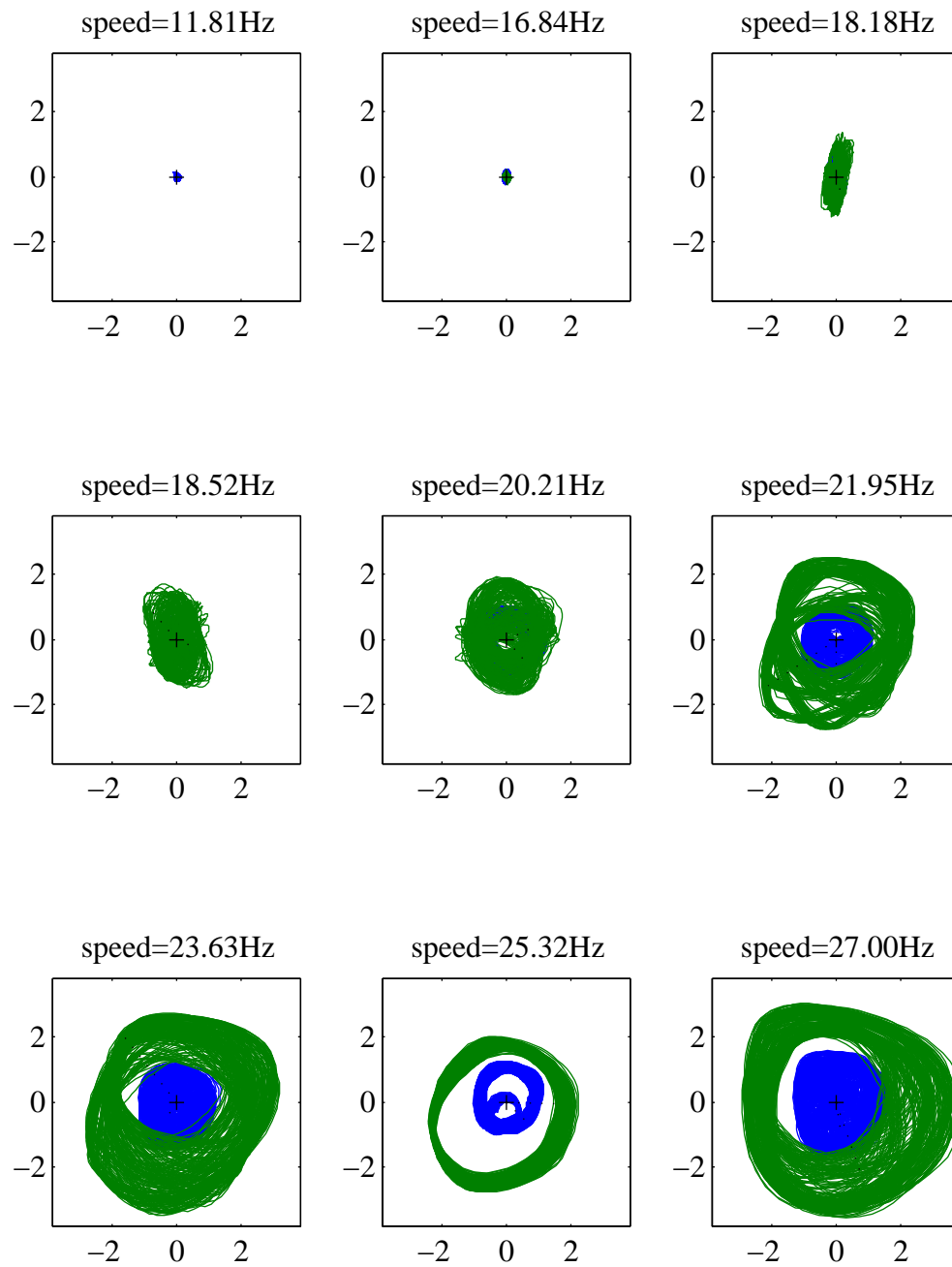
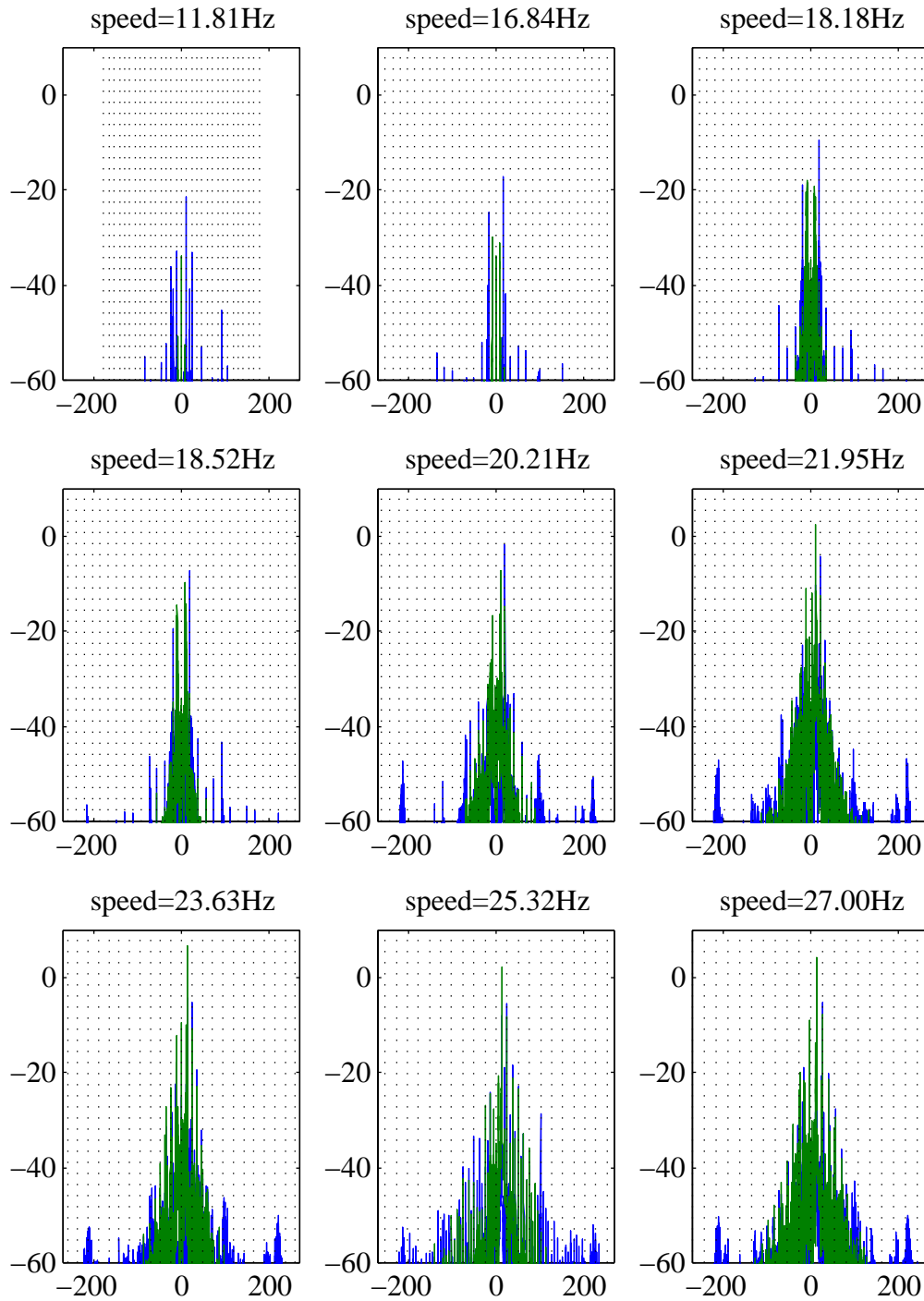Figure 6.6: setup D: orbits [mm] at various speeds

Figure 6.7: setup D: frequency spectra [Hz] at various speeds
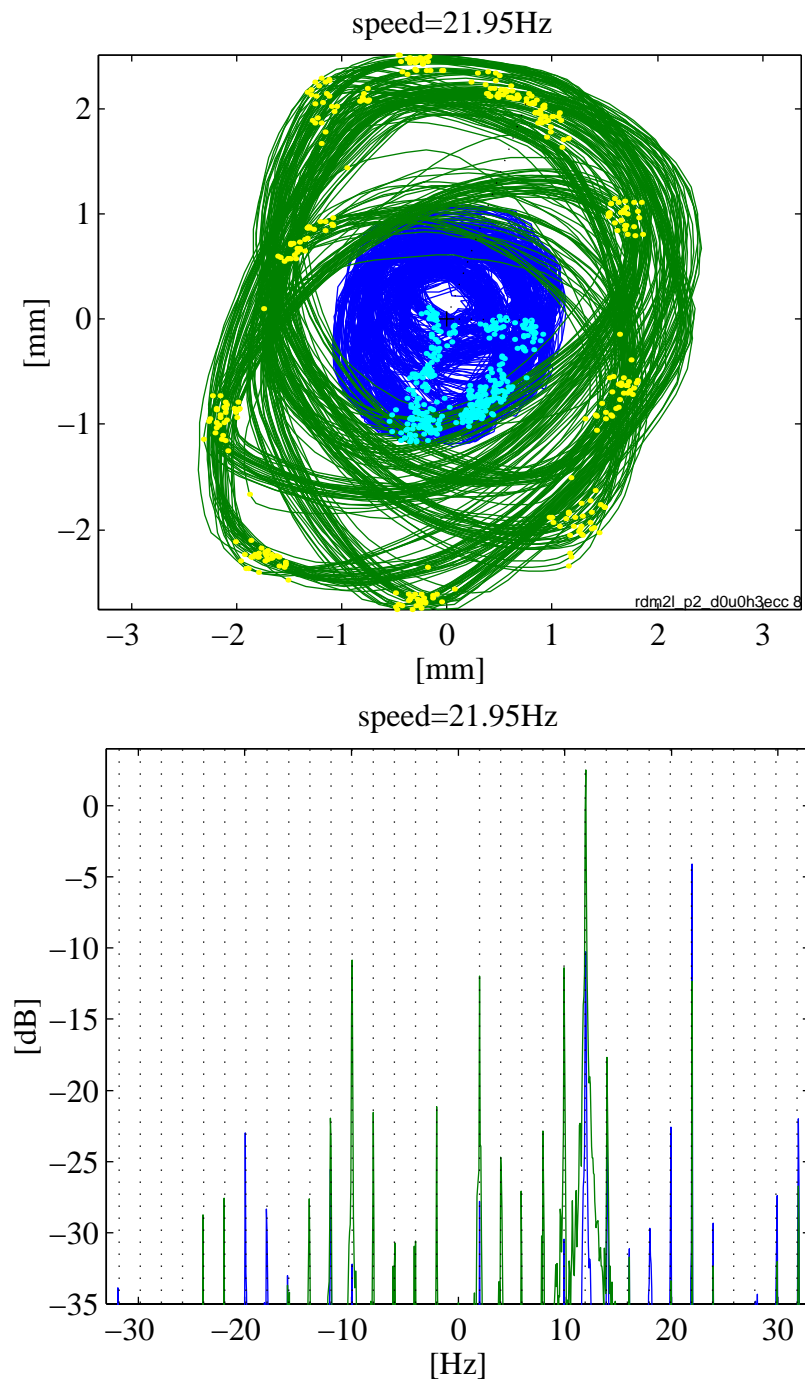
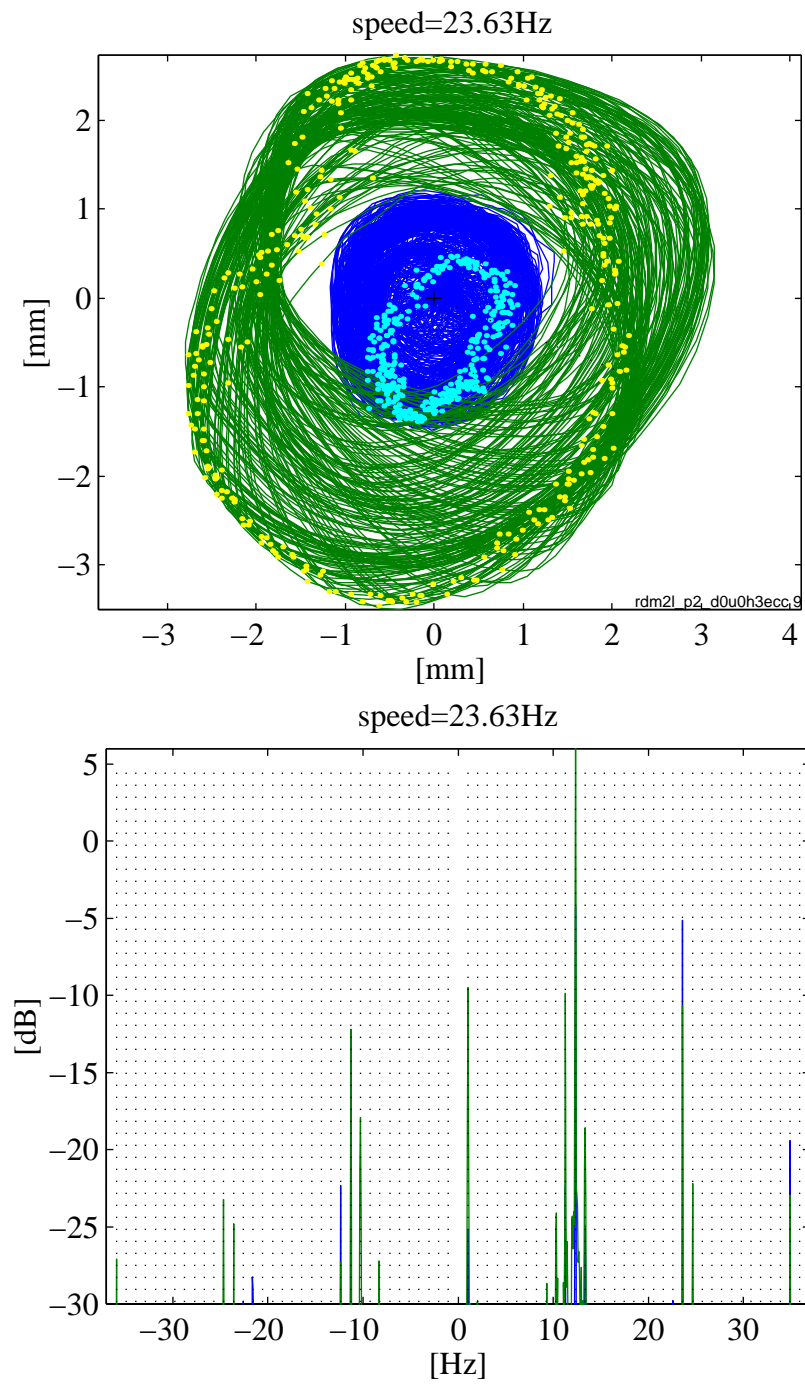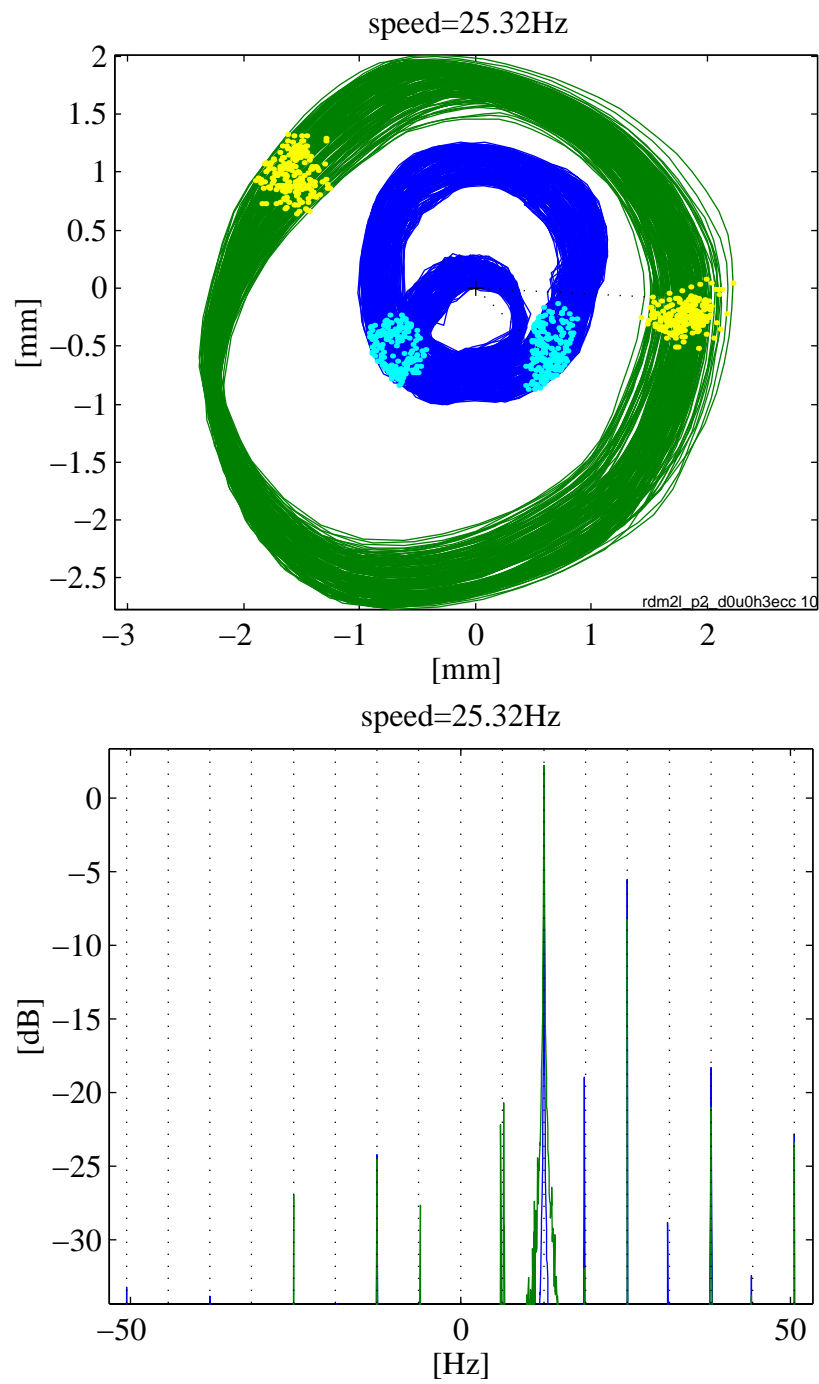Figure 6.8: periodic orbit at $\frac{1}{11}$ shaft speed

Figure 6.9: quasi-periodic orbit at $\approx \frac{1}{23}$ shaft speed

Figure 6.10: periodic orbit at $\frac{1}{4}$ shaft speed
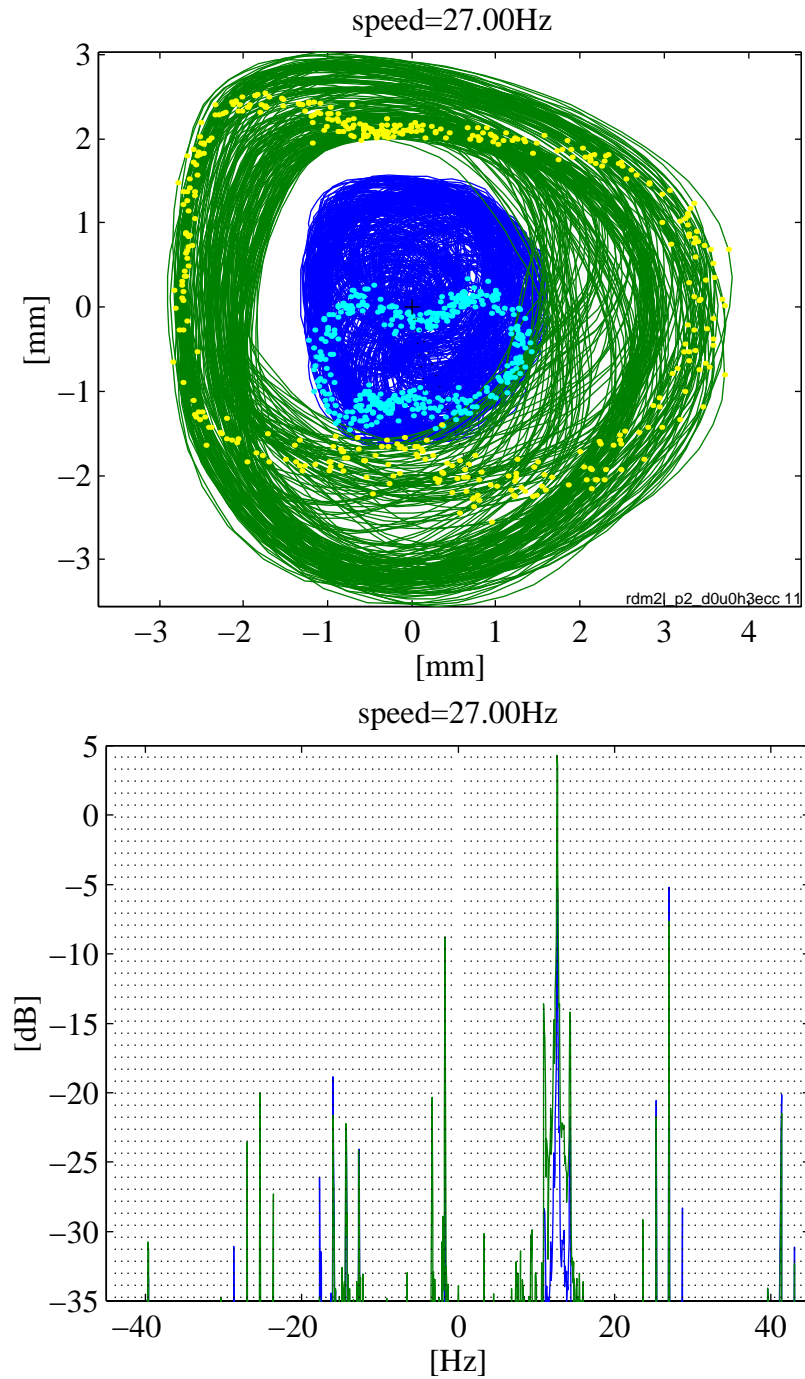
Figure 6.11: quasi-periodic orbit $\approx \frac{1}{32}$ shaft speed

The dominant frequency component around 12Hz (which features in all these figures) is the resonance frequency of the combined rotor/stator system which, of course, varies with magnitude of deflection as the system is non-linear. At the given speeds, this resonance frequency always seems to be strongly excited, sometimes even more than the 1EO excitation. The other frequency components can also be linked in two ways: (i) the number of 1/rev clusters in the orbit plots (only in Figures 6.8 and 6.10 are they distinct) yields the spacing of the frequency grid, the lowest sub-engine order and its multiples that are excited, and (ii) the ratio of resonance frequency over speed of rotation can be approximated by a ratio of integer numbers, where the denominator is equal to the EO fraction that again makes up the spacing in the frequency grid.

The mechanism that seems to be at work here has significant implications for the windmilling scenario, in that even very low sub-harmonics can feature strongly in the response spectrum. Figures 6.8, 6.9, and 6.11 show components at EO/11, EO/23, EO/16, respectively, that are only 4–7 dB lower that the 1EO component, which is, after all, the frequency of the exciting out-of-balance force.

6.3.4   Lubrication and Contact Material

Figures 6.12–6.15, show typical results of the test rig under similar conditions to each other with (i) dry aluminium (Al₂ on rotor and stator) with no lubrication, (ii) plenty of WD40 spray used as lubricant, and (iii) a high density polyethylene (PE) rim melted onto the rigid disc. In between these test runs, parts of the rig had to be dismantled, for example to facilitate the mounting of the rigid disc with the new PE rim. Attempts were made to keep the assembled structure condition the same throughout the test, but changes in residual unbalance and gap size due to the PE rim and different positioning of the disc are inevitable. When looking at the orbit plots and spectra in the following figures, it can be said there appears to be no difference in the rig behaviour under the chosen contact conditions.
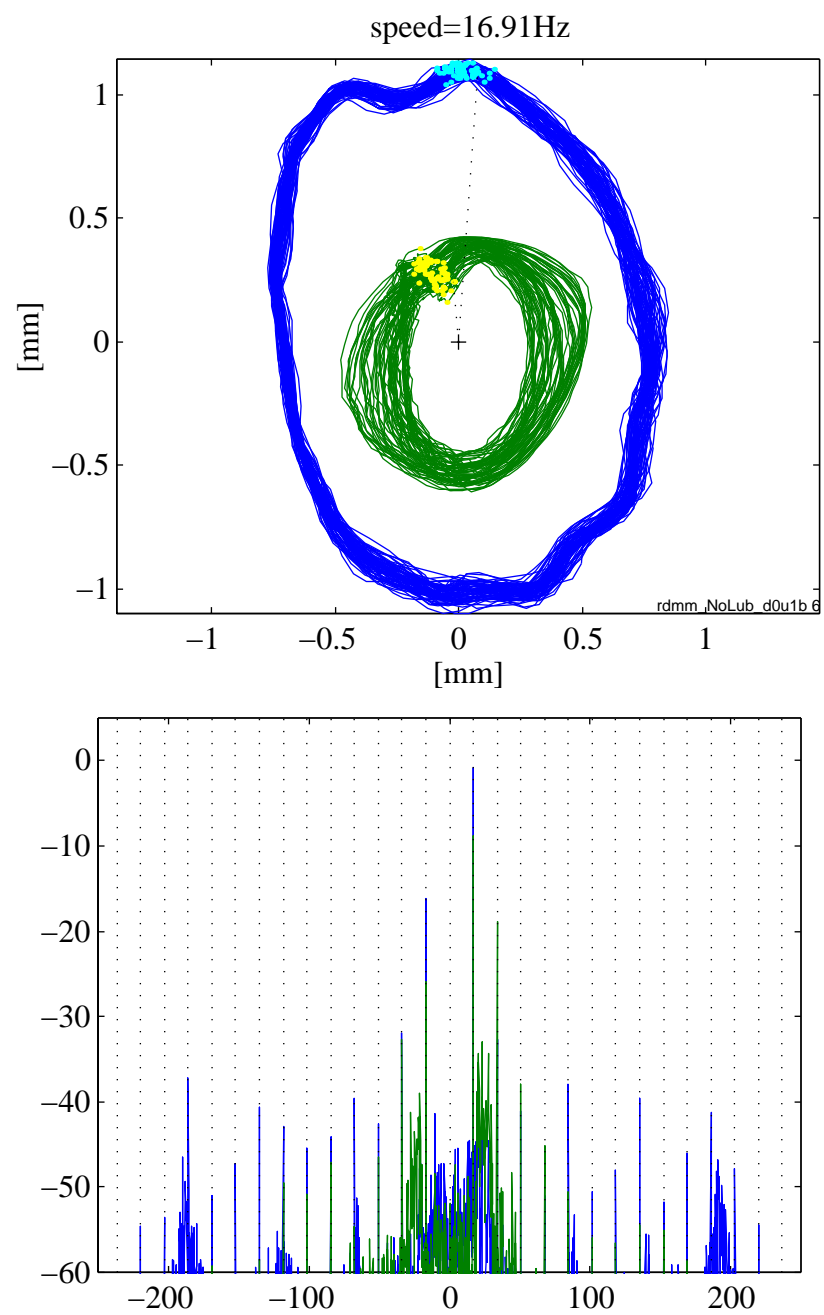
Figure 6.12: setup A, $\Omega = 17\,\mathrm{Hz}$, no lubrication

speed=16.93Hz

speed=16.93Hz
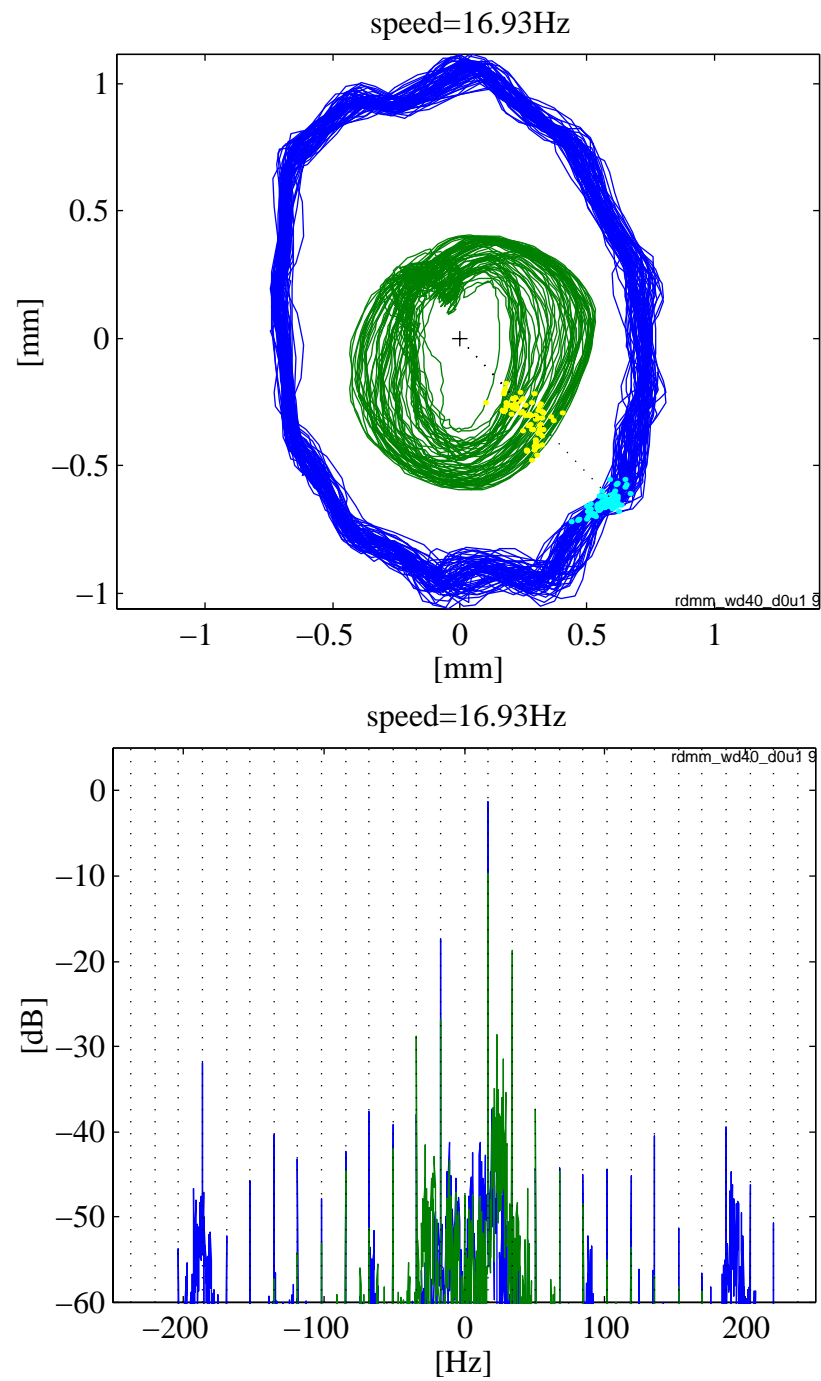
Figure 6.13: setup A, $\Omega = 17\,\mathrm{Hz}$, lubrication: WD40
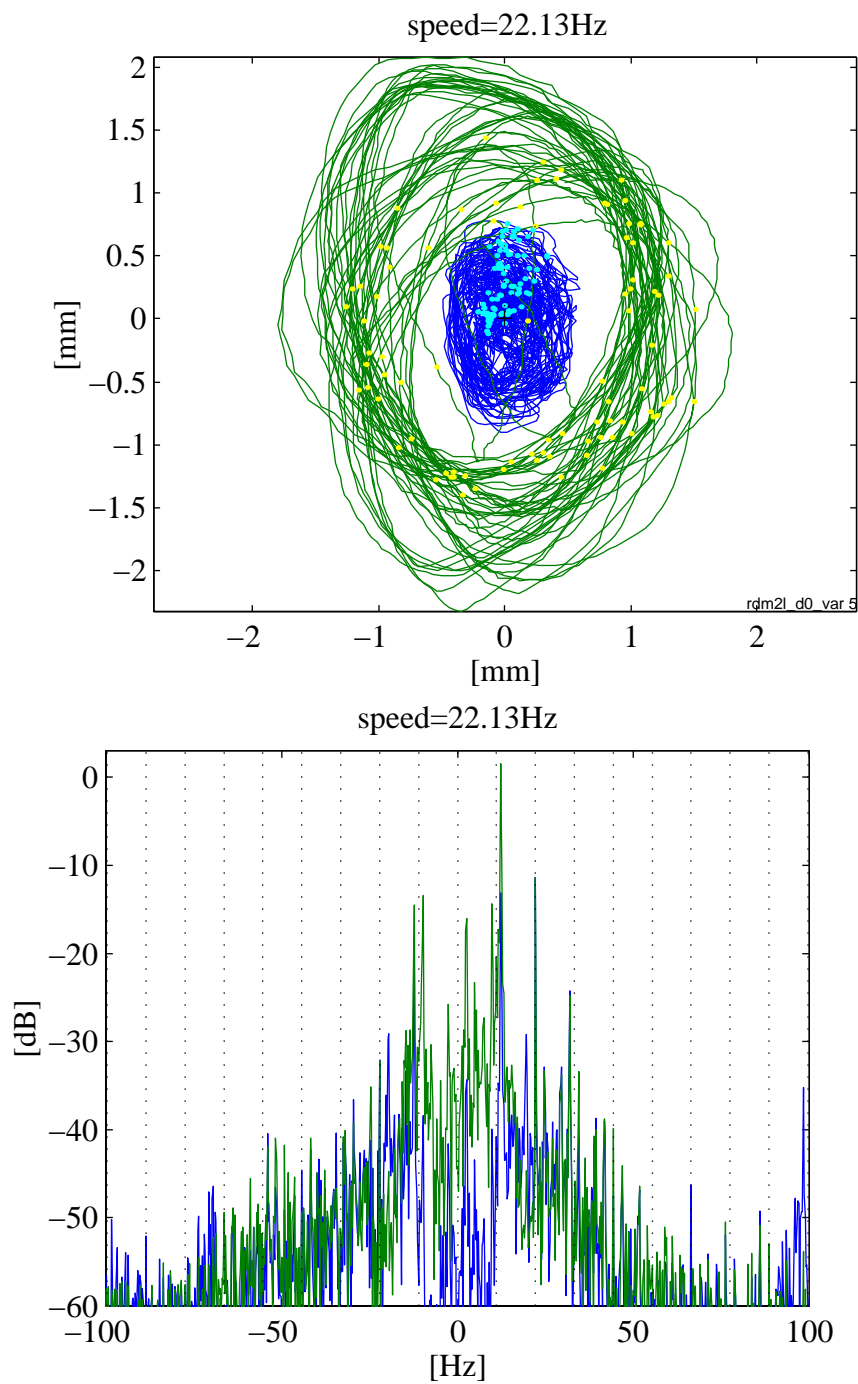
Figure 6.14: setup D, $\Omega = 22\,\text{Hz}$, lubrication: WD40, $\frac{1}{2}$EO grid
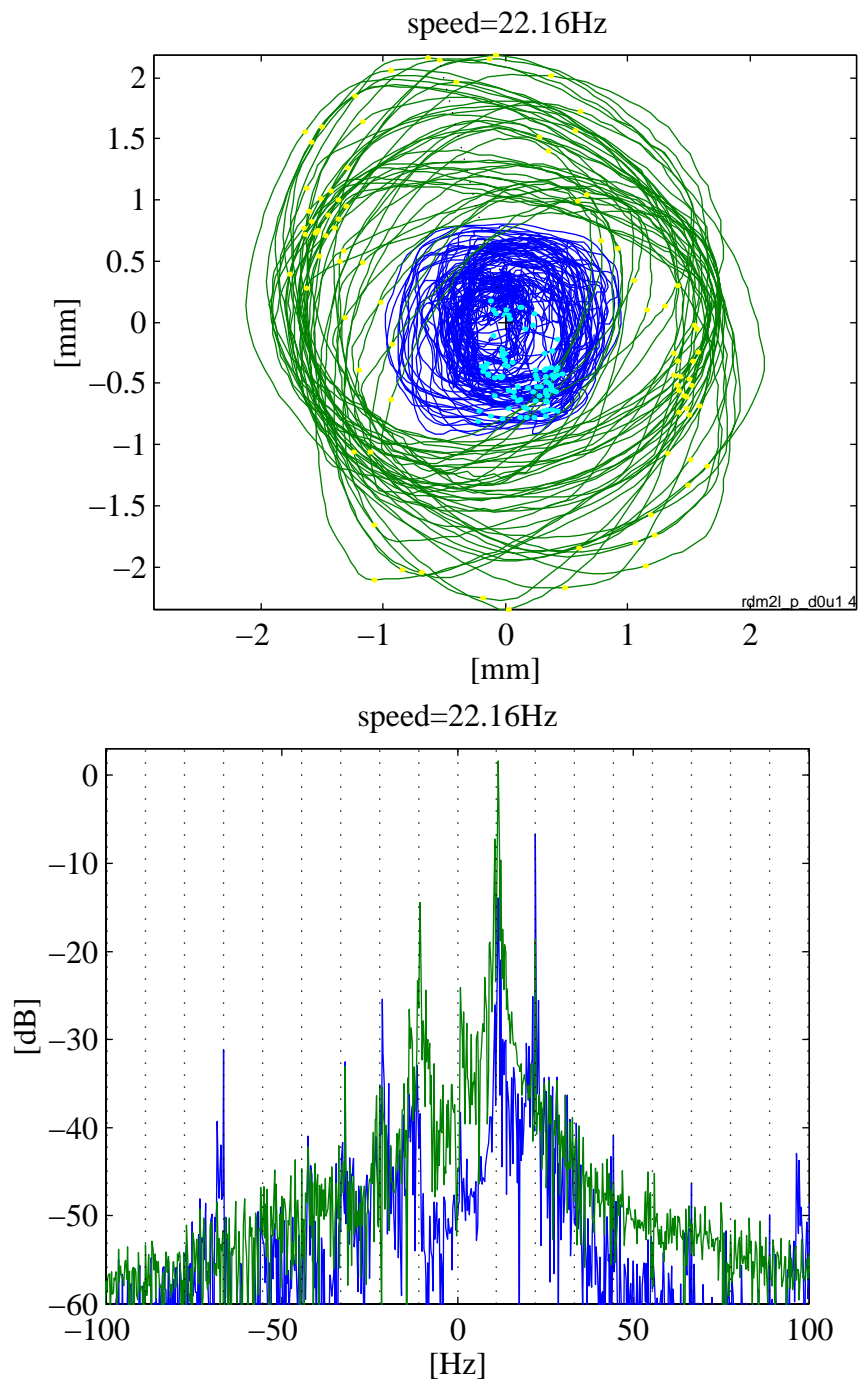
speed=22.16Hz

speed=22.16Hz

Figure 6.15: setup D, $\Omega = 22\,\text{Hz}$, plastic rim, $\frac{1}{2}$EO grid

6.4 Bladed Disc, Rigid Stator

6.4.1 Configuration

The rig was also run in the two main setups in a bladed (flexible) disc/rigid stator configuration: (i) low and (ii) medium stator support stiffnesses (stator system has (i) lower and (ii) higher natural frequency than rotor). These combinations will be abbreviated as G and H in the text (see Table 6.4 for details). In between measurement runs, the amount of out-of-balance ϵ_m in conjunction with the number of blades, and stator eccentricity ϵ_s were varied. The value of the natural frequency of the joint rotor/stator system, ω_{rs}, is left in Table 6.4 although the flexibility of the blades will allow rotor and stator to move far more independently of each other compared to the rigid disc configuration.

Table 6.4: rig parameters for bladed disc configuration

setup	$m_r\,[\,\mathrm{kg}\,]$	$m_s\,[\,\mathrm{kg}\,]$	$\omega_r\,[\,\mathrm{Hz}\,]$	$\omega_s\,[\,\mathrm{Hz}\,]$	γ_m	γ_s	$\approx \omega_{rs}\,[\,\mathrm{Hz}\,]$
G	1.8	7.0	21.3, 22.9	20.5	3.8	3.5	21
H	1.8	7.0	24.2, 25.9	10.6	3.8	0.74	14

6.4.2 Amplitude Jumps

For the bladed disc configurations the amplitude jump phenomenon exists just as it does for the rigid disc cases. The steady-state orbits for a stiff stator are shown in Figure 6.16, and it is clear that rotor and stator drop out of contact for speeds about 21Hz. Figure 6.17 shows the orbit plots for a flexible stator, and the speed of rotation was taken over 23Hz without rotor and stator losing contact.
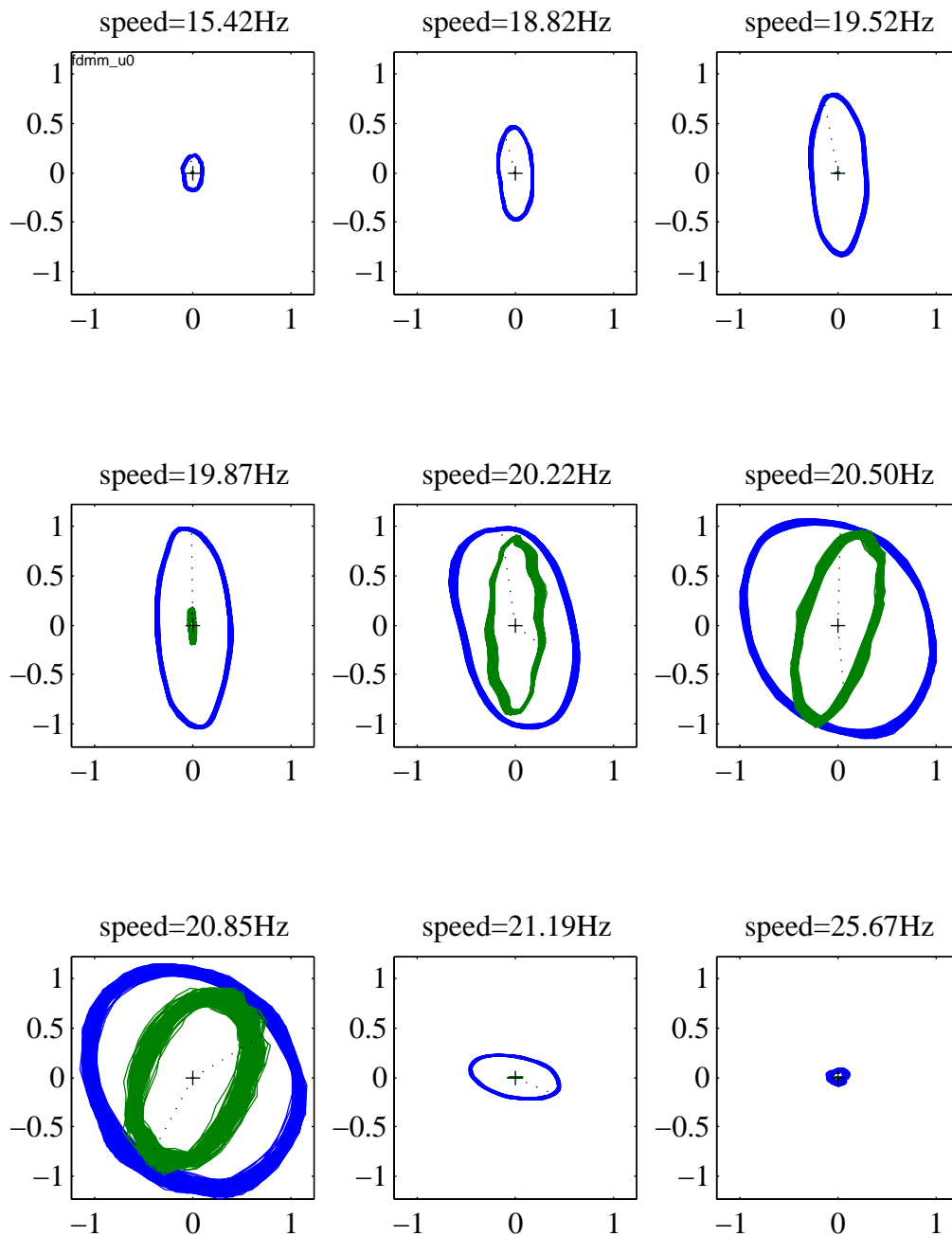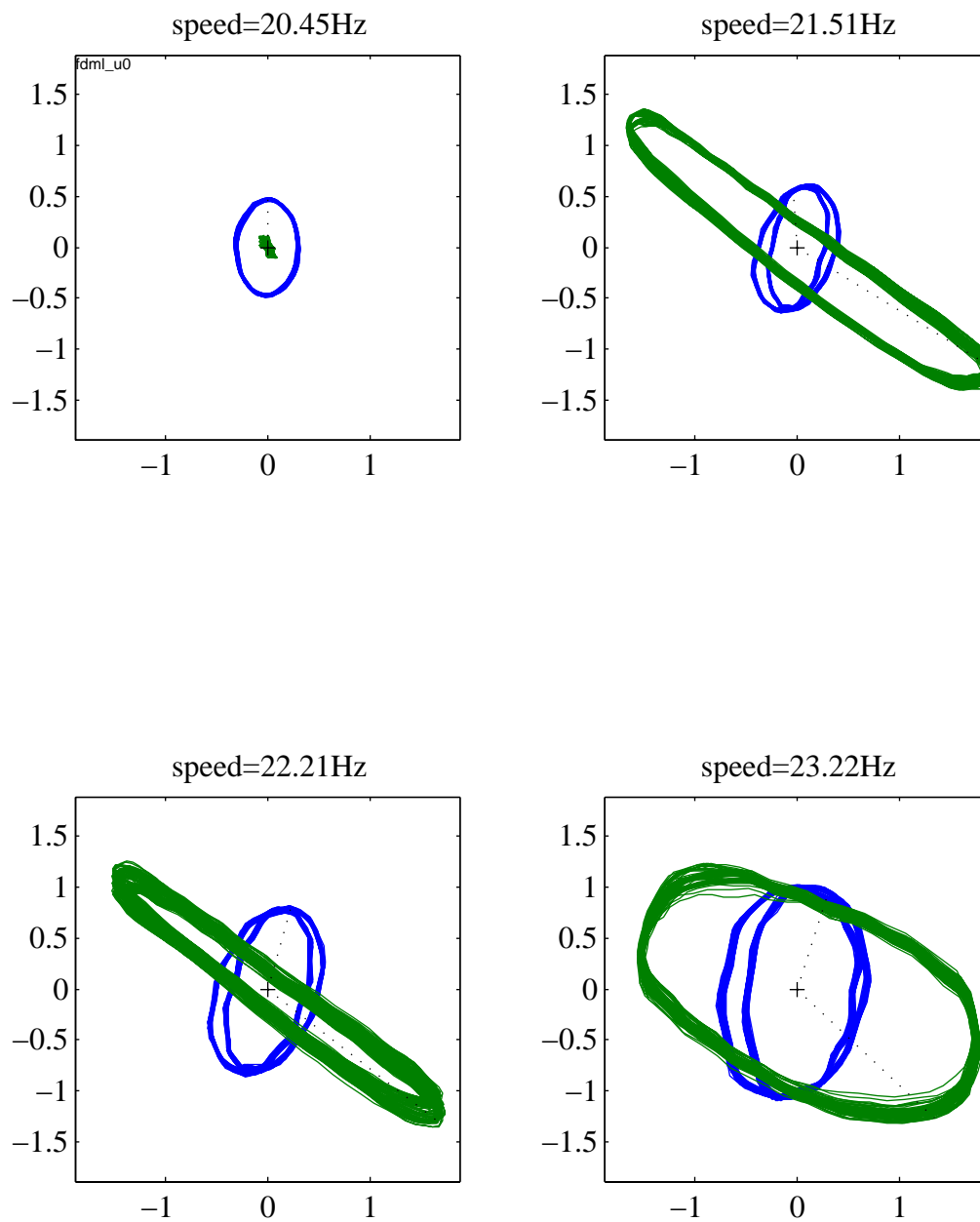
Figure 6.16: orbits [mm] with setup G

Figure 6.17: orbits [mm] with setup H

6.4.3　Sub- and Super-Harmonics

As can be seen in the following Figures 6.18–6.21, the blades allow for a more indepen-dent movement of rotor and stator compared with the rigid disc. The shaft, which has its dominant frequency component at 1EO, is rotating at roughly twice the resonance frequency of the stator, and the stator is chiefly vibrating in its first mode, which is a linear movement along a 45 ° line (an explanation for the mode as 45 ° can be found in the inevitably slightly mistuned setup of the 4 suspension bars). Correspondingly, the stator has its dominant frequency components at 1/2 EO, and the rotor at 1EO. The spectral lines in these plots are usually quite sharp, a notable exception being Figure 6.18, where the flanks of the 1/2 EO frequency components for the stator rise considerably, indicating that the stator movement is not quite in tune with the rotor disc movement. This has not been observed in the rigid disc configuration. Conversely, no evidence is found that the system responds with its joint rotor/stator frequency, which is so often the dominant frequency component in the rigid disc configuration. A-gain, this is explained with the much more compliant contact interface that the blades provide.

When the stator natural frequency is higher, as in setup G, in other words the shaft speed is not in a range as above, where it is close to an integer multiple of the stator frequency, the response of rotor and stator is much more unified and dominated by 1EO with some higher engine orders present. Figure 6.21 and 6.22 are enlargements of the orbits shown in Figure 6.16 and provide examples of this more EO oriented behaviour.
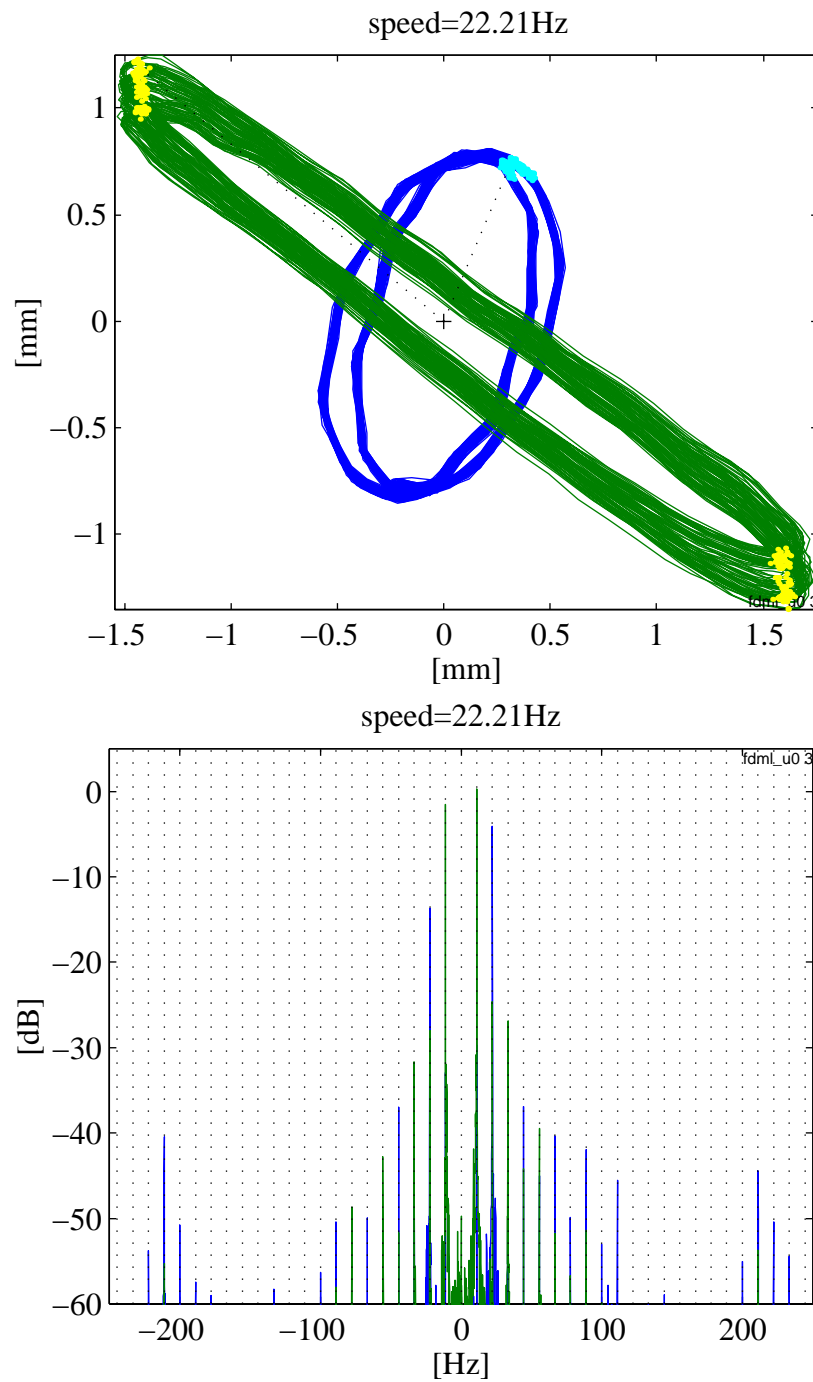
Table 6.5: frequencies with bladed discs/soft stators: setup H

Figure	$\Omega \, [\text{Hz}]$	$\omega_{\text{s}} \, [\text{Hz}]$	$\approx \frac{\omega_{\text{s}}}{\Omega}$
6.18	21.51	10.6	$\frac{1}{2}$
6.19	22.21	10.6	$\frac{1}{2}$
6.20	23.22	10.6	$\frac{1}{2}$

Table 6.6: frequencies with bladed discs/stiff stators: setup G, $\epsilon_{\text{s}} = 1.1 \, \text{mm}$

Figure	$\Omega \, [\text{Hz}]$	$\omega_{\text{s}} \, [\text{Hz}]$	$\approx \frac{\omega_{\text{s}}}{\Omega}$
6.21	19.87	20.5	$\frac{1}{1}$
6.22	20.85	20.5	$\frac{1}{1}$
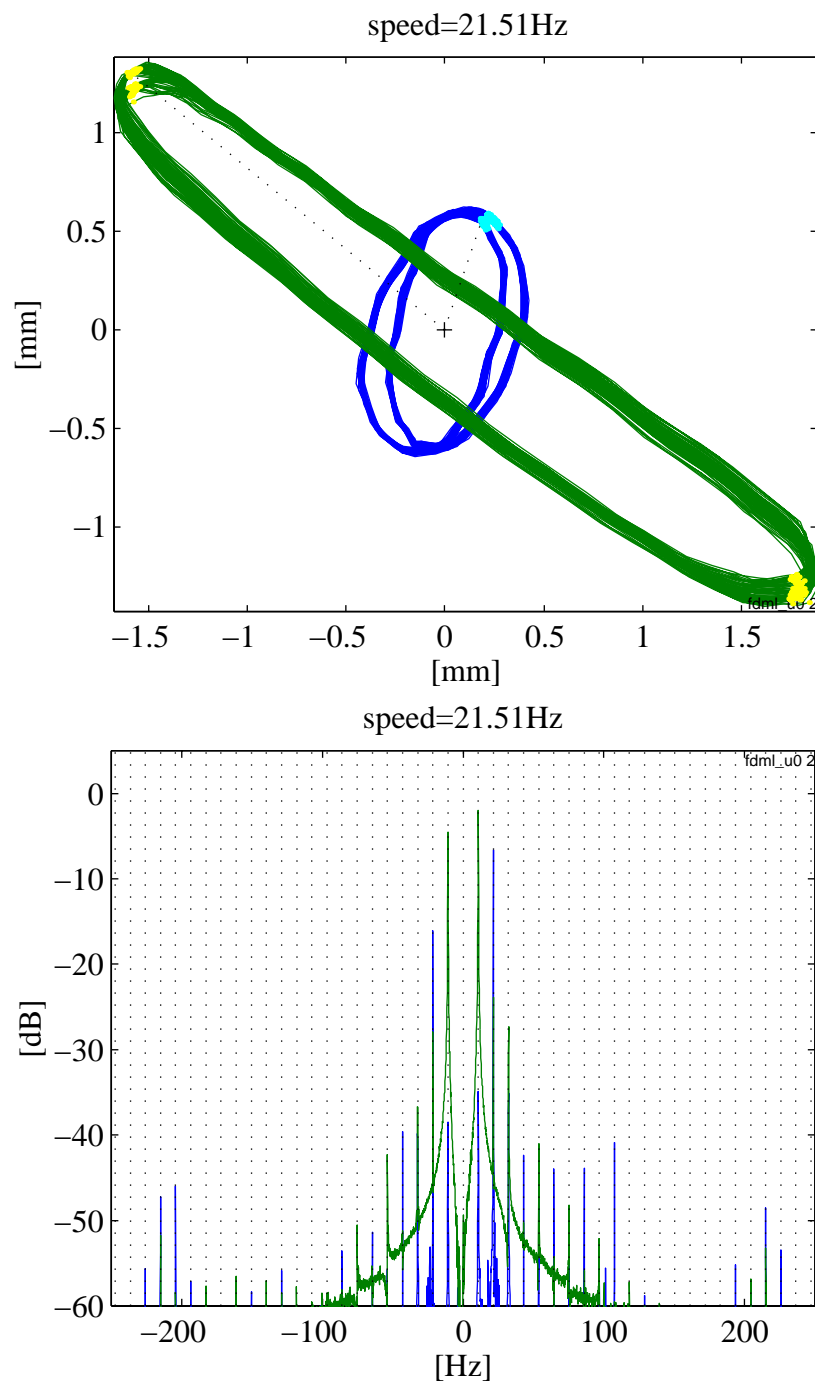
Figure 6.18: setup H, 21.51Hz, $\frac{1}{2}$EO grid

speed=22.21Hz

speed=22.21Hz

Figure 6.19: setup H, 22.21Hz, $\frac{1}{2}$EO grid

speed=23.22Hz

speed=23.22Hz
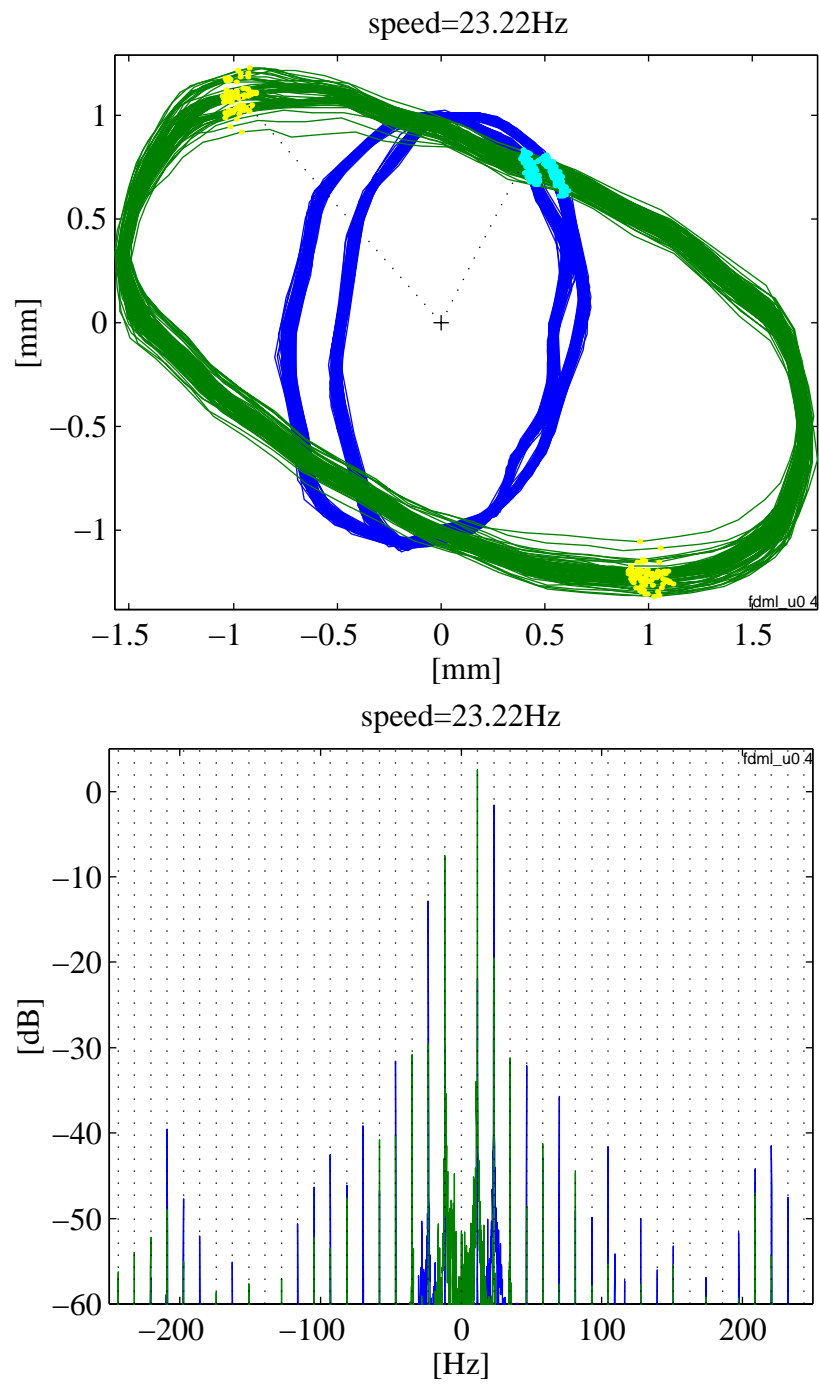
Figure 6.20: setup H, 23.22Hz, $\frac{1}{2}$EO grid
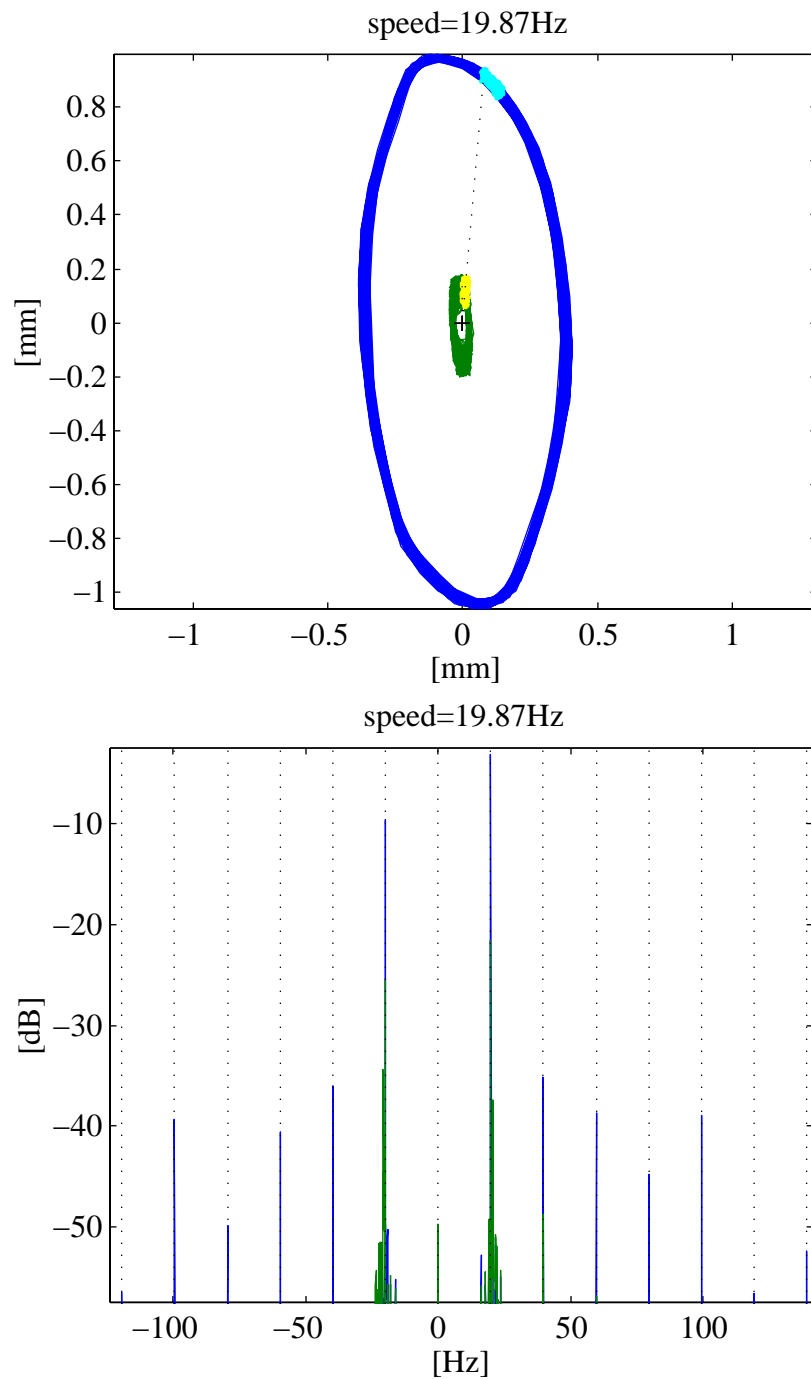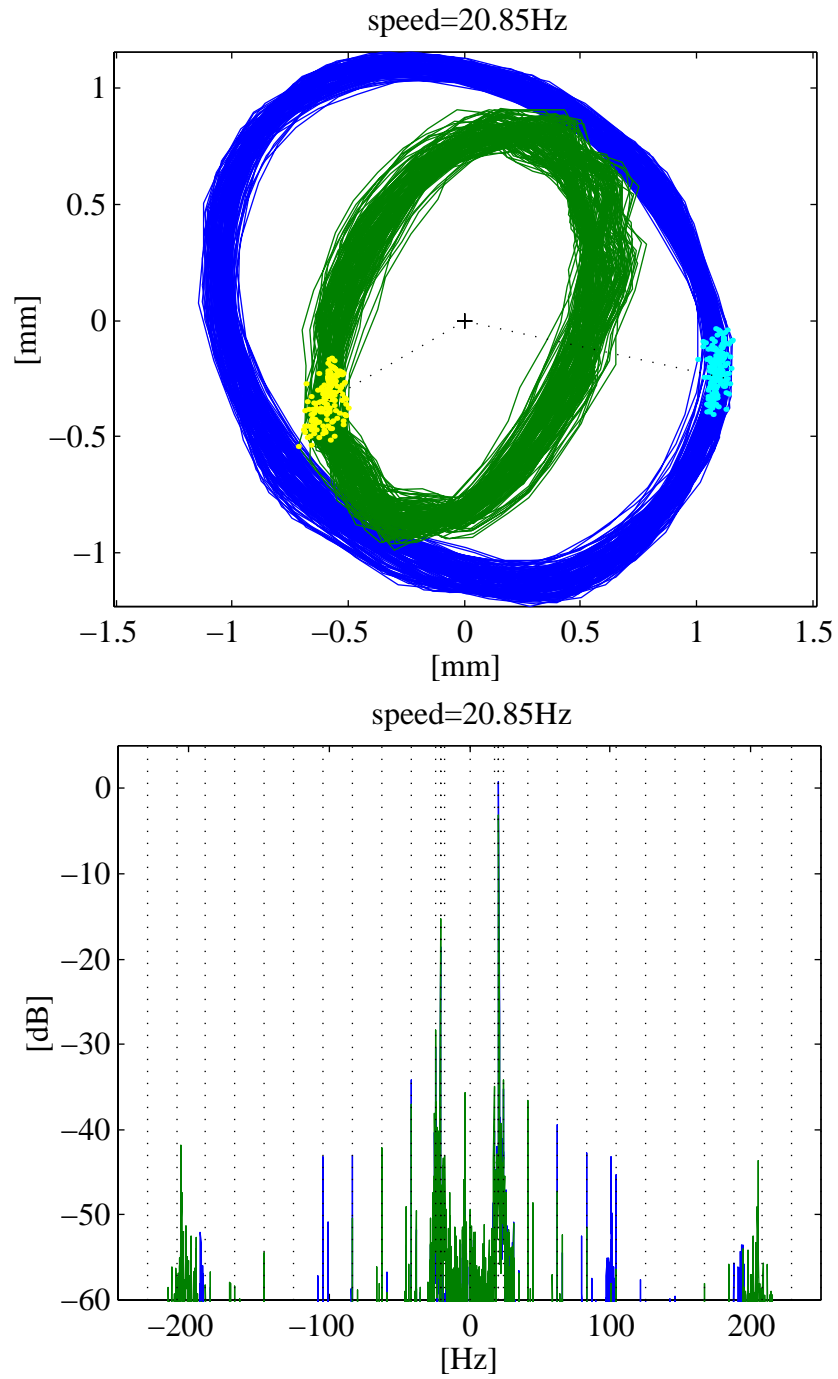
Figure 6.21: setup G, 19.87Hz

Figure 6.22: setup G, 20.85Hz, with $\frac{1}{6}$EO side bands

6.5   Summary

- The observed behaviour is generally in line with the simulation results presented in Chapter 4.

- The rotor showed non-linear behaviour even without any stator intervention. However, at higher speeds (over 12Hz) the frequency components due to the non-linearities were over 15–20dB lower than the 1EO frequency response, providing a lower limit as to what the range for interpreting the rotor/stator interaction might be (all measurements of rotor/stator contact were made at speeds well above 12Hz).

- Soft/stiff stator support conditions had an influence on whether or not the system would stay in contact at higher speeds. This is in line with the numerical predictions of the simple lumped mass model in Chapter 4.

- With a rigid disc, the 1EO response was the dominant frequency component in most cases. Super-harmonics were always observed, sometimes as high as 9 EO within 40dB of the maximum amplitude of the strongest harmonic.

- In some configurations, strong responses at the joint rotor/stator natural frequency were observed, occurring independently of shaft speed. Sub-harmonics were measured as low as 1/32 EO within 40dB of maximum amplitude.

- The different lubrication and contact materials chosen did not seem to make a difference in terms of encouraging or discouraging larger backward whirl components due to increased friction or a richer frequency spectrum of the response due to a harder contact. It is concluded that the test rig is not particularly sensitive to the parameters associated with friction and contact hardness.

- For both stiff and soft stator supports, the response spectra of the bladed disc configuration contained fewer frequency components than for the the rigid disc configuration.

- In the bladed disc configuration it was possible for the rotor and stator to vibrate more independently of each other, allowing the scenario of high stator responses at stator natural frequency and high rotor responses at 1EO simultaneously.

- There are no indications in the measured response spectra that the number of blades plays a significant role in enhancing certain frequencies which might have some relationship between blade number and running speed. Various blade numbers and irregularly spaced blade patterns were tested, and in all cases the fairly smooth motion with few frequency components was found that is already described above.

- Bladed disc and rigid disc configurations had a propensity to vibrate at natural frequencies or a combined natural frequency, respectively, especially when the unbalance force was not strong enough to force full annular contact.

- Geometric eccentricity of rotor and stator rings generally causes non-engine order components to appear.

- As the rotor orbits are never purely circular, there are always backward whirl components in the spectrum. However, the main direction of the whirl is forward, and, indeed, a friction-induced violent backward whirl is not excited.

Chapter 7

Comparison of Analytical and Experimental Results

7.1 Overview

With the measurements reported in the previous Chapter and the numerical results from Chapter 4, these two sets of experimental and simulated data can now be used for the validation procedure of the analytical approach. This chapter begins with a correlation of FE model predictions and modal tests that were carried out on the test rig structures. The FE model was brought in line with the modal test by simple manual model updating. This FE model was then used to validate the 4-degree-of-freedom lumped mass model, which was extensively used in the numerical parameter studies, as a sufficiently sophisticated reduction of the FE model. Finally, the results of the measurements are compared with predictions from the parameter studies of the 4DOF model. It is not intended here to repeat all the numerical results presented in Chapter 4 or the measurement results presented in Chapter 6, but to establish the level of qualitative and quantitative agreement between measurements and analysis on a few fundamental features. The level of agreement can then serve as a good indicator of how realistic the numerical predictions are with parameter configurations for which no corresponding measurement set exists.

7.2 Correlation of FE Model against Modal Tests

Correlation between modal test data and FE models and subsequent model updating are vast (and very active) research areas. In this case, however, the FE model is very simple, and the task of performing the correlation and updating was done manually in a few simple steps. The aim was to gain confidence that the FE model resembles the

windmill test rig well enough in its basic dynamic behaviour that it could be used as input into the windmill simulation code.

The first step was to perform a simple hammer test to obtain the frequency response function of the rotor shaft without any attachments. As the rotor shaft was uniform (no changes in cross-section), the FE representation consisted only of a few Timoshenko beam elements, all of equal diameter and material properties. The density was chosen such that the FE model matched the measured weight of the shaft. Damping was not included in the FE model at this stage, so the only remaining variable with minor uncertainty was Young's modulus, which was tuned such that the first 5 bending natural frequencies of the FE model prediction matched the measured ones well within 1% deviation (Figure 7.1). The next step was to test the rotor shaft with its three devices mounted that would carry the bearing races and rotor disc. These adaptor devices clamp onto the shaft with a taper/collet arrangement. Two ways to implement these in the model were tried.
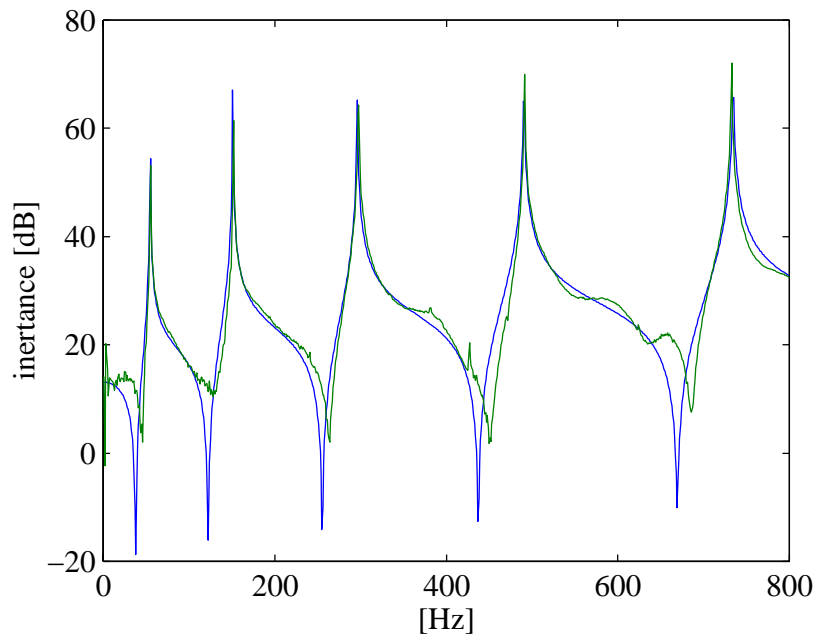

Figure 7.1: FRFs of rotor shaft: measurements (green) & FE model predictions (blue)

One way was to consider the taper/collet arrangement as extremely tight, treating the assembly as almost welded together and thus simply to increase the diameter of the relevant shaft elements to new values reflecting the thickness of the adaptors, as shown in Figure 7.2. The resulting FRF from the FE calculations is overlaid with the measured FRF, shown in Figure 7.3. The first two natural frequencies matched well, the higher remaining 4 frequencies were overestimated by the FE model, indicating that the model was too stiff.
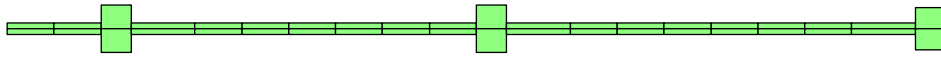
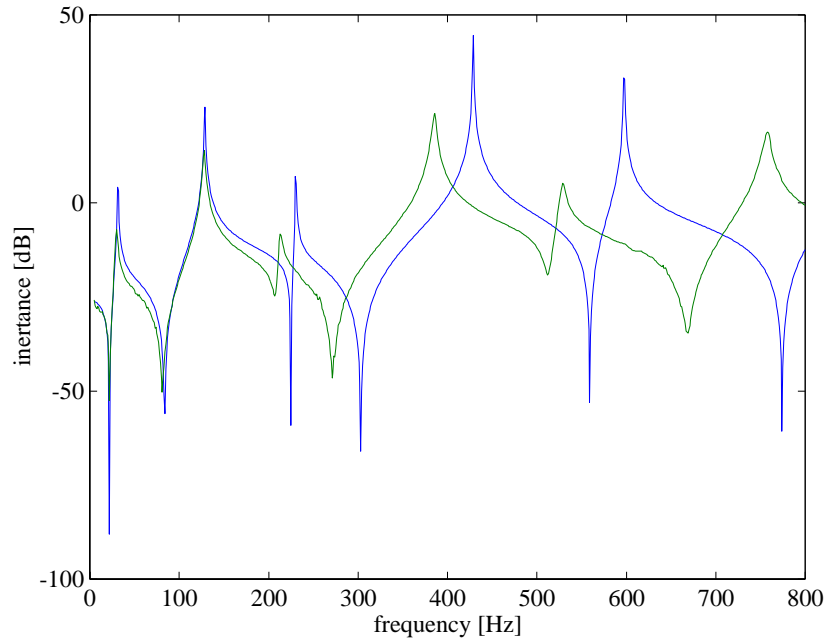Figure 7.2: FE model of rotor shaft, bearing collets modelled as discs

Figure 7.3: rotor measurements (green) & FE model predictions (blue, bearing collets modelled as discs)

Another way was to treat the adaptor arrangement as clamping the shaft only on a few points, without restricting the bending movement very much, and so not causing any local stiffening. This was implemented by simply adding lumped masses on the first and last nodes of each attachment element on the shaft to account for the extra inertia, as shown in Figure 7.4. Figure 7.5 shows the resulting FRF from the FE calculations versus the measured FRF. The first natural frequency matched well, but the other ones were underestimated, indicating that this approach was too soft.

Figure 7.4: FE model of rotor shaft, bearing collets modelled as masses

Not surprisingly, the truth seems to lie somewhere in the middle of these two approaches. By using the model of the second approach and simply increasing Young's modulus for the shaft elements where the adaptors are mounted, one can tune the system to match the measured FRF, shown in Figure 7.6. Modal analysis (Ewins, 1984) was conducted on the measured FRF to obtain damping values for the individual modes, and these values were used later in the windmill simulation runs.
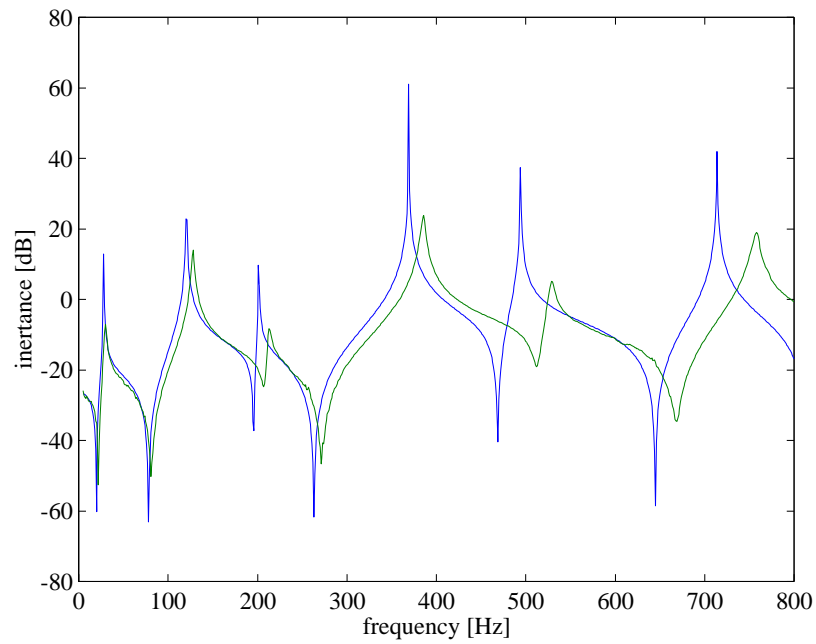
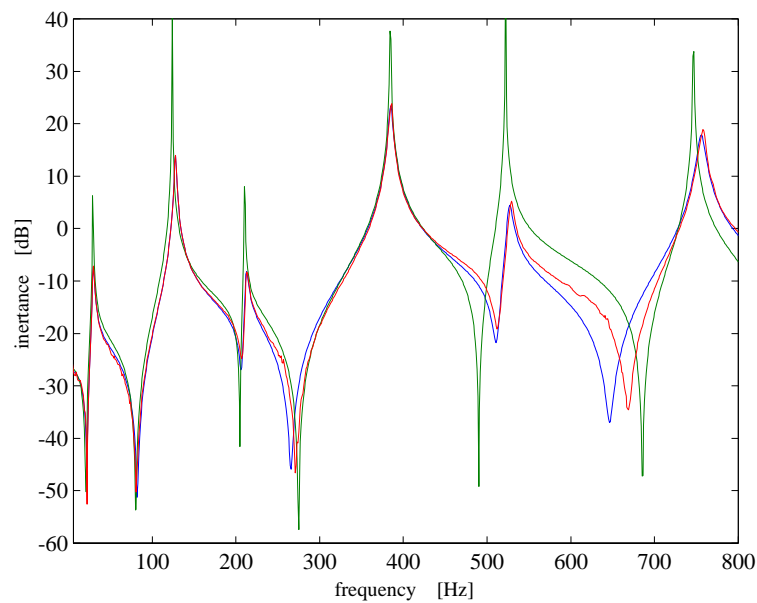Figure 7.5: rotor measurements (green) & FE model predictions (blue, bearing collets modelled as masses)

Figure 7.6: shaft measurements (red), regenerated FRF from modal analysis (blue) & FE model predictions after updating (green)

7.3   Validation of 4DOF Lumped Mass Model against FE Model

This section is a comparison of the 4DOF model that was used in the simulations of Chapter 4 and the FE model from the previous section that has been validated and tuned to the test rig measurements. The rotor with a rigid disc located at the mid-span position was modelled as a small FE model with 84 DOF. The time-marching solution method was chosen for both models over HBM as it does not require any knowledge about the frequencies occurring in the spectrum. The system was transformed into modal space and the first 5 modeshapes of the FE model were kept. At each time step the modal space was expanded back into physical space to calculate the contact forces, which were then transformed into modal space. In this way the model size was kept to a minimum without compromising on the ability to include the non-linear contact forces. It can be observed that the results for the FE model correlate well with the results from the 4DOF lumped mass model: both the orbits and the frequency spectra are very similar. In particular, no evidence is found in the spectra of the FE model response that the higher shaft modes like second (69Hz) or third (116Hz) bending modes are excited or at least facilitate a stronger response at higher frequencies compared to the 4DOF lumped mass model. This indicates that the 4DOF model is an adequate representation for the present configuration.
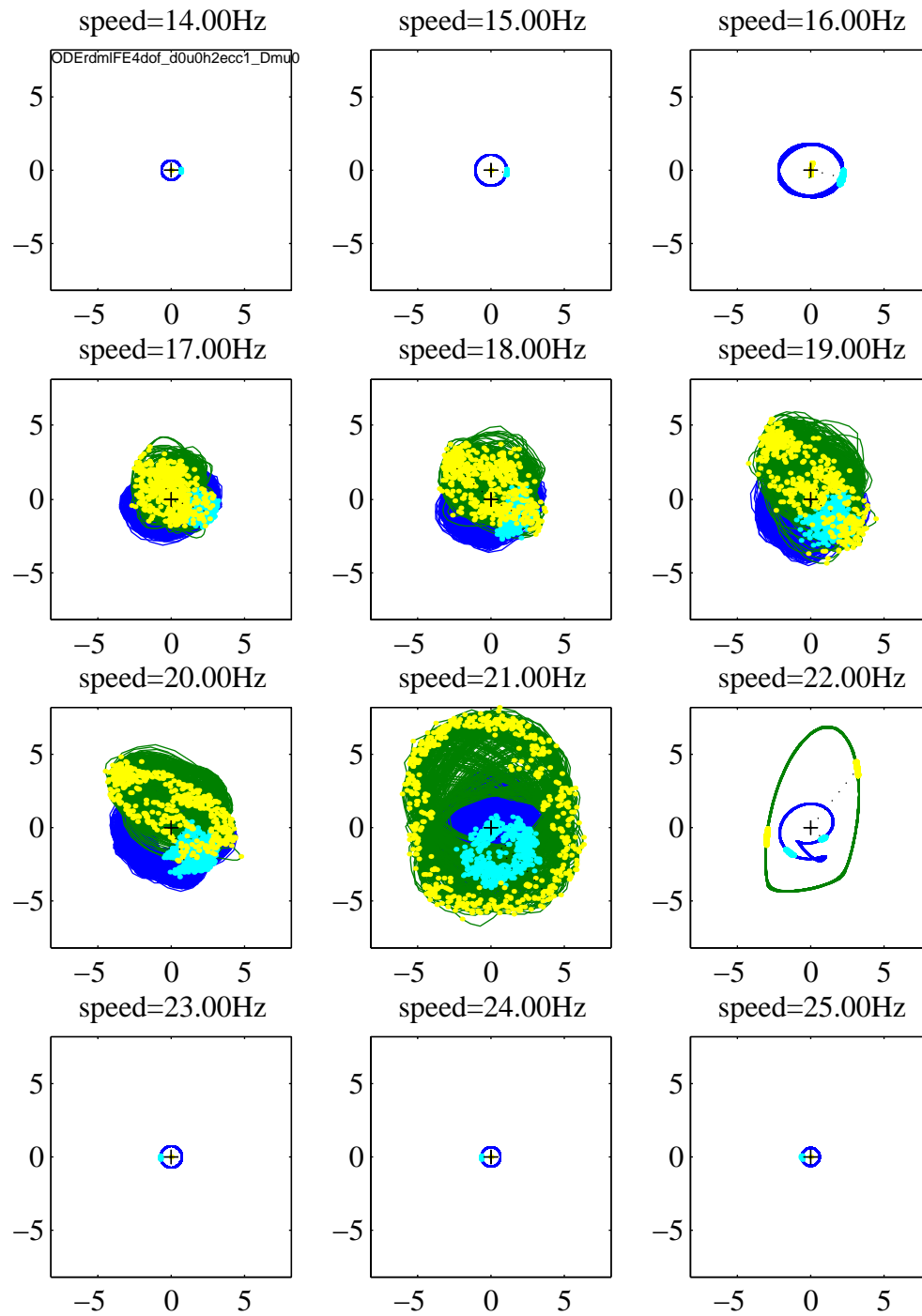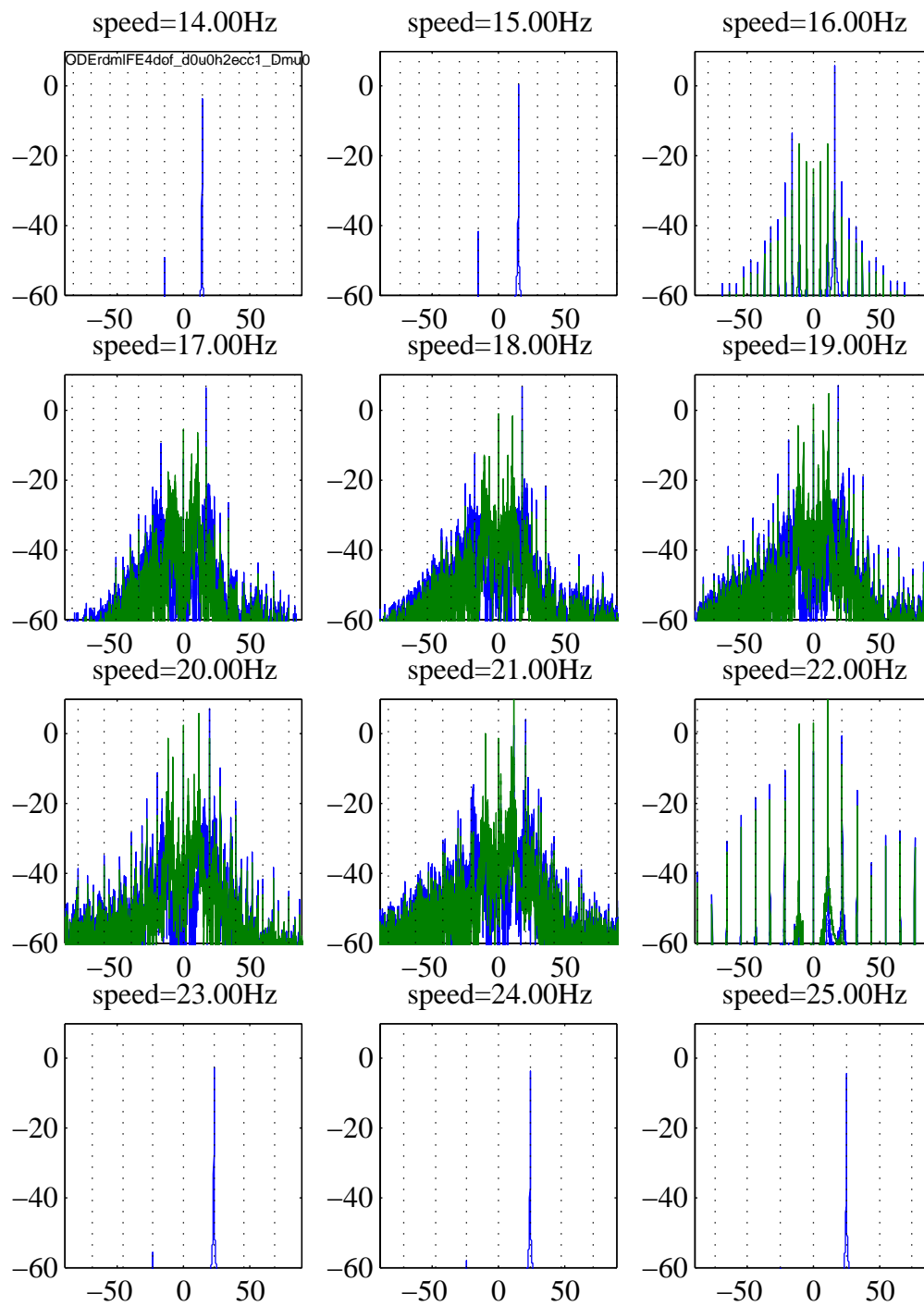
Figure 7.7: orbits [mm] of 4DOF model

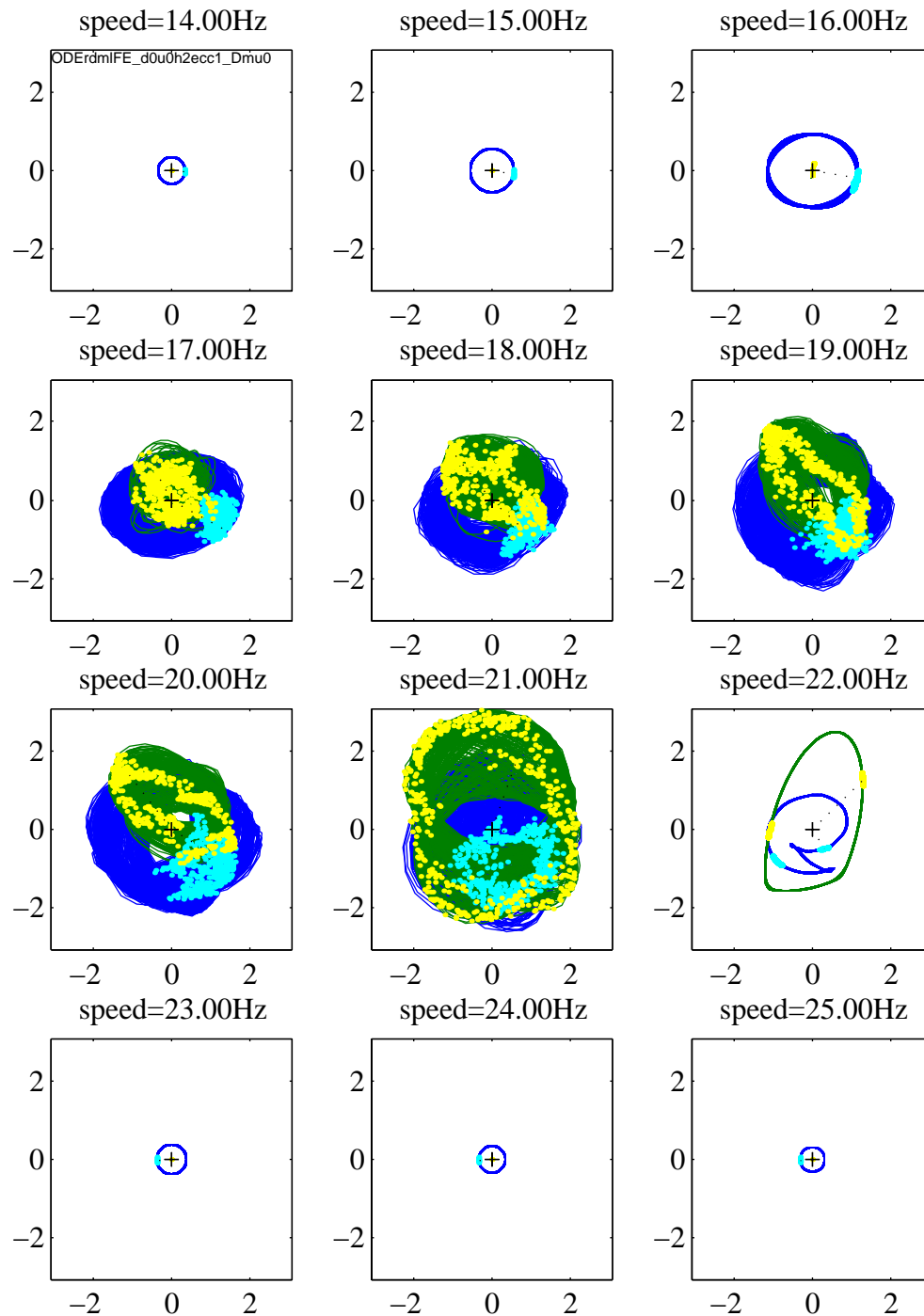Figure 7.8: frequency spectra [Hz] of 4DOF model
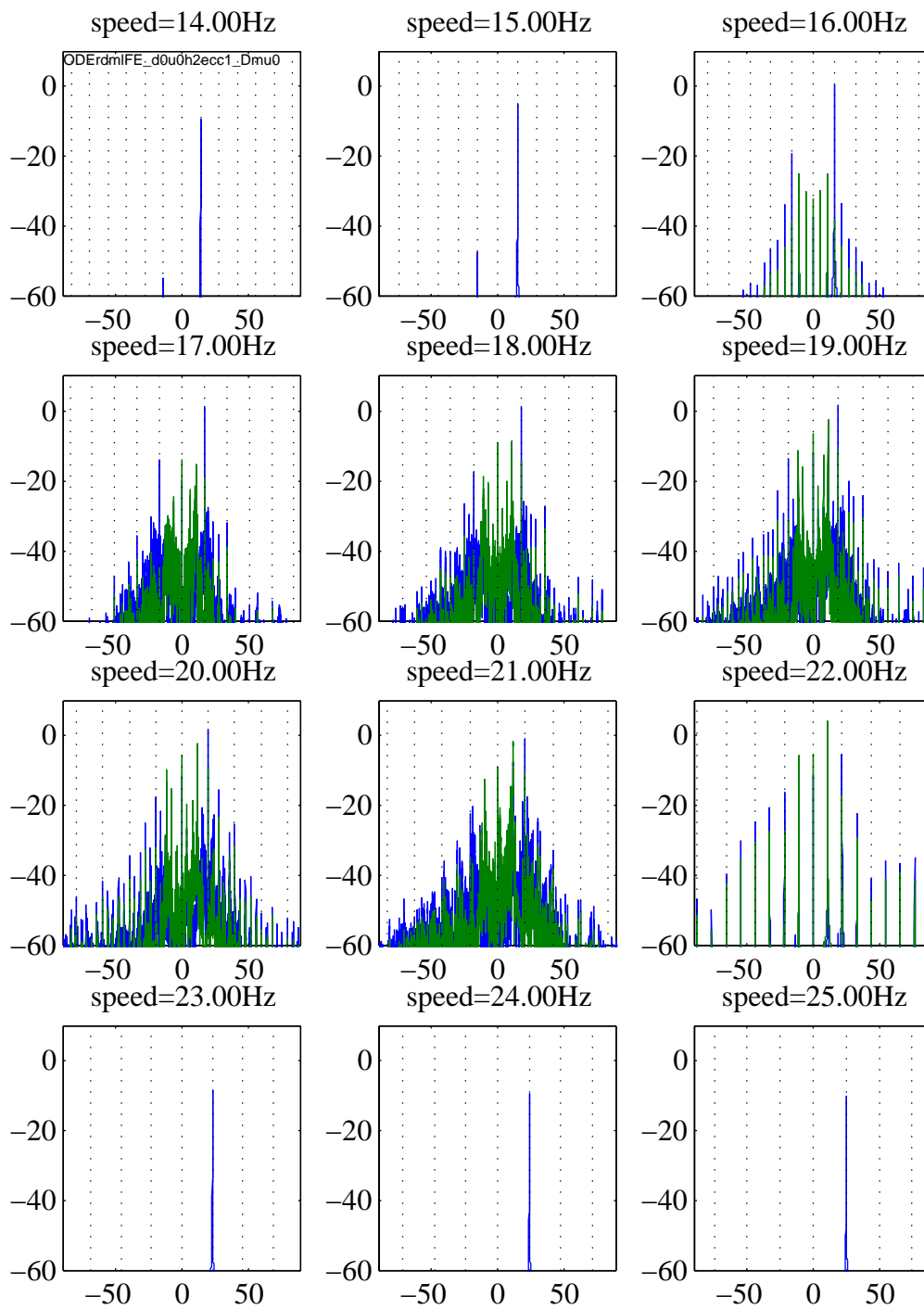
Figure 7.9: orbits [mm] of FE model

Figure 7.10: frequency spectra [Hz] of FE model

7.4   Comparison of simulation and windmill measurements

7.4.1   Amplitude jumps

One of the fundamental effects to check is the speed range over which rotor and stator remain in contact. In Figure 7.11 the amplitudes of the rotor and stator responses, predicted by the 4DOF model, are plotted for a range of stator stiffnesses. The main parameters, which were chosen to resemble the test rig structure, are: $\gamma_k = 0.6, 4$, and $\gamma_m = 2$. As will be discussed below, the qualitative agreement of simulated and measured behaviour is very high.

(a) stiff stator, $\gamma_k = 4$ (b) soft stator, $\gamma_k = 0.6$
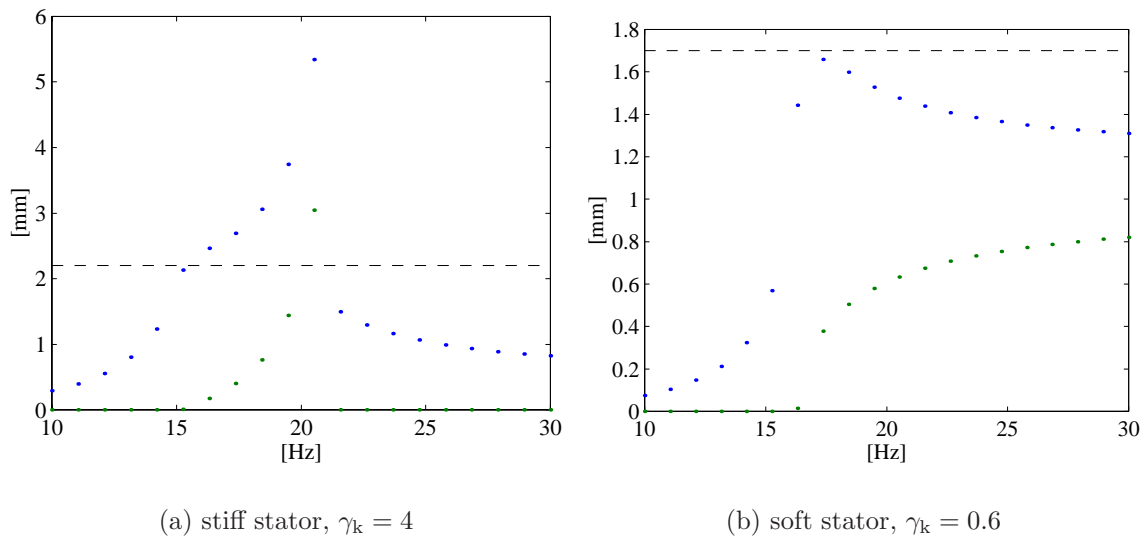
Figure 7.11: rotor/stator contact ranges (predictions)

Following the curve in Figure 7.11 for a stiff stator, $\gamma_k = 4$, from lower speeds to higher ones, one sees the jump phenomenon occurring (unstable part of solution not plotted) and afterwards rotor and stator are out of contact. One can see that, for the parameters used, at speeds $\Omega < 15\,\text{Hz}$ the rotor unbalance response is too low to overcome the clearance (dashed line) and the rotor and stator are not in contact (stator response zero). At speeds $15\,\text{Hz} < \Omega < 20\,\text{Hz}$ rotor and stator are in contact (non-zero stator response). At speeds $\Omega > 20\,\text{Hz}$, above the natural frequency of the rotor ($\omega_r = 17\,\text{Hz}$), the super-critically running rotor loses contact with the stator. Again, as observed in similar plots before, for a stator with a natural frequency lower than the rotor, rotor and stator keep in contact at higher speeds ($\gamma_k = 0.6$). No abrupt jump occurs and rotor and stator remain in contact over the entire range of higher speeds.

The full set of measurements have already been presented in Chapter 6, and reference will be made to that Chapter for the following discussion. Figure 6.5 shows

the orbits of setup A, which corresponds to the case of a stiff stator, $\gamma_k = 4$. It must be noted that the rotor measurements are not taken at the same axial location as the stator measurements. One could use the FE model presented in the previous section to obtain amplitude predictions for the rotor measurement location. However, the stator measurements are taken at the location of rotor/stator interaction, and thus allow a straight comparison. The measurements show a stator orbit of 0.5mm at the amplitude jump speed of $\Omega \approx 19\,\mathrm{Hz}$. The prediction of the 4DOF model of the stator orbit at this speed is within 20% of the measured value. The model predicts the jump to occur at amplitudes around 20Hz, whereas the steady-state speeds in the experiments only shows that the amplitude jump in the measurements occurs somewhere between 18.6Hz and 20.3Hz. Before commenting on these values, the second case with a soft stator is briefly discussed: Figure 6.4 shows the orbits measured in setup D, which corresponds to the case of a soft stator, $\gamma_k = 0.6$. At speeds past rotor resonance, the amplitudes converge slowly. From the measurements, this value lies around 0.7mm for the stator. The simulation predicts 0.8mm.

When looking for ways in which to explain these discrepancies, generally there are quite a few parameters in the simulation whose values are uncertain: the coefficient of friction that is to be assumed, the eccentricity (misalignment) of rotor and stator centre, which could only be measured crudely, the exact amount of unbalance of the rotor, as the added weight is accurately known, but the inherent rotor unbalance could only be estimated from the measurements presented in section 6.2. In light of these areas of uncertainty, the agreement in quantitative terms (amplitudes, frequency location of jumps) is felt to be as good as could be expected.

7.4.2   Frequency components

The measurements shown in Figures 6.8–6.11 of Chapter 6 illustrate the vibration of rotor and stator with very rich frequency spectra. For convenience, the orbits of these figures are shown here again in Figure 7.12. It is attempted in this section to replicate the behaviour numerically with a time-marching solution. Remarkable similarities can be found: the orbits and frequency spectra of the numerical simulation are shown in Figures 7.13 and 7.14. For $\Omega = 22\,\mathrm{Hz}$ the simulated orbit shows 11 clusters of 1/rev points, and the same is true for the top left measurement shown in Figure 7.12 (originally 6.8). Then, both numerically and experimentally, there follows a speed range of quasi periodic orbits or orbits with very low sub-harmonics (simulation $\Omega = 23\,\mathrm{Hz}$, top right measurement in Figure 7.12, originally 6.9). This regime changes to orbits dominated by $\frac{1}{2}$EO (simulation $\Omega = 24\,\mathrm{Hz}$, bottom left measurement in Figure 7.12, originally 6.10), and again followed by quasi-periodic motion. The ability of the numerical simulation to exhibit this complex rotor/stator interaction in a very similar manner to the measured results indicates that the modelling of the dynamic behaviour and the numerical methods employed are adequate for the task at hand.
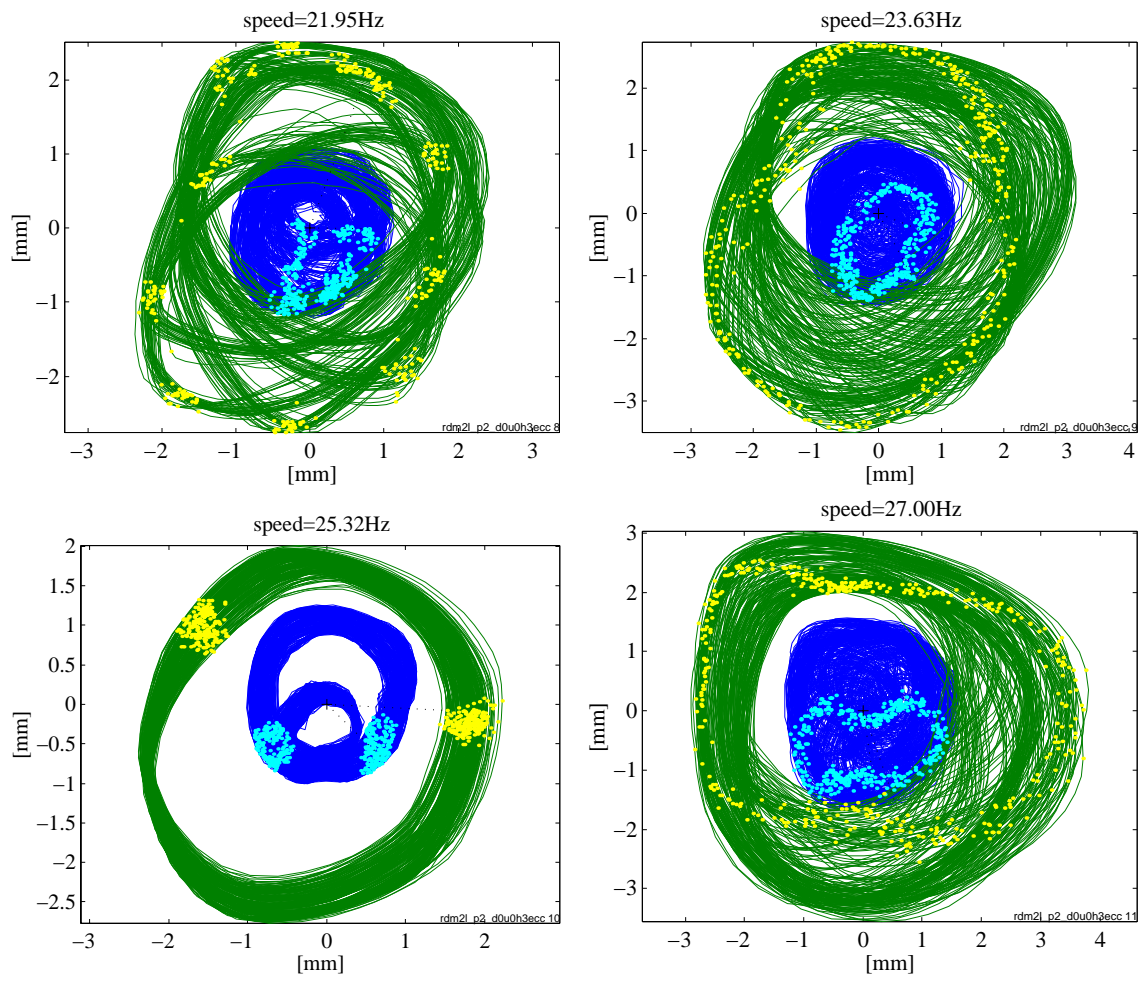
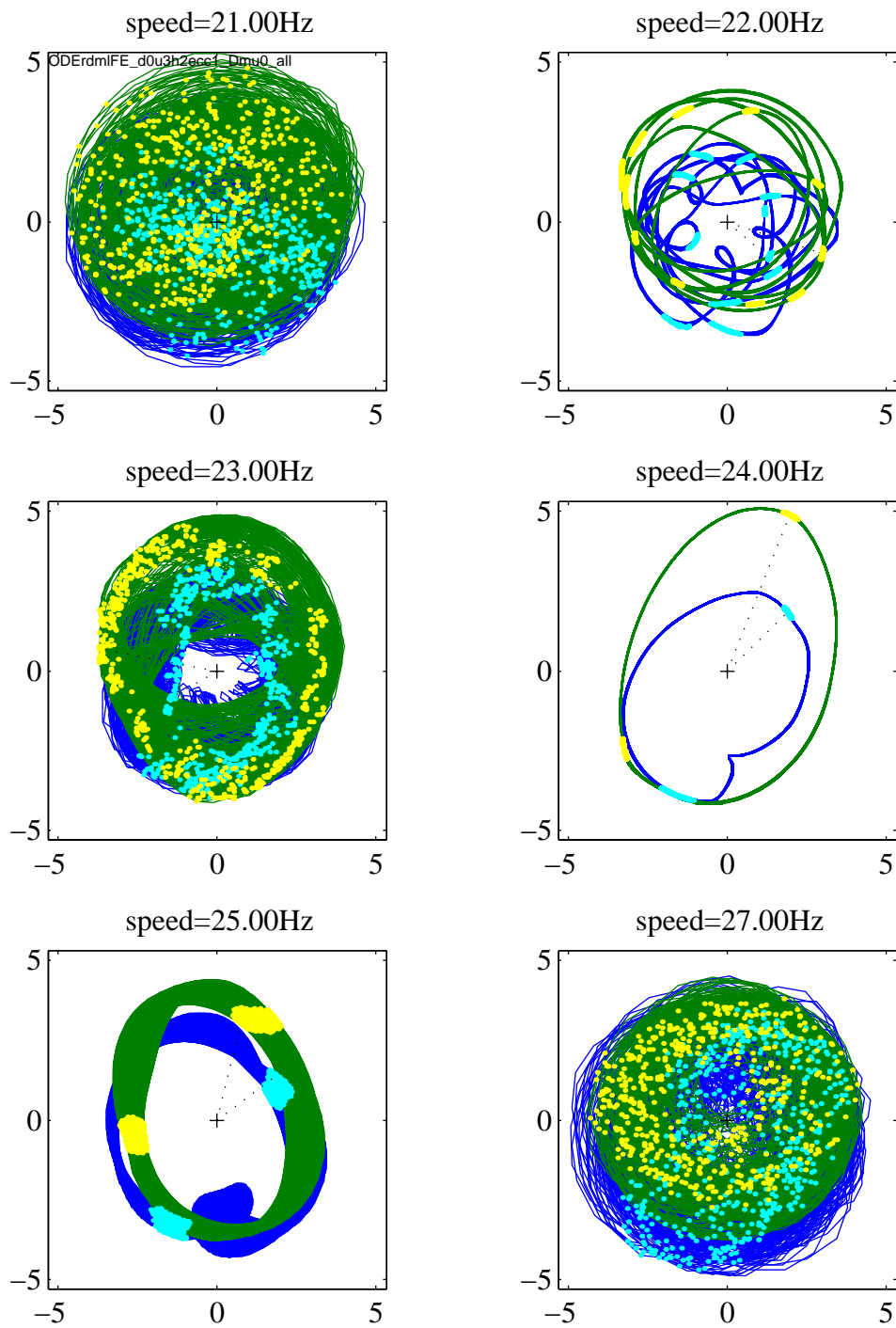Figure 7.12: measured orbits at steady speeds

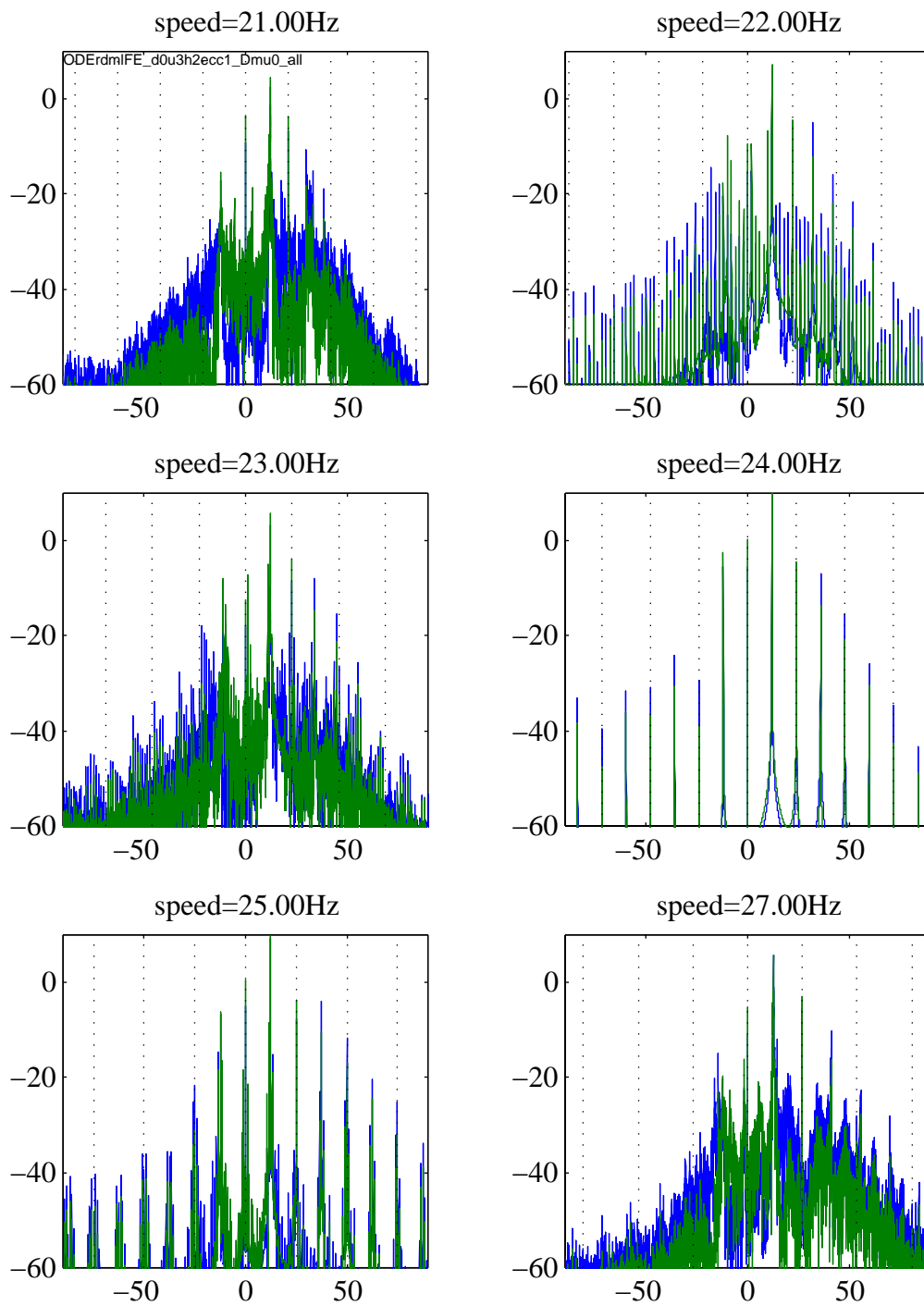Figure 7.13: orbits in [mm] of time-marching solutions at steady speeds

Figure 7.14: spectra [Hz] of time-marching solutions at steady speeds

Chapter 8

Conclusions

8.1 Thesis Summary

The first Chapter introduced the windmilling problem and identified and classified its physical elements. An approach to the modelling of the dynamic behaviour in the windmilling scenario was presented in Chapter 2. Using analysis and computational methods described in Chapter 3, numerical results from different rotor/stator configurations were presented and discussed in Chapter 4. The aim was to be able to model and to understand the dynamic aspects which distinguish the different parameter configurations possible and to investigate which parameters are responsible for which sort of particular behaviour. In order to provide a basis for validating the numerical simulations and to gain some experience of how accurately these simulations might model a physical system, a test rig was built according to the design principles laid out in Chapter 5. The measurement results obtained with that rig were evaluated in Chapter 6, and a comparison between measurements and simulation was carried out in Chapter 7. To close the circle, the present Chapter discusses how far the numerical and experimental efforts that led to these results have helped to achieve the objectives of the project that were laid out in the introduction of this thesis.

8.2 Project Objectives and Conclusions

This project set out to gain some insight into the rotor/stator interaction and overall system dynamics in a windmill situation. This insight consists of a physical understanding of the contributing dynamic mechanisms of the system, and the ability to model these mechanisms numerically. Thus, a suitable numerical model can then be used for windmill scenario predictions. The numerical predictions also help in obtaining an overview of characteristic features of the dynamic behaviour of a system under windmill conditions. The specific objectives of this project, which were stated in the introduction, were:

(i) to classify the physical elements and features of a windmilling system;

(ii) to build a mathematical model which describes the dynamic behaviour that includes a numerical representation for the nonlinear elements representing the rotor/stator contact;

(iii) to develop appropriate computation routines which are capable of solving the resulting non-linear differential equations which describe the dynamic behaviour of the model;

(iv) to build a test rig as a simple physical model with the basic elements of the windmill phenomenon, to measure its dynamic behaviour and to use these measurements to compare with the numerical simulations, thereby validating the numerical model, and

(v) to map out the range of dynamic behaviour and possible vibration phenomena in measurements and simulations of a windmill system.

Revisiting these objectives, and correlating them with the work done, allows us to establish what contributions have aided the understanding and handling of the windmill phenomenon and to what extend has the aim of the project been achieved.

In respect of (i)   As the windmilling problem is relatively new, no literature currently exists which deals with this problem explicitly. However, the literature review in the first Chapter covered a wide range of individual features that researchers had studied in different contexts for similar phenomena introducing rotor/stator interaction. From these features, a small range of physical elements were identified to form the fundamental set of ingredients in a windmill scenario.

In respect of (ii)   A simple 4DOF dynamics model was developed that translates the physical features of the system into numerical program modules. This model was shown to be capable of exhibiting a rich dynamic behaviour. Later on in the course of the project, a more detailed finite element representation of the system was developed. It showed very similar results to the lumped mass 4DOF system, thereby justifying the use of the simple dynamic system in this approach. However, being able to use a more general FE model opens the way to analysing more complex structures, and ultimately to a full engine model, thus proving that the numerical routines used to solve the non-linear ODE here are capable of handling more general multi-degree-of-freedom systems.

In respect of (iii)   Algorithms operating in the time-domain and frequency-domain were adapted to solve not only the equations for the small nonlinear 4DOF model but also those for a larger, more general FE model. Advantages and disadvantages of the time-domain and frequency-domain methods were discussed. A novel method that

facilitates the stability analysis of a solution in the frequency-domain was presented. Multiple periodic solutions were observed and some of these multiple solutions are easily found by following a solution branch with the arc-length continuation scheme. However, new periodic solutions (the so-called 'inverted' modes) have been presented which had not been encountered in the results of the literature dealing with related problems. These solutions are part of a different solution branch, and have so far only been found by a brute-force trial-and-error search approach.

In respect of (iv)   The measured behaviour of the test rig was generally in line with the results based on the numerical simulations. The measured sizes of the orbits, the speed ranges of rotor/stator contact and the occurrence of high super- (up to 9EO) and low sub-harmonic (down to $\frac{1}{32}$EO) frequency components were all well represented by the numerical model. The bladed disc configuration did not exhibit any fundamentally new behaviour by comparison with the the rigid disc. However, for both stiff and soft stator supports, the response spectrum of the bladed disc configuration contained fewer frequency components than the rigid disc configuration. It was also possible (in the case of the bladed disc) for the rotor and stator to vibrate more independently of each other, causing different dominant frequencies for rotor and stator movement.

From the above statements it is concluded that: (a), the relevant physical features are correctly translated into the numerical model and (b), the model and the algorithms do provide the capability to study the windmill scenario numerically. The results of these simulations show a rich dynamic behaviour that is also found in the experimental test rig. This may justify the conclusion that the simulation results that follow from the approach to the dynamic modelling of the problem together with the numerical solution procedures are not mock results only existing in numerical models but must be expected to occur in physical systems as well.

In respect of (v)   A further contribution of this study is the overview that emerged of the range of dynamic behaviour that a windmilling system could exhibit. Amplitude jumps are found and are caused by the nonlinear system stiffness. The levels of rotor and stator damping, as well as the choice of friction model, have an effect on the speed range over which rotor and stator stay in contact. The ratios of rotor/stator mass have an even stronger effect, which may cause the rotor and stator to stay in continuous contact almost irrespective of the speed of rotation. Multiple periodic solutions were found to exist over some speed ranges: experimentally, the upper branch was investigated during a slow acceleration and the lower branch during a deceleration. Super-harmonic vibration was predicted and measured and is attributed to non-isotropic geometry or stiffness — for example misalignment or a constant side force. In this scenario, sub-harmonics occurred when the contact between rotor and stator became intermittent. This led to the conclusion that not only the 1EO frequency (windmill-speed) needs to be checked against possible resonance frequencies of the wing/airframe structure,

but that sub-harmonic vibration components could potentially excite the lower modes, thereby causing larger vibration amplitudes of the wing/airframe structure.

8.3 Outlook

In light of the above conclusions it is felt that this exercise has established good confidence in the modelling of the fundamental mechanisms of windmilling and has given an insight to the occurrence of the related phenomena. The interpretation of these results with respect to their relative importance in a realistic windmilling situation will evolve over time as simulations in industry with full engine models are conducted. Also, there will be without doubt ongoing work in industry to achieve numerical models which resemble more closely full scale aero-engines. Much of that work will involve the 'fine tuning' of the models to achieve higher quantitative agreement between measurement and simulation. Part of this task will be: (i) improving the accuracy with which certain parameters, such as friction or contact stiffness of the blades, can be specified, (ii) extending the numerical contact module to allow for effects such as shortening (due to wear or plastic deformation) of the blades, and (iii) including a representation of mistuning, non-axisymmetric inertia, and flexible discs through a larger number of degrees-of-freedom in the model.

During the course of this study there were inevitably practical difficulties, both of numerical or experimental nature, that had to be resolved. Some of these difficulties would form a worthwhile project in their own right, and thus are beyond the scope of this work. It has already been mentioned that reverse or backward whirl is an active area of research, albeit the system configuration in these projects is quite different from a typical windmill configuration, most notably the absence of large out-of-balance forces. The test rig that was built for this project, as well as the simulations, did not show a high propensity to go into reverse whirl. However, it certainly would be interesting to extend the reverse whirl studies to include windmill configurations, even if the expected response frequencies are not very likely to be in the low sub-harmonic engine-order region and large out-of-balance forces might provide a disincentive for the system to go into reverse whirl.

Another area that might need to be tackled in the windmill context is the inclusion of torsional oscillation. This thesis takes its underlying assumption that the fan rotates at constant speed (which is determined by the speed of the aeroplane) from aerodynamic calculations carried out by the company sponsoring this project. The resulting torque on the shaft, in particular for the new generation of engines with wide-chord fan blades, is judged to be sufficiently large that friction forces from rotor/stator interaction are unlikely to change the rotor speed significantly. However, if, for specific configurations, this assumption no longer holds true, and the friction force *does* change the speed of the shaft, there would be an immediate feedback loop that affects the dynamic behaviour of the system, as the change in rotor speed also changes the amount

of unbalance force, and thus the rotor/stator contact force, which again influences the amount of friction. Torsional vibration of the rotor shaft is then coupled to the translatory motion of the engine assembly. The problems with implementing this feature into the analysis are much less of a numerical nature, as the algorithms that have been used in this project are sufficiently general to be able to handle the inclusion of torsional vibration. The challenge lies in providing an adequate fluid/structural dynamic model, where the change in shaft speed due to friction forces is coupled with the change in drive torque due to the changing aerodynamics on the blades. One can also easily imagine that it would be an immense task to build a test rig for this configuration.

References

Alford, J. (1965). Protecting turbomachinery from self-excited rotor whirl. *Transactions of the ASME, Journal of Engineering for Power*, pages 333–334.

Ascher, U., Mattheij, R., and Russel, R. (1995). *Numerical Solutions of Boundary Value Problems for ODEs*. SIAM.

Bently, D. E. (1974). Forced subrotative speed dynamic action of rotating machinery. *ASME Paper*, 74-PET-16.

Bucher, I. and Ewins, D. (1997). Multidimensional decomposition of time-varying vibration response signals in rotating machinery. *Mechanical Systems and Signal Processing*, 11(4):577–601.

Childs, D. W. (1978). The space shuttle main engine high-pressure fuel tubopump rotordynamic instability problem. *Transactions of the ASME, Journal of Engineering for Power*, 100(1):48–57.

Childs, D. W. (1982). Fractional-frequency rotor motion due to nonsymmetric clearance effects. *Transactions of the ASME, Journal of Engineering for Power*, 104(3):536–541.

Choi, Y.-S. and Noah, S. T. (1987). Nonlinear steady-state response of a rotor support system. *Journal of Vibration, Acoustics, Stress, and Reliability in Design*, 109(1):255–261.

Choi, Y.-S. and Noah, S. T. (1988). Forced periodic vibraton of unsymmetric piecewise-linear systems. *Journal of Sound and Vibration*, 121(1):117–126.

Choy, F. K. and Padovan, J. (1987). Non-linear transient analysis of rotor-casing rub events. *Journal of Sound and Vibration*, 113(3):529–545.

Choy, F. K., Padovan, J., and Batur, C. (1989). Rub interactions of flexible casing rotor systems. *Transactions of the ASME, Journal of Engineering for Gas Turbines and Power*, 111:652–658.

Crandall, S. and Lingener, A. (1990). Backward whirl due to rotor/stator contact. In *Proc. XII Intl. Conf. Nonlinear Oscillations*, Krakow, Poland.

Crandall, S. H. (1987). Nonlinearities in rotor dynamics. In *Proceedings of the eleventh*

international conference on nonlinear oscillations, pages 44–56, Budapest. Janos Bolyai Mathematical Society.

Crandall, S. H. (1990). From whirl to wip in rotordynamics. In Lalanne, M. and Henry, R., editors, *3rd International Conference on Rotordynamics*, Éditions du Centre National de la Recherche Science, pages 19–26, Lyon. IFToMM.

Dimarogonas, A. D. and Paipetis, S. A. (1983). *Analytical Methods in Rotor Dynamics*, chapter Heat-flow-Induced vibration of rotating shafts — the Newkirk effect, pages 112–142. Applied Science Publishers, London and New York.

Ehrich, F. F. (1966). Subharmonic vibrations of rotors in bearing clearance. *ASME Paper*, 66-MD-1.

Ehrich, F. F. (1969). The dynamics stability of rotor-stator radial rubs in rotating machinery. *ASME transactions: Journal of Engineering for Industry*, pages 1025–1028.

Ehrich, F. F. (1988). High order subharmonic response of high speed rotors in bearings clearance. *Transactions of the ASME, Journal of Vibration, Acoustics, Stress, and Reliability in Design*, 110(1):9–16.

Ehrich, F. F. (1989). A state-of-the-art survey in rotordynamics — nonlinear and self-excited vibration phenomena. In *Proceedings of the Second International Symposium on Transport Phenomena, Dynamics, and Design of Rotating Machinery*, volume Part II, pages 3–25, Honolulu.

Ehrich, F. F. (1992). Observations of subcritical superharmonic and chaotic response in rotordynamics. *Transactions of the ASME, Journal of Vibration and Acoustics*, 114:93–100.

Ehrich, F. F. (1993). Rotor whril forces induced by the tip clearance effect in axial flow compressors. In Wang, K. W. and Segalman, D., editors, *Vibration of Rotating Systems*, volume DE-Vol.60 of *The ASME Design Technical Conferences — 14th Biennial Conference on Mechanical Vibrations and Noise*, pages 7–17. The Design Engineering Division, ASME.

Ehrich, F. F. and O'Connor, J. J. (1967). Stator whirl with rotors in bearing clearance. *Transactions of the ASME, Journal of Engineering for Power*, pages 381–390.

Ek, M. C. (1980). Solution of the subsynchronous whirl problem in the high pressure hydrogen turbomachinery of the space shuttle main engine. *Journal of Spacecraft and Rockets*, 17(3).

Ewins, D. J. (1984). *Modal Testing: Theory and Practice.* Research Studies Press.

FAA (1999). FAA draft advisory circular: Transport airplane directorate propulsion Mega AC 25-XX. Federal Aviation Administration. Subsection E-1.

Flowers, G. T. and Wu, F. (1996). Disk / shaft vibration induced by bearing clearance effects: Analysis and experiment. *Transactions of the ASME, Journal of Vibration and Acoustics*, 118:204–208.

Fumagalli, M. and Schweitzer, G. (1996). Measurements on a rotor contacting its housing. In *Sixth International Conference on Vibrations in Rotating Machinery*, pages 779–788, Oxford. Institution of Mechanical Engineers.

Gasch, R. and Knothe, K. (1989). *Strukturdynamik II*. Springer.

Genta, G. (1988). Whirling of unsymmetrical rotors: A finite element approach based on complex co-ordinates. *Journal of Sound and Vibration*, 124(1):27–53.

Genta, G. (1999). *Vibration of Structures and Machines*. Springer, third edition.

Géradin, M. and Kill, N. (1988). Non-linear dynamic analysis of flexible rotors. In *Fourth International Conference on Vibrations in Rotating Machinery*, pages 627–634. Institution of Mechanical Engineers.

Ghauri, M. K. K., Fox, C. H., and Williams, E. J. (1996). Transient response and contact due to sudden imbalance in a flexible rotor-casing system with support asymmetry. In *Sixth International Conference on Vibrations in Rotating Machinery*, pages 383–394, Oxford. Institution of Mechanical Engineers.

Goldman, P. and Muszynska, A. (1993). Chaotic behaviour of rotor/stator systems with rubs. *ASME Paper*, 93-GT-387.

Hohlrieder, M. and Irretier, H. (1996). On modelling elastic disc and shaft systems for numerical eigenfrequency analysis. In *Sixth International Conference on Vibrations in Rotating Machinery*, pages 1–11, Oxford. Institution of Mechanical Engineers.

Hunt, K. H. and Crossley, F. R. E. (1975). Coefficient of restitution interpreted as damping in vibroimpact. *Transactions of the ASME, Journal of Applied Mechanics*, pages 440–445.

Isaksson, J. L. (1994). On the dynamics of a rotor interacting with non-rotating parts. Licentiate's thesis, Linköping University.

Isaksson, J. L. (1996). Unbalance response analysis of a two-mass rotor system including rubbing effects. In *Sixth International Conference on Vibrations in Rotating Machinery*, pages 395–403, Oxford. Institution of Mechanical Engineers.

Ishida, Y., Yasuda, K., and Murakami, S. (1997). Nonstationary oscillation of a rotating shaft with nonlinear spring characteristics during acceleration through a major critical speed (a discussion by the asymptotic method and the complex-FFT method). *Transactions of the ASME, Journal of Vibration and Acoustics*, 119(1):31–36.

Kellenberger, W. (1980). Spiral vibrations due to the seal rings in turbo-generators thermally induced interaction between rotor and stator. *Transactions of the ASME,*

Journal of Mechanical Design, 102:177–184.

Kim, Y. B. and Noah, S. T. (1991). Steady state analysis of a nonlinear rotor housing system. *Transactions of the ASME, Journal of Engineering for Gas Turbines and Power*, 113:550–556.

Kim, Y. B., Noah, S. T., and Choi, Y.-S. (1991). Periodic response of multi disk rotors with bearing clearances. *Journal of Sound and Vibration*, 144(3):381–395.

Kleczka, M., Kreuzer, E., and Schiehlen, W. (1992). Local and global stability of a piecewise linear oscillator. In Thompson, J. M. T. and Schiehlen, W., editors, *Nonlinear dynamics of engineering systems*, pages 533–546. The Royal Society.

Kroon, R. P. and Williams, W. A. (1939). Spiral vibration of rotating machinery. In *Proc. 5th Int. Congr. Appl. Mech.*, page 712, New York. John Wiley.

Liebich, R. and Gasch, R. (1996). Spiral vibrations — modal treatment of a rotor-rub problem based on coupled structural/thermal equations. In *Sixth International Conference on Vibrations in Rotating Machinery*, Oxford. Institution of Mechanical Engineers.

Lingener, A. (1990). Experimental investiagion of reverse whirl of a flexible rotor. In Lalanne, M. and Henry, R., editors, *3rd International Conference on Rotordynamics*, Éditions du Centre National de la Recherche Science, pages 13–18, Lyon. IFToMM.

Markert, R. and Wegener, G. (1995). Dynamik von elastischen Rotoren in Fanglagern. In *Schwingungen in Rotierenden Maschinen*, volume III. Vieweg.

Muszynska, A. (1984). Partial lateral rotor to stator rubs. In *Third International Conference on Vibrations in Rotating Machinery*, York. Institution of Mechanical Engineers.

Muszynska, A. (1989). Rotor-to-sationary eement rub-related vibration phenomena in rotating machinery — literature survey. *Shock and Vibration Digest*, 21(3):3–11.

Nayfeh, A. and Balachandran, B. (1995). *Applied Nonlinear Dynamics*. John Wiley & Sons.

Newkirk, B. L. (1926). Shaft rubbing. *Mechanical Engineering*, 48(8):830–832.

Padovan, J. and Choy, F. K. (1987). Nonlinear dynamics of rotor/blade/casing rub interactions. *Transactions of the ASME, Journal of Turbomachinery*, 109:527–534.

Parker, T. S. and Chua, L. O. (1989). *Practical Numerical Algorithms for Chaotic Systems*. Springer.

Randall, R. B. (1987). *Frequency Analysis*. ISBN 87 87355 07 8. Brüel & Kjær.

Schmiechen, P. (1997). *Travelling Wave Speed Coincidence*. PhD thesis, University of London, Imperial College of Science, Technology and Medicine.

Schmied, J. (1987). Spiral vibrations of rotors. In *The ASME Design Technical Conferences — 11th Biennial Conference on Mechanical Vibrations and Noise*, volume DE-Vol.2, pages 449–456. The Design Engineering Division, ASME.

Seydel, R. (1994). *Practical Bifurcation and Stability Analysis*. Springer.

Sundararajan, P. and Noah, S. T. (1997). Dynamics of forced nonlinear systems using shooting / arc-length continuation method — application to rotor systems. *Transactions of the ASME, Journal of Vibration and Acoustics*, 119:9–20.

Thomas, J. J. (1958). Instabile Eigenschwingungen von Turbinenläufern, angefacht durch die Spaltströmungen, Stopfbuchsen und Beschaufelungen. Technical report, AEG. Sonderdruck.

Tondl, A. (1990). Rotor instability due to the leakage flow induced pressure acting on the rotor disc. In Lalanne, M. and Henry, R., editors, *3rd International Conference on Rotordynamics*, Éditions du Centre National de la Recherche Science, pages 3–8, Lyon. IFToMM.

Wegener, G. and Markert, R. (1998/1999). Vibro-inpact phenomena in the dynamics of elastic rotors with retainer bearings. In *Proceedings of the EUROMECH Colloquium 386*. Springer.

Williams, R. J. (1996a). Measurements of reverse whirl. BRITE-EURAM project ROSTADYN technical report 4.10, 4.16, and 4.22.

Williams, R. J. (1996b). Parametric study of reverse whirl instability using an analytical equilibrium model. BRITE-EURAM project ROSTADYN technical report 4.17.

Williams, R. J. (1997). Prediction of rub induced reverse whirl using finite element transient dynamics time marching method. BRITE-EURAM project ROSTADYN technical report 4.23.

Xu and Gasch (1993). Kleiner Beitrag zur Behandlung linearer periodisch zeitvarianter Bewegungsgleichungen. ILR-Mitteilung 278, Institut für Luft- und Raumfahrt der Technischen Universität Berlin.

Yakubovitch, V. A. and Starzinskii, V. M. (1975). *Linear differential equations with periodic coefficients*. John Wiley & Sons, Jerusalem.

Zhang, W. (1988). Dynamic instability of multi-degree-of-freedom flexible rotor systems due to full annular rub. In *Fourth International Conference on Vibrations in Rotating Machinery*. Institution of Mechanical Engineers.

Ziegler, A. (1996). A state of the art review on Thomas/Alford forces. BRITE-EURAM project ROSTADYN technical report 2.03, University of Kaiserslautern.